Ultrasound-activated Agents for the Treatment of Chronic Wound Biofilms



Christopher Keith Campbell

St Edmund Hall
University of Oxford

October 26th, 2024

Nuffield Department of Orthopaedics, Rheumatology and Musculoskeletal Sciences

Supervisors: Dr. Dario Carugo, Dr. Gareth LuTheryn, Prof. Eleanor Stride
Prof. Nicholas D. Evans, Dr. Peter Glynne-Jones, Prof. Jeremy Webb

A thesis submitted for the degree of
Doctor of Philosophy

Abstract

Chronic wound (CW) biofilms present a significant therapeutic challenge due to their enhanced antibiotic tolerance and the protective effects of the extracellular polymeric substances (EPS) matrix. The development of ultrasound (US)-responsive, nitric oxide (NO)-loaded, perfluoropentane (PFP)-core perfluorocarbon droplets (PDs) was investigated as a novel treatment modality for CW biofilms. A controlled positioning apparatus was developed to enable repeatable manufacture of PDs, with the effect of adjusting manufacturing conditions on PD size characteristics comprehensively evaluated. Increasing PFP volumetric concentration significantly increased PD mean diameter, while increasing sonicator tip height strengthened this relationship. An oxygen-free NO-loading method was developed and characterised using chemiluminescence detection, achieving NO_x concentrations of 4.57 ± 0.34 µM in 20% v/v PFP formulations. High-speed imaging established parameters to achieve consistent acoustic droplet vaporization (0.5 MHz, 2.48 MPa peak negative pressure, 39 °C). When tested on a *Pseudomonas aeruginosa* CW biofilm model, PDs were

observed to cause the formation of gas pockets that produced distinct morphological changes in the biofilm structure, with hemispherical regions of disruption ranging in diameter from ∼15 to ∼100 µm. Enhanced disruption was observed in both NO-loaded conditions, with and without US stimulation. NO-loaded PDs combined with US-stimulation demonstrated the strongest anti-biofilm effects, with a 37.9 ± 8.20% reduction in biomass and 63.1 ± 0.03% reduction in coverage area. An estimated mean NO_x concentration of 67.5 ± 2.5 nM NO was applied to the biofilms, within the concentration range known to induce biofilm dispersal. This work establishes the potential of US-activated NO-loaded PDs as a therapeutic strategy for the management of CW biofilms. The effects of this treatment modality on the structure and biomass of biofilms warrant further investigation.

Declaration

I hereby declare that this submission is my own work and, to the best of my knowledge, it contains no materials previously published or written by another person, or substantial proportions of material which have been accepted for the award of any other degree or diploma at the University of Oxford or any other educational institution, except where due acknowledgement is made in the thesis.

Any contribution made to the research by others, with whom I have worked at the University of Oxford or elsewhere, is explicitly acknowledged in the thesis. I also declare that the intellectual content of this thesis is the product of my own work, except to the extent that assistance from others in the project's design and conception or in style, presentation and linguistic expression is acknowledged.



Christopher Keith Campbell

Acknowledgements

I would like to thank my supervisors Dr. Dario Carugo, Dr. Gareth LuTheryn, Prof. Eleanor Stride, Prof. Nicholas D. Evans, Dr. Peter Glynne-Jones, and Prof. Jeremy Webb for their support, guidance, and feedback throughout this project.

Above all, I am deeply grateful to my supervisor Dr. Dario Carugo, whose mentorship has been the foundation of this work from the start. His unwavering support, both professional and personal, has been invaluable to me. My sincere appreciation goes to Prof. Eleanor Stride, whose support enabled my project to reach its full potential and made me feel so welcome at Oxford.

I extend my heartfelt thanks to Dr. Gareth LuTheryn for his instrumental support throughout this project, particularly during the most challenging periods. I am extremely grateful to Prof. Nicholas Evans and Dr. Jon May for their support during the pandemic in particular, helping me to get started on my project. I owe special thanks to Dr. Luca Bau for his willingness to engage with my many ideas and for the generous time he devoted to our discussions. I want to recognise the crucial support provided by Dr. Tanveer Tabish and Dr. Qiang Wu, which was indispensable to completing major portions of this project. I also wish to thank Dr. Malavika Nair for her guidance in the final phases of my project, which was both insightful and reassuring during the last stretch.

I wish to acknowledge the staff at FEPS (MechEng), IDS (Bone & Joint) and NDORMS for their consistent and dedicated support. I'm especially grateful to Afsie and Sam at NDORMS for their wonderful assistance and kindness.

My heartfelt thanks go to all my friends in Oxford, Southampton, and beyond. There are too many wonderful people to name individually, but you know who you are and how much you mean to me. Your friendship has kept my spirits high through the toughest moments, and I'm eternally grateful. To Kirsten, thank you for all the support throughout the years, I couldn't have asked for a better collaborator for our first first-author paper! To Colm and Aaron, thank you for your steadfast moral (and sometimes experimental!) support. I'd like to express my appreciation to Sara and Veerle for supporting me through numerous science communication ventures - you have helped me grow tremendously.

A special thanks goes to Victor, whose encouragement and unwavering faith in my potential have helped me grow as a scientist. Thank you for believing in me and for accompanying me through countless late-late-afternoon experiments and discussions.

To my cherished travel companions - Aysha, Kai, Lochan, and Shannon - thank you for being there for me throughout this journey. I can't wait for our future adventures together. I'm grateful to all my friends with whom I've managed to stay connected, however sporadically. It's been heartening watching you all flourish and pursue your ambitions over the past few years.

To Shannon, thank you for being my constant, my partner, and my everything.
I would not be the same person without you, and I can't wait to see what our future together holds.

Finally, I owe everything to my parents. Thank you for your endless support, countless prayers, and unwavering love. This has been a long and exciting journey, and I am profoundly grateful for everything you have given to help me reach this point.

For my love,

Shannon

Dedicated to my loving parents,

Keith & Susanty

Attributions

Chapter 2 - Improving the Manufacture of Perfluorocarbon Droplets

This chapter includes work published in *Ultrasonics Sonochemistry*, as follows:

Christopher K. Campbell*, Kirsten O'Brien*, Dariusz Kosk, Robin M. H. Rumney, Peter Glynne-Jones, Peter R. Birkin, Gareth LuTheryn, Jeremy S. Webb, Eleanor Stride, Dario Carugo, Nicholas D. Evans, 2025.

Optimising the manufacture of perfluorocarbon nanodroplets through varying sonication parameters.

Ultrasonics Sonochemistry, 118, p.107332.

*These authors contributed equally to this work.

The majority of the work described in this chapter was jointly undertaken at the University of Southampton with my colleague and co-first author K. O'Brien.

Additional work was completed separately by C. K. Campbell in *Section 2.3.4*.

Chapter 3

- *Section 3.2.2* - Chemiluminescence apparatus

  Experiments were conducted together with Dr. T. A. Tabish using the CLD-Analyzer 88. PDs were manufactured and loaded with NO by C. K. Campbell.

Chapter 4

- *Section 4.2.1 - Characterisation of Acoustic Droplet Vaporisation*

  Experiments using the simultaneous high-speed imaging and acoustic characterisation were conducted together with V. Choi, with technical assistance from Dr. Q. Wu. PDs were manufactured by C. K. Campbell.

- *Section 4.2.3 - Treatment Conditions and Application*

  The custom coupling cone to stimulate biofilm culture dishes was designed by D. De Grandi and manufactured by J. Fisk.

Abbreviations

Abbreviation	Meaning
ADV	Acoustic droplet vaporisation
ANOVA	Analysis of variance
BB	Bolton broth
CFU	Colony forming unit
CLSM	Confocal laser scanning microscopy
CLD	Chemiluminescence detector
ConA	Concanavalin A
CW	Chronic wound
DDS	Drug delivery system
DFU	Diabetic foot ulcer
DiI	1,1'-Dioctadecyl-3,3,3',3'-Tetramethylindocarbocyanine Perchlorate
DLS	Dynamic light scattering
DPBS	Dulbecco's Phosphate-Buffered Saline
DSPC	1,2-distearoyl-sn-glycero-3-phosphocholine
eDNA	Extracellular DNA
EPS	Extracellular polymeric substances
FFT	Fast Fourier transform
FUS	Focused ultrasound
FWHM	Full-width at half maximum
LB	Luria-Bertani
LHB	Laked horse blood
MB	Microbubble

MI	Mechanical index
NO	Nitric oxide
NOPD	Nitric oxide loaded perfluorocarbon droplet
NP	Nanoparticle
NTA	Nanoparticle tracking analysis
PAO1	*Pseudomonas aeruginosa* strain PAO1
PCD	Passive cavitation detection
PD	Perfluorocarbon droplet
PDT	Photodynamic therapy
PEG	Polyethylene glycol
PEG40S	Polyoxyethylene (40) stearate
PFC	Perfluorocarbon
PFH	Perfluorohexane
PFP	Perfluoropentane
PI	Propidium iodide
PLA	Polylactic acid
PMT	Photomultiplier tube
PRF	Pulse repetition frequency
PTT	Photothermal therapy
ROS	Reactive oxygen species
RPS	Resistive pulse sensing
SD	Standard deviation
SNP	Sodium nitroprusside
SPION	Superparamagnetic iron oxide nanoparticle
ULPD	Unloaded perfluorocarbon droplet
US	Ultrasound
VBNC	Viable but nonculturable
WCM	Wound constituent medium

Contents

Abstract i

Declaration of Authorship (Statement of Originality) iii

Acknowledgements iv

Attributions vii

Abbreviations ix

List of Figures xxxii

List of Tables xxxii

1 Literature Review 1

1.1 Wound Healing 5

1.1.1 Acute Wound Healing 5

1.1.2 Chronic Wound Healing 8

1.2 Bacterial Biofilms in DFUs 10

1.2.1 Biofilm Life Cycle 10

1.2.2 Biofilm Tolerance Mechanisms 12

1.3 Treatment of Diabetic Foot Infections 17

1.4 Drug Delivery Systems for the Treatment of Chronic Wound Biofilms 20
1.4.1 Passive Drug Delivery Systems . . . 20
1.4.2 Active Drug Delivery Systems . . . 23
1.5 US-responsive Drug Delivery Systems . . . 27
1.5.1 Therapeutic US Parameters . . . 28
1.5.2 Gas Microbubbles . . . 30
1.6 Perfluorocarbon Droplets . . . 39
1.7 Particle Sizing Methods . . . 44
1.7.1 Dynamic Light Scattering . . . 45
1.7.2 Nanoparticle Tracking Analysis . . . 45
1.7.3 Resistive Pulse Sensing . . . 48
1.8 Nitric Oxide . . . 50
1.8.1 Nitric Oxide in Biofilm Dispersal . . . 50
1.8.2 Challenges in NO Delivery . . . 52
1.8.3 Gas Transport in Perfluorocarbons . . . 53
1.8.4 Perfluorocarbon-Based NO-Delivery Systems . . . 54
1.9 Perfluorocarbon Droplets as an Antibiofilm Therapy . . . 56
1.10 Research Aim & Objectives . . . 58

2 Improving the Manufacture of Perfluorocarbon Droplets 59

2.1 Introduction . . . 60
2.2 Materials and Methods . . . 67
2.2.1 Overview of PD Preparation . . . 67
2.2.2 Development of Sonicator Manufacturing Apparatus . . . 70
2.2.3 Temperature Control during PD Manufacture . . . 76

2.2.4 Characterisation of PDs using NTA 77
2.2.5 Characterisation of PDs using the Coulter Method 78
2.2.6 Evaluation of Manufacturing Parameters on PD Size Characteristics 79
2.2.7 Statistical Analysis 80
2.3 Results and Discussion 81
2.3.1 Selection of Sonication Pulse Parameters to Maintain Sample Temperature 81
2.3.2 Effect of Varying PFP Concentration Against Sonicator Tip Height on PD Characteristics 85
2.3.3 Effect of Varying Sonication Duration Against Intensity on PD Characteristics 95
2.3.4 Evaluating the Effect of Varying PFP Volumetric Concentration using the Coulter method 99
2.4 Conclusion 103

3 Development and Characterisation of Nitric Oxide Loading in Perfluorocarbon Droplets 105

3.1 Introduction 105
3.1.1 NO detection techniques 108
3.2 Materials and Methods 111
3.2.1 Preliminary Griess Assay Experiments 111
3.2.2 Pressurised NO-loading of PDs 114
3.2.3 Varying Volumetric Concentrations of PFP 119
3.2.4 Development of an Oxygen-free NO-Loading Method 120
3.2.5 Statistical Analysis 122

3.3 Results and Discussion . . . 123
3.3.1 Preliminary Griess Assay experiments . . . 123
3.3.2 Evaluation of a Pressurised NO Loading Method . . . 127
3.3.3 Modulation of PD size characteristics . . . 136
3.3.4 Sparging Evaluation . . . 142
3.3.5 Oxygen-free NO-loading of PDs . . . 144
3.4 Conclusion . . . 148

4 Evaluation of Ultrasound-Responsive Nitric Oxide-Loaded Perfluorocarbon Droplets for Chronic Wound Biofilm Treatment 151

4.1 Introduction . . . 152
4.2 Materials and Methods . . . 156
4.2.1 Characterisation of Acoustic Droplet Vaporisation . . . 157
4.2.2 Biofilm Growth and Preparation . . . 162
4.2.3 Treatment Conditions and Application . . . 164
4.2.4 Microscopy and Image Analysis . . . 167
4.2.5 Quantification Methods . . . 174
4.2.6 Preliminary Observation of Droplet-Biofilm Interactions . . . 176
4.2.7 Statistical Analysis . . . 178
4.3 Results and Discussion . . . 179
4.3.1 Acoustic Droplet Vaporisation . . . 179
4.3.2 Preliminary Evaluation of Droplet-Biofilm Interactions . . . 187
4.3.3 Evaluation of the Antibiofilm Effect of NO-Loaded Perfluorocarbon Droplets . . . 193
4.4 Conclusion . . . 221

5 Conclusions, Limitations and Future Directions **223**

5.1 Conclusions 223

5.2 Limitations and Future Work 229

5.3 Future Directions 234

A Additional Figures **285**

List of Figures

1.1 Wound healing typically progresses over three overlapping phases. **(A)** The inflammatory phase is characterised by a low oxygen environment (hypoxia) with a large number of neutrophils, bacteria and platelets present. The wound depicted is 24-48 hours after injury. A fibrin clot forms shortly after the injury to prevent further blood loss. Typical skin appendages are also shown, such as sweat glands, sebaceous glands, and hair follicles. **(B)** In the proliferative phase, which typically occurs 2-10 days after injury, new tissue formation (granulation tissue) occurs. An eschar (scab) has formed and new blood vessels are developing beneath. Immune cells such as monocytes and macrophages have begun to migrate away from the wound site. **(C)** Tissue remodelling is the final stage in wound healing, occurring between 1-12 months post-injury. Collagen has been deposited in place of the eschar, and the wound area has contracted.
From Gurtner et al. [44] 7

1.2 Typical stages of a biofilm life cycle. **(A)** Initial attachment of motile bacteria may be weak, but can become permanent, leading to stable attachment and aggregation of sessile (fixed) cells. **(B)** Small groups of cells begin to produce EPS that surround and support the growing microcolony. **(C)** Microcolony matures through intercellular signalling to form a three-dimensional structure. **(D)** Mature biofilm. **(E)** Biofilms can disperse, with motile individuals able to spread elsewhere and colonise other surfaces. Adapted from LuTheryn *et al.*, [89]. 11

1.3 FFT spectra obtained from stimulating albumin-shelled PFC MBs at different acoustic driving pressures. **(A)** P^-=10 kPa; no harmonic components are apparent. **(B)** P^- = 30 kPa; harmonic components appear. **(C)** P^- = 60 kPa; sub- and ultra-harmonic components appear. **(D)** P^- = 140 kPa; the broadband noise level increases and the sub- and ultra-harmonic components are suppressed. From Gu *et al.* [226] 35

1.4 As an acoustic wave travels longitudinally, it alternates between compression and rarefaction phases. Under US stimulation, a gas MB will respond by volumetrically expanding and contracting. Modified from Lee *et al.* [218]. 36

1.5 Typical structure of a PD. A liquid-perfluorocarbon core is coated by a lipid-surfactant shell. 40

1.6 NTA records the motion of particles over time to determine their diameter. A laser is passed through a sample of particles suspended in a liquid, and the light scattered by these particles is recorded by a digital camera with a microscope objective. The motion of particles is recorded at 30 frames per second, and tracks of particle motion (red) recorded for each frame ($0.0\overline{33}$ s). Adapted from *Singh & Toler*, 2012 [262] 47

1.7 Resistive pulse sensing (RPS). Left: Typical setup with two cells separated by an insulating membrane with a single pore. Right: Transient signal of current representing a (1) large-, (2) small-, and (3) medium-sized particle. Following calibration, the count rate, i.e., the number of pulses per time interval, reflects the concentration of the particle suspension to be analysed. From *Giebel & Helmbrecht*, 2016. [265] 49

2.1 Overview of the process employed for the production of PDs. **(A)** DSPC and PEG40S (in chloroform) are mixed in a 9:1 molar ratio and **(B)** the sample is left to dry overnight. **(C)** The produced dry lipid film is rehydrated with DPBS at 90 °C for 45 minutes. **(D)** A first sonication step is performed to fully disperse the lipids in DPBS. **(E)** PFP is added to the lipids in a 1.5 mL polylpropylene tube. The sample is briefly vortexed to form precursor droplets. **(F)** A second sonication step forms PFP core, lipid-shelled PDs. 69

2.2 Prototype PFC emulsion manufacturing setup. **(A)** Side view schematic showing the position of a 1.5 mL tube in relation to the sonicator tip. **(B)** Photograph showing the prototype manufacturing setup. A polystyrene container was used to insulate a mixture of water and crushed ice. A flexible plastic insert with a circular cut-out was used to stabilise the 1.5 mL tube containing PFP and lipids. 72

2.3 Controlled positioning apparatus overview. This figure illustrates a custom-built manufacturing apparatus designed to precisely control sonicator tip position during PD manufacture. The sonicator tip **(A)** is held vertically by a pair of optics clamps **(B)**, which are attached to a micrometer translation stage **(C)** allowing for precise control of sonicator tip height (Z-axis). The pillar post and clamp **(D)** allow for larger height adjustments between manufacturing phases. A pair of perpendicularly mounted single-axis translation stages **(E)** allow for X and Y axis adjustment. An aluminium breadboard with sorbothane feet **(F)** functions as a rigid, vibration-free base with M6 thread mounting points for the 3D-printed ice bath and lid **(G)**. Panel **(H)** shows a side-view of the ice-bath and lid, illustrating tip height variability. The apparatus enables reproducible positioning of the sonicator tip within a 1.5 mL sample vessel. 75

2.4 Sonication parameters were varied to mitigate heat production from manufacturing of PFP droplets. **(A)** Effect of two patterns of pulsed sonication at 60% amplitude (2 s on, 5 s off, '2/5' *vs.* 2 s on, 15 s off, '2/15') compared with ice-water (Water, 1.3 ± 0.2 °C) or saturated saline-ice (Saline, -8.6 ± 0.3 °C) cooling baths on PD sample temperature. Maximum temperatures for 2/5-Water, 2/5-Saline and 2/15-Water were 24.8 ± 2.3 °C, 14.8 ± 1.2 °C, and 14.2 ± 1.7 °C, respectively. **(B)** Effect of varying amplitude percentage on the temperature of PD samples. 2 s on, 15 s off pulse parameters were used, and both 60 % and 100 % amplitudes were tested. Maximum temperatures were 14.2 ± 1.7 °C and 24.3 ± 0.9 °C for 60 % and 100 % amplitudes, respectively. Mean temperature of n = 3 samples are plotted. A total sonication on time of 60 s was used for all samples. . 84

2.5 PFP concentration and sonicator tip height significantly influence perfluorocarbon droplet (PD) characteristics. (Figure caption cont. next page) 89

2.5 PFP concentration and sonicator tip height significantly influence PD characteristics. PDs were manufactured using sonication (60% amplitude, 60 s duration) with varying PFP concentrations (0-16.7% v/v) and tip heights (2-12 mm). PD size and concentration were measured using NTA. **(A)** PFP concentration versus PD concentration at 12 mm tip height ($R^2 = 0.569$). **(B)** PFP concentration versus PD median diameter at 12 mm tip height ($R^2 = 0.823$). **(C)** Bright-field microscopy images (40 × magnification) of PD samples manufactured with 12 mm tip height at 4.76% or 9.09% PFP concentration. Scale bar = 10 µm. **(D)** Sonicator tip height versus PD median diameter at 4.76% PFP concentration ($R^2 = 0.776$). **(E)** Sonicator tip height versus PD concentration at 4.76% PFP concentration ($R^2 = 0.784$). **(F)** R^2 values for correlations between PFP concentration and PD diameter (circles), and PFP concentration and particle concentration (squares) at different tip heights. Error bars represent standard deviation (n = 3 independent repeats). Statistical significance was determined using one-way ANOVA with Dunnett's T3 multiple comparisons test (ns $P > 0.05$, * $P < 0.05$, ** $P < 0.01$). 90

2.6 Median PD size increases with increasing PFP concentration when measured by NTA. PDs were manufactured using sonication (60% amplitude, 60 s duration). Each value is a mean of n = 3. Phases did not appear to mix for samples manufactured with a tip height of 2 mm with 16.7 % v/v PFP. For these samples the upper lipidic aqueous phase was measured by NTA. Statistical significance was determined using one-way ANOVA with Dunnet's T3 multiple comparisons test between each group and the 0 % PFP control at the same tip height (ns= not significant, ns > 0.05, * < 0.05, ** < 0.01, *** < 0.001, and **** < 0.0001) 91

2.7 PFP concentration influences the size distribution of PDs. NTA data showing the mean particle concentration vs. diameter for PFP concentrations in the range 0-16.7%. PDs were manufactured using sonication (60% amplitude, 60 s duration) with a tip height of 12 mm. Each line represents the mean of n = 3 samples. 94

2.8 Phases did not appear to mix for samples sonicated with intensities of 20% and 40%. Figure caption cont. next page 97

2.8 Sonication amplitude affects phase mixing in PD manufacture. **(A)** Visual observation shows a minimum of 60% sonicator amplitude was required for the PFP and lipid phases to mix during sonication-based emulsification. For 20% and 40% amplitudes, phase separation remained visible, and only the upper lipid phase was characterised by NTA. (B) Median diameter against total sonication durations from 15 s to 120 s. (C) Median diameter against sonicator amplitude, showing the effect of acoustic intensity on droplet formation. All measurements were performed with a 12 mm sonicator tip height. PFP concentration was maintained at 4.76% v/v. Diameter values reported are mean ± S.D. for n = 3 independent samples. 98

2.9 As PFP concentration increases, the proportion of particles with a diameter >1 µm increases. **(A)** Median diameter values ± SD at 4.76%, 9.09% and 16.7% PFP. A statistically significant difference ($P<0.01$) was found between each PFP concentration. **(B)** PDs were measured by RPS, with particle concentration plotted against particle diameter (n = 3). The minimum size detection limit of the RPS detector is 0.4 µm. Data represent mean ± SD (n = 3 independent samples). 101

3.1 Experimental setup for loading of NO gas into PDs (eNO generator). A vial with two inlets and one outlet allowed for the maintenance of an oxygen-free headspace flushed with nitrogen. Samples were sparged using nitrogen gas bubbled through the PDs for 30 mins prior to NO-loading The output from the eNO generator (1000 ppm NO and room air) was bubbled through the PD emulsion with a flow rate of 0.5 L / min for 30 min. 113

3.2 Pressurised NO-loading method. **(A)** The headspace of PD samples within a 50 mL syringe is flushed with ∼1000 ppm NO + room air for 5 min. **(B)** The headspace is sealed. **(C)** The syringe is compressed to 50% of the original volume and cooled to 4 °C for 1 h. After this, the pressure is gently released and samples' NO_x concentration measured. 116

3.3 Ozone-based chemiluminescent detector (CLD) apparatus. NO-loaded samples are introduced into a reaction chamber containing acidified vanadium (III) chloride heated to 90 °C by a water jacket. This reduces NO_x within the sample to NO gas, which is carried by helium gas bubbled through the reaction chamber. The helium and NO is passed through an NaOH trap to remove residual acidic vapor. NO is carried into the detector and reacts with ozone gas generated by the CLD. Photon emissions $h\nu$ are collected by the photomultiplier tube (PMT), converted to an electrical signal that is recorded on a computer. 119

3.4 Experimental setup for oxygen-free loading of NO gas into PDs. A vial with one inlet and one outlet allowed for sparging of samples with nitrogen and subsequent loading with NO. 400 ppm NO in Nitrogen was flowed over samples for 5 min, with gentle agitation from the gas flow encouraging gas exchange. 125

3.5 Preliminary Griess assay experiments measuring NO_x in PD emulsions. **(A)** Griess assay standard curve **(B)** NO_x concentration for room air and NO-loaded PD samples diluted at 1:5 and 1:10 with PBS prior to Griess assay measurement. No statistically significant difference (P>0.05) was found for either sample pair. Dilution factors have not been removed in NO_x concentration calculations. **(C)** Photograph of Griess assay standard curve wells **(D)** Photograph of sample wells containing NO-PDs. Assay wells with NO-PDs exhibited foaming and increased turbidity. (ns=not significant, P>0.05) . . 126

3.6 Mean concentration of PDs decreased after a pressurised NO-loading step. Mean concentrations ± S.D. are shown. Shaded error ± S.D. . 128

3.7 Griess assay measurements of NO_x concentrations in different formulations loaded with NO using a pressurised system. NO-PDs had significantly higher (P<0.01) NO_x concentrations than NO-Lipids. Both NO-Lipids and NO-PDs showed significantly higher NO_x concentrations compared to NO-DPBS (P<0.0001). (**, P<0.01). Mean of n=3 NO_x measurements, error bars ± S.D. 131

3.8 Chemiluminescence standard curve for NO quantification. **(A)** Raw voltage data from chemiluminescence measurements of NO standards (black circles) and samples (red square). **(B)** Calibrated NO concentration standard curve with linear regression (dashed line). The highest sample voltage value, extrapolated using the regression line, is highlighted in red. Linear regression equation: y = 0.0369x, R^2 = 0.987. NO_x concentrations in samples were calculated using this standard curve. 133

3.9 NO-Lipids and NO-PDs had significantly higher NO_x concentrations than NO-DPBS. Chemiluminescence data measuring NO_x in PD emulsions using a pressurised NO-loading system. Mean of n=3 NO_x measurements, error bars ± S.D. (*, P<0.05) 135

3.10 As PFP concentration increases, the particle concentration and median diameter (by number) increase. Size distribution by number of n = 3; shaded error is ± S.D. Mean values for particle concentration and median diameter ± S.D. 139

3.11 As PFP concentration increases, the particle volume and median diameter (by volume) increase. Size distribution by volume of n = 3; shaded error is ± S.D. Mean values for total particle volume and median diameter, ± S.D. 139

3.12 PFP precursor droplets in 40% and 50% v/v PFP samples occasionally fail to mix with the upper lipid phase. Representative photo of a 1.5 mL sample tube with phases of DSPC:PEG40S in DPBS (above) and precursor droplets (below). 141

3.13 A 5 mL volume of DPBS could be reduced to 0% oxygen saturation in less than 120 s. Mean time to reach 0% oxygen saturation was 114.6 s. (n = 3, dotted red line represents ± S.D.) 143

3.14 Chemiluminescence Standard Curve for NO Quantification. **(A)** Raw voltage data from triplicate chemiluminescence measurements of NO standards (black circles). **(B)** Calibrated NO concentration standard curve with linear regression (dashed line). Linear regression equation: y = 0.501x, R^2 = 0.997. NO_x concentrations in samples were calculated using this standard curve. 146

3.15 Chemiluminescence data measuring total NO_x in PD emulsions using a pressurised NO-loading system. 20% v/v PFP NO-PDs had significantly higher NO_x concentrations than NO-Lipids. Mean of n = 3 NO_x measurements, error bars ± S.D. (* = P<0.05, ns = not significant) 147

4.1 Setup for simultaneous optical and acoustic measurements. FUS = focused ultrasound; PCD = passive cavitation detector. Adapted from Wu *et al.* [242] 157

4.2 Pressure calibration curve for H107 FUS transducer driven at 0.5 MHz. The peak negative pressure was characterised from 0.4 to 3.09 MPa in water at the geometric focus (63.2 mm). Input voltage (peak negative) to the H107 is plotted against the measured peak negative pressure. 161

4.3 **(A)** Image showing an *in-vivo* example of a chronic wound biofilm on the left and the *in-vitro* Lubbock chronic wound biofilm on the right, highlighting the similarity in texture and consistency between the biofilms **(B)** Image of *P. aeruginosa* biofilms grown in an Ibidi® culture dish in WCM (BB, 5% LHB, 20% plasma) Adapted from Sun *et al.* [377]. 163

4.4 3D-slice representation of the biofilm US stimulation apparatus. **(A)** Ibidi® culture dish containing the biofilm placed at the geometric focus of the H107 tranducer. **(B)** Custom coupling cone (filled with water). **(C)** H107 single-element transducer. 165

4.5 Multi-scale imaging of biofilm structure. **(A)** Higher-resolution imaging: 10 × objective tile scan of a 4.192 mm × 4.192 mm region. Individual red squares represent 1048 µm × 1048 µm fields of view. This scan includes a z-stack acquisition, capturing 25 optical sections over a total depth of 128.19 µm. **(B)** Lower-resolution overview: 4 × objective tile scan covering an 8.192 mm × 8.192 mm area. Each red square delineates a 4096 µm × 4096 µm field of view. Representative 4 × objective tile scan image to illustrate scale differences between 4 × objective and 10 × magnification 171

4.6 Differences in thresholding methods for 10 × z-stack. **(A)** A representative slice of a post-treatment biofilm z-stack. **(B)** Automatic Otsu thresholding, with included areas coloured in blue. **(C)** Manual thresholding, with included areas coloured in pink, highlighting lower noise levels than the Otsu threshold. 173

4.7 Representative example of a series of high-speed images of PFP droplet vaporisation captured over the first 5 cycles of a 10,000-cycle US pulse at 0.5 MHz, peak negative pressure of 1.48 MPa. Scale bar = 20 µm. Images were taken at 5×10^6 frames/s with an exposure time of 200 ns per frame. The dashed lines indicate the approximate phase relationship between each frame and the incident US pulse, assuming that the speed of sound in the liquid is 1481 m/s. In the second cycle the formation of a microjet is visible. 180

4.8 Temperature threshold of droplet vaporisation. A series of high-speed images of PFP droplet vaporisation captured over the first 3 cycles of a 10,000-cycle US pulse at 0.5 MHz, and peak negative pressure of 1.48 MPa. Figure caption cont. on next page. 184

4.8 Images were taken at 5×10^6 frames/s with an exposure time of 200 ns per frame. There was a clear temperature-dependent effect, with an increase in temperature from 38.3 °C to 39 °C resulting in consistent ADV being observed. n = 3 repeats were performed at each temperature. Scale bar = 20 µm. 185

4.9 PCD measurements comparing acoustic emissions from ULPD and DPBS samples. **(A)** Representative PCD signals from DPBS and ULPD samples at 2.48 MPa peak negative pressure, showing increased acoustic emissions in ULPD samples. **(B)** Total acoustic energy at peak negative pressures ranging from 0.4 to 2.48 MPa for DPBS and ULPD samples. Data points represent mean ± S.D. (n = 3 independent samples). 185

4.10 Observation of large bubble clusters and gas pockets during high-speed imaging experiments. **(A)** Prior to a cluster of bubbles passing through the imaging field of view, a build-up in the number of droplets is visible. **(B)** Large clusters of bubbles pass through the image. **(C)** Once bubble clusters have passed through, the concentration of droplets returns to nominal levels. Scale bar = 50 µm. . . . 186

4.11 Wide-field microscopy image (100 × magnification) of simple media biofilm. *Pseudomonas aeruginosa* PAO1 biofilm cultured in LB media for 24 h at 37 °C and incubated with 4.76% v/v PFP PDs. The biofilm sample was stained with SYTO9 (green). Scale bar = 10 µm. 189

4.12 CLSM image (100 × magnification) of WCM biofilm. Pseudomonas aeruginosa PAO1 biofilm cultured in WCM for 48 h at 37 °C, incubated with 20% PFP PDs labeled with DiI (yellow). The biofilm sample was stained with SYTO9 (green) and ConA (Orange). Scale bar = 10 µm. 190

4.13 Representative images of *Pseudomonas aeruginosa* PAO1 cultured in LB for 24 h (top) compared to PAO1 cultured in WCM for 48 h (bottom). Bacteria cultured in WCM for 48 h appear to have a more discrete, aggregate morphology as opposed to the dense covering seen in the biofilm grown for 24 h in LB. Scale bar = 100 µm. 192

4.14 Representative 4 × tilescans of *P. aeruginosa* PAO1 biofilms cultured in WCM for 48 h, stained with SYTO9 (green), PI (red), and ConA (Blue) and treated with DPBS, US-Only, ULPD, NOPD, ULPD-US, or NOPD-US. Each panel is composed of 4 tiles covering a 8.192 mm × 8.192 mm area. Scale bars = 1 mm. 196

4.15 3D CLSM images of *P. aeruginosa* PAO1 biofilms cultured in WCM for 48 h and subjected to either DPBS or US-Only treatment conditions. Biofilms were stained with SYTO9 (green), PI (red), and ConA (Blue). Each panel represents an independent biological repeat across one of three experimental days, and comprises 16 tiles imaged at 10 × magnification covering a 4.192 mm × 4.192 mm area. Images show z-stacks consisting of 25 slices over a 128.19 µm depth. 200

4.16 3D CLSM images of *P. aeruginosa* PAO1 biofilms cultured in WCM for 48 h and subjected to either ULPD or NOPD treatment conditions. Biofilms were stained with SYTO9 (green), PI (red), and ConA (Blue). Each panel represents an independent biological repeat across one of three experimental days, and comprises 16 tiles imaged at 10 × magnification covering a 4.192 mm × 4.192 mm area. Images show z-stacks consisting of 25 slices over a 128.19 µm depth.. 201

4.17 3D CLSM images of *P. aeruginosa* PAO1 biofilms cultured in WCM for 48 h and subjected to ULPD-US or NOPD-US treatment conditions. Biofilms were stained with SYTO9 (green), PI (red), and ConA (Blue). Each panel represents an independent biological repeat across one of three experimental days, and comprises 16 tiles imaged at 10 × magnification covering a 4.192 mm × 4.192 mm area. Images show z-stacks consisting of 25 slices over a 128.19 µm depth. 202

4.18 Comparison of US field characteristics and corresponding biofilm (48 h WCM PAO1) morphology. **(A)** Lateral beam profile of H107 FUS transducer measured in free field conditions using a needle hydrophone (0.5 MPa peak negative pressure, 10 cycles, 0.5 MHz). **(B)** Representative CLSM microscopy image showing biofilm morphology after US-Only treatment (2.48 MPa peak negative pressure, 100 cycles, 1 Hz PRF, 60 s duration). Dashed circles in both panels indicate the 3.9 mm FWHM focal region. Scale bar = 1 mm. 204

4.19 Image showing PDs + biofilm after stimulation on 48 h WCM PAO1 biofilm prior to rinsing and removal of treatment. A foam with gas pockets across the growth area of the Ibidi dish is visible. Scale bar = 10 mm 206

4.20 Quantification of viable bacteria following treatment of 48 h WCM PAO1 biofilms. CFU/mL recovered from the combined treatment and rinse volumes of biofilms subjected to various treatment conditions. Treatments: US-Only (Ultrasound only), ULPD (Unloaded PDs), NOPD (NO-loaded PDs), ULPD-US (Unloaded PDs with US-stimulation), NOPD (NO-PDs with US-stimulation). Each bar represents the mean CFU/mL, and error bars indicate ± 1 S.D. 209

4.21 Effect of various treatments on WCM biofilm biomass. Quantification of remaining biofilm biomass following various treatments on 48 h WCM PAO1 biofilm. Biomass was quantified using a safranin stain and normalised to the DPBS control. Treatments: US-Only (Ultrasound only), ULPD (Unloaded PDs), NOPD (NO-loaded PDs), ULPD-US (Unloaded PDs with US-stimulation), NOPD (NO-PDs with US-stimulation). Each bar represents the mean normalised biomass, and error bars indicate ± 1 S.D. No significant difference between sample pairs (P>0.05). 212

4.22 Coverage area of 48 h WCM PAO1 biofilms was compared post-treatment between different treatment conditions, measured from SYTO9 staining. Treatments: US-Only (Ultrasound only), ULPD (Unloaded PDs), NOPD (NO-loaded PDs), ULPD-US (Unloaded PDs with US-stimulation), NOPD (NO-PDs with US-stimulation). Each bar represents the mean biofilm coverage area in mm^2, and error bars indicate ± 1 S.D. (* = P<0.05), (** = P<0.01). 214

4.23 PI (left) and ConA (right) stain coverage area of 48 h WCM PAO1 biofilms after exposure to different treatment conditions. Treatments: US-Only (Ultrasound only), ULPD (Unloaded PDs), NOPD (NO-loaded PDs), ULPD-US (Unloaded PDs with US-stimulation), NOPD (NO-PDs with US-stimulation). Each bar represents the mean biofilm coverage area in μm^2, and error bars indicate ± 1 S.D. (* = P<0.05), (** = P<0.01)/ 216

5.1 Test wound patch print using a 3D bioprinter (CELLINK BIO X6) performed in the present study. **(A)** Test prints of polypropylene glycol gel, forming a tight multilayered grid designed to emulate the morphology of a wound patch. **(B)** Optical microscopy to examine the geometry of apertures within the grid structure. These apertures could potentially be loaded with US-responsive therapies. 235

A.1 Representative surface slice 10 × tilescan images of 48 h WCM biofilms, before and after exposure to DPBS, ULPD, and NOPD treatment conditions. Biofilms were stained with SYTO9 (green), PI (red), and ConA (Blue) with each panel composed of 16 tiles imaged at 10 × magnification covering a 4.192 mm × 4.192 mm area. Scale bar = 1 mm. 286

A.2 Representative surface slice 10 × tilescan images of WCM biofilms before and after exposure to NOPD, ULPD-US, and NOPD-US treatment conditions. Biofilms were stained with SYTO9 (green), PI (red), and ConA (Blue) with each panel composed of 16 tiles imaged at 10 × magnification covering a 4.192 mm × 4.192 mm area. Scale bar = 1 mm. 287

A.3 Quantification of changes in SYTO9 biovolume before and after treatment. NO-loaded PDs combined with US show the greatest reduction in biofilm biovolume. Treatments: US-Only (Ultrasound only), ULPD (Unloaded PDs), NOPD (NO-loaded PDs), ULPD-US (Unloaded PDs with US-stimulation), NOPD (NO-PDs with US-stimulation) Bars represent mean ± S.D. from three independent experiments (n = 3). No significant difference between sample pairs ($P>0.05$) 288

A.4 Quantification of changes in PI (left) and ConA (right) biovolume before and after treatment. Treatments: US-Only (Ultrasound only), ULPD (Unloaded PDs), NOPD (NO-loaded PDs), ULPD-US (Unloaded PDs with US-stimulation), NOPD (NO-PDs with US-stimulation) Bars represent mean ± S.D. from three independent experiments (n = 3). No significant difference between sample pairs (P>0.05) 289

A.5 Quantification in changes to biofilm thickness post-treatment. Treatments: US-Only (Ultrasound only), ULPD (Unloaded PDs), NOPD (NO-loaded PDs), ULPD-US (Unloaded PDs with US-stimulation), NOPD (NO-PDs with US-stimulation) Each bar represents the mean thickness change from three independent biological replicates, with each replicate conducted on a separate experimental day using a freshly prepared bacterial stock culture. Error bars indicate standard deviation (S.D.) (n = 3). 290

List of Tables

2.1 Selection of studies using sonication to manufacture PFP-core NDs . 64

Chapter 1

Literature Review

Chronic wounds (CWs) represent a significant burden on both patients and health-care systems worldwide [1]. A common type of CW is the diabetic foot ulcer (DFU), with a global prevalence of 6.3% [2]. Costing the NHS an estimated £2.3–3.1 billion in 2005, the financial impact of the treatment and management of CWs is enormous, with expenditures increasing to an estimated £5.6 billion in 2017/18 [3, 4]. Combined with the ageing population, CWs are expected to continue to be a substantial clinical, social, and economic burden, underscoring the urgent need for more efficacious and cost-effective interventions. Fundamental to this challenge is the impaired healing process that defines CWs, leading to persistent, debilitating conditions such as venous leg ulcers, pressure ulcers, and DFUs that affect millions of patients worldwide [5, 6, 7, 8].

A significant factor contributing to the persistence of CWs is the formation of bacterial biofilms within the wound bed. Biofilms are complex, heterogeneous communities of microorganisms such as *Pseudomonas aeruginosa* and *Staphylococcus aureus* that form aggregates and produce a protective matrix of extracellular polymeric substances (EPS) [9]. The EPS matrix serves as a physical barrier to diffusion, impeding the penetration and action of conventional antibiotic compounds, and diminishes the efficacy of host immune responses [10]. Crucially, biofilm infections often tolerate up to 1000 × the dosage of similar planktonic (free-swimming) infections [11]. Consequently, systemic antibiotic administration, whether administered orally or intravenously, often fails to achieve these necessary therapeutic concentrations at the target site [12]. Insufficient levels of antibiotics can contribute to the spread of antimicrobial resistance [13].

Although topical antibiotic application can help to potentially circumvent these issues, many antimicrobial therapeutics still struggle to effectively penetrate beyond the biofilm matrix [14]. In addition, the EPS matrix can trap and sequester essential nutrients, creating a nutrient-rich microenvironment that supports the growth and proliferation of the biofilm community [15]. Biofilm-associated bacteria also exhibit altered metabolic and physiological states, such as the formation of persister cells. These dormant, metabolically inactive cells comprise a subpopulation of bacteria

that develop a high tolerance to antibiotics, and reach this state without undergoing genetic modifications. While genetically susceptible to antibiotics, persister cells exist in a quiescent state that enables survival in stressful conditions such as antibiotic exposure or starvation [16]. Importantly, persister cells in biofilms are often responsible for the recalcitrance of chronic infections, as they remain viable and can recolonise biofilms once antibiotic treatment ceases [17, 18, 19].

The limitations of conventional antibiotic therapies in the treatment of biofilm-associated infections have motivated the exploration of alternative approaches, including the use of therapeutic ultrasound (US). A minimally invasive and cost-effective technique, US has attracted significant appeal due to its ability to induce targeted and localised mechanical effects [20, 21]. Indeed, low-frequency US (20-100 kHz) has shown potential in decreasing the concentration of antibiotics required to induce a bactericidal effect, likely due to enhanced cell membrane permeability to bioactive compounds [22, 23, 24]. However, US alone does not appear to have a significant impact on bacterial viability within biofilms [25, 26].

The combination of US with cavitation nuclei, such as gas microbubbles (MBs), has garnered significant attention as a means to increase the effectiveness of US-based treatments [27, 28]. Gas MBs can mediate a variety of physical effects through rapid changes in their volume in response to US stimulation (called cavitation) [28].

This synergistic approach can significantly enhance biofilm disruption and increase the penetration of therapeutic agents across biological barriers [25, 29, 30]. Physical disruption of the biofilm matrix, paired with the controlled delivery of antimicrobials, offers a multifaceted strategy to combat persistent biofilms.

Perfluorocarbon droplets (PDs), also known as nanodroplets (NDs), represent a promising advancement in US-responsive drug delivery. PDs consist of a liquid perfluorocarbon (PFC) core stabilised by a shell, typically composed of phospholipids or polymers [31]. Upon exposure to sufficient rarefactional pressures, the liquid core of PDs can undergo a phase transition to form acoustically responsive gas-core MBs, allowing temporal control over their activation using US [32]. Beyond this, the unique properties of PDs, such as their high gas solubility, have led to various applications in the field of intravenous gas transport, including oxygen delivery and volatile anaesthetic administration [33, 34, 35]. Recent research has also demonstrated the potential of PDs as carriers for nitric oxide (NO), a molecule of considerable interest in mediating biofilm dispersal and promoting wound healing [36, 37, 38].

Combining the mechanical effects of acoustically activated PDs with the biofilm dispersing properties of NO presents an intriguing approach to address the challenges posed by chronic wound biofilms [39]. US-mediated physical disruption of the biofilm

matrix, facilitated by the cavitation effects of vaporised PDs could enhance the penetration and accessibility of the wound bed for the delivery of NO-based therapeutics [30]. PD-mediated biofilm disruption has the potential to reduce the reliance on systemic antibiotics and decrease the antibiotic concentrations required for effective treatment, overcoming the intrinsic resistance of biofilm-associated infections.

This project aims to investigate this multifunctional approach by improving the manufacture of PD formulations, quantifying the loading of NO within the core of PDs, evaluating the acoustic capabilities of the manufactured PDs, and finally assessing the anti-biofilm effects of US-activated NO-loaded PDs on a chronic wound biofilm model.

1.1 Wound Healing

1.1.1 Acute Wound Healing

The skin serves as the primary barrier between the body and the external environment, playing a vital role in maintaining homeostasis and protecting the body from external threats such as pathogens and environmental stressors [40, 41, 42]. However, when the skin is damaged, the resulting acute wound triggers a coordinated biological response to restore tissue integrity and prevent the spread of infection [43]. The wound healing process involves multiple overlapping phases, including inflam-

mation, proliferation, and tissue remodelling, which are orchestrated by various cell types, signalling pathways, and molecular mechanisms **(Fig. 1.1)** [43, 44, 45, 46]. The inflammatory phase **(Fig. 1.1 A)** is the initial response to tissue injury, characterised by vasoconstriction to prevent further blood loss and restore homeostasis [47]. Platelet activation triggers the coagulation cascade, leading to the formation of a fibrin clot that seals the wound [46, 48, 49]. Immune cells are rapidly recruited into injured tissue through the release of antimicrobial substances and pro-inflammatory mediators, first with neutrophils, then macrophages and circulating lymphocytes [47, 50, 51]. The proliferative phase **(Fig. 1.1 B)** overlaps with the inflammatory phase and serves to rebuild damaged tissues and close the wound [52, 53]. This phase involves the construction of new vasculature (angiogenesis), connective tissue (fibroplasia), and epidermis (re-epithelialisation) for up to 14 days post-injury [52, 53, 54]. Keratinocytes migrate over the wound bed, restoring the barrier function of the epithelium [44, 55]. The remodelling phase **(Fig. 1.1 C)** occurs throughout the healing process, beginning with the replacement of the fibrin clot with granulation tissue to prevent further microbial invasion and injury [46, 54, 56]. Fibroblasts within the granulation tissue remodel the extracellular matrix into new tissue, increasing its tensile strength [52, 57]. Acute wound healing mechanisms have been extensively covered in further cellular and molecular detail elsewhere [51, 52, 53, 58].

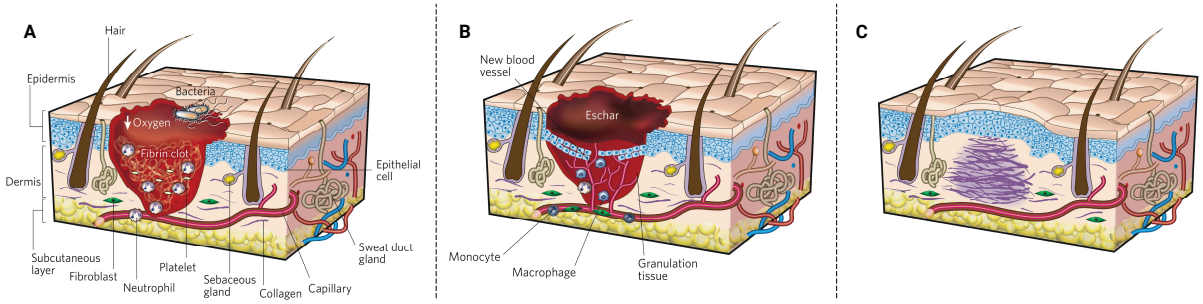

Figure 1.1: Wound healing typically progresses over three overlapping phases. **(A)** The inflammatory phase is characterised by a low oxygen environment (hypoxia) with a large number of neutrophils, bacteria and platelets present. The wound depicted is 24-48 hours after injury. A fibrin clot forms shortly after the injury to prevent further blood loss. Typical skin appendages are also shown, such as sweat glands, sebaceous glands, and hair follicles. **(B)** In the proliferative phase, which typically occurs 2-10 days after injury, new tissue formation (granulation tissue) occurs. An eschar (scab) has formed and new blood vessels are developing beneath. Immune cells such as monocytes and macrophages have begun to migrate away from the wound site. **(C)** Tissue remodelling is the final stage in wound healing, occurring between 1-12 months post-injury. Collagen has been deposited in place of the eschar, and the wound area has contracted.

From Gurtner et al. [44]

1.1.2 Chronic Wound Healing

Acute wounds typically follow an ordered healing process that spans several days to a few weeks. However, if a wound fails to move through the typical healing stages and takes more than 4 weeks to heal, it is classified as a chronic wound [58, 59, 60]. Several critical factors can contribute to the development of chronic wounds, including infection, inadequate tissue oxygenation, patient age, and underlying diseases such as diabetes mellitus [60, 61]. According to recent estimates, diabetes mellitus affects approximately 537 million adults worldwide, a number projected to increase to 783 million by 2045 [62].

Approximately 25% of diabetic patients experience delayed wound healing [63]. Patients with diabetes mellitus often have poor wound healing due to a decrease in vasculature density caused by damage to the endothelial cells that make up blood vessels. This damage is triggered by an increase in oxidative stress resulting from hyperglycaemia [64]. The resulting impaired blood flow can lead to poor tissue oxygenation (hypoxia) [65, 66]. In addition, a diabetes patient's weakened immune response and nerve damage (neuropathy) allow relatively minor injuries to develop into chronic wounds [64, 67]. Diabetic wounds are typically characterised by impairment in each phase of the wound healing process, causing a delayed, incomplete, or uncoordinated process. This hinders the formation of granulation tissue and reduces

the tensile strength of the wound [65, 66]. Beyond this, mitochondrial overproduction of reactive oxygen species (ROS) creates a high oxidative stress environment, affecting angiogenesis, platelet function, and vasoconstriction to further compromise the healing process [68, 69, 70]. The innate immune response in injured tissue is compromised due to down-regulation of key initiators such as Toll-like receptors (TLRs). This dysfunction weakens the chemotactic signals that normally recruit inflammatory cells to the wound site [71]. Dysregulation of these immune cells can itself induce damage to wound tissue and further exacerbate inflammation, delaying the transition to the proliferative phase [51, 72]. A common risk factor in the chronicity of diabetic wounds such as DFUs is infection. Bacteria that colonise the wound bed benefit from the prolonged inflammatory response, as it provides a source of nutrients [73].

The development and persistence of CWs is driven by a complex interplay of factors. Prolonged inflammation, inadequate tissue oxygenation, and bacterial colonisation form a self-perpetuating cycle that impedes healing indefinitely. Bacteria within the wound often exist within a biofilm state that protects individual bacteria from antimicrobial agents and interrupts the healing process, prolonging infection and contributing to the high rate of lower limb amputation observed in diabetic patients with CWs [74].

1.2 Bacterial Biofilms in DFUs

1.2.1 Biofilm Life Cycle

Bacterial biofilms play an important role in both normal bacterial life cycles and bacterial pathogenicity. Although biofilms are not necessarily harmful and can be found in a wide range of environments, they can be detrimental in the context of wound healing [75]. The presence of bacterial biofilm infections is one of the key factors contributing to the development and perpetuation of CWs such as DFUs [76, 77]. A bacterial biofilm is broadly defined as a complex community of microorganisms surrounded by a self-produced EPS matrix [78, 79]. These biofilms often contain a diverse range of bacterial species and, increasingly, exhibit multi-drug resistance [80, 81, 82]. Common species found in infected wound beds include *S. aureus*, *P. aeruginosa*, and various anaerobic bacteria such as *Clostridium* spp. [83, 84, 85]. These bacteria can originate from environmental sources or the patient's own skin or mucosal membranes [77].

The biofilm life cycle involves several stages: initial cell attachment, micro-colony formation, maturation, and dispersal **(Fig 1.2)**. Motile planktonic bacteria that are not in the biofilm-forming phase attach to a surface **(Fig 1.2 A)** and aggregate, forming a small colony **(Fig 1.2 B)** [86]. The EPS produced by this group

of cells leads to firm surface attachment and microcolony formation **(Fig 1.2 C)**. These microcolonies then mature through intercellular signaling, forming a three-dimensional structure **(Fig 1.2 D)**. Finally, mature biofilms can undergo partial or complete dispersal, releasing clusters of planktonic cells that can colonise new areas of the wound and further the spread of infection **(Fig 1.2 E)**. Dispersal can be initiated in response to a range of environmental stressors, such as oxygen or nutrient gradients [87, 88].

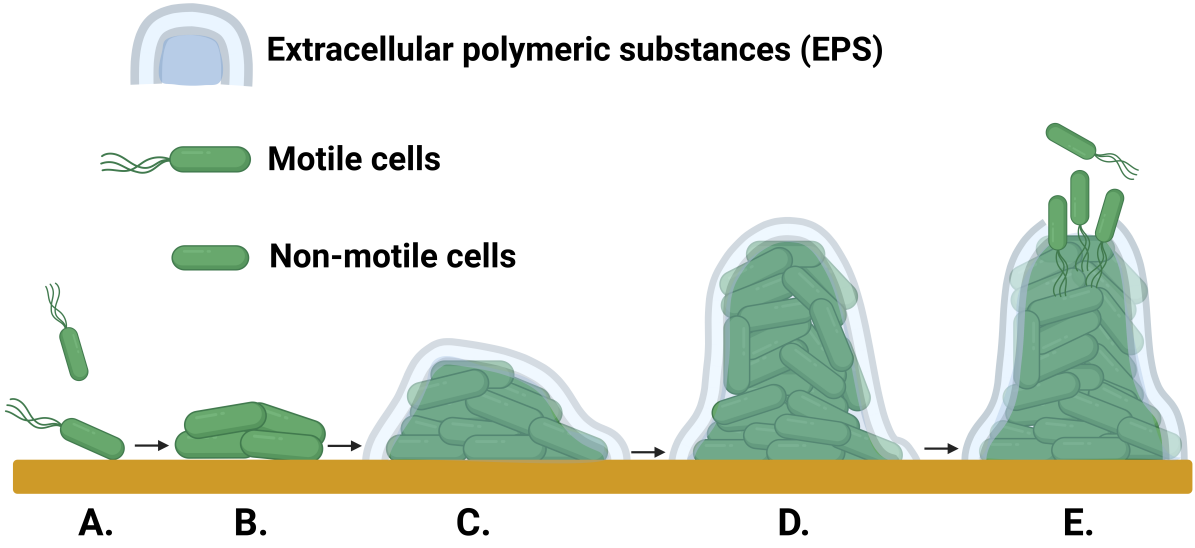

Figure 1.2: Typical stages of a biofilm life cycle. **(A)** Initial attachment of motile bacteria may be weak, but can become permanent, leading to stable attachment and aggregation of sessile (fixed) cells. **(B)** Small groups of cells begin to produce EPS that surround and support the growing microcolony. **(C)** Microcolony matures through intercellular signalling to form a three-dimensional structure. **(D)** Mature biofilm. **(E)** Biofilms can disperse, with motile individuals able to spread elsewhere and colonise other surfaces. Adapted from LuTheryn *et al.*, [89].

1.2.2 Biofilm Tolerance Mechanisms

One of the most prominent phenotypic differences between biofilms and planktonic cells is the decreased susceptibility of biofilms to antimicrobial agents [90, 91]. Indeed, bacterial cells in a biofilm have exhibited up to 1000 × more resistance to antimicrobials than their planktonic counterparts [92]. The increased tolerance of biofilms to antimicrobials is generally accepted to be a complex multifactorial process [91, 93]. The specific mechanisms underlying this resistance and tolerance vary considerably, depending on factors such as the type of antimicrobial agent, the bacterial species and strain, the maturity of the biofilms, and the growth conditions [93]. Importantly, no single mechanism can fully explain the increased antimicrobial recalcitrance exhibited by biofilms [94].

EPS Matrix

The self-produced EPS matrix serves as the architectural and functional backbone of biofilms, playing a pivotal role in the persistence and pathogenicity of CW infections. Although typically composed of polysaccharides, proteins, lipids, and extracellular DNA (eDNA) [95, 96], the specific composition can vary depending on the bacterial species and the environmental conditions of the biofilm. The EPS provides several key functions that contribute to the resilience of biofilms in CWs.

Firstly, the EPS matrix acts as a protective barrier, shielding the embedded bacterial cells from various environmental stresses, such as host immune defences and antimicrobial agents [96, 97]. Beyond being just a diffusion barrier, the charged nature of the EPS matrix makes it able to sequester and neutralise antimicrobial compounds, preventing them from reaching their target site within biofilm-embedded cells [98, 99]. Enzymes within the biofilm EPS matrix can also degrade antibiotics, increasing tolerance to treatment [97].

In addition, the EPS matrix also plays a crucial role in mediating cell-to-cell communication and coordinating collective behaviour within the biofilm. This behaviour (a process known as 'quorum sensing') enables bacterial cells to coordinate the expression of genes involved in the biofilm life cycle, virulence, and persistence of CW biofilms [100]. The EPS matrix also facilitates the adhesion of bacterial cells to the wound bed and helps to maintain the structural integrity of the biofilm [101]. Polysaccharides and proteins within the matrix can bind to abiotic surfaces and extracellular components, anchoring the biofilm in place and preventing its detachment [96]. In CWs, this adhesive property allows the biofilm to to better withstand the various mechanical forces exerted by both wound exudates and wound management procedures [102].

Persister Cells

Persister cells are a subpopulation of bacteria within biofilms that exhibit remarkable tolerance to antimicrobial agents and other stressors [103]. Although these cells are not inherently resistant to antibiotics, they enter a transient, dormant state that allows them to survive exposure to lethal doses of antimicrobials that typically target cellular metabolic or division processes. When these persistant pathogenic microbes cannot be eliminated by the host immune system, they can serve as a reservoir from which infection can recur [19]. Moreover, this reservoir of persister cells could provide additional opportunities for antibiotic resistance to develop, either randomly or through horizontal gene transfer [104].

Although the molecular mechanisms underlying persister cell formation and antimicrobial tolerance are not yet fully understood, it is thought that toxin-antitoxin systems and stress responses may initiate a stochastic genetic switch within a stationary microbial population. Specifically, it is not clear whether this genetic switch is triggered by the presence of an antimicrobial stressor or as part of the biofilm life cycle [97]. However, persister cells can return to a functional state upon the removal of stress, through processes such as chemotaxis and activation of hibernating ribosomes [105]. Although this resuscitation can often lead to infection relapse, it is important to note that the resuscitation of persister cells (such as through mechani-

cally induced biofilm dispersal) may render them susceptible to antibiotic treatment [105].

Aetiology of Chronic Wound Infections

Exposure of subcutaneous tissue following an injury provides a moist and nutritious environment conducive to microbial colonisation and proliferation [77]. Unlike surgical wounds, the presence of foreign material and devitalised tissue in traumatic wounds often facilitates microbial proliferation through infiltration of the surrounding microflora [106]. Wound contaminants are most likely to originate from three main sources: exogenous microorganisms introduced either from the environment or through injury; normal skin microflora such as *Staphylococcus epidermidis*; or endogenous microfloras of mucous membranes such as the gastrointestinal or genitourinary mucosa [77, 107].

A comprehensive study involving 2,963 patients with diverse CW types, including DFUs, venous leg ulcers, and pressure ulcers, revealed that *Pseudomonas* and *Staphylococcus* were the most identified bacterial genera [108].

Commensal microorganisms, typically part of the normal skin flora, can gain access to the wound bed through injury and exhibit opportunistic behaviour in the altered wound environment [109]. Although some commensal bacteria may play a beneficial role in modulating the wound microbiome and supporting the host immune

response, others may potentially contribute to the persistence and pathogenicity of chronic infections [109]. The co-existence of different bacterial species within CW environments is a crucial factor in understanding the complex dynamics of these polymicrobial infections [110]. A recent systematic review found the average prevalence of biofilms in CWs to be 78.2% [111].

Bacteria in CW biofilms can engage in symbiotic relationships, and through horizontal gene transfer and bacterial communication enhance their overall survival and persistence. For example, *P. aeruginosa* and *S. aureus* have been observed to grow together within the wound bed [112]. Interestingly, the spatial distribution of these bacterial species within the CW can vary, with *P. aeruginosa* often found in deeper tissues, while *S. aureus* is more commonly found near the wound surface [113]. This spatial stratification may be attributed to factors such as the differential oxygen and nutrient requirements of these bacteria, as well as their ability to exploit specific micro-niches within the wound environment. *S. aureus* can increase the attachment of *P. aeruginosa* to keratinocytes, which in turn benefits both species [109].

1.3 Treatment of Diabetic Foot Infections

As a result of the recalcitrant, antibiotic-tolerant nature of CW biofilms in DFUs, treatments are centered on three approaches, often performed concurrently: debridement, broad-spectrum antibiotics, and topical therapy [114]. In the management of CWs, debridement is essential to remove necrotic and devitalised tissue and bacterial elements that can inhibit wound healing [59, 114]. By reducing the bacterial burden and disrupting biofilms, debridement mitigates pro-inflammatory responses and promotes granulation tissue formation in the wound bed [115].

Various debridement techniques can be used, including surgical, enzymatic, mechanical, and biological [116]. The nature of surgical debridement often leads to adverse events, which can require secondary closure or tissue grafting. Likewise, enzymatic and biological debridement are often contraindicated in heavily infected wounds due to high bioburden [117]. However, critically, debridement treatment protocols often require weekly maintenance to enhance outcomes, as biofilms have been observed to quickly re-establish within wounds in as little as 72 hours post-debridement [115]. Efficacy of debridement therefore often parallels cost and time, with a cohort study of 312,744 wounds showing that approximately 30% of wounds do not heal following standard debridement protocols [118].

Systemic antibiotics (parenteral or oral) are often administered as soon as possible for suspected clinically invasive infections, with the choice of antimicrobial taking into account the severity of infection, the risk of complications, and microbiological results [119]. Systemic antibiotic use in DFU patients, however, often suffers from poor penetration into the poorly vascularised target site, leading to sub-therapeutic doses present in infected tissues [120]. In fact, significantly higher dosages of antimicrobials are often required to overcome this limitation, bringing about systemic toxicity risks [121, 122]. In particular, at these dosages, the development of antimicrobial resistance is a major concern [123]. Indeed, 67.1% of bacteria in wounds have been found to be multidrug resistant, adding more complexity to the management of wound infection [124].

Topical antibiotics offer a promising alternative, alone or with systemic agents, to address the challenges posed by CW infections. Compared to systemic therapies, topical applications can achieve a high and sustained concentration at the infection site, enhancing the efficacy of the treatment while minimising systemic toxicity and overcoming poor tissue penetration of systemic therapies [125]. Beyond that, topical applications allow for the use of novel antimicrobial agents otherwise not suitable or approved for systemic administration, thereby expanding the array of treatment options. Indeed, a study examining 47 multi-resistant organisms isolated

from CWs found that these bacteria were susceptible to a range of 11 commonly used topical antibiotics and antiseptics, suggesting that topical therapies may be an effective strategy in managing CW infections, even in the face of systemic antibiotic resistance [126].

Unfortunately, very few antibiotics have been proven effective as topical therapies in clinical trials, and even fewer have been granted approval in the face of antimicrobial resistance risks [127]. Furthermore, almost all have minimal penetration across intact skin or soft tissue, limiting their use to shallow open wounds to avoid systemic absorption. Therefore, the focus has been on the use of natural antimicrobial substances such as silver, iodine, or honey incorporated within wound dressings to help improve the conditions of the wound bed and facilitate healing [128]. However, many of these approaches often do not directly address the state of the biofilm, allowing recolonisation by persister bacteria and the recurrence of infection.

1.4 Drug Delivery Systems for the Treatment of Chronic Wound Biofilms

CW biofilms present significant challenges to conventional pharmacological therapies such as unintended side effects in patients, low bioavailability, insufficient half-life *in vivo*, and the need for tissue-specific targeting [129]. To address these limitations, nanoparticle (NP)-based drug delivery systems (DDS) have been explored, including liposomes, micelles, and solid metal NPs [130, 131]. Many of these systems are designed for topical application to wound sites, and can be classified into passive and active delivery systems [132].

1.4.1 Passive Drug Delivery Systems

Passive DDS rely on the inherent properties of NPs to achieve antibiofilm effects, and include liposomes and metal NPs.

Liposomes

Liposomes are small spherical vesicles composed of a phospholipid bilayer shell encapsulating an aqueous core, and have been established as viable carriers of various therapeutics such as vaccines and anticancer drugs [133, 134, 135, 130]. Liposomes have been effective at improving the efficacy of antimicrobial agents against *P. aerug-*

inosa biofilms [136]. They have good biocompatibility and can protect unstable and volatile compounds by encapsulation for delivery to biofilms [136]. Using liposome-encapsulated aminoglycosides such as gentamicin and tobramycin, Mugabe *et al.* showed that liposomes can fuse to the bacterial membrane in planktonic cultures of *P. aeruginosa*, increasing antibiotic penetration [137]. Liposome penetration into a biofilm is affected by their size and charge [97]. Despite their potential, liposomes have several limitations, including instability due to aggregation and potential cytotoxicity (particularly for cationic liposomes) [136]. Aggregation can cause the fusion of neighbouring liposomes, creating larger liposomes and reducing the availability of loaded bioactive compounds [138].

Metal NPs

Silver and gold solid metal NPs have garnered interest as a potential wound therapeutic, due to their intrinsic antimicrobial properties [130]. Several studies have demonstrated the effectiveness of metal NPs against biofilms. For example, Park *et al.* assessed the effect of silver NPs on *P. aeruginosa* biofilms reporting a 3.5-log reduction in biofilm coverage [130, 139]. Similarly, Kalishwaralal *et al.* recorded significant (95% biofilm formation inhibition) antimicrobial effects of silver NPs on *P. aeruginosa* and *S. aureus* biofilms [130, 140]. Gold NPs have also shown promise in combating bacterial biofilms. Boda *et al.* demonstrated that gold NPs can cause

lysis of bacterial membranes in gram-positive bacteria (*S. aureus* and *S. epidermidis*), causing up to a 5-log reduction in bacterial growth after 5 h [141]. However, the use of metal NPs is not without concerns. For silver NPs, there are concerns about dose-dependent effects that can decrease keratinocyte activity and viability [142]. Additional risks of DNA damage and general cytotoxicity have been noted as key areas that require further investigation [143].

Concerning gold NPs, there is contradictory evidence regarding potential toxicity, and no overall consensus has been reached [144]. Furthermore, recent studies have challenged the established view that bacteria do not develop resistance to metal NPs, with some studies observing potential mechanisms by which bacteria could develop resistance to metal NPs over time [145, 146]. Although passive DDS offer several advantages, they also have limitations. A key limitation is that they generally do not physically disrupt the biofilm matrix, which could allow the biofilm to re-establish more easily. To address this limitation, active DDS are being developed that respond to specific stimuli or external activation, enabling targeted drug release and potentially enhancing biofilm disruption.

1.4.2 Active Drug Delivery Systems

Active DDS offer greater control over the release of therapeutic agents when compared to passive systems. These can broadly be categorised into two groups: responsive DDS and externally activated DDS.

Responsive DDS

Responsive DDS are engineered to release therapeutic agents in response to specific environmental stimuli found within the biofilm microenvironment, such as changes in pH, enzymatic activity, or temperature [147].

pH-Responsive Systems

pH-responsive systems take advantage of the acidic microenvironment that is often characteristic of bacterial biofilms. These carriers are typically designed to remain stable at physiological pH but to release their cargo under acidic conditions. For example, pH-sensitive micelles have been shown to effectively deliver antibiotics to *P. aeruginosa* biofilms, with enhanced penetration and antibacterial activity compared to free antibiotics [148].

Enzyme-Responsive Systems

Enzyme-responsive systems rely on the overexpression of specific enzymes found in biofilms, which can be used to trigger controlled drug release. These systems

typically incorporate enzyme-cleavable linkers or enzyme-degradable materials that respond to the biofilm microenvironment. The enzymes found in the biofilm environment depend on the species present and include hyaluronidases, lipases, glycosidases, and azoreductases [149, 150]. For example, Wang *et al.* used enzyme-responsive multilayer films to deliver gentamicin to *Staphylococcus aureus* biofilms. These films degraded after exposure to hyaluronidase, resulting in controlled antibiotic release and prevention of bacterial attachment [151].

Temperature-Responsive DDS

Temperature-responsive DDS exploit the increased temperature seen in infected or cancerous tissues, or use targeted localised heating to trigger release. These systems typically employ thermosensitive polymers that undergo conformational changes at specific temperatures, thereby releasing their payload. Thermosensitive liposomes have been explored for tumour therapy applications, which typically have elevated temperatures compared to surrounding tissue [152]. However, for antibiofilm and other therapeutic applications, the use of temperature-responsive drug carriers often requires external stimuli to induce the temperature increase necessary to cause drug release.

Externally Activated DDS

DDS that can be activated through external stimuli offer additional spatial and temporal control of therapeutic delivery. These systems respond to external triggers such as magnetic fields, light, and ultrasound, allowing for precise control over drug release.

Magnetically Responsive Systems

Magnetically responsive systems have been explored for their ability to guide drug carriers to specific locations and trigger release through external magnetic fields. These systems often incorporate superparamagnetic iron oxide NPs as the responsive element [153]. External magnetic fields can be used to generate localised hyperthermia, triggering drug release from thermosensitive carriers [154, 155].

Light-Responsive Systems

Light-responsive DDS generally fall into different therapeutic categories: photodynamic therapy (PDT) and photothermal therapy (PTT), both being of considerable interest in anticancer research [156, 157]. In PDT, light and a light-activatable compound known as a photosensitiser (PS) react together with oxygen, undergoing a photodynamic reaction to produce ROS [158]. ROS generation is in turn used to induce localised cytotoxic effects within the target tissue.

In the context of biofilm therapy, PDT and PTT are often used in combination with NO-donors [149]. For example, an L-Arginine-rich amphiphilic dendritic peptide (Arg-ADP) was used by Zhu *et al.* [159] with the photosensitiser Chlorin e6 (Ce6) to induce NO release after NIR irradiation. They showed that PDT could be used to generate both singlet oxygen and NO for a combined antibacterial and biofilm eradication effect.

In contrast, PTT uses near-infrared (NIR) light, typically in the 700 - 900 nm wavelength range. NIR light is absorbed by the drug carrier and converted into thermal energy, leading to a localised temperature increase [156]. For example, Zhao *et al.* used an NO-donor bound to a graphene platform. Upon NIR irradiation, local hyperthermia induced the release of NO and mediated an antibiofilm effect [160]. A key limitation of light-responsive therapies is the limited penetration depth of the light beam, which restricts the use of these therapies to superficial layers of tissue [161]. US-responsive DDS have been explored as a potential alternative as they can offer deeper tissue penetration capabilities and because of the wide clinical acceptability of ultrasound instrumentation.

1.5 US-responsive Drug Delivery Systems

Ultrasound (US) is defined as sound with a frequency above the upper limit of human hearing (20,000 hertz, Hz), and has several applications in both diagnosis and therapy [162, 163, 164]. US waves are generated by transducers that convert electrical signals into mechanical waves, which can be precisely focused [165]. Diagnostic US is routinely used as a noninvasive method to image internal organs and tissues. As US waves travel through tissues, reflections at tissue interfaces caused by differences in acoustic impedance can be detected and used to generate an image [163, 166, 167]. Diagnostic US typically uses a range of frequencies from 2 to 15 megahertz (MHz), with some specialised applications using frequencies up to 60 MHz [168].

Both diagnostic and therapeutic US applications can make use of focusing to achieve improved outcomes. In diagnostic US, focusing can allow for improved spatial resolution, while in therapeutic US a reduction in off-target effects is possible through more precise spatial delivery of acoustic energy [169, 170].

Therapeutic US applications make use of a range of intensities and frequencies that depend on the intended biological effect.

Low-intensity focused ultrasound is being investigated as a method to induce a number of neuromodulatory effects and enhance drug delivery [171, 172, 173]. High-intensity focused ultrasound is instead generally used to induce tissue necrosis through localised hyperthermia (>56 °C) and is being explored for a variety of applications including tumour ablation and targeted drug delivery [174, 175]. These thermal effects are achieved in part through the use of continuous US. Instead, the use of short pulses of high-intensity ultrasound has been used to non-thermally destroy target tissues [176, 177]. Pulsed US is commonly used in therapeutic applications to avoid thermal effects that can result in tissue damage of surrounding non-target tissue [178].

1.5.1 Therapeutic US Parameters

In addition to frequency, the parameters used to describe the US include acoustic pressure (often expressed in MPa), duty cycle (%), and pulse repetition frequency (PRF, in Hz) [179]. The duty cycle is an expression of the percentage of time a US signal is 'on' during a given pulse, while the PRF is the number of pulses emitted by the transducer per second [180]. US intensity is traditionally expressed as watts per square centimeter (W/cm^2), with most diagnostic imaging performed at intensities of 0.05–0.50 W/cm^2 [17]. Generally, low-intensity US has intensities of <3 W/cm^2 and high-intensity US has intensities of >3 W/cm^2.

In clinical settings, the mechanical index (MI) is used as an indicator of the potential for cavitation bubbles to be generated within tissues and as a safety metric for clinical US [181].

$$MI = p_r/\sqrt{f} \tag{1.1}$$

The MI (**Equation 1.1**) is defined as the rarefactional pressure p_r (MPa) divided by the square root of the frequency f (MHz). The British Medical Ultrasound Society identified an MI >0.7 as a potential hazard, advising limited exposure to US of MI of >0.3 for lungs and intestine [182]. Due to the use of US cavitation nuclei, the suitability of MI is debated for therapeutic US applications as a measure of safety [183]. This is in part due to the differences in frequency and pulse length used in diagnostic imaging systems compared to therapeutic applications [184]. Therapeutic US typically uses lower frequencies and longer pulse lengths than diagnostic US, which can lead to the underestimation of potential bio-effects when using MI alone as a metric [164].

For therapeutic applications, pulsed US is typically used over continuous US to avoid thermal effects [185]. PRF in therapeutic US typically ranges from 0.5 Hz up to several kHz, with duty cycles also implemented over a wide range depending on the application [178, 186, 187, 188]. Several alternatives to MI have been proposed, including the Cavitation Aggressiveness Index (CAI) and the Thermal Index, al-

though no consensus has been reached [189, 190, 183]. US-responsive DDS comprise a wide range of approaches, including gas MBs, liposomes, and PDs [191, 192, 193]. Gas MBs are one of the most widely studied platforms for US-mediated drug delivery, in part due to their ubiquity in diagnostic US imaging as a contrast agent [194].

1.5.2 Gas Microbubbles

MBs are well established contrast-enhancing agents in diagnostic US imaging, enabling augmented imaging of the vasculature [195, 196]. These spherical structures typically comprise a gas core surrounded by a shell composed of denatured proteins, polymers or lipids, with diameters typically between 1 and 10 µm [195, 197]. The composition and properties of the MB shell significantly influence both MB stability and acoustic response [198]. MBs can be manufactured through several methods, including sonication, mechanical agitation, and microfluidics [199]. Sonication involves the use of low-frequency US (15-25 kHz) applied at the liquid-gas interface of a liquid dispersion of the MB coating material [200]. Mechanical agitation involves shaking a closed container containing a liquid and gas phase [201]. The microfluidic approach, while more complex, typically leads to a much narrower distribution of bubble size than sonication or agitation, at the cost of lower production rates. Microfluidics uses small channels to direct both gas and liquids in such a way that

small bubbles can 'pinch off' from the gas stream at the region where the flows of liquid and gas meet [202]. Uncoated MBs within a liquid are inherently unstable, as the effect of Laplace pressure contributes to greater pressure inside the gas core, leading to rapid MB dissolution rates on the order of microseconds [203, 204, 205].

The Young-Laplace equation **(Equation 1.2)** describes the pressure difference (ΔP) between the inside and outside of the bubble caused by the surface tension (σ) at the interface between the bubble core and the surrounding liquid [206].

$$\Delta P = P_{inside} - P_{outside} = \frac{2\sigma}{r} \tag{1.2}$$

where P_{inside} is the pressure inside a bubble, $P_{outside}$ is the pressure outside a bubble, σ is the surface tension, and r is the radius of the bubble. In a MB shell, phospholipids organise into a uniformly-oriented monolayer, with the hydrophilic phosphate headgroup orienting towards the aqueous medium and the hydrophobic acyl chain (or 'tail') orienting towards the gaseous core [197]. The length of the phospholipid carbon chain influences the transition temperature (T_m): as temperature increases past the T_m, phospholipids transition from a crystalline or 'gel-like' state and enter a liquid-crystalline or 'fluid-like' state [197]. Below the T_m, packing (organisation) of the lipid monolayer will manifest in a more ordered manner, while above the T_m lipid packing is less ordered [207].

Lipids such as 1,2-distearoyl-sn-glycero-3-phosphocholine (DSPC) and 1,2-dipalmitoyl-sn-glycero-3-phosphocholine (DPPC) are often selected as the primary component of the MB shell due to their T_m (above physiological temperature) and increased rigidity over shorter chain length phospholipids: generally, longer acyl chains lead to increased MB stability [208, 209, 210]. To reduce coalescence and improve stability, emulsifying agents such as polyethylene glycol (PEG) are incorporated into the MB shell. PEG acts as a 'brush' or barrier to prevent coalescence between bubbles [210, 211]. PEG can be incorporated into the MB shell using PEGylated phospholipids such as DSPE-PEG(2000) or through the use of a surfactant such as PEG-40-stearate (PEG40S) [207, 212, 213].

The core of MBs is usually filled with a gas that is inert and biocompatible. PFCs are frequently selected due to their low solubility and diffusivity in blood, which improves the half-life of MBs *in vivo* [214]. Furthermore, PFCs are biologically inert, minimising toxicological risks [215].

Despite their advantages, gas MBs have a relatively short circulation time in the bloodstream, typically less than 5 minutes in the case of commercially available gaseous perfluoropropane Definity® MBs [216]. The high compressibility and low density of the gas core make MBs particularly useful in US imaging due to the large difference in acoustic impedance between the bubble and surrounding tissues

or fluids [217].

Response of MBs to US

Gas-core MBs respond to US exposure through volumetric oscillations, expanding and contracting during the rarefaction and compression phases of the pressure waves, respectively. These oscillations, termed acoustic cavitation, are generally classified into either stable or inertial cavitation. Below a critical acoustic pressure threshold, MBs can undergo repeated oscillations (often referred to as stable cavitation) **(Fig. 1.4)**, creating localised vortical flow patterns known as microstreaming [218]. When proximal to a surface such as a cell membrane, these fluid streams can impart shear forces that can lead to formation of transmembrane pores (a phenomenon known as 'sonoporation') that can increase membrane permeability and allow greater uptake of therapeutic compounds [28, 197, 219]. However, beyond a certain acoustic pressure level, MBs can be driven to collapse, a process known as inertial cavitation [220]. MBs will first expand rapidly before violently collapsing under the effect of fluid inertia, generating fluid jets and/or shockwaves that can also cause pore formation in cell membranes [221, 222]. The effectiveness of US-assisted wound debridement has been attributed to these physical effects, with cavitation able to emulsify necrotic tissue and stimulate wound healing [223].

Passive cavitation detection (PCD) is a method used to detect the acoustic emissions of US-stimulated MBs [224]. The acoustic energy released from bubble oscillations can be detected using this approach [217, 224, 225]. The general trends seen in the acoustic emissions of stable or inertial MB cavitation are summarised by Gu *et al.* [226] **(Fig. 1.3)**. Briefly, Fast Fourier Transforms (FFTs) are performed on recorded acoustic emissions to obtain the frequency content of the signals [227]. At low acoustic pressures, no harmonic signals are apparent, and only a peak is visible at the transducer driving frequency (fundamental frequency, f_0), as shown in **(Fig. 1.3 A)**. As acoustic pressure is increased, peaks at harmonic frequencies are present and indicate stable MB oscillation, as shown in **(Fig. 1.3 B)**. Further increasing the pressure towards the inertial cavitation threshold, the presence of sub- and ultra-harmonic peaks is apparent, as in **(Fig. 1.3 C)**. Finally, at sufficient peak rarefactional pressures, inertial cavitation leads to an elevation in the broadband noise level, as illustrated in **(Fig. 1.3 D)**.

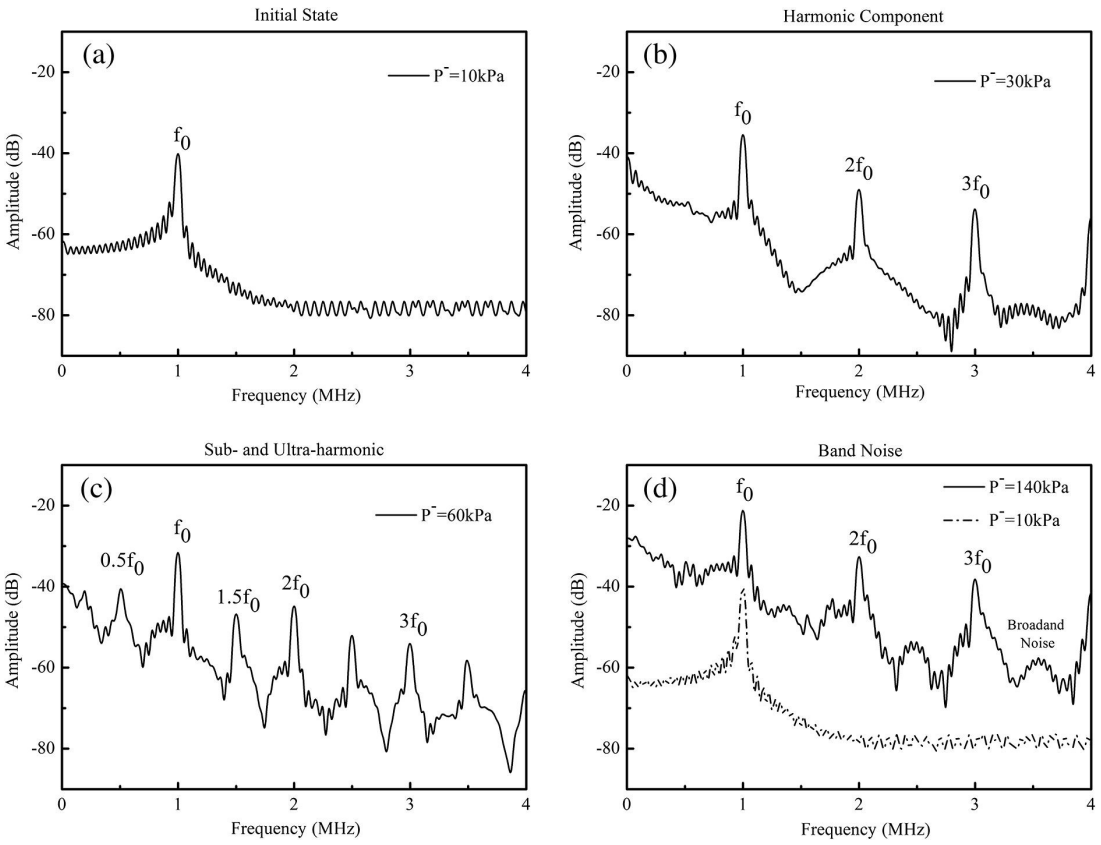

Figure 1.3: FFT spectra obtained from stimulating albumin-shelled PFC MBs at different acoustic driving pressures. **(A)** P^{-}=10 kPa; no harmonic components are apparent. **(B)** P^{-} = 30 kPa; harmonic components appear. **(C)** P^{-} = 60 kPa; sub- and ultra-harmonic components appear. **(D)** P^{-} = 140 kPa; the broadband noise level increases and the sub- and ultra-harmonic components are suppressed.
From Gu *et al.* [226]

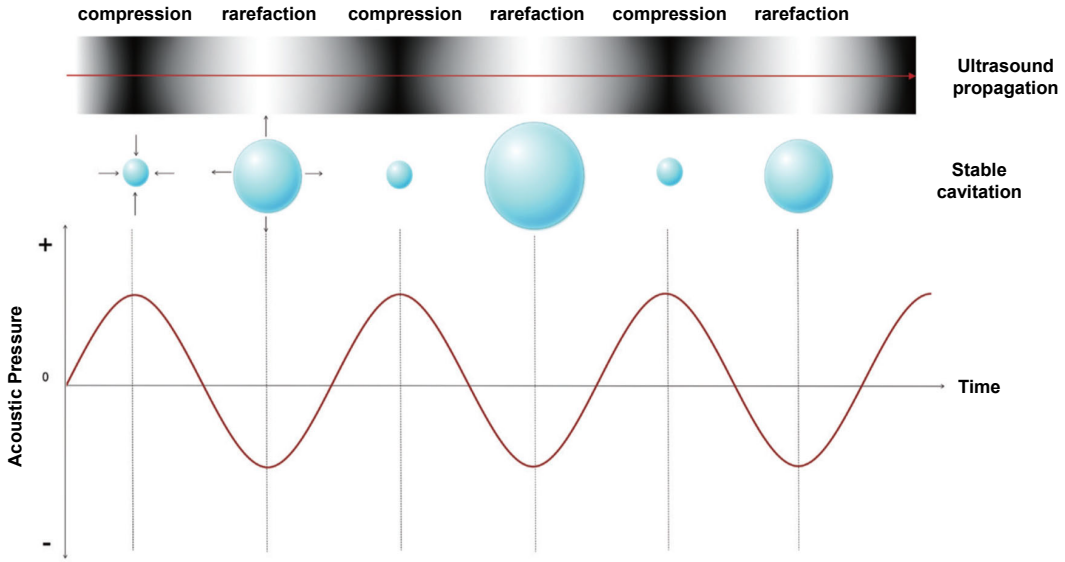

Figure 1.4: As an acoustic wave travels longitudinally, it alternates between compression and rarefaction phases. Under US stimulation, a gas MB will respond by volumetrically expanding and contracting. Modified from Lee *et al.* [218].

Antibiofilm Applications of MBs

MBs combined with US are emerging as a promising strategy for managing chronic bacterial biofilms. The effects of MB cavitation can physically disrupt the biofilm matrix as well as enhance the delivery and efficacy of antimicrobials (an approach recently termed 'sonobactericide') [228]. Multiple mechanisms mediate these effects across a range of timescales. MB oscillations occur on the order of microseconds, while biological effects (seconds - minutes) and outcomes of clinical relevance (days to months) occur over much longer timescales [228]. These mechanisms have been demonstrated across a range of biofilm models.

For instance, He *et al.* [26] showed that the use of US-activated (80 kHz, 1.0 W/cm^2, 50% duty cycle, 10 min duration) SonoVue®MBs created distinct pores within *S. epidermidis* biofilms. Additionally the combination of US and MBs enhanced the effect of vancomycin, significantly reducing the biofilm density and viability of *S. epidermidis* cells recovered post-treatment. Similar work by Dong *et al.* [229] concluded that US + MBs (300 kHz, 0.5 W/cm^2, 50% duty cycle, 5 min duration) enhanced the bactericidal effect of vancomycin on rabbit-implanted catheter biofilms compared to US and vancomycin, suggesting a potentiating effect of cavitating MBs.

Ronan *et al.* [230] demonstrated that Definity® MBs combined with 0.5 MHz US (1.1 MPa peak negative pressure, 16-cycle tone burst, 1 kHz PRF for 5 minutes) resulted in distinct structural changes in *P. aeruginosa* PAO1 biofilms. Exposure to US and MBs led to the formation of craters (5-20 µm diameter) in the biofilm structure and, when combined with gentamicin, significantly reduced biofilm metabolic activity compared to either treatment alone.

Although MBs have shown promise for biofilm treatment, their size (1-10 µm) could limit their ability to penetrate deeply into biofilm matrices. PDs are of research interest due to the potential for smaller particles (<1 µm) to penetrate the biofilm matrix and undergo cavitation within the biofilm structure itself. Additionally,

the high gas solubility of PFCs could be exploited to deliver bioactive gases (such as nitric oxide) to the biofilm. This approach would enable the combination of anti-biofilm effects induced by specific bioactive gases with the physical action of US-activated PDs.

Biofilm Response to Mechanical Stimuli

The development of antibiotic resistance in bacterial biofilms is a well-established concern. However, the development of tolerance to other aspects of stimuli-responsive therapies is less well understood. In the context of antibiotic-free approaches, understanding bacterial responses to treatment exposure can mitigate the emergence of deleterious resistance mechanisms. Exposure to US leads to changes in intracellular signalling within a biofilm [231]. Biofilms respond to mechanical stresses: a review by Gloag *et al.* showed that in general, biofilms that develop under exposure to higher shear stresses are highly adherent and more robust [232].

Mechanical stimuli, such as mechanical shear imparted on a biofilm under exposure to US or through US-activated cavitation nuclei can significantly alter biofilm structure, potentially contributing to more robust biofilm formation. Bharatula *et al.* showed that *Pseudomonas aeruginosa* biofilms exposed to increasing intensities of US had increased levels of cyclic di-GMP, an intracellular signalling molecule key in the regulation of biofilm formation [231]. When developing thera-

pies that impart shear stresses on the biofilm EPS, monitoring of changes to biofilm characteristics can establish a baseline to assess treatment effectiveness. The incorporation of ultrasound-only controls is key to enable differentiation of the biofilm response to therapeutic agents from the response to US itself. The contribution of other factors such as bacterial species, growth conditions, and ultrasound stimulation conditions will affect how a biofilm model responds to treatment.

Where viable, reducing the US exposure required to activate cavitation nuclei could be beneficial in mitigating the biological response. To monitor biofilm characteristics, techniques such as fluorescence microscopy or electrochemical impedance spectroscopy can be used to monitor biofilm model growth and subsequent response to treatment *in situ* [233, 234]. Depending on how novel treatments are administered, long treatment times may not be clinically practical, especially those requiring active stimulation of the wound biofilm with US [89].

1.6 Perfluorocarbon Droplets

PDs typically comprise a liquid PFC core stabilised by a phospholipid shell, and range in size from ∼200 nm up to several microns in diameter **(Fig. 1.5)** [214, 235]. The development of PD emulsions aims to overcome the limitations of gas-filled MBs, particularly in terms of stability both during storage and in physiological

environments [236].

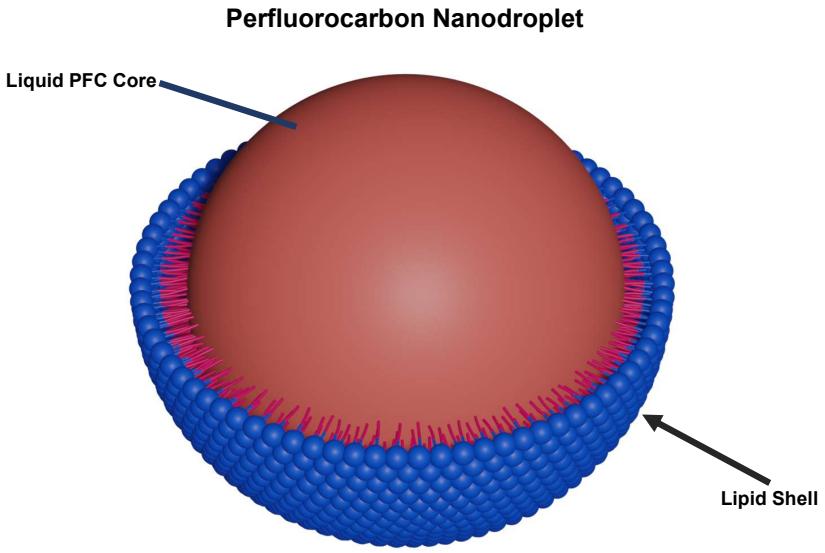

Figure 1.5: Typical structure of a PD.
A liquid-perfluorocarbon core is coated by a lipid-surfactant shell.

A key property of PDs is their ability to undergo acoustic droplet vaporisation (ADV). Under sufficient US stimulation, PDs can be converted into gas-filled MBs by phase-transition of the liquid PFC core into a gas [31]. This is accompanied by an increase in size of approximately 4-10 times depending on the initial droplet diameter [236]. The resultant gas-core PFC MBs can then undergo cavitation upon further exposure to US, mediating various physical effects as described previously.

The ability to control when US-responsive MBs are generated is an advantage being exploited for internal applications, whereby PDs of sufficiently small diameter may be capable of leaving the vasculature and enter the interstitial space of solid tumors *via* the enhanced permeability and retention (EPR) effect [67, 237]. This

potentially enables the localised delivery of therapeutic agents and physical effects to areas not accessible by MBs.

In the liquid state, PFCs have a high capacity to dissolve gases, due to the low polarisability of fluorine molecules, leading to strong intramolecular forces but weak intermolecular (Van der Waals) forces [238]. Consequently, PFC emulsions are being explored as carriers for various bioactive gases, including oxygen and nitric oxide [238, 239]. The acoustic behaviour of PDs, in particular the threshold of ADV, is influenced by several factors, including droplet diameter and composition of the PD core and/or shell. Common PFCs used to generate PDs include perfluoropentane (PFP) and perfluorohexane (PFH), which have bulk boiling points of 29.2 °C and 57 °C, respectively [240]. In general, a higher-boiling point PFC will require a greater peak rarefactional pressure to undergo ADV. Similarly, as the diameter of the PDs decreases, the threshold ADV pressure increases due to the increase in associated Laplace pressure **(see Equation 1.2)** [241, 242] . The Laplace pressure significantly increases the boiling point of the PD liquid core [31].

Wu *et al.* summarised values of ADV threshold (and associated US exposure parameters) found in the literature for a range of PFC droplet formulations. For example, Fabilli *et al.* showed that lipid-shelled PFP droplets (1.7 µm diameter) had a mean ADV threshold of 3.8 MPa (37 °C, 83 Hz PRF, 13 cycles burst, 3.5

MHz frequency), while Schad and Hynynen showed that 3.6 µm diameter lipid-shelled PFP droplets had an ADV threshold of 2.4 MPa (37 °C, single 10 ms burst, 1.736 MHz frequency) [243, 244]. In general, the ADV threshold decreases with increasing pulse length, PRF, PD concentration, temperature, and with decreasing US frequency [242]. Additionally, the presence of other cavitation nuclei can reduce the energy required to induce ADV; for example, an adjacent collapsing MB can induce ADV in a droplet population [243].

PD Manufacturing Methods

Methods used to manufacture PDs include sonication, MB condensation, mechanical agitation, and microfluidics [245, 246]. MB condensation is often used with low boiling point PFCs such as perfluorobutane (boiling point: -1.6 °C). This method involves first creating PFC-core gas MBs and subsequently condensing them into liquid droplets through the combination of cooling and pressurisation [245]. Although this method allows the formation of a narrow distribution of PD sizes, it can be a challenging process to implement depending on the PFC used [242]. Sonication, mechanical agitation and microfluidic methods are often used when manufacturing PDs with PFCs that are liquid at room temperature, such as PFP and PFH. Microfluidic methods have the advantage of generating a narrow size distribution of PDs; however, production rates are generally lower than in methods such as sonication

[245].

Sonication uses a probe immersed in a vial containing both PFC and shell constituents, in order to emulsify them together [246]. This process uses low-frequency (i.e., typically 20-60 kHz), high-intensity US to induce the formation of cavitation bubbles that upon collapse generate strong shear forces in the liquid. When applied to a mixture of two immiscible fluids, these forces result in the generation of droplets that break up into progressively smaller ones over time. This process can create smaller droplets compared to microfluidic-based techniques, and creates fewer surfactant-only structures than condensation methods [247, 248].

Controlling the average size (diameter) and size dispersity of a droplet emulsion will have an effect on the ADV threshold and acoustic response: a more disperse range of PD sizes will lead to less uniform acoustic activation and therefore result in a less efficient therapeutic delivery method [245]. The shell composition of a PD can also have an effect on the surface tension, and therefore on the ADV threshold [249]. Ferri *et al.* demonstrated that increasing the volumetric concentration of PFCs in relation to shell constituents led to an increase in the average diameter of PDs produced by sonication, while increasing the sonication intensity and time led to a decrease in the average PD diameter [250]. Similar to lipid-shelled MBs, the shell of PDs can also be loaded with therapeutic compounds (in addition to

those compounds that may be loaded within the PD core) [197, 251]. PDs are often formulated using the similar shell compositions to MBs [242, 252, 253]. Drug delivery can be activated in a similar way to MBs: once droplets have vaporised into MBs, similar cavitation effects can be mediated through further US stimulation [254]. PDs represent an advancement of US-activated particles, particularly as a result of their increased stability and gas solubility compared to similar MB formulations. The high gas solubility of liquid PFCs has generated significant interest, particularly for their potential as oxygen carriers [239].

A key factor in the design and manufacture of MBs and PDs is the characterisation of their size and size distribution. The diameter of particles such MBs and PDs affects how they interact with physiological systems, governs their storage and physiological stability, and for PDs governs the acoustic pressure needed to induce ADV.

1.7 Particle Sizing Methods

As discussed above, the characterisation of particle size and size distribution is crucial in the development of PDs, directly affecting their ADV threshold, stability, and potential therapeutic suitability. Among the range of particle sizing techniques, dynamic light scattering (DLS), nanoparticle tracking analysis (NTA), and resistive

pulse sensing (RPS) are commonly used when characterising PDs. Each method offers advantages and limitations that affect their suitability in characterising PD populations.

1.7.1 Dynamic Light Scattering

DLS is used to characterise the hydrodynamic diameter of particles by measuring fluctuations in intensity of laser light scattered by the Brownian motion of particles in a suspension [255]. For particles with a wide size distribution, DLS is often limited due to the method's reliance on scattered light intensity. As such, NTA is often used as an alternative approach to account for a wide range of particle sizes [256].

1.7.2 Nanoparticle Tracking Analysis

While DLS measures ensemble fluctuations in the light scattered by a sample, NTA tracks the movement of individual particles in a suspension to determine their diffusion coefficient **(Fig. 1.6)** [257]. The motion of a single particle is tracked frame-by-frame, and particle size is calculated using a two-dimensional Stokes-Einstein equation **(Equation 1.3)**.

$$\langle x, y \rangle^2 = \frac{\kappa_B T t_s}{3\pi\eta d_h} \tag{1.3}$$

where $\langle x, y \rangle^2$ is the mean squared displacement, κ_B is Boltzmann's constant, T is the absolute solvent temperature, t_s is the time between samples, η is the solvent dynamic viscosity, and d_h is the particle's hydrodynamic diameter [258]. NTA is suitable for measuring particles between 30-1000 nm in diameter. NTA has advantages over DLS when measuring particle samples with a relatively large size dispersity: the intensity of light scattered by particles is proportional to the sixth power of their diameter. As DLS measures the intensity of light scattered through the whole sample over time, it is much more sensitive to the presence of a small number of larger particles [258, 259, 260, 261]. This can result in a large bias in the average diameter reported.

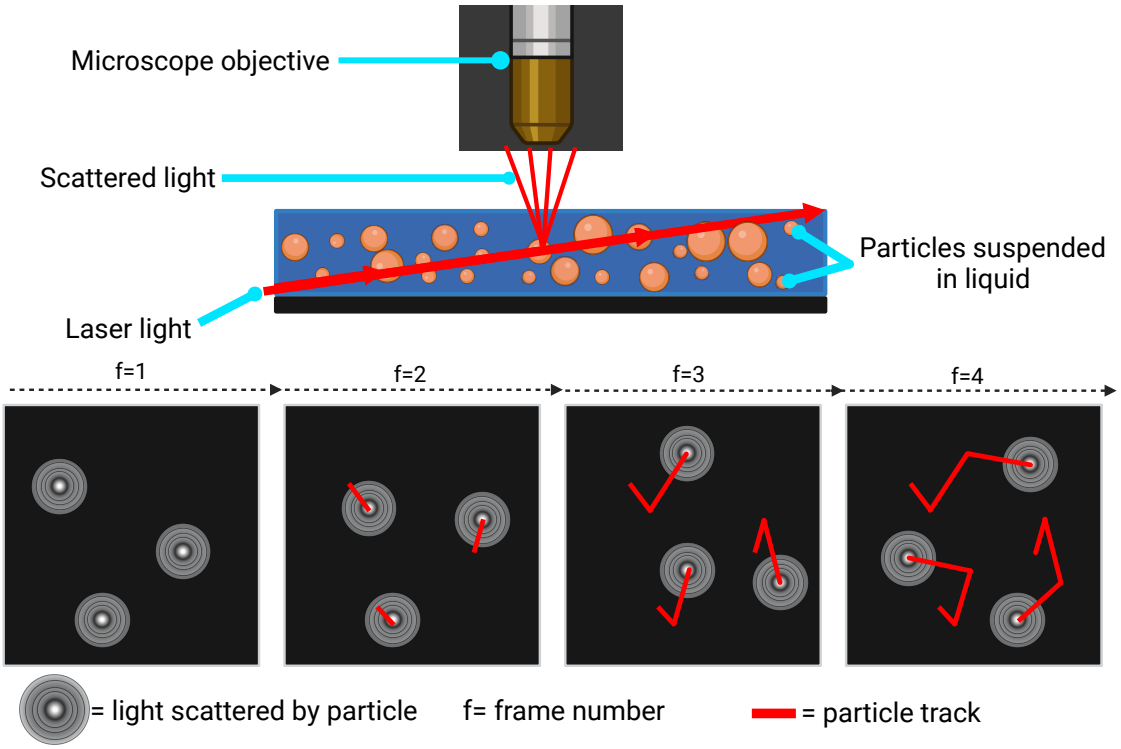

Figure 1.6: NTA records the motion of particles over time to determine their diameter. A laser is passed through a sample of particles suspended in a liquid, and the light scattered by these particles is recorded by a digital camera with a microscope objective. The motion of particles is recorded at 30 frames per second, and tracks of particle motion (red) recorded for each frame ($0.0\overline{33}$ s).

Adapted from *Singh & Toler*, 2012 [262]

1.7.3 Resistive Pulse Sensing

RPS, also known as the Coulter principle, is a technique capable of counting and sizing particles larger than the 1000 nm upper size limit of NTA [263, 264]. A typical RPS detector contains two electrodes submerged in an electrolyte separated by an insulating membrane and a pore or aperture/orifice **(Fig. 1.7)** [265, 266]. As a particle passes through the pore, it transiently increases the electrical resistance between the two electrodes [266, 267]. Changes in electrical resistance as particles pass through the aperture are recorded as pulses, the amplitude of which is proportional to the volume of the particles [266, 267]. Thus, the number of particles of a given volume in the suspension can be determined to produce both the particle size distribution and the particle concentration [268].

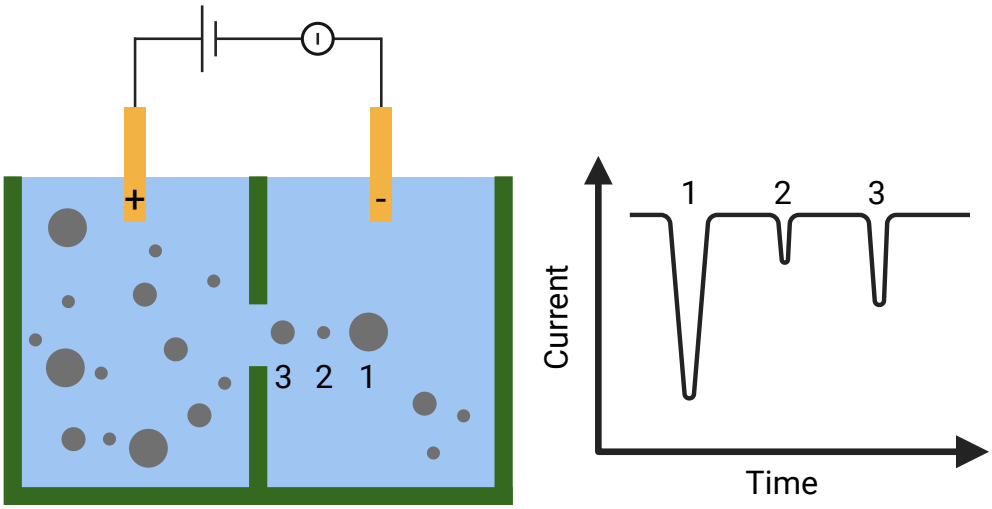

Figure 1.7: Resistive pulse sensing (RPS). Left: Typical setup with two cells separated by an insulating membrane with a single pore. Right: Transient signal of current representing a (1) large-, (2) small-, and (3) medium-sized particle. Following calibration, the count rate, i.e., the number of pulses per time interval, reflects the concentration of the particle suspension to be analysed.
From *Giebel & Helmbrecht*, 2016. [265]

1.8 Nitric Oxide

NO is a key signaling molecule in both mammalian and bacterial biology. Its lipophilicity and small size enable rapid diffusion across biological membranes, allowing it to act as both an intracellular and intercellular messenger [269, 270]. Early research first discovered the role of NO in the regulation of vascular tone [271, 272]; research has since spread and spans a variety of disciplines including cardiovascular medicine, cancer biology, and wound healing [273, 274, 275, 276]. NO is fundamental in the promotion of angiogenesis and modulates components of the inflammatory phase of wound healing [276]. NO has been shown to induce biofilm dispersal in various species of bacteria, including *Pseudomonas aeruginosa*, *Escherichia coli* and some *Staphylococcus* species [277].

1.8.1 Nitric Oxide in Biofilm Dispersal

NO acts as a potent signaling molecule in multiple phases of wound healing such as inflammation, angiogenesis and cell proliferation [278], while in bacterial species such as *P. aeruginosa*, NO acts as a potent biofilm dispersal signal [279, 280]. NO functions by reducing intracellular levels of cyclic di-GMP, which is a crucial messenger in the regulation of biofilm dispersal [37]. Dispersal has been associated with the activation of a periplasmic cysteine protease (LapG) [281]. LapG is known to

degrade the LapA, a protein that mediates bacterial adhesion [282]. In DFU wound exudate, NO levels are lower than in normal and healthy wound exudate [38]. Importantly, low levels of NO are a factor in the delayed healing and diminished immune response seen in CWs [283].

The concentration of NO sufficient to induce biofilm dispersal effects varies considerably in the literature from the pico- to micro-molar range [277, 284]. Barraud *et al.* showed that a wide range of concentrations (25 nM - 2.5 mM) of the NO donor sodium nitroprusside (SNP) could induce the dispersal of single-species biofilms of both Gram-negative and Gram-positive bacteria [279, 285]. Important to note is the approximate 1000-fold reduction between SNP concentrations and molecular NO concentrations, giving a range of suitable biofilm-dispersing NO concentrations of 25 pM - 2.5 µM. When dispersal is initiated, several mechanisms work in conjunction to degrade and solubilise the EPS matrix, allowing motile cells to leave the aggregate structure of the biofilm and migrate elsewhere [281].

The wide NO-concentration range in the literature varies considerably, makes direct comparisons challenging. This variability is influenced by several factors, including exposure duration, bacterial species and difference in NO-donor release profiles as opposed to gaseous NO delivery [285].

Care must be taken to avoid excessive NO concentrations, as these can damage underlying wound tissues and cause inflammation. The involvement of NO in both bacterial signalling and wound healing pathways increases the difficulty of designing therapies in the wound context. Paradoxically, low endogenous concentrations of NO can reduce collagen deposition and weaken the wound, highlighting the complex interplay of the associated molecular signaling mechanisms [283]. NO has been investigated as a means to potentiate the effect of antibiotics in biofilm treatment, as dispersed bacteria are much more susceptible without the protective EPS structure [286, 287].

1.8.2 Challenges in NO Delivery

The therapeutic use of NO is made difficult by its short half-life and high reactivity. A key barrier to the delivery of NO is its high reactivity with oxygen, with the half-life of NO in oxygenated environments on the order of seconds [288, 289]. NO rapidly reacts predominantly into nitrite (NO_2^-) and a small amount of nitrate (NO_3^-) [273]. NO donors such as SNP and various diazeniumdiolates (NONOates) have been explored in the delivery of NO to biofilms [290]. NO donors can act as a means of protecting molecular NO, until release is activated through triggers such as ROS generation or changes in pH [291].

1.8.3 Gas Transport in Perfluorocarbons

The high gas-dissolving capacity of PFCs is primarily attributed to their unique molecular structure. This property makes PFCs effective as gas carriers, capable of dissolving significantly more gas than water at the same partial pressure [292]. Oxygen transport using PFC emulsions is one of the primary research avenues being investigated for these agents, with applications including blood substitutes and vascular embolisation therapies .

Henry's Law and Gas Solubility

The dissolution of gases in PFCs follows Henry's Law, which states that at a constant temperature, the amount of dissolved gas is directly proportional to its partial pressure in the gas phase:

$$c = k_H \times p \tag{1.4}$$

where c is the concentration of dissolved gas, k_H is Henry's constant (specific to the gas-liquid pair), and p is the partial pressure of the gas [293]. For PFCs, the Henry's constant for gases such as oxygen are notably higher than in water [238].

1.8.4 Perfluorocarbon-Based NO-Delivery Systems

The high diffusivity and reactivity of NO makes it a challenging molecule to load and retain in therapeutic agents. MBs can be used for delivering biologically active gases, whereby gas release can be controlled through US stimulation. For example, MBs with an oxygen core have been shown to reverse blood hypoxemia in a rabbit model [294]. Tong *et al.* assessed the ability of NO MBs in improving the transplantation of mesenchymal stem cells [295], while Liang *et al.* investigated the delivery of NO MBs co-loaded with sulfur hexafluoride to treat arterial thrombi in rats [296].

NO delivery in combination with MBs as cavitation nuclei has also shown promise as an antibiofilm therapy. For example, LuTheryn *et al.* assessed the antibiofilm effect of NO-core MBs stimulated by US (0.9 MHz, 20 % duty cycle, 500 Hz PRF, 40 s duration) in combination with sub-inhibitory (4 µg/µL) gentamicin. NO-loaded MBs with free gentamicin achieved up to a 99.9% reduction in both surface area and cell viability of *P. aeruginosa* biofilms *in vitro* [287]. The efficacy of sub-inhibitory concentrations of gentamicin was shown to be significantly increased.

PFC emulsions constitute a promising platform for the delivery of NO, although work in this area remains limited, with only 3 studies directly characterising NO loading in PFC emulsions to date. Ortiz *et al.* reported the increased solubility of NO in liquid PFC in comparison to water, with partition coefficients up to 2.4

times higher, highlighting the potential for larger amounts of NO to be delivered [36] PFC emulsions have been explored for the transport of NO within the bloodstream. Ortiz *et al.* showed that a perfluorooctyl bromide-soybean lecithin emulsion could effectively transport NO in the bloodstream. They showed that the partition coefficient of NO was 2.4 times higher in the PFC emulsion than in aqueous solution, highlighting the potential for a higher NO payload using PFCs [36].

Choi *et al.* showed that lipid-shelled perfluorodecane PDs released the majority of loaded NO within 10 min, with a total released amount of 2.0 µM/mL in 18 min [297]. This is in contrast with the evidence for NO release from MBs, where Lafond *et al.* have shown that passive release of NO from gas-core MBs can be rapid, on the order of seconds [298]. This could suggest the potential of an extended the release duration of NO from liquid-core PDs, however the evidence is limited and more detailed characterisation and comparison of release kinetics is needed. Earlier work by Choi *et al.* remains the only work to date exploring the effect of NO-loaded PFCs on bacterial cells, and showed that NO-loaded perfluorooctane droplets could accelerate the killing of planktonic *S. aureus*, with a 30% decrease in dead cells after 12 h. Notably, there has been no work exploring the potential of NO-loaded PFCs as an antibiofilm therapy for topical applications.

1.9 Perfluorocarbon Droplets as an Antibiofilm Therapy

Recent studies have demonstrated the potential of US-activated PDs for biofilm treatment, although this remains an emerging area of research [228]. The combination of PDs with antimicrobials has shown particular promise.

Durham *et al.* [30] used octafluoropropane-core, lipid-shelled PDs combined with tobramycin and rhamnolipids as a treatment modality against *S. aureus* biofilms. When stimulated with US (1 MHz, 1.2 MPa peak negative pressure, 5 kHz PRF, 40-cycle burst), they recorded a 94% reduction in viable cells accompanied with a significant decrease in biomass.

Similar synergistic effects have been observed in other studies. For example, Xin *et al.* demonstrated enhanced efficacy against *P. aeruginosa* biofilms using PFP PDs and US when combined with the antibiotic meropenem (1.5 W/cm^2, 50% duty cycle, 1 MHz frequency, 10 min treatment duration), achieving a ∼95% reduction in bacterial viability [299].

However, several limitations exist in current approaches. Studies utilising PDs as an anti-biofilm agent very often lack characterisation of PDs' acoustic behaviour, which is beneficial to understand the physical effects reported. This is also a necessary pre-requisite towards treatment standardisation and potential clinical translation. Guo *et al.* suggested that liquid core PDs present an advantage over MBs due to their density, allowing them to sink and facilitate interaction with the biofilm matrix [300]. Indeed, the work by LuTheryn *et al.* using MBs on a biofilm model required the inversion of the culture dish to achieve MB interaction with the biofilm.

Additionally, while both NO and US-activated PDs have individually shown promise in biofilm treatment, their combination for chronic wound applications remains unexplored. The unique properties of PDs, specifically their high gas solubility in combination with the ability to vaporise into acoustically-responsive MBs, make them particularly promising as carriers for both NO delivery and US-mediated physical disruption of biofilms. Biofilm dispersal effects induced by NO could potentially increase biofilm sensitivity to the mechanical effects of US-mediated cavitation. This combinatorial approach could potentially provide a more effective treatment modality for CW biofilms. Literature in this area of research however suffers from several limitations, including the lack of comprehensively characterised particle manufacturing methods, quantitative characterisation of particle properties (including NO

loading capacity and acoustic response), and evaluation of the physical effects that PDs exert upon bacterial biofilms.

1.10 Research Aim & Objectives

The aim of this project is to develop a treatment solution for biofilms in chronic wounds. It is hypothesised that NO-loaded perfluorocarbon droplets exert anti-biofilm effects due to the combined action of physical (US-induced) and bio-chemical (NO-induced) dispersal. To the best of the author's knowledge, this is the first study evaluating this combinatorial modality as an anti-biofilm treatment.

The research in this *Thesis* comprises four main objectives, which are articulated across three Chapters. The first objective, addressed in Chapter 2, focuses on developing and characterising a repeatable manufacturing method for perfluorocarbon droplets (PDs). Chapter 3 is dedicated to the second objective: developing a nitric oxide (NO)-loading method and evaluating the NO-loading capacity of the manufactured PDs. The final two objectives are explored in Chapter 4, which determines the ultrasound (US) parameters suitable for PD vaporization and evaluates the effects of NO-loaded PDs on a chronic wound biofilm model.

Chapter 2

Improving the Manufacture of Perfluorocarbon Droplets

2.1 Introduction

Perfluorocarbon droplet (PD) emulsions have been of research interest for several decades for applications in magnetic resonance and US contrast imaging, and as oxygen carriers in blood substitution [34, 239, 301]. The refinement of PD manufacture towards specific applications is dependent on the characterisation of particle size and size dispersity. Sonication is a widely used method for producing PD emulsions and other particulate formulations due to its simplicity and scalability [302, 303, 304]. However, compared to other methods such as microfluidisation, emulsions manufactured by sonication typically have wider size distributions [305].

For applications requiring intravascular administration, factors such as the ability to extravasate from within the vasculature and the circulation time are highly dependent on the particle size distribution [306]. In particular, the size (spherical diameter) of PDs will determine the degree to which they can penetrate the various biological barriers of the body and the speed with which they are cleared [307]. A key characteristic of PDs is their ability to undergo acoustic droplet vaporisation (or ADV), a process in which liquid-core PDs are converted to gas-core MBs upon exposure to US above a certain acoustic pressure level.

These US-responsive MBs can then oscillate volumetrically and collapse violently, mediating a variety of biophysical effects [308, 309]. This characteristic makes PDs of particular research interest for targeted drug delivery and biofilm disruption [89]. The ADV threshold is affected by PD size, with smaller PDs generally requiring greater acoustic pressure magnitudes to undergo vaporisation, while larger PDs can be induced to vaporise at lower pressure levels [32, 310]. The size dispersity of a droplet emulsion will also an affect on the ADV threshold: a more disperse range of PD sizes will lead to less uniform acoustic activation and therefore result in a less efficient therapeutic delivery method [245]. PD shell composition can also affect the surface tension, and therefore the ADV threshold [249].

Sonication is a common laboratory technique used to manufacture PDs with PFCs that are liquid at room temperature (i.e., having a longer-chain than perfluorobutane). In this method, a sonicator probe generates low-frequency (i.e., typically 20-60 kHz), high-intensity US to induce the formation of cavitation bubbles that upon collapse generate high shear forces in the surrounding liquid [311]. When applied to a mixture of two immiscible fluids, these forces result in the generation of droplets that break up into progressively smaller particles over time. Surfactants are typically added to stabilise newly formed droplets, preventing them from coalescing [312].

Sonication is less costly than alternative techniques such as high-pressure homogenisation, can create smaller droplets than current microfluidic-based techniques, produces fewer surfactant-only structures than gas condensation methods, and avoids harmful solvents used in current solvent exchange methods [247, 248, 313]. However, sonication is inherently a variable process: cavitation is a highly stochastic phenomenon and, therefore, there can be substantial variability in particle characteristics from batch to batch [250].

Moreover, sonication parameters used in PD production are inconsistent between published studies.

Variables such as the type of sample vessel, the relative location of the sonicator tip with respect to the liquid sample, and the sample cooling method are not consistently reported in the literature. Furthermore, the rationale for the selection of parameters such as the sonication amplitude or the PFC concentration is not always presented, and sonication power values vary greatly between studies **(Table 2.1)**. Typically, a sonicator has a fixed maximum output power, and the output intensity is modified by changes in the percentage amplitude setting (typically a target % of the maximum peak-to-peak amplitude). Unfortunately, unless the sonicator has a real-time readout of power, it may not be possible to report this parameter without calibrating the system using a laser vibrometer.

Several techniques can be used to characterise the diameter and/or concentration of the manufactured PDs. These include dynamic light scattering (DLS), nanoparticle tracking analysis (NTA), and resistive pulse sensing (RPS) [248, 250, 314, 315]. Both DLS and NTA are optical characterisation methods, while RPS (also known as the Coulter method) is based on electrical resistance measurements [260, 316]. Despite the broad range of sonication intensities and durations used to manufacture PFP-core PDs, the majority of particle diameters reported are within a range of 100 - 400 nm **(Table 2.1)**.

Table 2.1: Selection of studies using sonication to manufacture PFP-core NDs

Study	Sonicator Model	Power (W)	Duration (On Time)	Duty Cycle	PFP Volumetric Concentration*	Droplet Diameter	Sizing Method
Ferri *et al.* 2021 [317]	Model 120 Sonic Dismembrator, Fisher Scientific, UK	48 or 72 W	20 s, 40 s or 60 s	15% or 30%	5.00-15.0% v/v	200-300 nm	DLS
Zhang P & Porter T 2009 [318]	VC505, Sonic & Materials, USA	Unspecified	30 sec	Unspecified	3.00% v/v	193.3 nm	DLS
Matsuura *et al.* 2009 [319]	Sonicator 3000 (Misonix), Bioventus Inc., USA	10 W	5 min	50%	2.90% v/v	100-300 nm	DLS
Williams *et al.* 2013 [320]	S-450D, Branson Ultrasonics, USA	2 W	5 min	50%	3.13% v/v	212 nm	DLS
Reznik *et al.* 2014 [321]	Sonifier 250, Branson, USA	100 W	40 s	80%	5.00% v/v	400 nm	DLS
Aliabouzar *et al.* 2018 [314]	Q500, QSonica, USA	125 W	10 s	Unspecified	9.09% v/v	890 nm	RPS
Ho YJ & Yeh CK 2016 [322]	UTR200, Dr Hielscher Company, Germany	200 W	20 min	Unspecified	6.98% v/v	373 nm	NTA
Zhang *et al.* 2023 [323]	Unspecified	90 W	36 min to 75 min	Unspecified	1.00 - 2.00% v/v	100 - 110 nm	DLS

DLS= dynamic light scattering, RPS= resistive pulse sensing, NTA= nanoparticle tracking analysis,
$*$ volumetric concentration of PFP prior to sonication step

The use of multiple particle size characterisation techniques can inform the adjustment of the manufacturing process and confirm the suitability of a PD emulsion for a given specific application. Although each particle sizing method offers certain advantages, relying on a single technique can limit the validity of sizing data. For example, NTA has a lower detection limit of ∼10 nm and an upper detection limit of 1 µm, which restricts the detection of larger PDs [324, 325]. As sonication can generate PDs with a wider size distribution compared to other techniques, it is important to evaluate the presence of larger particles. Conversely, RPS is limited by the type of pore utilised. Commercially available RPS detectors (e.g., Coulter Multisizer) use fixed-size pores that can be used to detect a set size range of particles. Pore clogging when using smaller apertures often necessitates the use of larger apertures (e.g., 0.4 to 12 µm instead of 0.2 to 8 µm), which compromises the detection of smaller droplets. Both NTA and RPS particle detection methods are explored in this study.

The work in this *Chapter* aims to develop the PD manufacturing process by evaluating several key parameters. The objectives of the work described in this Chapter are as follows: First, to develop a controlled positioning apparatus that enables repeatable positioning of a sonicator probe within a cooled sample vessel. Second, to establish optimal sonication pulse parameters that maintain sample temperature during PD production. Third, to determine improved PD manufacturing parameters suitable for subsequent NO loading experiments by investigating the effects of varying PFP volumetric concentration and sonicator tip height on PD size characteristics, assessing the effects of varying sonication intensity and duration on PD size characteristics, and comparing the effects of varying PFP volumetric concentration using complementary sizing techniques. In the broader context of the *Thesis*, these findings will inform the selection of PDs suitable for NO-loading in *Chapter 3*. To characterise PD size distributions and concentrations, two complementary analytical techniques were employed: nanoparticle tracking analysis (NTA) and resistive pulse sensing (RPS).

2.2 Materials and Methods

2.2.1 Overview of PD Preparation

PDs were manufactured using a method adapted from Ferri *et al.* [250]. To prepare the PD shell components (hereafter referred to as 'lipids'), 621 µL of a 25 mg/mL stock solution of 1,2-distearoyl-sn-glycero-3-phosphocholine (DSPC) (Avanti Polar Lipids, USA) and 447 µL of a 10 mg/mL stock solution of polyoxyethylene (40) stearate (PEG40S) (Sigma-Aldrich, USA) were dissolved in a 7 mL vial (27151, Merck, Germany) in chloroform (Fisher Scientific, UK) **(Fig. 2.1 A)**. As outlined in *Section 1.5.2*, DSPC and PEG40S are commonly used in a 9:1 molar ratio for the manufacture of gas MBs [212, 326]. Emulsifying agents such as PEG40S or DSPE-PEG(2000) are used to increase MB stability and can aid in improving the production yield of MBs [210, 327]

The chloroform was left to evaporate overnight, rendering a dry lipid film **(Fig. 2.1 B)**. Dulbecco's phosphate buffered saline without calcium and magnesium (DPBS) (Corning Inc., USA) was used to rehydrate the dry lipid films on a hot plate, stirring at 500 rpm for 45 minutes at 90 °C to obtain final concentrations of 3.92 mM and 0.436 mM for DSPC and PEG40S, respectively, to give a 9:1 DSPC:PEG40S molar ratio **(Fig. 2.1 C)**.

A Model 120 Sonic Dismembrator (Fisher Scientific, UK) with a 3.2 mm diameter sonicator tip was used in two stages. The sonic dismembrator (or sonicator) has a maximum power output of 120 W, with an operating frequency of 20 kHz. According to the manufacturer's instruction manual, sonication intensity was controlled by varying the percentage of the maximum probe amplitude (approx. 120 µm), with overall power output dependent on several factors, including sample viscosity. The instrument automatically varies the power output to maintain the target percentage amplitude.

The lipids were sonicated for 2 min 30 s at a 40% amplitude setting **(Fig. 2.1 D)**. Between the first and second sonication steps, the lipid samples were kept on ice. This intermediate cooling step eliminated the need for an additional cooling step prior to the second sonication, and improved consistency in the initial temperature of the samples.

Perfluoropentane (dodecafluoropentane or perfluoro-n-pentane, PFP) (STREM Chemicals UK Ltd., UK) was added to the lipid dispersion and vortexed for 5 s at 500 rpm prior to the second sonication step **(Fig. 2.1 E)**. PFP is the shortest chain PFC that is liquid at room temperature, with a bulk boiling point of 29.2 °C. Unless otherwise stated, a pulsed sonication pattern of 2 s on, 15 s off was used to manufacture PDs **(Fig. 2.1 F)**.

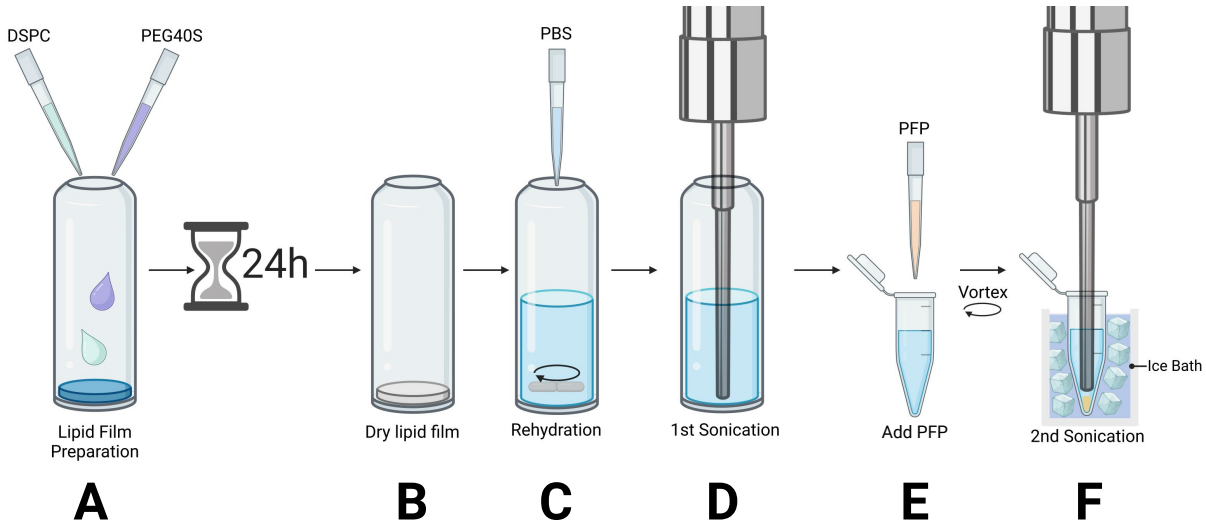

Figure 2.1: Overview of the process employed for the production of PDs. **(A)** DSPC and PEG40S (in chloroform) are mixed in a 9:1 molar ratio and **(B)** the sample is left to dry overnight. **(C)** The produced dry lipid film is rehydrated with DPBS at 90 °C for 45 minutes. **(D)** A first sonication step is performed to fully disperse the lipids in DPBS. **(E)** PFP is added to the lipids in a 1.5 mL polylpropylene tube. The sample is briefly vortexed to form precursor droplets. **(F)** A second sonication step forms PFP core, lipid-shelled PDs.

2.2.2 Development of Sonicator Manufacturing Apparatus

The literature describing the use of probe sonication for manufacturing PDs lacks detail regarding temperature control and sonicator positioning. Often, these crucial parameters are briefly mentioned in the methodology of previous studies with references to an 'ice bath' or 'on ice' as a cooling method, without specifying the exact positioning of the sonicator probe. This lack of information presents challenges in reproducing results and could contribute to inconsistency in droplet size characteristics across studies.

To address this gap, a manufacturing apparatus was developed that allowed for precise positioning of the sonicator probe within the sample vessel. Coupled with the characterisation of the sample cooling environment, this strategy offers several benefits. By clearly defining the crucial parameters for PD manufacture, other researchers will be able to reproduce these results in different laboratories, allowing direct comparison of results between studies [328].

Prototype Manufacturing Apparatus

Initial work on this project used a prototype manufacturing setup inspired by the work by Ferri *et al.* [250]. A 1.5 mL polypropylene sample tube (DNA LoBind Tubes, Eppendorf SE, Germany) was positioned within a styrofoam container filled

with a water-ice mixture **(Fig. 2.2)**. To support the sample tube, a flexible plastic panel sourced from a pipette-tip rack lid (TipOne, STARLABS) was used, with a circular cutout to place the 1.5 mL sample tube: the friction between the lid and tube held it in place.

Although this prototype set-up provided basic functionality for PD manufacturing, it had several limitations compared to the controlled positioning apparatus. Manual positioning of the sample tube and sonicator tip introduced variability between experiments. The styrofoam container, while providing insulation, lacked the mechanical stability, potentially allowing unwanted movements during sonication. Inconsistencies with the plastic panel used to hold the 1.5 mL sample tube led to differences in the positioning of the sonicator tip, as well as the depth of the tube itself in the surrounding ice water bath. This variability in positioning occasionally led to the precursor droplets and bulk lipids failing to mix. Additionally, if the 1.5 mL tube was not consistently placed within the water-ice bath then the rate of sample cooling would differ between samples.

To address the limitations of the prototype manufacturing setup, several changes were made. A multiaxis-control apparatus was assembled, allowing repeatable and precise positioning of the sonicator probe **(Fig. 2.3)**. This apparatus is used to manufacture PDs throughout the present *Thesis*.

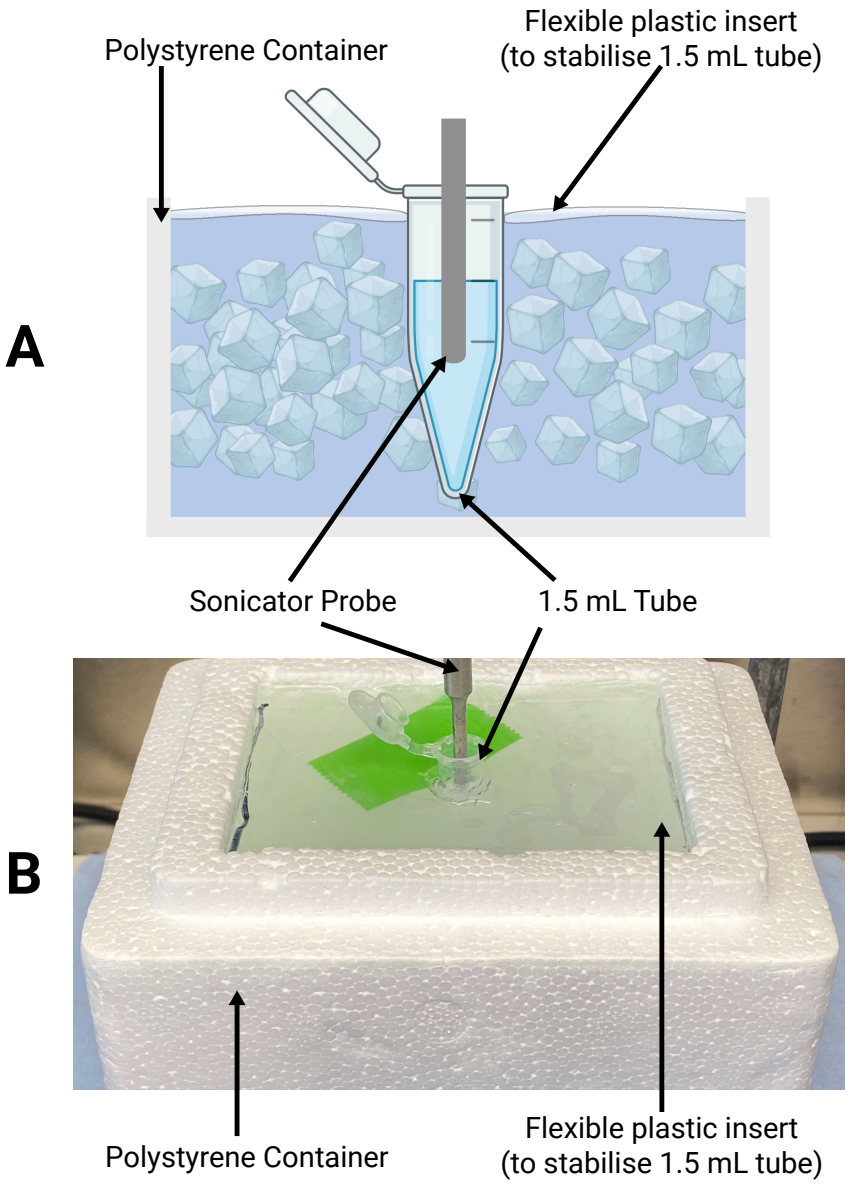

Figure 2.2: Prototype PFC emulsion manufacturing setup.

(A) Side view schematic showing the position of a 1.5 mL tube in relation to the sonicator tip. **(B)** Photograph showing the prototype manufacturing setup. A polystyrene container was used to insulate a mixture of water and crushed ice. A flexible plastic insert with a circular cut-out was used to stabilise the 1.5 mL tube containing PFP and lipids.

Controlled Positioning Apparatus for Manufacturing PDs

To securely hold the sonicator tip **(Fig. 2.3 A)** in position, a pair of clamps (VG100/M, Thorlabs Inc., USA) **(Fig. 2.3 B)** was used, secured to a single-axis translation stage with micrometer (PT1/M, Thorlabs Inc., USA) **(Fig. 2.3 C)**. A 25 mm diameter post clamp (C1045/M, Thorlabs Inc., USA) attached the clamp assembly to a pillar post (RS300/M, Thorlabs Inc., USA) **(Fig. 2.3 D)** to allow for large height adjustments when removing/replacing samples to be sonicated. The post was attached to a pair of dovetail stages (DTS50/M, Thorlabs Inc., USA) mounted perpendicular to each other, allowing adjustment of the X and Y axes **(Fig. 2.3 E)**.

This three-dimensional positioning system enabled accurate control of the sonicator tip location relative to the sample, a significant improvement over the prototype apparatus. This allowed for reliable and precise positioning of the sonicator tip in the center of the sample tube (on the XY plane). An aluminium breadboard (MB3030/M, Thorlabs Inc., USA) with sorbothane feet (AV4/M, Thorlabs Inc., USA) was used as a rigid base for the assembly **(Fig. 2.3 F)**, providing a stable platform that minimises unwanted vibrations during sonication.

To ensure reproducible position of the sample container, a custom 3D printed ice bath and lid (Original Prusa i3 MK2, PLA filament) was designed to hold 1.5 mL Eppendorf tubes (DNA LoBind Tubes, Eppendorf SE, Germany) in place **(Fig. 2.3 G)**. This custom-designed ice bath not only secures the sample tube but also enables cooling using a water-ice bath. These components allowed for precise control of the height and position of the sonicator tip within the sample vessel **(Fig. 2.3 H)**.

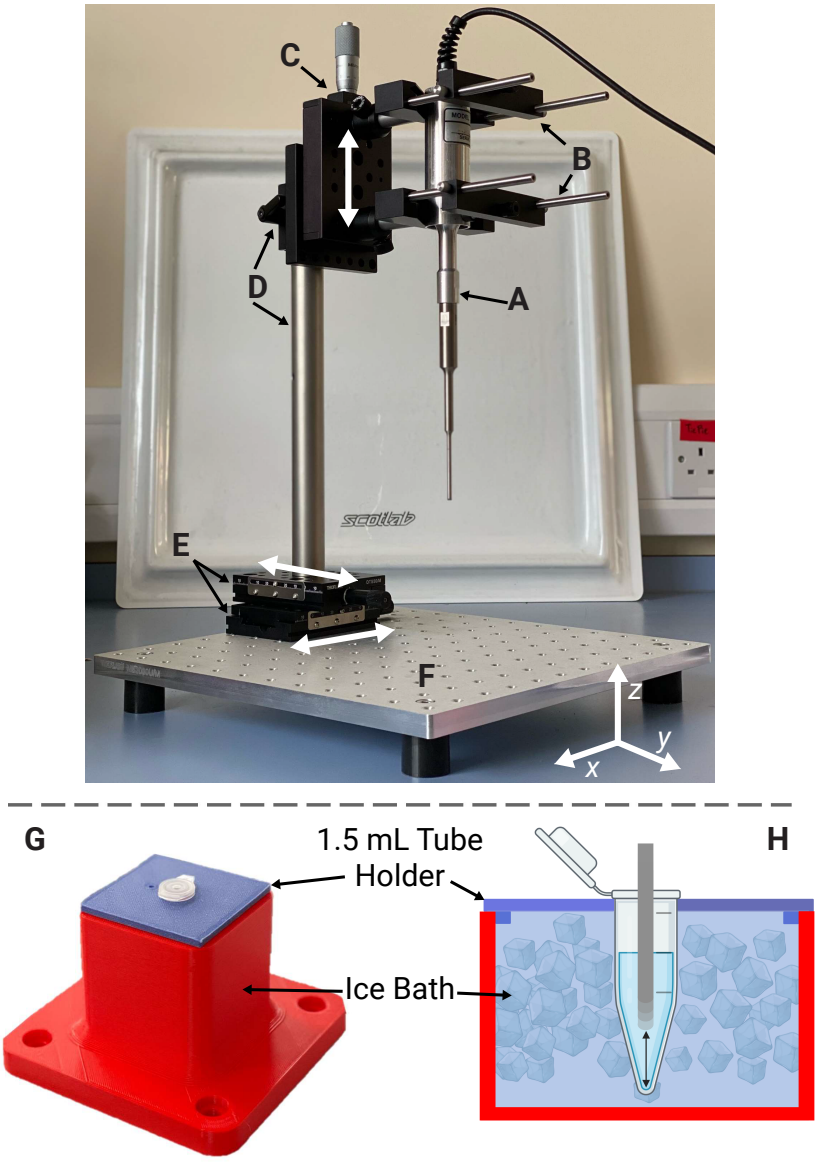

Figure 2.3: Controlled positioning apparatus overview. This figure illustrates a custom-built manufacturing apparatus designed to precisely control sonicator tip position during PD manufacture. The sonicator tip **(A)** is held vertically by a pair of optics clamps **(B)**, which are attached to a micrometer translation stage **(C)** allowing for precise control of sonicator tip height (Z-axis). The pillar post and clamp **(D)** allow for larger height adjustments between manufacturing phases. A pair of perpendicularly mounted single-axis translation stages **(E)** allow for X and Y axis adjustment. An aluminium breadboard with sorbothane feet **(F)** functions as a rigid, vibration-free base with M6 thread mounting points for the 3D-printed ice bath and lid **(G)**. Panel **(H)** shows a side-view of the ice-bath and lid, illustrating tip height variability. The apparatus enables reproducible positioning of the sonicator tip within a 1.5 mL sample vessel.

2.2.3 Temperature Control during PD Manufacture

Temperature control is required due to the low boiling point of bulk PFP at 29.2 °C and the heat generated by sonication. Temperature management prevents or minimises the loss of PFP due to vaporisation during manufacturing [254].

To evaluate temperature control during the manufacturing process, this study compared two pulsed sonication patterns and two types of cooling bath, as follows: the first sonication pattern consisted of 2 seconds of active sonication followed by 5 seconds of rest (labeled as 2/5), while the second pattern employed 2 seconds of active sonication with a longer rest period of 15 seconds (labeled as 2/15). The first cooling bath utilised a ice-water bath, which maintained a temperature of 1.3 ± 0.2 °C. The second configuration employed a saturated saline-ice bath (approximately 26% w/v), which achieved a lower temperature of -8.6 ± 0.3 °C.

Temperature fluctuations within the sample during sonication were measured using a thermocouple data logger (TC-08, Pico Technology, UK) with two type K thermocouple probes (RS Components, UK). The sensitivity of the TC-08 is the sum of each individual reading ± 0.2% and an additional ± 0.5 °C. Samples were allowed to cool to the temperature of the cooling bath before initiating sonication.

Samples of 80 µL and 800 µL rehydrated DSPC:PEG40S (9.09 % v/v PFP) were first vortexed for 5 s at 500 rpm, then sonicated at 60 % amplitude. Three independent repeats were performed for each condition, and the mean temperature was calculated for each time point. Results demonstrated that the 2 s on, 15 s off pulsed sonication pattern combined with an ice-water bath was optimal, maintaining sample temperatures below 15 °C whilst avoiding sample freezing prior to sonication. Separately, the effect of 100% sonication amplitude using the 2 s on, 15 s off pulse pattern was assessed. Temperature data was compared with the 60 % amplitude, 2 s on, 15 s off samples to understand the effect of higher sonication intensity on sample heating.

2.2.4 Characterisation of PDs using NTA

NTA was performed using a NanoSight NS300 (Malvern Panalytical, UK). This method was used to measure the hydrodynamic diameter of the particles and assess the overall size dispersity of a sample. Following manufacturer recommendations on the ideal number of particles visible within the camera field-of-view, the samples were diluted 1:5000 in DPBS prior to measurement. A low volume flow cell with syringe pump (speed setting 50) was attached to a 488 nm laser module within the NS300. For each sample, five 90-second video recordings were captured under flow conditions.

The videos were recorded at 30 frames per second by the sCMOS camera within the NS300. The NanoSight NTA software (Malvern Panalytical, UK) analysed the movement of individual particles within the video frames to determine their hydrodynamic diameter. Additionally, the software calculated the median hydrodynamic diameter and particle concentration for each sample. For each condition, three independent samples were prepared and measured. Particle size distribution data were recorded across the three independent repeats. The data were organized into 999 bins, with a bin width of 0.5 nm and a bin range from 0.5 nm to 999.5 nm diameter. This frequency distribution data were used to calculate the mean, median, and standard deviation of the combined population of particles recorded by the NTA. All NTA measurements were performed on the same day as PD manufacture by sonication, to ensure consistency. For specific sonication parameters used to manufacture PDs measured by NTA, refer to *Section 2.2.6*

2.2.5 Characterisation of PDs using the Coulter Method

To further evaluate particles larger than ∼1 µm in diameter, a Coulter counter (Multisizer 4e, Beckman Coulter, USA) was used. A total sonication duration of 60 s (2 s on, 15 s off pulse, 30 cycles), a sonication intensity of 60 % amplitude, and a sonicator tip height of 12 mm were used. Volumetric concentrations of 4.76, 9.09, and 16.7 % v/v PFP were assessed. 10 µL of a 1:10 dilution in DPBS of each PD sample was added to a 10 mL volume of ISOTON II diluent (Beckman Coulter,

USA), and gently agitated. 50 µL of PDs diluted in ISOTON was flowed through a 20 µm aperture (particle detection range 0.4 µm to 12 µm) and median particle diameter, SD, and particle concentration data were collected.

2.2.6 Evaluation of Manufacturing Parameters on PD Size Characteristics

This study investigated the effects of four key manufacturing parameters on the size characteristics of PDs. The parameters evaluated were PFP volumetric concentration, sonicator tip height, sonication duration, and sonication intensity. For each pair of parameters described below, three independent samples were prepared and measured using NTA. To account for the upper detection limit of NTA, the presence of particles larger than 1 µm diameter was qualitatively assessed optically using a Zeiss (Zeiss Axiovert 200) inverted microscope. The samples were imaged using a 40 × objective (400 × magnification) under bright-field illumination.

Effect of PFP Volumetric Concentration and Sonicator Tip Height

PFP Volumetric concentrations of 0, 1.23, 2.44, 4.76, 9.09, and 16.7 % v/v were evaluated, corresponding to 0, 10, 20, 40, 80 and 160 µL of added PFP, respectively. A volume of 800 µL of the rehydrated lipid dispersion was used for all conditions. Sonicator tip heights were varied at 2, 5, 8, 10, and 12 mm, with 0 mm defined as

the position where the probe contacted the bottom of the 1.5 mL tube. In these experiments, a total sonication duration of 60 s (2 s on, 15 s off pulse, 30 cycles) and a sonication intensity of 60 % amplitude were used.

Effect of Sonication Duration and Intensity

For these experiments, a PFP concentration of 4.76 % v/v and sonicator tip height of 12 mm were used. Sonication durations of 15, 30, 45, 60, 75, 90, 105, and 120 s and sonication intensities of 20, 40, 60, 80, and 100 % were tested.

2.2.7 Statistical Analysis

One-way analysis of variance (ANOVA) with Dunnet's T3 multiple comparison test was performed using GraphPad Prism, with $p = 0.05$ as the significance level.

2.3 Results and Discussion

2.3.1 Selection of Sonication Pulse Parameters to Maintain Sample Temperature

A key limitation of the sonication process is the increase in temperature as a result of the energy output of the sonicator. It is inevitable that any process resulting in large shear forces and cavitation will generate heat [329]. As discussed previously, the combination of pulsed sonication and an ice bath are often used in the literature to mitigate this. However, the effects of these parameters on sample temperature and the dimensional properties of the produced PDs are often not characterised in a systematic or quantitative way. Pulsed sonication creates gaps in the build-up of thermal energy, and the ice bath facilitates the dissipation of this energy [330]. The composition of the cooling bath will depend on the acceptable temperature range of the emulsion constituents.

In the present study, the precursor droplet mixture consisted of lipids (suspended in DPBS) vortexed with PFP. This presents a challenge due to the narrow temperature range for all components to remain liquid (DPBS freezing point of $\sim$ -1 °C, and PFP boiling point of 29.2 °C). To mitigate for variability between samples, a target maximum bulk temperature of 15 °C was selected. It should be noted that

temperature increases local to the tip of the sonicator (and other cavitation sites) are likely to be significantly higher than those in the bulk liquid but are likely to dissipate quickly [331].

To achieve the selected temperature target, 2 s on, 5 s off pulsed sonication (60% amplitude setting) and two ice baths were tested: an ice-water bath (1.3 ± 0.2 °C) and and an ice-saline bath (-8.6 ± 0.3 °C) **(Fig. 2.4 A)**. The maximum sample temperature measured with the 2 s on, 5 s off sonication regime in an ice-water bath was 24.8 ± 2.3 °C, which exceeded the 15 °C temperature target. The ice-saline bath reduced the maximum sample temperature by 10.0 °C to 14.8 ± 1.2 °C. However, on several occasions, it was observed that the lipid suspension would freeze prior to the start of the second sonication, which introduced significant variability. This occurs as the temperature of the ice-saline bath is significantly lower than the freezing point of DPBS. To compensate for this, the ice-water bath (1.3 ± 0.2 °C) was retained and paired with a longer 15 s gap between the sonication pulses. This prevented sample freezing and resulted in a reduction of the maximum temperature to 14.2 ± 1.7 °C.

In the literature, it is established that the intensity of sonication directly affects the size of the produced droplets, with a decrease in droplet size with increasing intensity [332, 333, 334]. The heating of PD samples was therefore assessed at the 100% amplitude setting using the 2 s on, 15 s off pulsed sonication regime and compared with the 60% amplitude data, to evaluate whether this would overheat the sample **(Fig. 2.4 B)**. A maximum temperature of 24.3 ± 0.9 °C was recorded for the 100% amplitudes, an increase of 10.1 °C when compared to the 60% amplitude setting with the same pulse regime. While these temperatures are above the 15 °C target, the bulk temperature of the sample remained below the bulk boiling point of PFP. It should be noted that the boiling point of PFP-core droplets can increase significantly when encapsulated by a lipid shell [252], and therefore these increased temperatures may be acceptable/non-detrimental.

The 2 s on, 15 s off regime with an ice-water bath at 60% amplitude was selected for all subsequent experiments in this *Thesis*, unless otherwise specified. Together, these findings enabled identification of methods for temperature control when manufacturing PDs with low boiling-point PFCs, by increasing the time between pulses and characterising sample temperature at different sonication intensities. In combination, these identified parameters will reduce the loss of PFP through unnecessary sample heating.

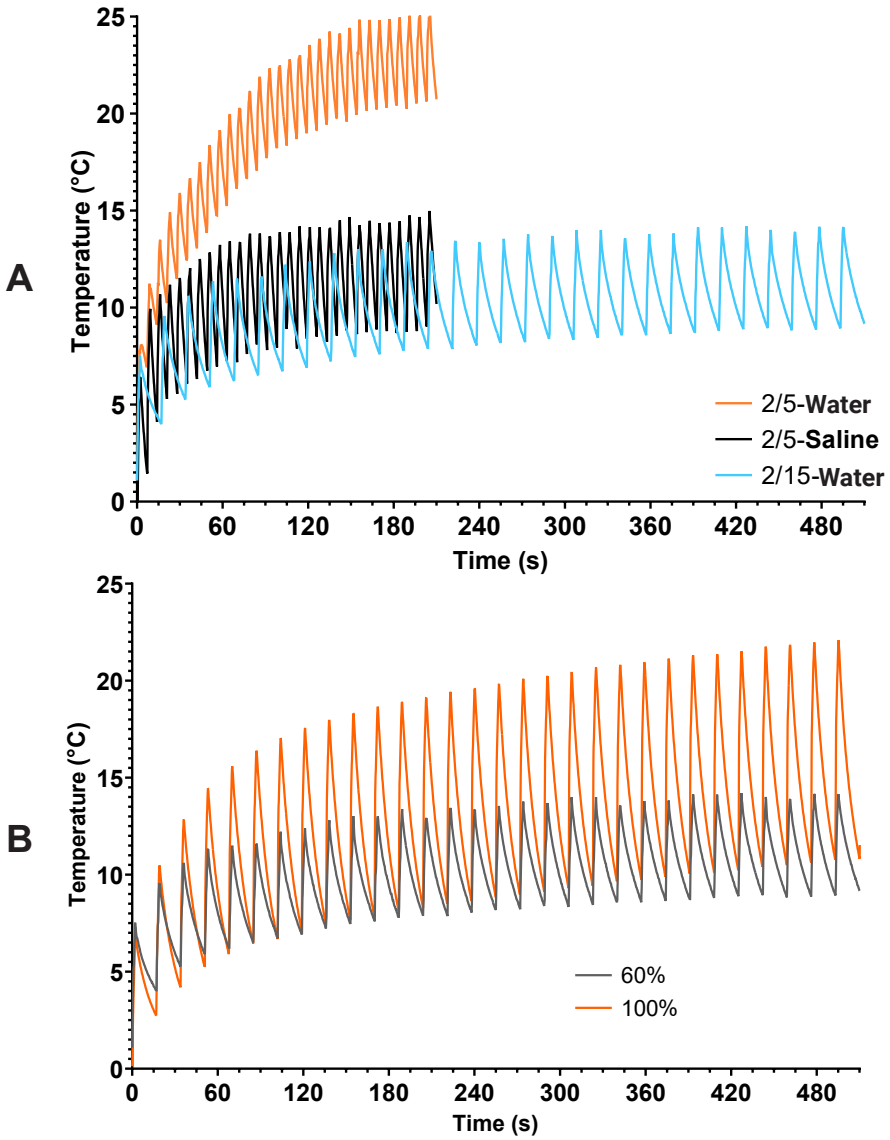

Figure 2.4: Sonication parameters were varied to mitigate heat production from manufacturing of PFP droplets. **(A)** Effect of two patterns of pulsed sonication at 60% amplitude (2 s on, 5 s off, '2/5' *vs.* 2 s on, 15 s off, '2/15') compared with ice-water (Water, 1.3 ± 0.2 °C) or saturated saline-ice (Saline, -8.6 ± 0.3 °C) cooling baths on PD sample temperature. Maximum temperatures for 2/5-Water, 2/5-Saline and 2/15-Water were 24.8 ± 2.3 °C, 14.8 ± 1.2 °C, and 14.2 ± 1.7 °C, respectively. **(B)** Effect of varying amplitude percentage on the temperature of PD samples. 2 s on, 15 s off pulse parameters were used, and both 60 % and 100 % amplitudes were tested. Maximum temperatures were 14.2 ± 1.7 °C and 24.3 ± 0.9 °C for 60 % and 100 % amplitudes, respectively. Mean temperature of n = 3 samples are plotted. A total sonication on time of 60 s was used for all samples.

2.3.2 Effect of Varying PFP Concentration Against Sonicator Tip Height on PD Characteristics

Using the previously determined pulse parameters, the effect of sonicator tip placement was evaluated on PD size characteristics **(Fig. 2.5)**.

Effect of Varying PFP Concentration on PD Characteristics

The effect of varying PFP concentration and sonicator probe tip height on various PD characteristics is summarised in **Fig. 2.5**. All samples were sonicated at 60% amplitude for a total duration of 60 s. A weak negative correlation ($R^2 = 0.569$) was found between PFP concentration and particle concentration at 12 mm tip height **(Fig. 2.5 A)**. In contrast, a strong positive correlation ($R^2 = 0.823$) was observed between PFP concentration and PD median diameter **(Fig. 2.5 B)**, consistent with previous results (as reported in Ferri *et al.* [250]). No significant difference ($P>0.05$) was found between 0% PFP and both 1.23% and 2.44% PFP.

As NTA is limited to size characterisation and does not provide information on chemical composition, it is not possible to confirm the presence of PFP droplets at these lower PFP concentrations due to the potential presence of lipid-only structures. These findings are qualitatively consistent with the phase diagram proposed in a study by Gao *et al.* when interpreting the size distribution of polymer-stabilised

PFP droplets [335]. In this previous study, authors suggest a PFP concentration-dependent transition from lipid-only structures (e.g., micelles) to a PFP droplet-dominated phase.

Despite the lack of a statistically significant difference in both particle diameter and particle concentration between the 4.76% and 9.09% PFP samples, a qualitatively significant difference could be observed optically **(Fig. 2.5 C)**. The 9.09% PFP sample exhibited considerably more large, circular particles compared to the 4.76% PFP sample. This observation is not reflected in the results shown in **(Fig. 2.5 B)**, as many of these particles are larger than the >1 µm diameter limit of NTA and therefore could not be detected.

Based on these results, a 4.76% PFP concentration was selected for subsequent experiments exploring the effects of varying sonication intensity and sonication duration. Notably, this concentration strikes a balance between a significant amount of PFP droplet being produced and the achievement of a particle size distribution that is more suited to detection by NTA.

Effect of Varying Sonicator Probe Tip Height on PD Characteristics

A qualitative effect was observed at a PFP concentration of 4.76% when varying the sonicator tip height. At 2 mm tip height, samples appeared to only partially emulsify. This effect was even more evident at 16.7% PFP concentration, where a distinct phase boundary between PFP and lipidic phases was visible, indicating incomplete emulsification. For tip heights greater than 2 mm, several trends were observed. A negative correlation ($R^2 = 0.776$) was observed between the median diameter and sonicator tip height. Statistically significant differences were found between tip heights of 5 mm and 10 mm ($P = 0.011$) and tip heights of 5 mm and 12 mm ($P = 0.0013$) **(Fig. 2.5 D)**.

A positive correlation ($R^2 = 0.784$) was observed between sonicator tip height and particle concentration, with a statistically significant difference ($P = 0.027$) between 2 mm and 12 mm tip heights **(Fig. 2.5 E)**. The correlation between PFP concentration and median PD diameter strengthened as the tip height increased. The R^2 value rose from 0.181 at 2 mm tip height to 0.851 at 12 mm tip height **(Fig. 2.5 F)**. In contrast, the relationship between PFP concentration and particle concentration remained consistent, with R^2 values of 0.543 at 2 mm tip height and 0.569 at 12 mm tip height. These results suggest that increasing sonicator tip height leads to improved sample mixing and potentially more efficient emulsification.

It is probable that as the tip is raised, a greater proportion of the sample is exposed for a longer duration to the cavitation effects in the emulsification zone of the sample vessel [336]. This is consistent with the work of Ferdous *et al.*, who modelled mixing in a 1.5 mL Eppendorf tube driven by a sonicator tip [337]. Their work showed that the size of the circulation zone within the tube increases with increasing tip height, which implies that a larger portion of the sample is exposed to the US field. Conversely, at lower tip heights, less of the sample is subject to disruption or circulation. This could result in a greater contribution of lipid-only structures, which could obscure the relationship between PD diameter and PFP concentration. Data reflecting all conditions tested are shown in **(Fig. 2.6)**.

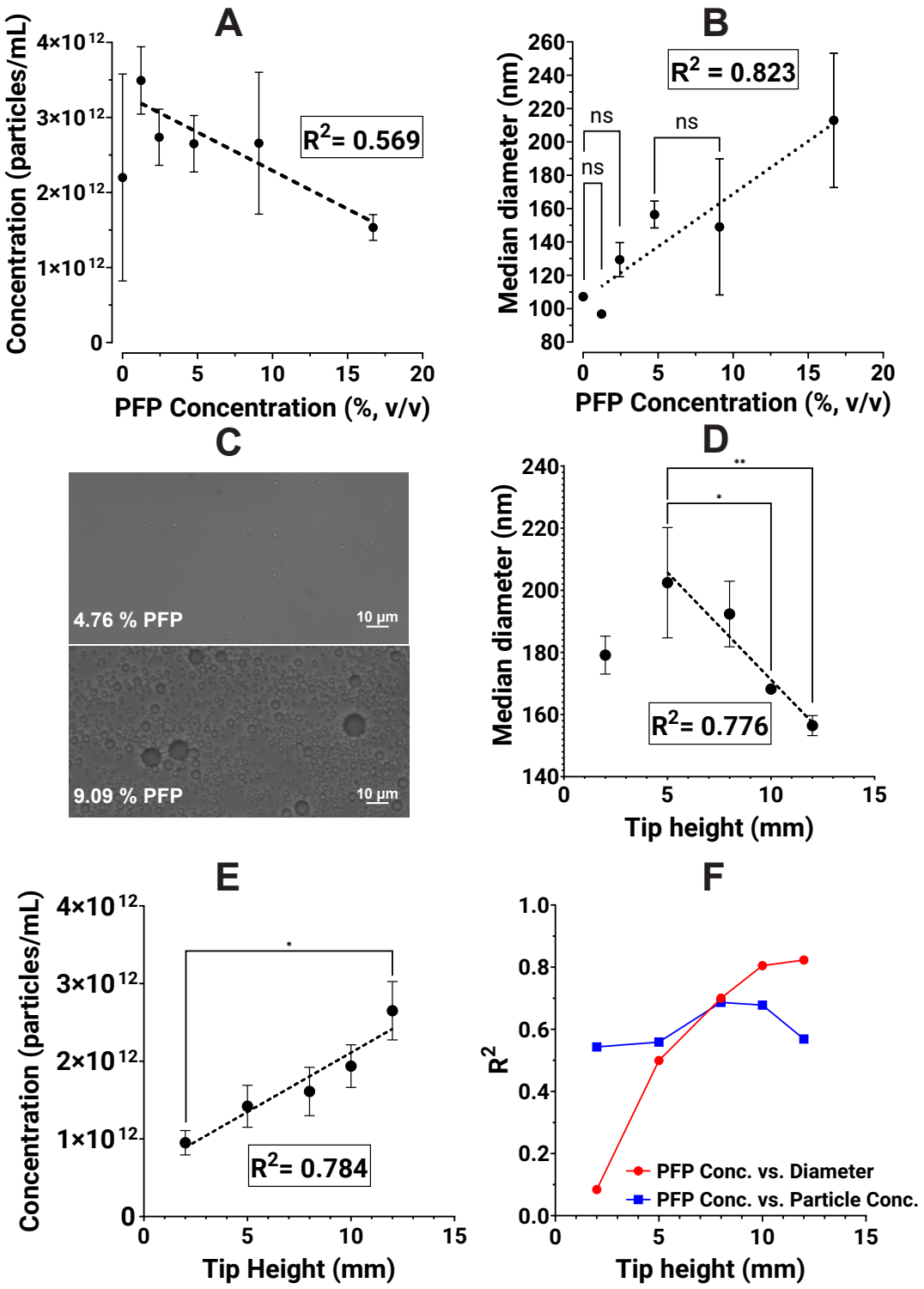

Figure 2.5: PFP concentration and sonicator tip height significantly influence perfluorocarbon droplet (PD) characteristics. (Figure caption cont. next page)

Figure 2.5: PFP concentration and sonicator tip height significantly influence PD characteristics. PDs were manufactured using sonication (60% amplitude, 60 s duration) with varying PFP concentrations (0-16.7% v/v) and tip heights (2-12 mm). PD size and concentration were measured using NTA. **(A)** PFP concentration versus PD concentration at 12 mm tip height ($R^2 = 0.569$). **(B)** PFP concentration versus PD median diameter at 12 mm tip height ($R^2 = 0.823$). **(C)** Bright-field microscopy images (40 × magnification) of PD samples manufactured with 12 mm tip height at 4.76% or 9.09% PFP concentration. Scale bar = 10 µm. **(D)** Sonicator tip height versus PD median diameter at 4.76% PFP concentration ($R^2 = 0.776$). **(E)** Sonicator tip height versus PD concentration at 4.76% PFP concentration ($R^2 = 0.784$). **(F)** R^2 values for correlations between PFP concentration and PD diameter (circles), and PFP concentration and particle concentration (squares) at different tip heights. Error bars represent standard deviation (n = 3 independent repeats). Statistical significance was determined using one-way ANOVA with Dunnett's T3 multiple comparisons test (ns $P > 0.05$, * $P < 0.05$, ** $P < 0.01$).

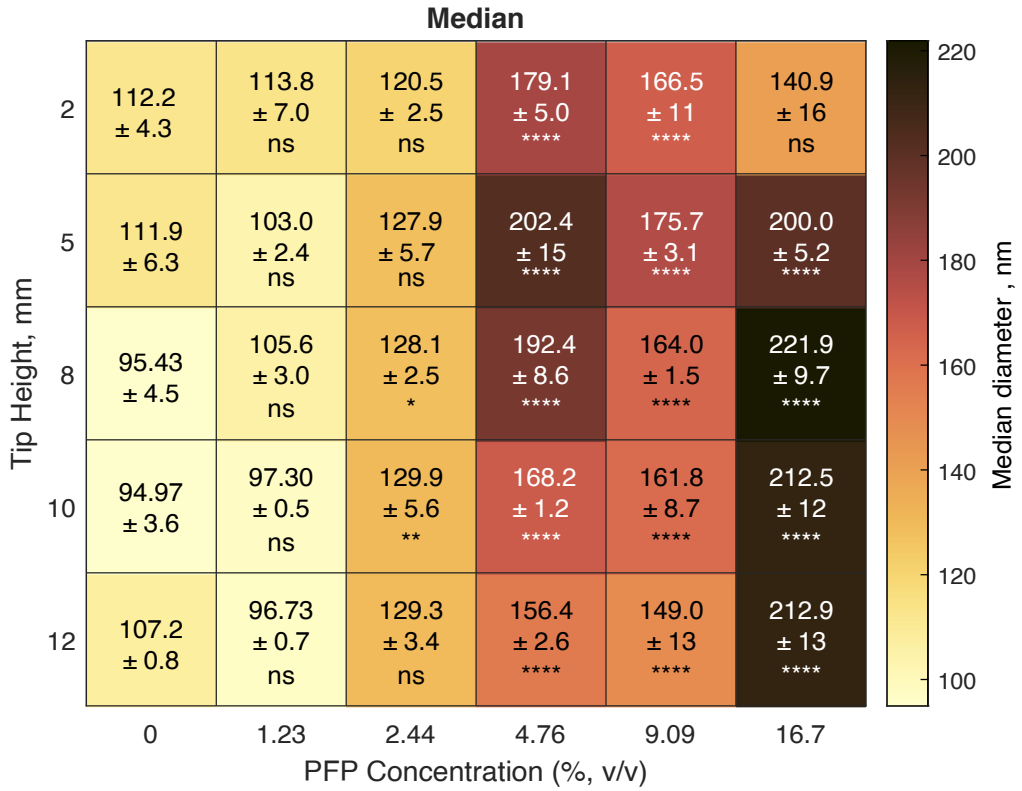

Figure 2.6: Median PD size increases with increasing PFP concentration when measured by NTA. PDs were manufactured using sonication (60% amplitude, 60 s duration). Each value is a mean of n = 3. Phases did not appear to mix for samples manufactured with a tip height of 2 mm with 16.7 % v/v PFP. For these samples the upper lipidic aqueous phase was measured by NTA. Statistical significance was determined using one-way ANOVA with Dunnet's T3 multiple comparisons test between each group and the 0 % PFP control at the same tip height (ns= not significant, ns > 0.05, * < 0.05, ** < 0.01, *** < 0.001, and **** < 0.0001)

The effect of increasing PFP concentration on particle size distribution is illustrated in **(Fig. 2.7)**. As PFP concentration increases, a right shift in the size distribution is observed, due to the formation of a secondary population of larger particles. This shift is accompanied by a decrease in the overall particle concentration, particularly in the smaller diameter peak, which agrees with the trend from **Fig. 2.5 A**. This overall broadening of the size distribution could be due to a combination of factors: as discussed earlier, the increase in particle size is expected with increasing PFP concentration, while the presence of large particles can affect the detection of smaller particles by NTA. Larger particles scatter significantly more light, and can potentially obscure the detection of smaller particles. As previously shown by Filipe *et al.*, the presence of 1,000 nm diameter beads in a sample decreased the number of 100 nm diameter beads detected by up to 70% [338].

Although NTA tracks the Brownian motion of individual particles, there are limits to the range of brightness values that can be captured by the CMOS or CCD sensor utlised by NTA devices. This suggests that the light scattered by larger particles obscures the detection and tracking of smaller particles. Griffiths *et al.* suggest that the amount of light scattered by particles larger than 1,000 nm can make it difficult for the NTA software to locate the center of individual particles through Gaussian profiling [324].

Additionally, Chan *et al.* discuss how the error associated with locating the center of large particles nears the magnitude of the particles' Brownian motion [325]. Furthermore, the presence of particles larger than 1 µm in the 9.09 and 16.7 % PFP samples could affect the flow of particles through the flow cell of the NTA device. In follow-up experiments, a lower concentration of PDs could be analysed to mitigate for the presence of larger particles, especially for samples with higher PFP concentrations. However, this would significantly increase the acquisition time for each sample (approx. 10 min per sample in these experiments).

Based on these results, a PFP concentration of 4.76% and a sonicator tip height of 12 mm were selected for subsequent experiments. These parameters were chosen to manage the balance between efficient emulsification and the desired particle characteristics.

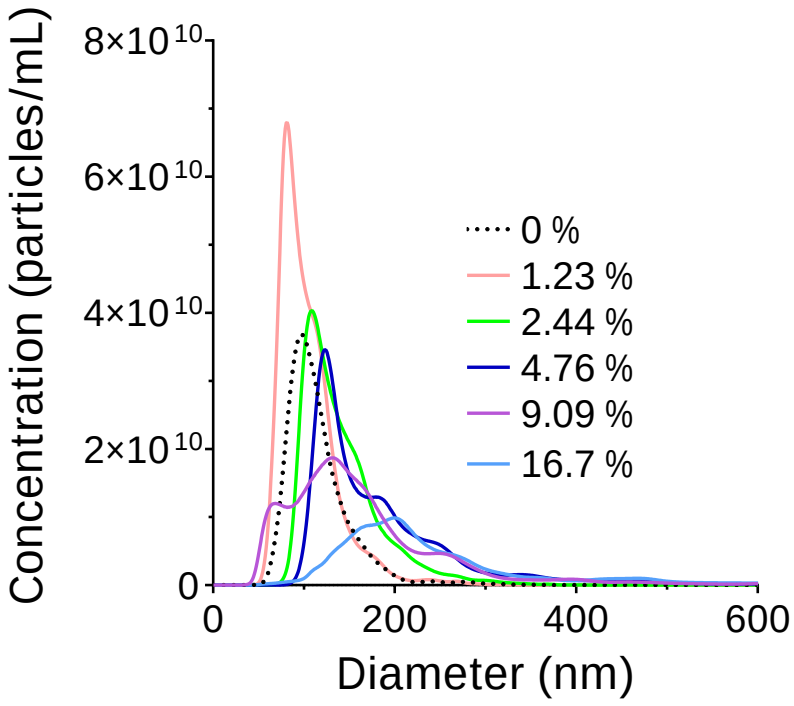

Figure 2.7: PFP concentration influences the size distribution of PDs. NTA data showing the mean particle concentration vs. diameter for PFP concentrations in the range 0-16.7%. PDs were manufactured using sonication (60% amplitude, 60 s duration) with a tip height of 12 mm. Each line represents the mean of n = 3 samples.

2.3.3 Effect of Varying Sonication Duration Against Intensity on PD Characteristics

The effect of varying sonication duration and intensity on PD size characteristics was investigated using a 4.76% v/v PFP concentration and 12 mm tip height. Sonication amplitudes ranging from 20% to 100% were evaluated at sonication durations between 15 and 120 s. Sonication amplitudes of 20% and 40% were insufficient to mix the PFP and lipidic aqueous phases, as evidenced by clear stratification between the PFP precursor droplet and lipidic phases that still existed post-sonication. Conversely, 100% amplitude resulted in excessive foaming and so it was deemed unsuitable **(Fig. 2.8 A)**.

A minimum amplitude of 60% was required to achieve visible mixing of the PFP and lipidic aqueous phases. To characterise the content of the unmixed upper lipidic phase upon sonication, the 20% amplitude sample was selected for comparison with the 60%, 80% and 100% amplitude samples **(Fig. 2.8 B)**. It is important to note that each sonication duration tested represented a separate experimental day, which could account for some of the variability between sonication durations evaluated. As no clear trend was observed, a 60 s sonication duration was chosen for future PD manufacturing, as a balance between processing time and reduced sample exposure to heat cycles. At this sonication duration, there was a statistically significant

($P<0.0001$) difference between the 20% and 60% amplitude samples. No statistically significant differences ($P>0.05$) were instead found between the 60% and 80% amplitude samples or between the 20% and 100% amplitude settings **(Fig. 2.8 C)**. A 60% amplitude setting was selected for future experiments as it represented the lowest amplitude tested that achieved emulsification of the lipid and PFP phases. Additionally, the sample temperature control was carefully characterised at this amplitude setting in 2.3.1. Although this study did not explore intermediate amplitudes, the results from this *Chapter* can inform the fine-tuning and development of detailed manufacturing protocols in future studies.

In summary, conditions selected for PD manufacture were determined to be: 4.76% PFP volumetric concentration, 12 mm sonicator tip height, 60% sonication amplitude, and 60-second sonication duration, giving a median PD diameter of 156 nm and particle concentration of 1×10^{12} particles/mL. The PFP volumetric concentration was primarily chosen due avoid the presence of large particles (>1 µm) outside the NTA detection limit. Additionally, the results in *Section 2.3.2* suggest that increasing sonicator tip height leads to improved sample mixing and potentially more efficient emulsification. The subsequent section explores the effect of PFP concentrations above 4.76% on particle size distribution, using RPS to quantify the presence of larger particles previously only qualitatively assessed by optical methods.

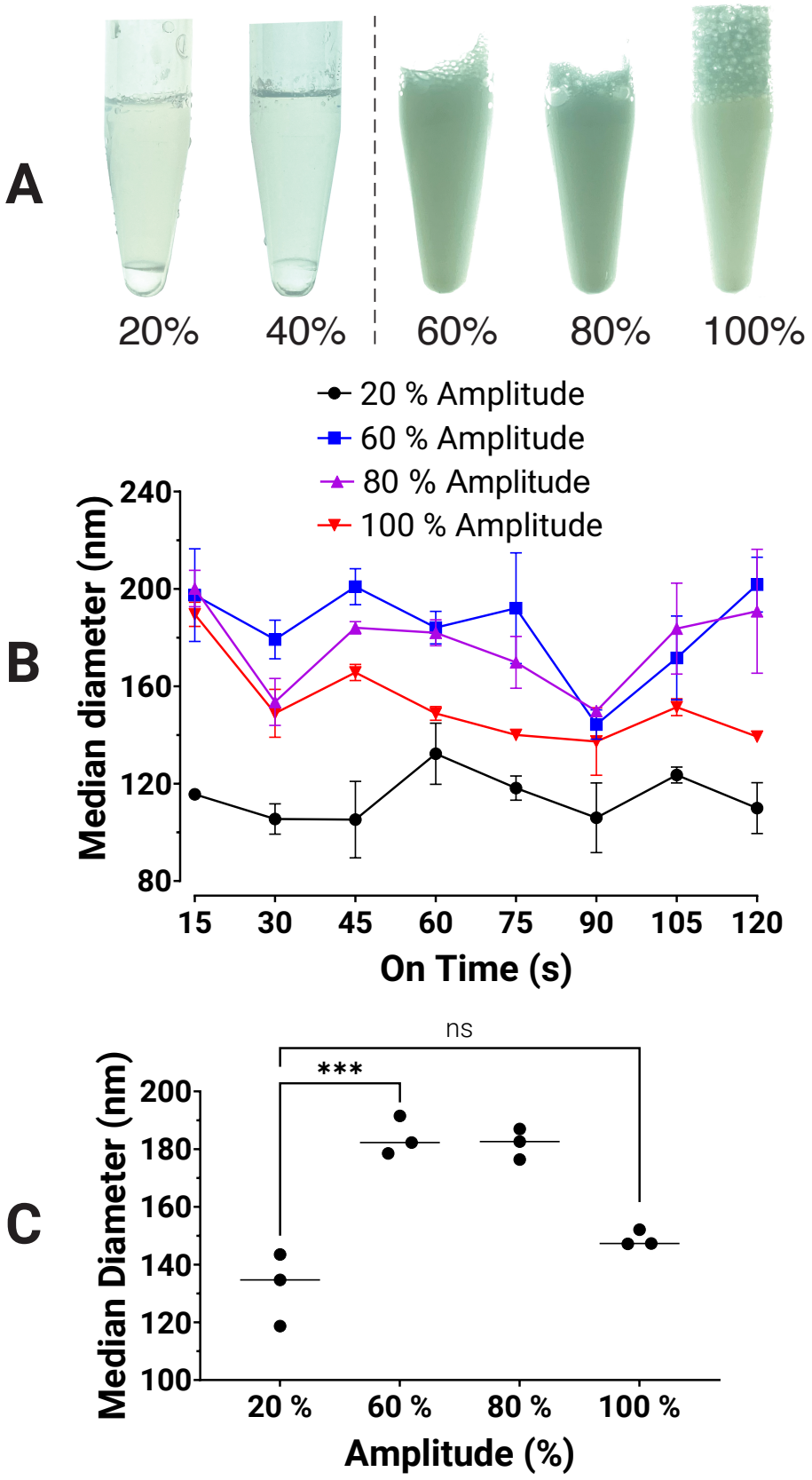

Figure 2.8: Phases did not appear to mix for samples sonicated with intensities of 20% and 40%. Figure caption cont. next page

Figure 2.8: Sonication amplitude affects phase mixing in PD manufacture. **(A)** Visual observation shows a minimum of 60% sonicator amplitude was required for the PFP and lipid phases to mix during sonication-based emulsification. For 20% and 40% amplitudes, phase separation remained visible, and only the upper lipid phase was characterised by NTA. (B) Median diameter against total sonication durations from 15 s to 120 s. (C) Median diameter against sonicator amplitude, showing the effect of acoustic intensity on droplet formation. All measurements were performed with a 12 mm sonicator tip height. PFP concentration was maintained at 4.76% v/v. Diameter values reported are mean ± S.D. for n = 3 independent samples.

2.3.4 Evaluating the Effect of Varying PFP Volumetric Concentration using the Coulter method

To evaluate the presence of particles larger than the upper detection limit of NTA, PD samples were measured using RPS. The median diameter of PDs increased significantly ($P<0.01$) with increasing PFP concentration, from 0.54 ± 0.008 µm at 4.76% v/v PFP to 0.76 ± 0.03 µm at 16.7% v/v PFP **(Fig. 2.9 A)**. A broadening rightward shift of the particle size distribution was observed **(Fig. 2.9 B)**, which can be attributed to the formation of a secondary population of larger particles.

Specifically, PDs manufactured with 4.76, 9.09, and 16.7 % v/v PFP, had median diameters of 0.54 ± 0.008 µm, 0.62 ± 0.003 µm, and 0.76 ± 0.03 µm, respectively **(Fig. 2.9 A)**. The median diameter increased with increasing PFP concentration, with statistically significant ($P<0.01$) differences observed between all samples.

This trend is consistent with the NTA data in **(Fig. 2.5 B)**. The particle size distribution also exhibited a distinct right shift as PFP concentration increased **(Fig. 2.9 B)**. Similar to the trend seen in **(Fig. 2.7)**, the distribution of particles broadened with increasing PFP concentration and this observation could be attributed to the formation of a secondary population of larger particles. The RPS detector enabled the measurement of particles outside the detection range of the NTA.

While the minimum detection limit for the RPS is 0.4 µm, it overlaps with the NTA detection range (10 nm to 1 µm) between 0.4 µm and 1 µm. The data suggest the presence of many particles between 0.4 µm and 1 µm that were not fully represented in the NTA data, possibly due to the large difference in relative frequency of particles in the lower (10 nm to 400 nm) vs. upper (400 nm to 1000 nm) size range. This discrepancy could be also be attributed to particles in this size range nearing the lower detection limit of RPS, thus introducing additional uncertainty. The presence of particles larger than 1 µm in the 4.76% PFP PDs could also have interfered with NTA image acquisition and contributed to the lack of particles detected above 0.4 µm in **(Fig. 2.7)** [264, 338].

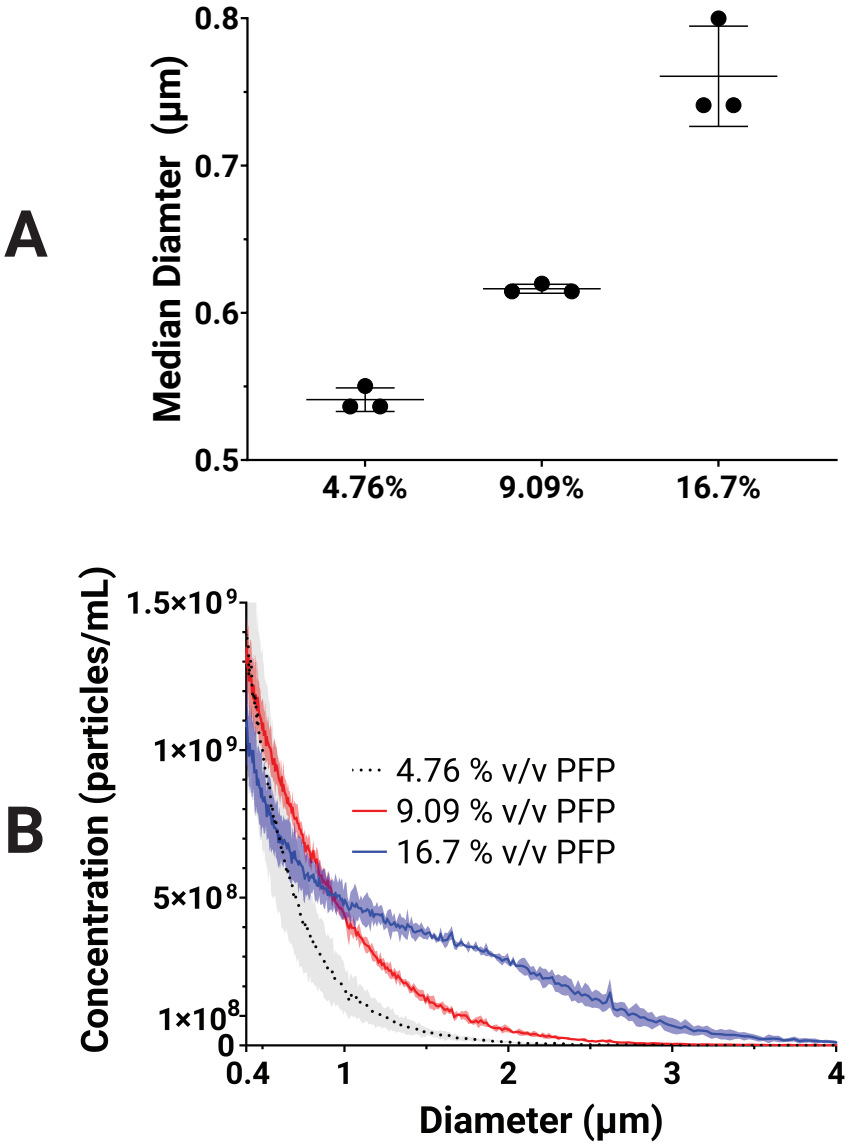

Figure 2.9: As PFP concentration increases, the proportion of particles with a diameter >1 µm increases. **(A)** Median diameter values ± SD at 4.76%, 9.09% and 16.7% PFP. A statistically significant difference (P<0.01) was found between each PFP concentration. **(B)** PDs were measured by RPS, with particle concentration plotted against particle diameter (n = 3). The minimum size detection limit of the RPS detector is 0.4 µm. Data represent mean ± SD (n = 3 independent samples).

Post-processing steps may be implemented in combination with a fine-tuning of the PFC concentration to better suit the intended application. If using filtration, further characterisation may be necessary, as droplets could coalesce as they are processed through a membrane or may vaporise due to changes in pressure. For size isolation of larger droplets, centrifugation has been explored in previous studies. Mercado *et al.* demonstrated that the isolation of PDs with diameters between 1-3 µm and 2-5 µm was possible using this technique. The range of particle sizes was wide (between 1 µm and 10 µm) [339]. Their approach demonstrates a method for the selection of a droplet size distribution to meet application-specific requirements.

2.4 Conclusion

In this *Chapter*, the development of a manufacturing apparatus that enables precise and repeatable positioning of the sonicator tip for the production of PFP PDs was described. It was evident that both PFP concentration and sonicator tip height had a significant effect on PD size characteristics. Pulse parameters were crucial in regulating the sample temperature during sonication. A 2 s on, 15 s off pulse regime at 60% amplitude kept samples temperature below 16 °C. Higher sonication intensities (80-100% amplitude) were shown to lead to increased sample heating and foam production.

Increasing the volumetric concentration of PFP from 4.76% to 16.7% resulted in a larger median droplet diameter (0.54 ± 0.008 µm to 0.76 ± 0.03 µm, respectively). Increasing sonicator tip height from 2 mm to 12 mm was shown to strengthen the relationship between PFP concentration and median droplet diameter, possibly due to improved sample mixing and emulsification efficiency. When comparing a range of PFP concentrations, both NTA and RPS demonstrated a broadening rightward shift of the size distribution, attributed to the formation of a secondary population of larger diameter particles.

Overall, these results also highlight the importance of utilising a range of characterisation techniques when developing PD emulsions, especially when evaluating particles across a wide range of diameters. The relationship between manufacturing parameters underscores the need to evaluate a range of conditions when formulating PD emulsions. Moving forward, the 4.76% PFP PDs produced in this *Chapter* will serve as a starting point for the work in *Chapter 2*.

The knowledge gained in this *Chapter* will inform the development of PDs in the context of bioactive (i.e NO) gas delivery and US-stimulation to induce ADV. Specifically, the manufacture of PDs larger than 1 µm could be beneficial for topical applications. Primarily, larger droplets could affect the gas-dissolution capacity and release rate, owing to a lower surface area to volume ratio [340]. Additionally, the ADV threshold is known to decrease with increasing PD diameter, which could reduce the US pressure magnitudes needed to induce vaporisation [32]. These factors will be considered when developing PDs in subsequent experiments: the ultimate manufacturing, gas-loading and US-stimulation parameters will depend on the findings in subsequent steps of the present research.

Chapter 3

Development and Characterisation of Nitric Oxide Loading in Perfluorocarbon Droplets

3.1 Introduction

Expanding on the development of PD manufacturing methods established in *Chapter 2*, this *Chapter* explores the loading and quantification of NO gas in PDs. As described in *Chapter 1*, NO is a molecule involved in a variety of physiological processes and has attracted significant research interest as a result of its potential to induce the dispersal of bacterial biofilms [87]. The delivery of NO is impeded by its

reactivity and short half-life (on the order of seconds) in oxygenated environments [288]. As biofilm dispersal effects are mediated by NO (and not by its breakdown products), care must be taken to reduce or remove the presence of oxygen prior to NO delivery. Recent studies have shown promising results using NO-loaded cavitation nuclei for biofilm treatment. LuTheryn *et al.* showed that NO-loaded MBs with free gentamicin achieved up to a 99.9% reduction in both surface area and cell viability of *P. aeruginosa* biofilms [287]. The efficacy of sub-inhibitory concentrations of gentamicin was shown to increase significantly. While PDs have been extensively studied as oxygen carriers due to their high gas solubility, research on NO delivery using PDs remains limited [35, 341].

To date, only three key studies have investigated NO delivery using PD emulsions. Initial work by Ortiz *et al.* evaluated NO-loaded perfluorocarbons in blood, using 300 ppm NO purified from nitrogen oxides and a 4-hour nitrogen degassing protocol. Their study focused primarily on the vascular effects of NO and its conversion to various NO_x species in blood.

Choi *et al.* published two studies exploring the loading of NO into different PD formulations. Their first study using perfluorooctane (PFO) PDs (318 nm mean diameter) reported substantial NO release (87.4 mM) over a 12 h period [342]. A 100 µL dispersion of these NO-loaded PDs increased the death of planktonic *S. aureus*

5-fold but showed insignificant effects in planktonic *P. aeruginosa* cultures.

In their second study, Choi *et al.* used perfluorodecalin (PFD) PDs (220 nm in diameter) and reported substantially different NO release profiles, with 2 mM being released over just 18 minutes. While both studies used similar loading conditions (2 hours, 1 bar, 25 °C, unspecified NO concentration), the lack of detailed methodology and significant discrepancy in reported NO concentrations highlights a critical need for detailed methodology and characterisation reporting [297].

In this *Chapter*, the loading and quantification of gaseous NO in PDs were explored.

The specific objectives of the work described in this *Chapter* are as follows: First, to explore various methods for loading NO into PDs using different NO sources and loading protocols. Second, to evaluate how varying PD size characteristics influence NO-loading. Third, to identify and optimise an NO-loading protocol capable of achieving therapeutically relevant NO concentrations suitable for biofilm dispersal applications, which will be further evaluated in *Chapter 4*. To quantify NO concentration within the PD emulsions, two complementary analytical techniques were employed: the Griess assay and ozone-based chemiluminescence detection. The experimental approach in this chapter proceeded as follows: Initially, preliminary validation of NO-loading was conducted using Griess assay quantification to estab-

lish measurement feasibility.

This was followed by the development of a pressurised NO-loading method utilising on-demand cold-plasma NO generation. Subsequently, both Griess and chemiluminescence NO quantification methods were compared to allow selection of the most suitable measurement technique. Following this, an oxygen-free NO-loading method to minimise NO oxidation during the loading process was developed. Further work evaluating how PD size characteristics changed when varying PFP concentrations was completed to enable to comparison between droplet size and NO-loading capacity. Finally, an assessment of NO-loading capacity was conducted using the optimised oxygen-free method to determine the ideal effective formulation for biofilm dispersal applications.

3.1.1 NO detection techniques

As indicated above, two methods were used to quantify the concentration of NO within PDs: the Griess assay and ozone-based chemiluminescence detection.

Griess Assay

The Griess assay is a prevalent colorimetric method that indirectly quantifies NO concentration through the detection of nitrite (NO_3^-) [343]. As nitrite is often further oxidised to nitrate in biological fluids, a nitrate reductase enzyme is typically

used to reduce nitrate to nitrite [343, 344].

The Griess assay works as a two-step diazotization reaction, starting with dinitrogen trioxide formed either by autoxidation of NO or by an acid-catalyzed reaction of nitrite [345]. In the first step, dinitrogen trioxide reacts with sulfanilamide to form a diazonium ion which then is coupled to *N*-(1-napthyl)ethylenediamine in the second step, forming a brightly coloured azo product (λ_{max}=540 nm) [344, 345].

NO concentration is calculated using a reference absorbance curve of known concentrations of a standard, such as sodium nitrite [346]. The advantages of the Griess assay include its relative simplicity, high throughput, and adaptability to a wide range of biological applications [347]. The Griess assay has a detection limit in the low micromolar range [347, 348]. As the Griess assay indirectly measures NO through nitrite levels, the amount of NO reported can be distorted if precautions are not taken to limit other sources of nitrite or compounds that affect light absorption [349].

Chemiluminescence

An ozone-based chemiluminescent detector (CLD) operates by detecting light emitted from the reaction between NO and ozone (O_3) **(Equation 3.1)**

$$\begin{aligned} NO + O_3 &\longrightarrow {NO_2}^* + O_2 \\ {NO_2}^* &\longrightarrow NO_2 + h\nu \end{aligned} \tag{3.1}$$

Where ${NO_2}^*$ in the excited state returns to the ground state and emits a photon ($h\nu$) [350]. Light generated from this chemiluminescence reaction is detected by a photomultiplier tube (PMT), which amplifies and converts the optical signal into an electrical signal, which is then recorded by a computer software [351]. Reducing agents such as vanadium (III) chloride are used to convert nitrogen oxides (NO_x) such as nitrite (${NO_2}^-$) and nitrate (${NO_3}^-$) into NO. This allows for the measurement of NO and any NO breakdown products contained within a sample.

An advantage of measuring NO by chemiluminescence is the low detection limit in the ppb range allowing for picomolar levels of NO to be measured [352]. Furthermore, NO CLDs are highly specific for the reaction between NO and ozone, minimising the effect of contaminating compounds [351].

Other methods used to measure NO include fluorescence, electrochemical, and magnetic resonance techniques [353].

3.2 Materials and Methods

3.2.1 Preliminary Griess Assay Experiments

Preliminary NO loading experiments were conducted using an apparatus from LuTheryn *et al.* [287]. Briefly, an eNO generator (NitricGen, USA) was used to produce NO at a concentration of 1000 ppm. PDs were prepared as described previously in *Chapter 1*, with 4.76% v/v PFP, 60% amplitude, a total sonication time of 60 s, and a tip height of 12 mm. Nitrogen gas (BOC, UK) was bubbled through 5 mL of PDs for 30 min within a 7 mL container (27151, Merck, Germany); sparging of dissolved oxygen from water using nitrogen gas is a common technique and has been used to purge perfluorocarbons prior to NO loading [36, 354].

Once sparged, the PDs were loaded with NO by bubbling the gas through the emulsion at a concentration of 1000 ppm and a flow rate of 0.5 L / min for 30 min (**Fig. 3.1**). Once NO was loaded, the concentration of dissolved NO was assessed using a colorimetric NO Assay Kit (ab35328, Abcam, UK). In summary, the NO oxidation product nitrate is converted to nitrite by nitrate reductase, and subsequently a Griess reagent converts the nitrite into a purple azo compound. Due to the inherent presence of oxygen in the output of the eNO generator, the concentration of NO and associated nitrogen-oxides (NO_x) was reported.

The NO_x concentration of NO-loaded PDs was evaluated, with 'Room-air' PDs as an unloaded control without NO-loading or nitrogen sparging steps taken.

The absorbance was measured at 540 nm using a plate reader (FLUOstar Omega, BMG Labtech), with sample blanks deducted from all values. A 1:5 or 1:10 dilution with PBS of both sample types was measured. A standard curve was prepared according to the manufacturer's instructions using a nitrate standard, and the fitted curve was used to convert the absorbance (a.u.) at 540 nm to the concentration of NO_x.

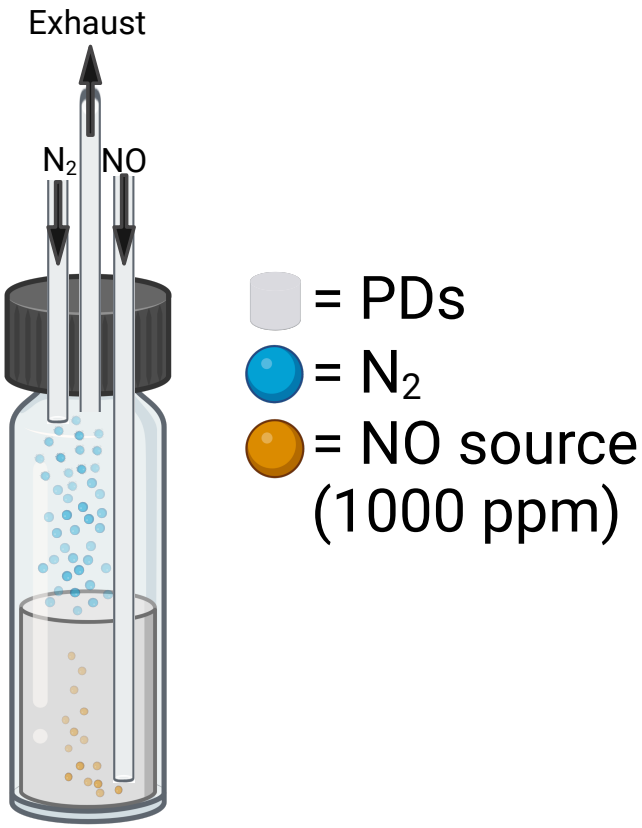

Figure 3.1: Experimental setup for loading of NO gas into PDs (eNO generator). A vial with two inlets and one outlet allowed for the maintenance of an oxygen-free headspace flushed with nitrogen. Samples were sparged using nitrogen gas bubbled through the PDs for 30 mins prior to NO-loading The output from the eNO generator (1000 ppm NO and room air) was bubbled through the PD emulsion with a flow rate of 0.5 L / min for 30 min.

3.2.2 Pressurised NO-loading of PDs

Following insights from preliminary experiments, several changes were made to explore the effect of loading NO into PDs including a pressurised step. A different NO generator was acquired and incorporated into a different NO loading process involving the use of a pressurised headspace as detailed below. NO was generated using a NOxLab Model D (Fourth State Medicine, UK). The output concentrations of ROS varied depending on the input flow rate of air. Using a 0.5 ln / min input flow rate, an output of 565 ppm NO and 433 ppm NO_2 was generated. NO_2 was converted to NO using a catalytic converter (CG-2, M&C TechGroup, Germany), yielding a total NO concentration of approximately 1000 ppm.

As from the atmostphere is used in this setup for the generation of NO, the gas output from this setup is referred to as NO + room air. To load samples with NO, 1.5 mL tubes (DNA LoBind Tubes, Eppendorf SE, Germany) with 500 µL of each sample type, were placed into a 50 mL syringe (BD300866, BD, UK) flushed with nitrogen gas (BOC, UK) for 30 min. Subsequently, the headspace was flushed with ∼1000 ppm NO + room air for 5 min. The syringe was then sealed, cooled to 4 °C and the headspace was reduced in volume by ∼50% (**Fig. 3.2**). This approach is based on Henry's law, which states that the amount of dissolved gas in a liquid is proportional to its partial pressure above the liquid [355].

By increasing the pressure, the aim was to increase the solubility of NO in the perfluorocarbon phase. Undiluted 4.76 % v/v PFP PDs (NO-PDs), DSPC:PEG40S in PBS (NO-Lipids) and PBS (NO-PBS) were evaluated. The effect of pressurisation and cooling on the particle size distribution was evaluated by RPS, using the method described in *Chapter 2*. Due to the increase in headspace pressure, there were concerns that it could affect droplet stability. Three independent samples of PDs were measured before and after the pressurised NO-loading step.

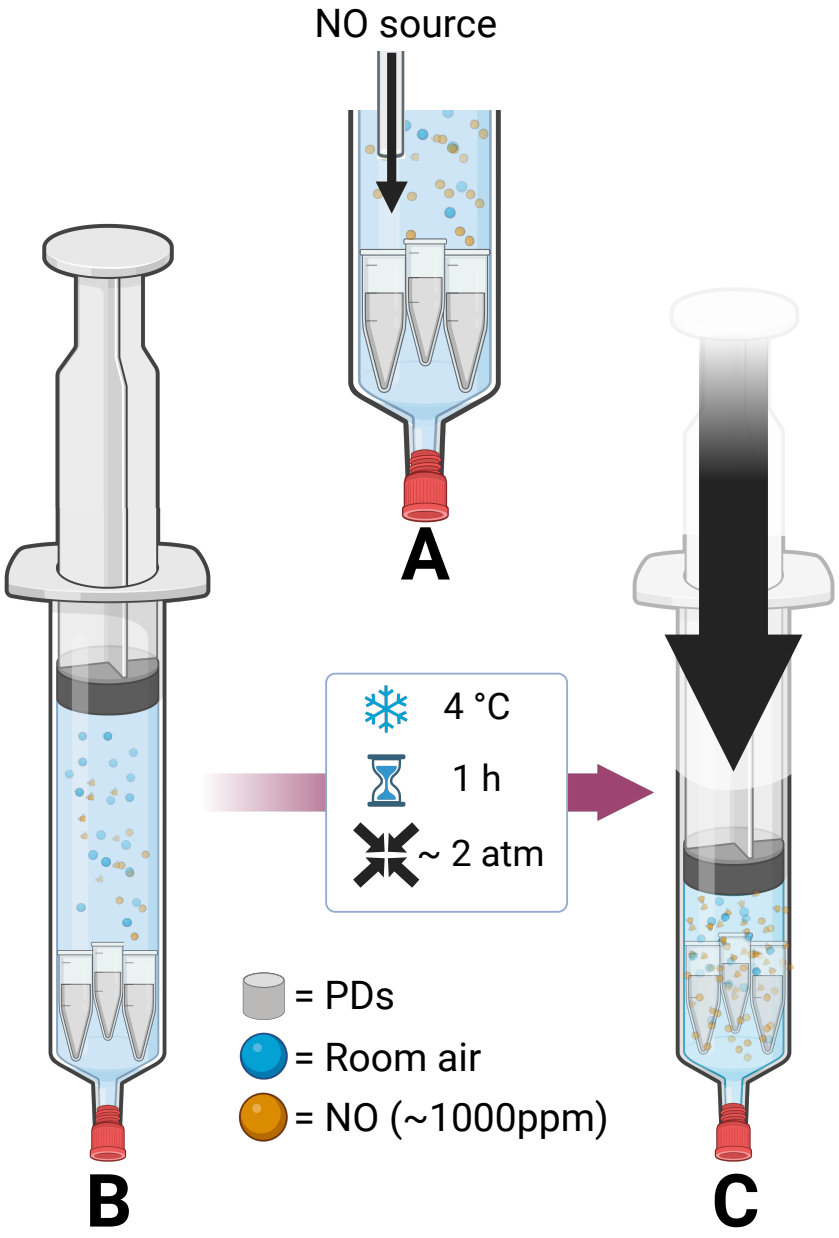

Figure 3.2: Pressurised NO-loading method. **(A)** The headspace of PD samples within a 50 mL syringe is flushed with ~1000 ppm NO + room air for 5 min. **(B)** The headspace is sealed. **(C)** The syringe is compressed to 50% of the original volume and cooled to 4 °C for 1 h. After this, the pressure is gently released and samples' NO_x concentration measured.

Griess Assay

Quantification of NO_x was evaluated using a NO assay kit (ab65328, Abcam , UK) as described in Section 3.2.1 following the manufacturer's instructions. Due to the high absorbance values seen in the preliminary experiments, the samples were further diluted to 1:100 in PBS and centrifuged after reaction with Griess reagents to remove the PDs. The samples were centrifuged at 11,000 × g for 5 min and then the supernatant of each sample was pipetted into a 96-well plate. A standard curve was prepared according to the manufacturer's instructions using a nitrate standard, and the fitted curve was used to convert the absorbance (a.u.) at 540 nm to the concentration of NO_x.

Chemiluminescence

The concentration of NO_x was evaluated using a CLD (ANALYZER CLD 88, ECO MEDICS AG, Switzerland). Undiluted 4.76 % v/v PFP PDs (NO-PDs), DSPC:PEG40S in PBS (NO-Lipids) and PBS (NO-PBS) were loaded with NO using the pressurised method described in Section 3.2.2. The chemiluminescence apparatus is shown in **(Fig. 3.3)**.

Briefly, samples are introduced into a heated reaction chamber (90 °C) filled with 50.8 mM vanadium (III) chloride in 1 M HCl. NO_x within the sample is rapidly reduced to NO gas, which is carried by helium gas (BOC, UK). The helium + NO gas mixture is cooled by a condenser and passed through an NaOH trap to remove acidic vapor and volatile contaminants [351]. Once the gas mixture enters the CLD, NO reacts with O_3 to form NO_2, of which the excited-state NO_2* can relax to the ground-state, releasing light that is converted to an electrical signal by the PMT and recorded on a computer.

The amount of NO_x within a sample was calculated using a standard curve generated the same day. Following a method used by Tabish *et al.*, serial dilutions (0 - 50 µM) of sodium nitrite ($NaNO_2$) were introduced into the reaction chamber and the peak voltage was plotted at each standard concentration [356]. Between each measurement, sufficient time was allowed for the voltage to reach the baseline. The 0 µM control was confirmed to not produce any signal. For both samples and standards, 10 µL volumes were introduced using a 10 µL Hamilton syringe (Hamilton Company, USA). Samples were diluted 1:10 in DPBS prior to NO-loading, with calculated NO_x concentrations accounting for dilution factor.

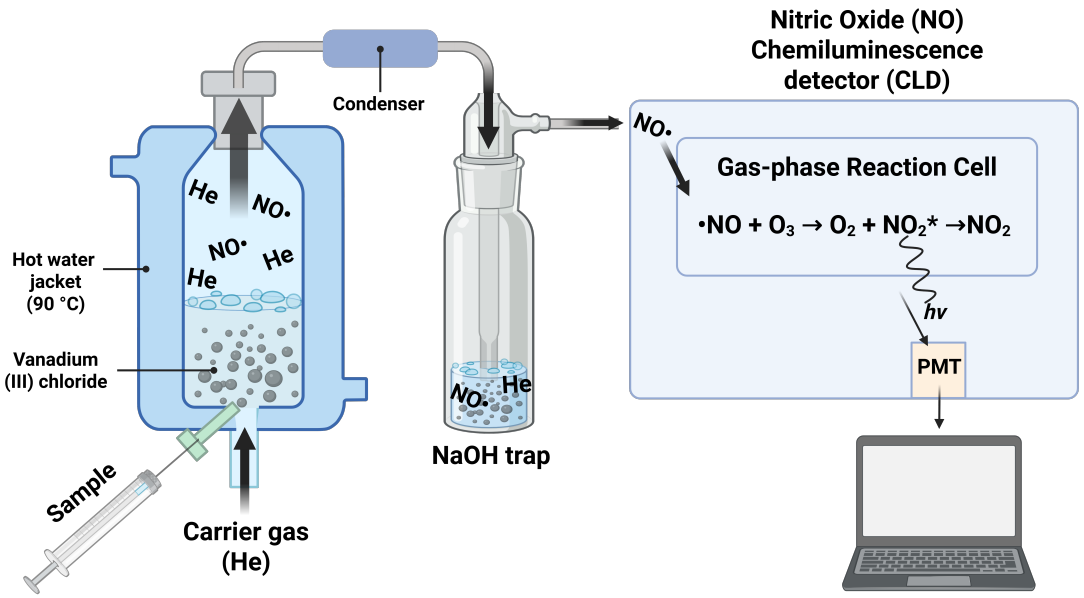

Figure 3.3: Ozone-based chemiluminescent detector (CLD) apparatus.
NO-loaded samples are introduced into a reaction chamber containing acidified vanadium (III) chloride heated to 90 °C by a water jacket. This reduces NO_x within the sample to NO gas, which is carried by helium gas bubbled through the reaction chamber. The helium and NO is passed through an NaOH trap to remove residual acidic vapor. NO is carried into the detector and reacts with ozone gas generated by the CLD. Photon emissions *hv* are collected by the photomultiplier tube (PMT), converted to an electrical signal that is recorded on a computer.

3.2.3 Varying Volumetric Concentrations of PFP

PDs were prepared as described previously in *Chapter 2*, with a few exceptions. To assess a wider range of volumetric concentrations of PFP, the total sample volume was maintained at 800 µL. Instead of adding PFP to 800 µL lipids, the amount of both PFP and lipids were varied, maintaining a total sample volume 800 µL.

Volumetric concentrations of PFP of 10, 20, 40, and 50 % v/v were evaluated and corresponded to 80, 160, 320, and 400 µL of PFP, respectively. The lipid volumes added for 10, 20, 40, and 50% v/v PFP were 720, 640, 480, and 400 µL of lipids in DPBS, respectively. A total sonication time of 60 s, sonication amplitude of 60%, and tip height of 12 mm were used.

As described previously in *Chapter 2*, 10 µL of a 1:10 dilution in DPBS of each PD sample was added to a 10 mL volume of ISOTON II diluent (Beckman Coulter, USA), and gently agitated. 50 µL of PDs diluted in ISOTON was flowed through a 20 µm aperture (particle detection range 0.4 µm to 10 µm). Three independent PD samples were measured at each PFP volumetric concentration, and size characteristics were analysed by particle count and particle volume determinations.

3.2.4 Development of an Oxygen-free NO-Loading Method

In water, NO reacts with oxygen to form NO_2^- (nitrite) primarily **(Equation 3.2)**

$$\begin{aligned} 2NO + O_2 &\longrightarrow 2\,NO_2 \\ 2NO_2 + 2\,NO &\rightleftharpoons 2\,N_2O_3 \\ 2N_2O_3 + 2\,H_2O &\longrightarrow 4\,NO_2^- + 4\,H^+ \end{aligned} \tag{3.2}$$

This represents the oxidation of NO to NO_2^- in an aqueous environment, with

dinitrogen trioxide N_2O_3 as a reversible intermediate [273]. The removal of dissolved oxygen from PFC emulsions can be achieved by bubbling inert gases such as nitrogen or argon through a sample [36, 342]. The introduction of numerous small bubbles increases the rate of gas transfer and allows the majority of dissolved oxygen to be removed without heating the sample [354]. The displacement of dissolved oxygen using these gases has been shown to be effective in other research areas [357, 358]. The use of a nitrogen or argon headspace facilitates both removal of dissolved oxygen and maintenance of an oxygen-free environment when preparing samples.

Sparging Confirmation

To minimise gas consumption during the sparging process, the deoxygenation rate was evaluated for 5 mL aliquots of DPBS. An OxyMini oxygen meter (World Precision Instruments, UK) was used to monitor the level of dissolved oxygen within the sample. Three independent samples of oxygen-saturated water were sparged with nitrogen (BOC, UK) for 120 s. Due to the rapid reaction between NO and oxygen, an oxygen-free loading method was developed to reduce the production of NO_x prior to quantification (**Fig. 3.4**). By reducing NO_x concentrations before measurement, the objective was to potentially improve accuracy of the NO concentration measurements. Reducing the presence of oxygen and subsequent NO_x generation will be beneficial for any therapeutic applications that need to maximise

NO concentration.

The NO source was switched to a compressed gas mixture of 400 ppm NO in nitrogen (BOC, UK). Prior to NO loading, samples were sparged with nitrogen for 3 min to remove dissolved oxygen. During the loading process, 400 ppm NO was flowed through a needle to ensure that the sample was gently agitated to encourage gas exchange for 5 min. Samples were sealed after the loading period to maintain an oxygen-free environment. 500 µL of each type of sample was loaded: MilliQ water (NO-Water), DSPC:PEG40S in DPBS (NO-Lipids), 10% v/v PFP PDs (NO-PDs), and 20% v/v PFP PDs (NO-PDs).

Quantifying NO concentrations of Oxygen-free Loading Method

NO_x concentrations were evaluated using the chemiluminescence method described in Section 3.2.2, with a key modification. The standard curve was measured over a different range (0 - 12.5 µM) that was within the linear response range of the CLD. All standards were measured in triplicate.

3.2.5 Statistical Analysis

GraphPad Prism was used to run unpaired t-tests and test for any statistically significant differences in samples, with P = 0.05 as the significance level.

3.3 Results and Discussion

3.3.1 Preliminary Griess Assay experiments

Following the development of the PD manufacturing process in *Chapter 2*, the NO loading capacity of 4.76% v/v PFP PDs was explored. This formulation was selected as greater amounts of PFP (such as 9.09% PFP) led to PDs suspensions with a significant number of particles >1µm in diameter. To evaluate the concentration of NO_x in PDs, a Griess assay calibration curve was generated using sodium nitrite ($NaNO_2$) standards. As shown in **(Fig. 3.5 A)**, the standards exhibited a linear relationship up to 80 µM NO_x, beyond which the response appeared to plateau. However, all measurements were conducted below this threshold concentration and, therefore, the validity of the assay was not affected in this regard. The non-linear section of the standard curve could have been caused by improper solubilisation of the individual standard wells during preparation.

At both a 1:5 and a 1:10 dilution in PBS, there were no statistically significant differences between samples loaded with room air and NO-loaded samples **(Fig. 3.5 B)** ($P>0.05$). Qualitative evaluation of standard wells **(Fig. 3.5 C)** and NO-loaded PD wells **(Fig. 3.5 D)** revealed substantial turbidity in all wells containing PDs.

This turbidity was attributed to the stratification of the PDs, which led to the appearance of two layers, an upper foam-like layer and a sedimented translucent layer.

This could lead to additional scattering of the light emitted by the spectrophotometer and affect the absorbance readings [359]. The low pH of the Griess assay reagents could affect the stability of the PDs, leading to these observations. The spontaneous vaporisation of some PDs could lead to the foam-like layer. In future experiments, a centrifugation step was added to mitigate these unwanted effects.

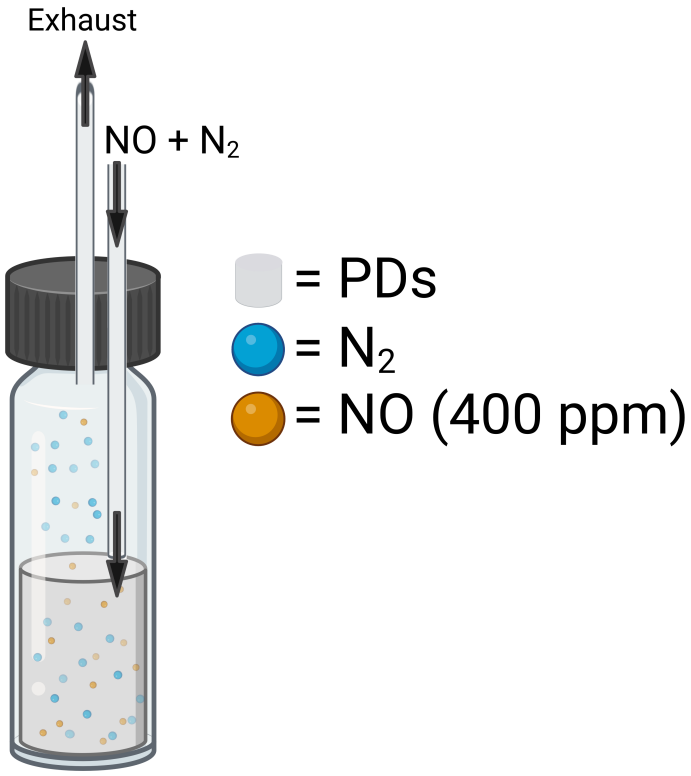

Figure 3.4: Experimental setup for oxygen-free loading of NO gas into PDs.
A vial with one inlet and one outlet allowed for sparging of samples with nitrogen and subsequent loading with NO. 400 ppm NO in Nitrogen was flowed over samples for 5 min, with gentle agitation from the gas flow encouraging gas exchange.

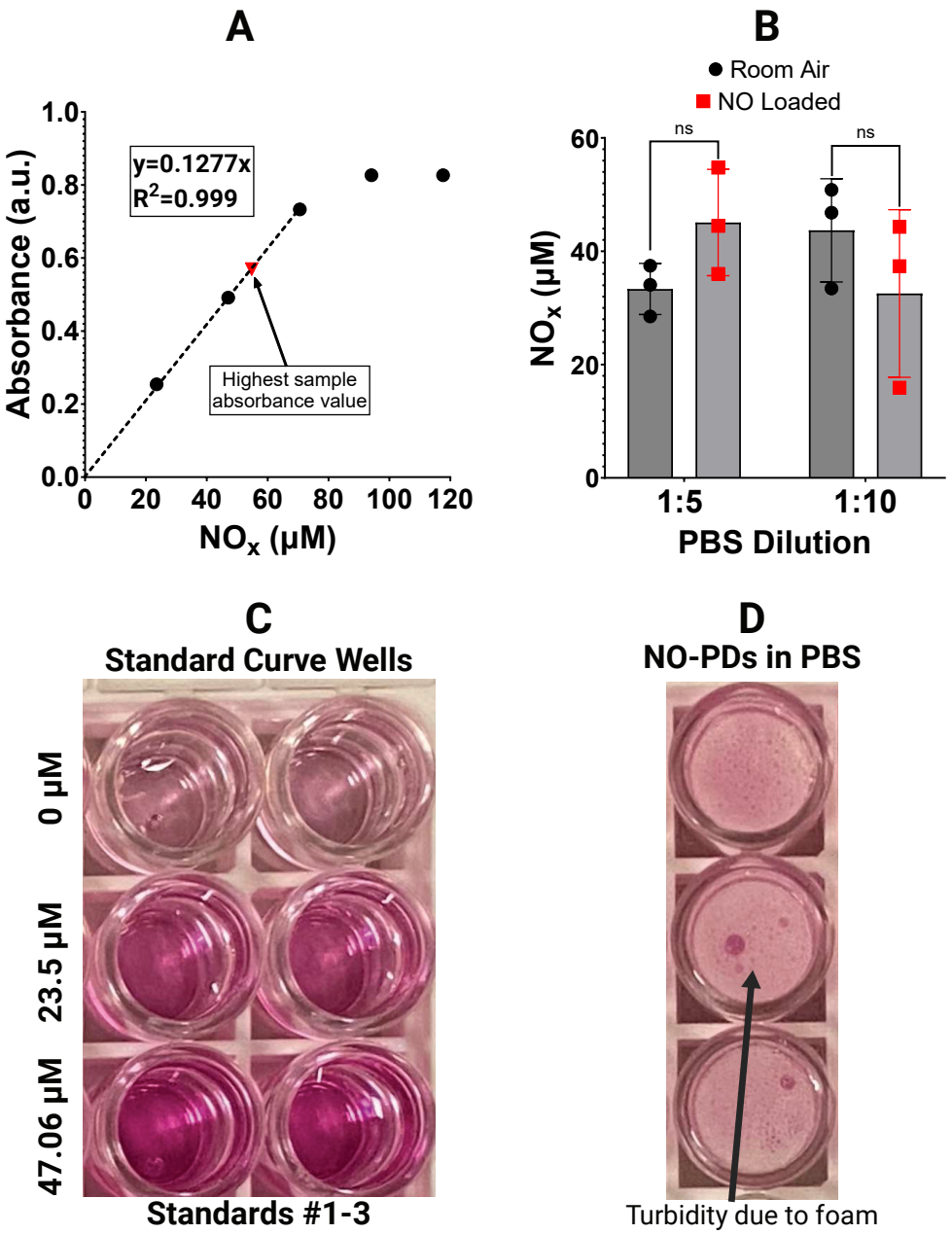

Figure 3.5: Preliminary Griess assay experiments measuring NO_x in PD emulsions. **(A)** Griess assay standard curve **(B)** NO_x concentration for room air and NO-loaded PD samples diluted at 1:5 and 1:10 with PBS prior to Griess assay measurement. No statistically significant difference (P>0.05) was found for either sample pair. Dilution factors have not been removed in NO_x concentration calculations. **(C)** Photograph of Griess assay standard curve wells **(D)** Photograph of sample wells containing NO-PDs. Assay wells with NO-PDs exhibited foaming and increased turbidity. (ns=not significant, P>0.05)

3.3.2 Evaluation of a Pressurised NO Loading Method

Following relocation to the University of Oxford, the experimental setup was upgraded to incorporate a NO_x generator with NO_2 scrubber. This new system provided equivalent NO concentrations (in ppm) to the previous setup, but with the benefit of a calibration by the National Physical Laboratory to confirm NO/NO_2 levels. A pressurisation and cooling step was added to the NO loading process to explore its effectiveness.

The pressurisation step, which increased the pressure surrounding the PDs to approximately 2 atmospheres, was implemented to increase the amount of gas that could be loaded into the PDs.

By increasing the pressure, the aim was to increase the solubility of NO in the perfluorocarbon phase. Cooling the sample to 4°C while pressurised was another strategy to increase the amount of NO that could dissolve in the PD emulsion. This leverages the inverse relationship between temperature and gas solubility in liquids [360]. In general, gases become more soluble in liquids as the temperature decreases. To validate whether the pressurisation and cooling steps affected the particle size distribution and concentration of 4.76% v/v PFP PD emulsions, measurements were taken using RPS before and after NO-loading (**Fig. 3.6**). PDs had a median diameter of 0.61 ± 0.02 µm before NO-loading and a median diameter of 0.63 ±

0.02 µm after NO-loading.

The particle concentration before the NO-loading step was 5.01 × 10^{10} ± 3.60 × 10^{8} particles/mL compared to 4.42 × 10^{10} ± 1.88 × 10^{9} particles/mL after loading. There was a statistically significant difference (p=0.013) in particle concentration after the NO-loading step. However, there was no statistically significant difference (p>0.05) in the median particle diameter after the NO-loading step. This suggests that the pressurised NO-loading step leads to a decrease in the overall concentration of the particles, but not a significant shift in terms of particle size.

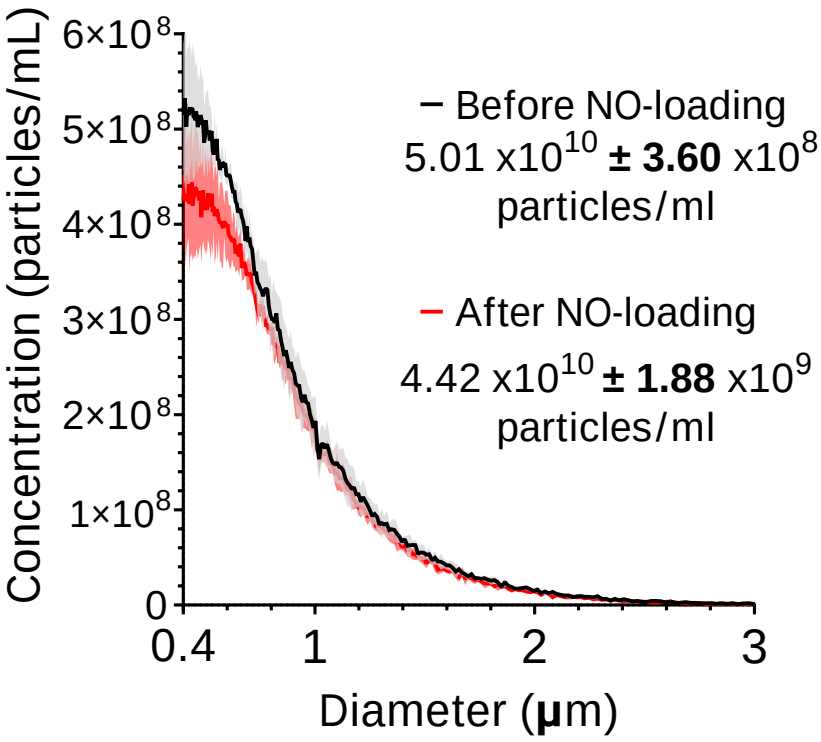

Figure 3.6: Mean concentration of PDs decreased after a pressurised NO-loading step. Mean concentrations ± S.D. are shown. Shaded error ± S.D.

To address the turbidity issues encountered in the preliminary Griess assay experiments (described in Section 3.3.1), modifications were made to the sample preparation method. The primary change was to centrifuge the samples after reaction with the Griess assay components to remove particles that could interfere with the light path of the spectrophotometer. The combined sample and Griess assay supernatant was then pipetted into a 96-well plate for measurement. To achieve effective separation of large PDs from the Griess reagents, samples were centrifuged at 11,000 g for 5 min.

This centrifugation step separated the larger droplet population from the rest of the sample. Mercado *et al.,* 2016 demonstrated that centrifugation of 230 × g for 1 min could isolate albumin-coated PFP droplets above a diameter of 2.5 µm [339]. Kramer *et al.* showed that perfluorooctylbromide (PFOB) droplets with a diameter of 268 nm could be separated using centrifugation of 12,000 × g for 2 min [361]. Although they were using this technique to remove excess liposomes from their sample, it shows that PDs can be removed from a sample by centrifugation. Three sample types were loaded with NO using the pressurised method and the Griess assay **(Fig. 3.7)**. Mean NO_x concentrations of 893.2 ± 25.7 µM, 1987 ± 40.4 µM, and 2301 ± 59.3 µM were calculated for NO-DPBS, NO-Lipids, and 4.76% v/v PFP NO-PDs, respectively.

Both NO-Lipids and NO-PDs had a statistically significant difference ($P<0.0001$) in NO_x concentration when compared to NO-DPBS. Although a statistically significant difference ($P<0.01$) in NO_x concentration was found between NO-Lipids and NO-PDs, both had a more than 2-fold increase compared to NO-DPBS. The increase in NO solubility in NO-Lipid samples could be attributed to the lipophilic nature of NO and the preferential partioning of NO into hydrophobic environments [362]. Additionally, during the NO-loading procedure, the removal of pressure within the syringe was difficult to control and rapid depressurisation could potentially affect the stability of the PDs.

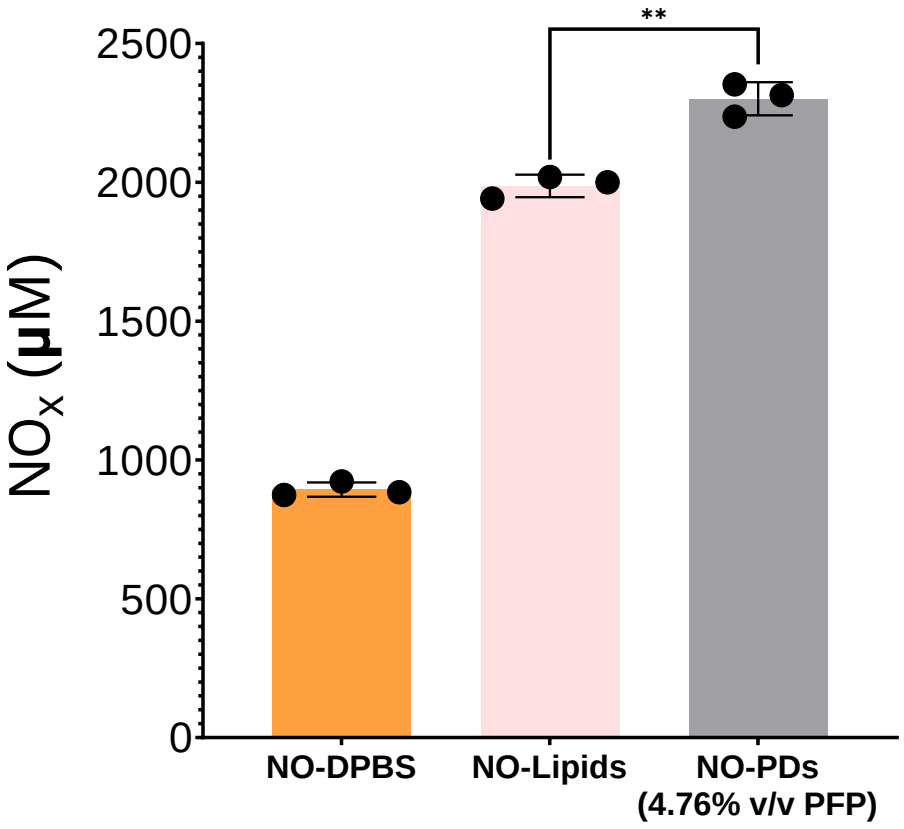

Figure 3.7: Griess assay measurements of NO_x concentrations in different formulations loaded with NO using a pressurised system. NO-PDs had significantly higher (P<0.01) NO_x concentrations than NO-Lipids. Both NO-Lipids and NO-PDs showed significantly higher NO_x concentrations compared to NO-DPBS (P<0.0001). (**, P<0.01). Mean of n=3 NO_x measurements, error bars ± S.D.

To further validate the results obtained from the Griess assay, a chemiluminescence method was used. An ozone-based CLD of an established manufacturer was utilised to measure the same sample types [351]. The Eco Medics CLD88 has been used with vanadium chloride as a method to measure NO_x concentrations previously [363, 364]. This method offers several advantages over the Griess assay, including higher sensitivity and the ability to directly measure NO [345].

The standard curve for chemiluminescence using the pressurised NO loading method is shown in **(Fig. 3.8)**. Notably, the highest sample voltage exceeded the highest standard voltage, which may compromise the accuracy of the measurements at higher concentrations. Beyond a certain NO-concentration, the detector may respond non-linearly, and it is important to keep sample voltage values within the known standard curve. This can be achieved through dilution or the use of smaller sample volumes injected into the CLD [365]. To address this issue and account for the sensitivity and intra-day variability of the chemiluminescence method, a calibration curve with triplicate peaks within the linear range of the detector was used for subsequent experiments [366].

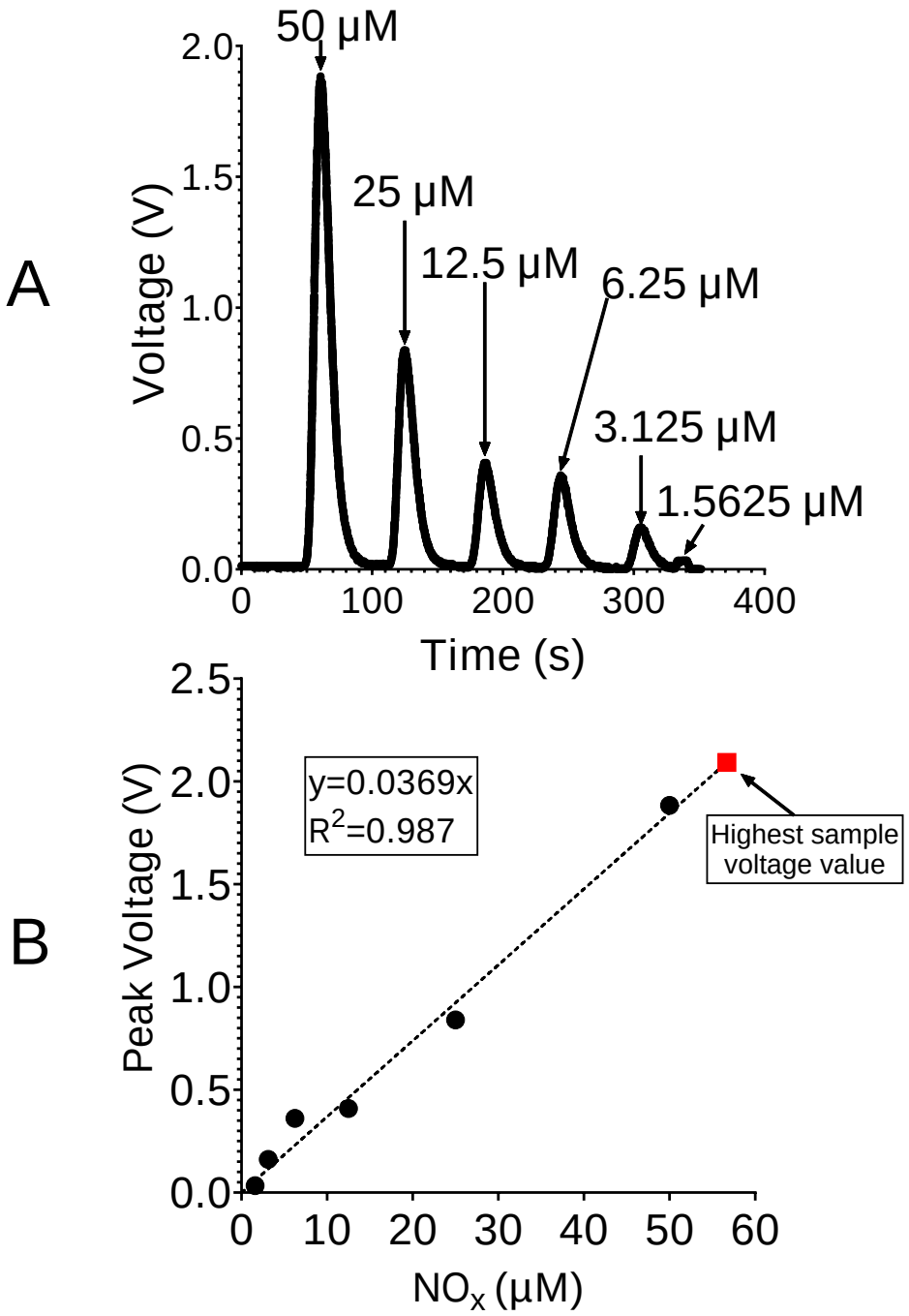

Figure 3.8: Chemiluminescence standard curve for NO quantification.

(A) Raw voltage data from chemiluminescence measurements of NO standards (black circles) and samples (red square). **(B)** Calibrated NO concentration standard curve with linear regression (dashed line). The highest sample voltage value, extrapolated using the regression line, is highlighted in red. Linear regression equation: $y = 0.0369x$, $R^2 = 0.987$. NO_x concentrations in samples were calculated using this standard curve.

Mean NO_x concentrations of 88.7 ± 8.3 µM, 485.4 ± 41.8 µM, 558.9 ± 5.8 µM were calculated for NO-DPBS, NO-Lipids, and 4.76% v/v PFP NO-PDs, respectively **(Fig. 3.9)**. Both NO-Lipids and NO-PDs had a statistically significant difference ($P<0.0001$) in NO_x concentration when compared to NO-DPBS. Although a statistically significant difference ($P<0.05$) in NO_x concentration was found between NO-Lipids and NO-PDs, both had more than 5-fold increase in NO_x concentration compared to NO-DPBS. These results align with the results from the Griess assay, showing an increase in NO-loading capacity of lipid-containing formulations compared to DPBS. The substantial increase in NO_x concentration in both NO-Lipids and NO-PDs compared to NO-DPBS suggests that these formulations may serve as effective NO delivery vehicles. The slight increase in NO_x concentration between NO-Lipids and NO-PDs suggests that the presence of PFP could provide additional NO-capacity, but further investigation will be needed.

Although the trend observed in the chemiluminescence analysis aligns with that of the Griess assay, the absolute values are approximately four-fold lower. This disparity could be attributed to several factors. The chemiluminescence method may have sensitivity issues, particularly at higher concentrations of NO resulting in a sample voltage that exceeded the standard curve range. As the Griess assay is an absorbance-based method there could be interference from other components in the

PD samples such as lipid-only structures, potentially leading to an overestimation of NO_x concentrations. However, NO_x concentrations were within therapeutically relevant levels of NO needed to have a biofilm-dispersing effect, which is typically in the nanomolar to micromolar range [284, 279]. Chemiluminescence was selected for further experiments due to its greater sensitivity and direct measurement of NO and NO_x, which would allow a more precise comparison of the difference in NO-capacity between NO-Lipids and NO-PDs.

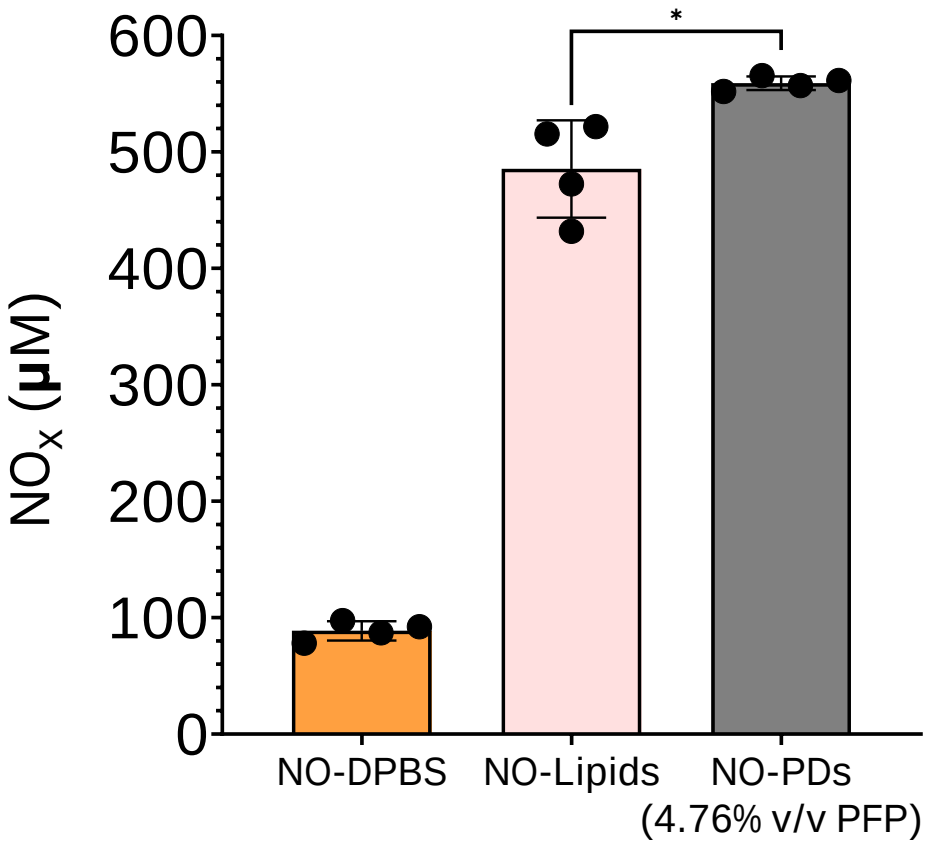

Figure 3.9: NO-Lipids and NO-PDs had significantly higher NO_x concentrations than NO-DPBS. Chemiluminescence data measuring NO_x in PD emulsions using a pressurised NO-loading system. Mean of n=3 NO_x measurements, error bars ± S.D. (*, $P<0.05$)

3.3.3 Modulation of PD size characteristics

Modulation of PD size characteristics presents several potential advantages for NO delivery. Larger droplets possess a higher surface area-to-volume ratio, which could theoretically slow the release of NO from the droplet [340]. For topical applications, larger droplets are less likely to enter the systemic circulation, mitigating the risk of vascular blockage that is present in intravenous situations [335]. The generation of PFP droplets larger than 1 µm is advantageous when a lower ADV threshold is desired to reduce off target thermal effects. Wu *et al.* showed that 0.52 µm diameter PFP droplets had an ADV of -3.4 MPa (peak rarefactional pressure), while PFP droplets with a smaller diameter of 0.24 µm had a higher ADV threshold of -3.9 MPa. The generation of larger droplets will allow for lower intensity pressures to be used [242].

To adjust the PD size, the PFP volumetric concentration was varied. This was similar to the study in *Chapter 2*, however the total volume of lipids and PFP was limited to 800 µL. This allowed for a wider range of PFP concentrations to be evaluated, as if the method described in *Chapter 2* was used, the volume of the sample would approach the top of the 1.5 mL sample tube at higher PFP concentrations, leading to a risk of sample loss.

An increase in PFC concentration was correlated with a decrease in particle concentration (**Fig. 3.10**). A corresponding increase in total PD volume was observed (**Fig. 3.11**). There was an increase in median particle diameter with increasing PFP concentration, observed in both number (particle count) and volume ($\mu m^3/mL$) distributions. For example, comparing 10% to 50% v/v PFP concentrations, the median diameter increased from 0.66 ± 0.04 µm to 2.69 ± 0.12 µm (by count) and from 1.62 ± 0.06 µm to 5.75 ± 0.06 µm (by volume).

These trends appear to be consistent with observations made by RPS measurement in *Chapter 2*. As PFP volumetric concentration increases, there is a corresponding decrease in lipid volumetric concentration in the sample. As these two parameters are inversely related, it is difficult to isolate their individual contributions to the observed increase in particle diameter. Observation of droplets left undisturbed showed gravitational settling, with a distinct, optically translucent upper phase forming after a short time period. However, without measuring the lipid concentration in this upper phase, it is not possible to determine whether excess lipids remain after droplet formation. It therefore remains uncertain which factor predominates in determining particle size characteristics. It is likely that both the Lipid:PFP volumetric ratio and the position of the initial Lipid:PFP interface relative to the sonicator tip collectively contribute to this trend.

Comparing 10% to 50% v/v PFP PDs, the total particle volume increased from $1.34 \times 10^{10} \pm 2.17$ x 10^9 µm^3/mL to $1.32 \times 10^{11} \pm 9.71 \times 10^9$ µm^3/mL. RPS can output size distributions in several formats, including by particle count and by particle volume. The size distribution by count allows for the number of particles to be shown across a range of sizes. However, the influence of larger volume particles can be under-represented as part of the whole sample volume. The size distribution by volume highlights the contribution of the larger particles in the sample [367]. A bimodal peak distribution was observed for PFP concentrations above 10%, suggesting the formation of a larger PD population.

The aperture used for these RPS measurements has a lower diameter limit of 0.4 µm. Due to the sharp peak at 0.4 µm in the 10% v/v PFP PDs, it is expected that a significant portion of this population is outside the detection range of the RPS.

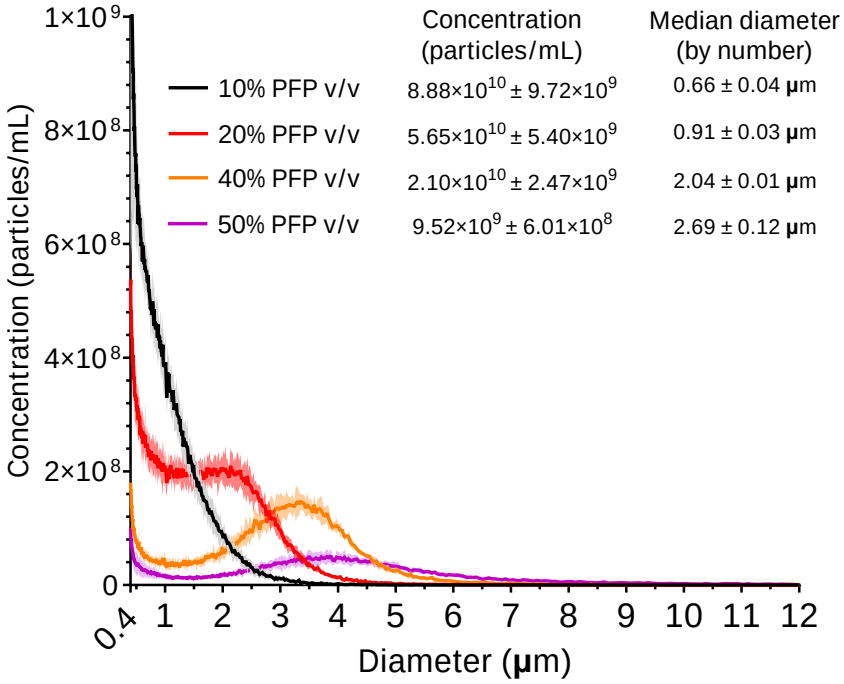

Figure 3.10: As PFP concentration increases, the particle concentration and median diameter (by number) increase. Size distribution by number of n = 3; shaded error is ± S.D. Mean values for particle concentration and median diameter ± S.D.

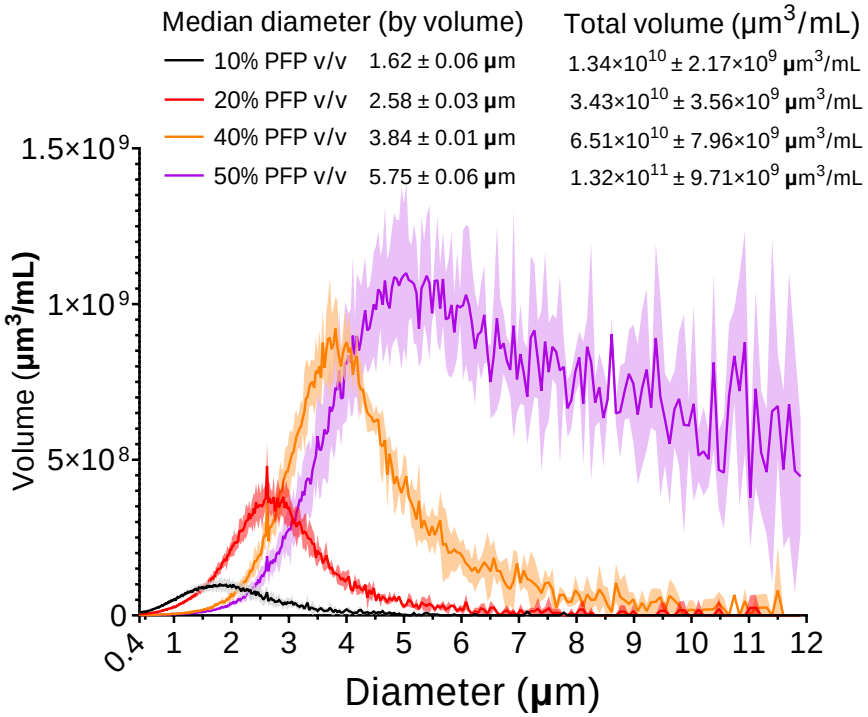

Figure 3.11: As PFP concentration increases, the particle volume and median diameter (by volume) increase. Size distribution by volume of n = 3; shaded error is ± S.D. Mean values for total particle volume and median diameter, ± S.D.

While higher PFP concentrations (40% and 50%) showed the generation of large diameter droplets, there was inconsistent mixing observed across batches, with some samples retaining a clear precursor droplet phase (**Fig. 3.12**). The corresponding increase in height of the PFP:Lipid interface at higher PFP concentrations results in a shorter distance between the interface and the sonicator tip, and may lead to a risk of phases failing to mix. The 20% PFP PDs had a larger droplet population than the 10% PFP PDs, and theoretically would have a slower diffusion rate of NO across the lipid shell. Additionally, the larger droplet population of the 20% PFP PDs would require a lower US peak negative pressure to vaporise [252]. As a result, 10% and 20% PFP concentrations were selected for further NO-loading experiments.

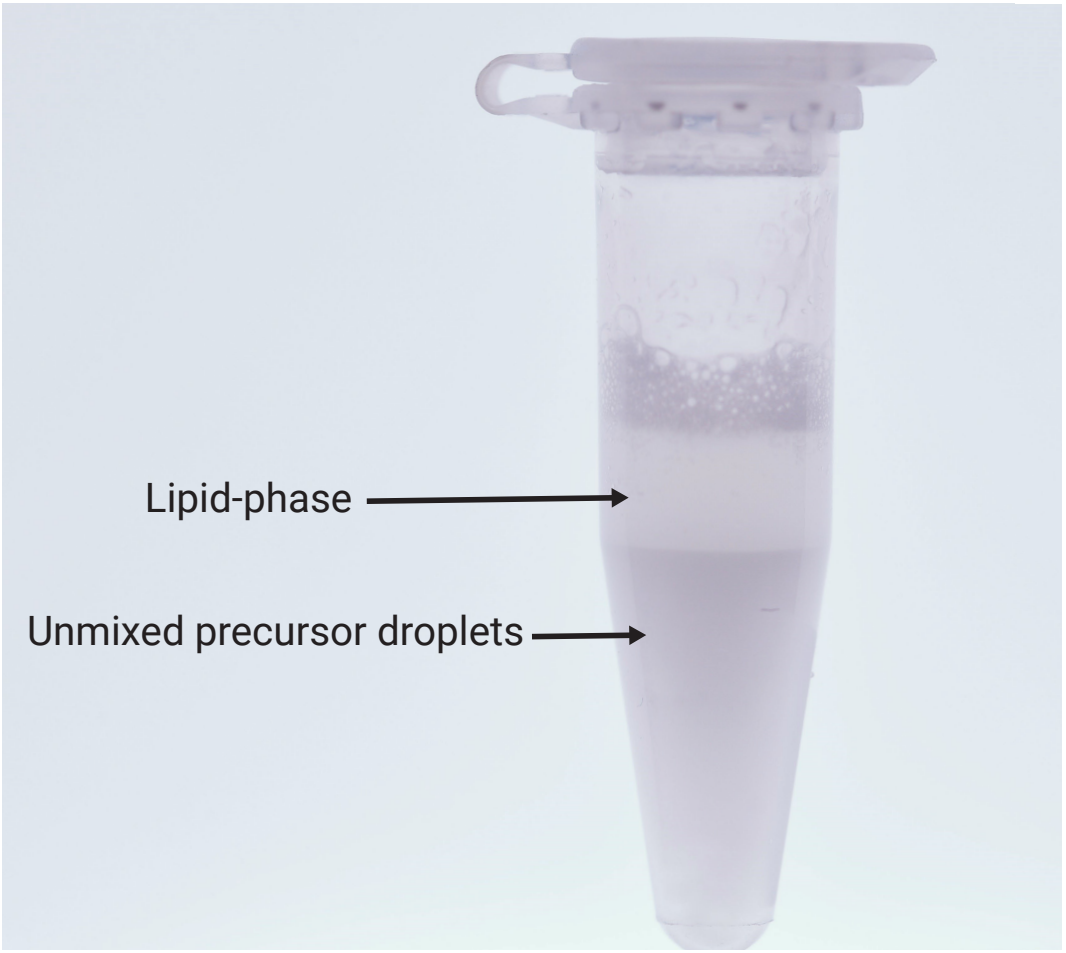

Figure 3.12: PFP precursor droplets in 40% and 50% v/v PFP samples occasionally fail to mix with the upper lipid phase. Representative photo of a 1.5 mL sample tube with phases of DSPC:PEG40S in DPBS (above) and precursor droplets (below).

3.3.4 Sparging Evaluation

Prior to conducting further NO-loading experiments, the sparging step was evaluated to reduce the sparging time and excess gas consumption. To achieve this, the deoxygenation rate was evaluated for 5 mL aliquots of DPBS using an OxyMini oxygen meter (World Precision Instruments, UK) to monitor dissolved oxygen levels. As shown in **(Fig. 3.13)**, 5 mL volumes of DPBS reached a measured oxygen saturation of 0% in less than 2 min. This rapid deoxygenation rate allowed for a significant reduction in the sparging time required for sample preparation.

As a result of this, the sparging time was reduced to 3 min compared to 30 min in the pressurised NO-loading method. To further decrease the presence of oxygen, an oxygen-free NO source (400 ppm NO in nitrogen) was used. These modifications serve to reduce the amount of oxygen available for reaction with NO, thereby improving the efficiency of NO loading and the potential for therapeutic application.

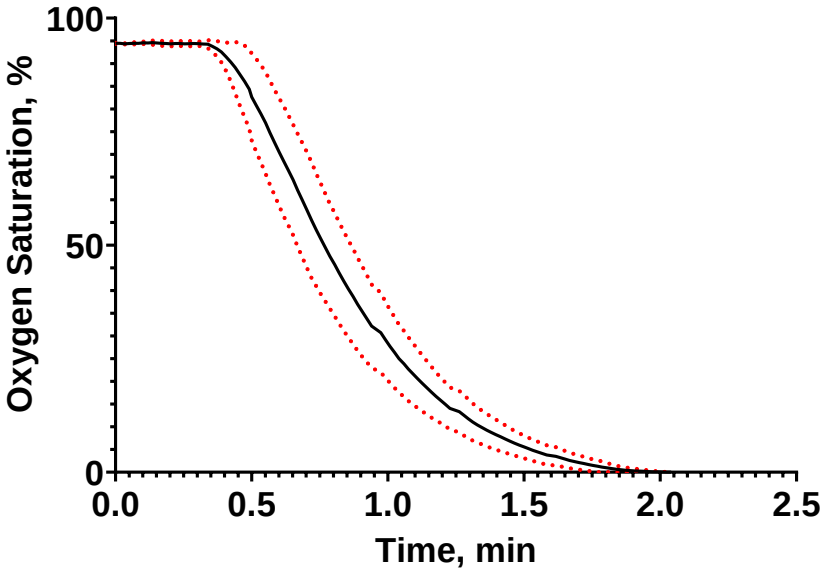

Figure 3.13: A 5 mL volume of DPBS could be reduced to 0% oxygen saturation in less than 120 s. Mean time to reach 0% oxygen saturation was 114.6 s. (n = 3, dotted red line represents ± S.D.)

3.3.5 Oxygen-free NO-loading of PDs

A calibration curve was measured on the experimental day to account for instrument variability, with $NaNO_2$ standards measured in triplicate over a narrower concentration range (0 - 12.5 µM) than previous experiments **(Fig. 3.14 A)**. The standards appeared to be within the linear response range of the CLD **(Fig. 3.14 B)**.

Mean NO_x concentrations of 4.31 ± 0.92 µM and 4.57 ± 0.34 µM were measured for the 10% v/v and 20% v/v PFP PD samples, respectively (**Fig. 3.15**). Unpaired t-tests between 20% v/v PFP NO-PDs and NO-Lipids showed a significant difference ($P<0.05$), while no significant difference was observed between 10% v/v PFP NO-PDs and NO-Lipids. Notably, there was no statistically significant difference between the 10% v/v and 20% v/v PFP PD samples. This could be attributed to the short NO-loading period combined with the theoretically slower gas diffusion rate of larger diameter droplets in the 20% v/v PFP PDs. This is based on the principle that droplet size affects the interfacial area and consequently the reaction kinetics at the droplet interface in emulsion systems, as demonstrated for rates of lipid oxidation [368]. Ten Klooster *et al.* showed that lipid oxidation rates for oil-in-water emulsion droplets increased with decreasing droplet diameter [368].

Although the shorter, oxygen-free NO-loading method resulted in NO_x concentrations substantially lower than the pressurised methods, the concentrations achieved (∼4.5 µM) remain biologically relevant. Dispersal of *P. aeruginosa* clinical isolates from cystic fibrosis (CF) sputum was observed at NO concentrations as low as 450 pM up to a NO concentration of 450 nM [369].

By minimising the amount of interaction between oxygen and NO, the degradation of NO could be reduced, reducing the possible disparity between measured NO_x concentration and the true concentration of NO. The NO_x concentrations achieved in both the 10% v/v and 20% v/v PFP PDs are in excess of 4 µM, allowing for flexibility when determining suitable PD concentrations for application to biofilm models. In the context of US-activation, the concentration of PDs is often in the range of 1×10^6 to 1×10^9 particles/mL [244, 253, 370]. These particle concentrations can be easily achieved with a dilution step prior to biofilm treatmentwhile maintaining a suitable final NO_x concentration.

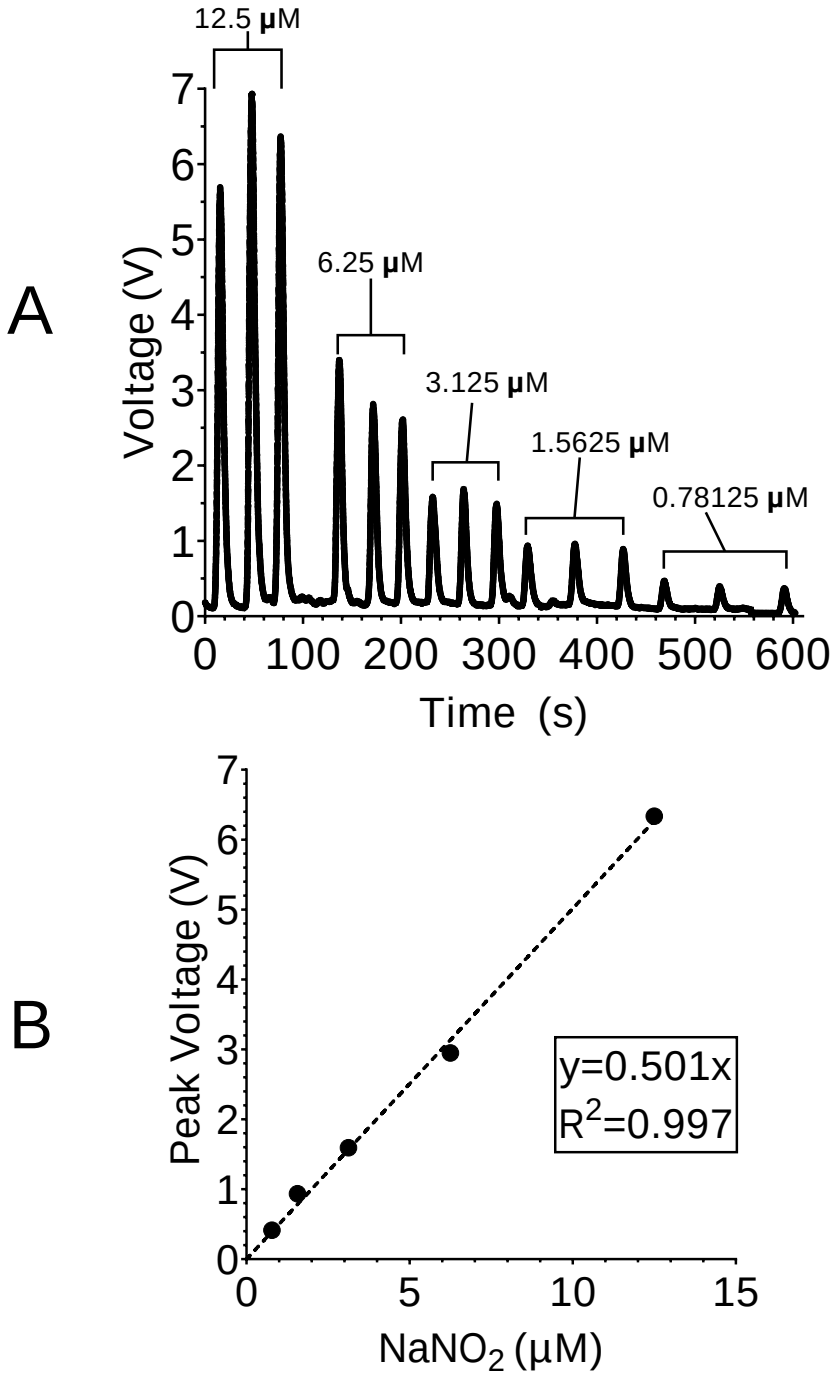

Figure 3.14: Chemiluminescence Standard Curve for NO Quantification.

(A) Raw voltage data from triplicate chemiluminescence measurements of NO standards (black circles). **(B)** Calibrated NO concentration standard curve with linear regression (dashed line). Linear regression equation: y = 0.501x, $R^2 = 0.997$.

NO_x concentrations in samples were calculated using this standard curve.

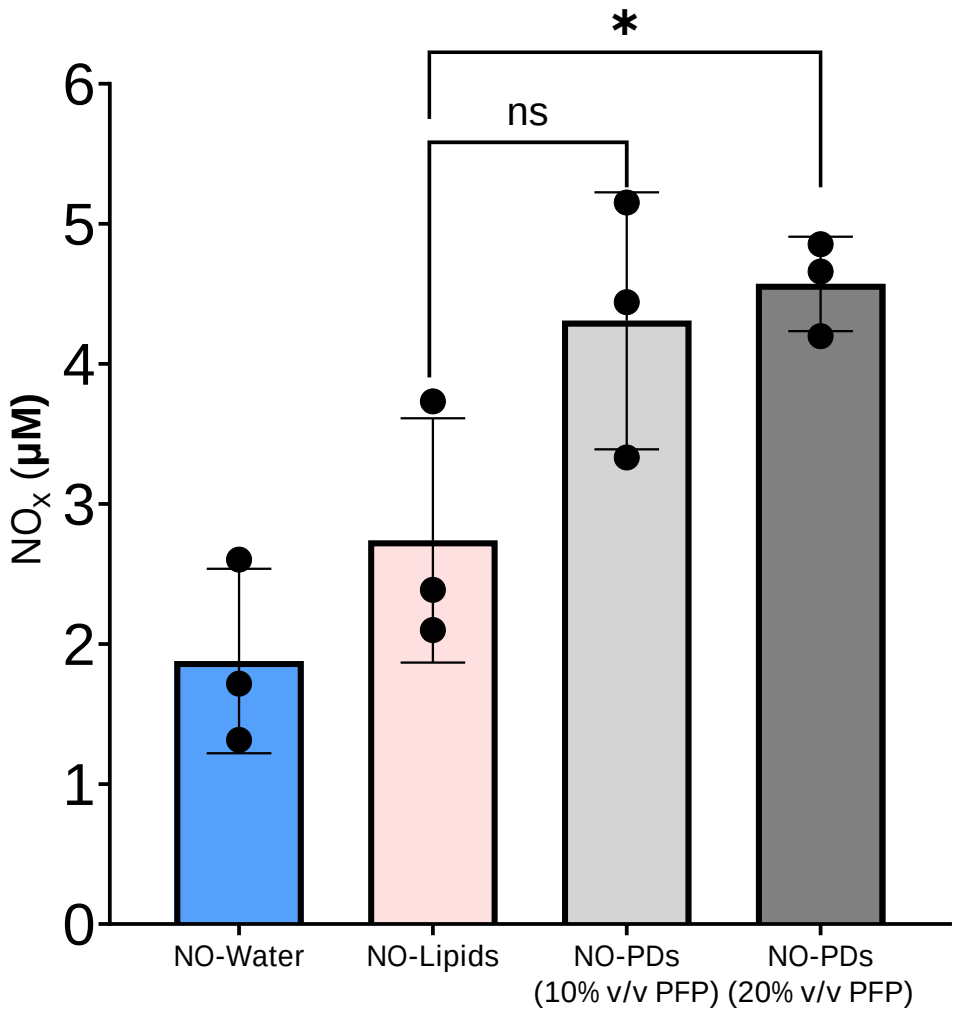

Figure 3.15: Chemiluminescence data measuring total NO_x in PD emulsions using a pressurised NO-loading system. 20% v/v PFP NO-PDs had significantly higher NO_x concentrations than NO-Lipids. Mean of n = 3 NO_x measurements, error bars ± S.D. (* = P<0.05, ns = not significant)

The sonication manufacturing method demonstrates sufficient production volume for practical applications. Based on a target particle concentration of 1×10^9 particles/mL), the stock concentration reported in (**Fig. 3.11**, 5.65×10^{10} particles/mL) for 20% PFP PDs would require a dilution of approximately 56 x. An 800 µL volume of PDs would dilute to an treatment volume of approx 45 mL. Given a typical treatment volume of 1 mL for a 3.5 cm^2 biofilm area [287], there is sufficient particle concentration and diluted treatment volume to apply to a large biofilm area. Additionally, larger sonication vessels could readily be switched to and the sonication process couldbe developed for a significantly larger production volume. Furthermore, the manufacturing process could be adapted to larger vessels and optimised for increased production volumes.

3.4 Conclusion

In this *Chapter*, the loading of NO into PDs was characterised in terms of the concentration of NO_x as well as the PD size characteristics. Preliminary Griess assay experiments highlighted problems with turbidity and foaming in PD samples, which affected absorbance readings. To address these issues, centrifugation was incorporated into the subsequent NO-loading methods. An NO-loading method incorporating a NO_x generator was developed, along with pressurisation and cooling steps

explored as a means to increase the NO-dissolving capacity. This method did not significantly alter the size characteristics of PDs but resulted in a decrease in overall particle concentration. Both Griess assay and chemiluminescence methods showed increased NO-loading capacity in lipid-containing formulations (NO-Lipids and NO-PDs) compared to NO-DPBS. While chemiluminescence measurements showed lower absolute NO_x concentrations than the Griess assay, they followed similar trends. Subsequently, the effect of increasing PFP volumetric concentration in PD formulations was assessed using RPS, and led to a decrease in particle concentration, and increased median particle diameter and total particle volume. A distinct, larger population of droplets was observed at higher concentrations of PFP.

Both 10% and 20% PFP concentrations were selected for further NO-loading experiments. Subsequently, an oxygen-free NO-loading method using 400 ppm NO in nitrogen and a shortened sparging time of 3 min was developed. Although this method resulted in lower NO concentrations compared to the pressurised method, the concentrations achieved ($\sim$ 4.5 µM) remained within biologically relevant ranges for biofilm dispersal, when taking treatment dilution factors in account.

Notably, 20% v/v PFP NO-PDs showed significantly higher NO_x concentrations compared to NO-Lipids, while 10% v/v PFP NO-PDs did not. There was no significant difference observed in NO_x concentration between 10% and 20% v/v PFP NO-PDs. The oxygen-free method may provide a more accurate measure of the true NO content by minimising the degradation of NO due to oxygen interaction.

The 20% v/v PFP PD sample was selected for further development to evaluate acoustic droplet vaporisation parameters and antibiofilm effects, as described in *Chapter 4*. Firstly, there was a significant difference in NO_x concentration between the 20% v/v PFP sample and the NO-lipids, indicating a higher potential for NO delivery. Secondly, the larger droplet size of this sample is expected to allow for slower NO diffusion out of the droplets, potentially leading to a slower release profile. Finally, an increased droplet size will likely have a lower ADV threshold.

Chapter 4

Evaluation of Ultrasound-Responsive Nitric Oxide-Loaded Perfluorocarbon Droplets for Chronic Wound Biofilm Treatment

4.1 Introduction

CW biofilms present a significant challenge in wound healing, often contributing to delayed healing and increased healthcare costs [371, 372].

Although CW biofilms comprise multiple bacterial species, evidence suggests that these bacteria often exist as spatially distinct single-species aggregates within the wound environment [373]. *Pseudomonas aeruginosa* is one of the most common bacterial species found in chronic wounds: a study by Gjødsbøl *et al.* [374] found that *P. aeruginosa* is present in 52.2% of chronic venous leg ulcers, with its prevalence strongly associated with larger wound sizes. A more recent study by Wu *et al.* [375] identified *P. aeruginosa* as the most prevalent Gram-negative species in DFUs, present in 19.4% of cases.

Several factors complicate the treatment of CW biofilms. The EPS matrix acts as a physical barrier, restricting the penetration of antimicrobial agents. This effect, in combination with the compromised vasculature present in CWs, results in sub-therapeutic antibiotic concentrations reaching the site of infection [12]. A range of approaches has been explored to tackle these challenges. One approach of particular significance focuses on NO, which functions as an ubiquitous signaling molecule known to induce biofilm dispersal in various bacterial species. In *P. aeruginosa*, NO

produces a decrease in intracellular cyclic di-GMP levels [279].

Although the use of NO as a biofilm dispersal agent has shown promise in various studies, its clinical application has been limited due to its short half-life and high reactivity. Another promising strategy in the treatment of CW biofilms is US-mediated biofilm disruption therapy. In particular, the combination of US with US-responsive nuclei such as MBs, has been shown to directly impact on bacterial cells and physically disrupt the biofilm matrix [228].

Several key studies have demonstrated the efficacy of US-mediated approaches, especially in terms of potentiating the effect of antibiotics. He *et al.* [26] showed that the use of US-activated (80 kHz, 1.0 W/cm^2, 50% duty cycle, 10 min duration) SonoVue®MBs created distinct pores within *S. epidermidis* biofilms. Furthermore, the combination of US + MBs enhanced the effect of vancomycin, significantly reducing the biofilm density and viability of *S. epidermidis* cells recovered post-treatment. Similarly, Dong *et al.* [229] demonstrated an enhanced bactericidal effect against catheter-associated biofilms using US-activated (300 kHz, 0.5 W/cm^2, 50% duty cycle, 5 min duration) MBs with vancomycin, compared to US + vancomycin.

Ronan *et al.* demonstrated that Definity® MBs combined with 0.5 MHz US (1.1 MPa peak negative pressure, 16-cycle tone burst, 1 kHz PRF) for 5 minutes resulted in distinct structural changes in *P. aeruginosa* PAO1 biofilms [230]. Exposure to

US + MBs led to the formation of substantial craters (5-20 µm diameter) in the biofilm structure and, when combined with gentamicin, significantly reduced biofilm metabolic activity compared to either treatment alone.

Recent studies combining NO with US-responsive carriers have shown particular promise. LuTheryn *et al.* assessed the antibiofilm effect of NO-core MBs (DSPC:PEG40S shell) stimulated by US (0.9 MHz, 20 % duty cycle, 500 Hz PRF, 40 s duration) in combination with sub-inhibitory (4 µg/µL) levels of gentamicin. NO-loaded MBs co-administered with gentamicin achieved up to a 99.9% reduction in both surface area and cell viability of *P. aeruginosa* biofilms [287]. The efficacy of sub-inhibitory concentrations of gentamicin was shown to be significantly increased. Importantly, stimulation of room-air core MBs increased the reduction in biomass approximately 8-fold (81.3% reduction) when compared to a non-US control, with NO-core MBs further enhancing this effect (99.9% reduction).

Perfluorocarbon droplets represent a potential advance over MBs for antibiofilm therapy. Recent studies have demonstrated the potential of US-activated PDs for biofilm treatment, although this remains an emerging area of research [228]. The combination of PDs with US and antimicrobials has shown particular promise. Durham *et al.* used [30] octafluoropropane-core, lipid-shelled PDs combined with tobramycin and rhamnolipids as antibiofilm modality against *S. aureus* biofilms.

When stimulated with US (1 MHz, 1.2 MPa peak negative pressure, 5 kHz PRF, 40-cycle burst), they recorded a 94% reduction in viable cells accompanied by a significant decrease in biofilm biomass. Similar synergistic effects have been observed in other studies. For example, Xin *et al.* demonstrated the efficacy of PFP-core PDs against *P. aeruginosa* biofilms using US (1.5 W/cm^2, 50% duty cycle, 1 MHz, 10 min) combined with the antibiotic meropenem, reporting a significant reduction in bacterial viability and biofilm biomass. Dang *et al.* [376] used PFP-core PDs (1 MHz, 3 W/cm^2, 50% duty cycle, 10 min duration) combined with 2% chlorhexidine on an *Enterococcus faecalis* dental biofilm model. They reported that US + PDs reduced cell viability (63.1%), and the addition of 2% chlorhexidine with US + PDs further reduced cell viability (96.2%).

Despite these promising research developments, significant gaps still exist in current research. While studies have demonstrated the efficacy of US-activated PDs against biofilms, many lack characterisation of ADV parameters. Furthermore, to the best of the author's knowledge, no studies have investigated the combination of NO-loaded PDs with US activation, specifically in the context of chronic wound biofilms. It is hypothesised that the combination of US-activated PDs with NO will have an additive effect, with NO-mediated dispersal enhanced by the physical disruption of vaporised PDs.

This chapter addresses these research gaps through two primary research objectives. Firstly, it aims to determine the US parameters required to achieve reliable ADV of PDs. This establishes the foundation for subsequent biofilm treatment experiments by defining specific conditions necessary for PD activation. Second, the chapter evaluates the effects of these PDs on a CW biofilm model under four distinct experimental conditions: unloaded PDs without US stimulation, NO-loaded PDs without US stimulation, unloaded PDs with US stimulation, and NO-loaded PDs with US stimulation. This approach enables evaluation of both the physical effects of US-activated PDs and the biochemical effects of NO-delivery by PDs, individually and in combination, on *P. aeruginosa* CW biofilm model.

4.2 Materials and Methods

This section describes the experimental procedures used to evaluate the effect of NO-loaded perfluorocarbon droplets in combination with US on a wound biofilm model. The characterisation of the US stimulation parameters, treatment conditions, processing of the samples, and quantification methods are described below.

4.2.1 Characterisation of Acoustic Droplet Vaporisation

Using an experimental setup from Wu *et al.* [242], simultaneous optical and acoustic measurements were made of PDs **(Fig. 4.1)**. The experimental setup and methodology are summarised below [242].

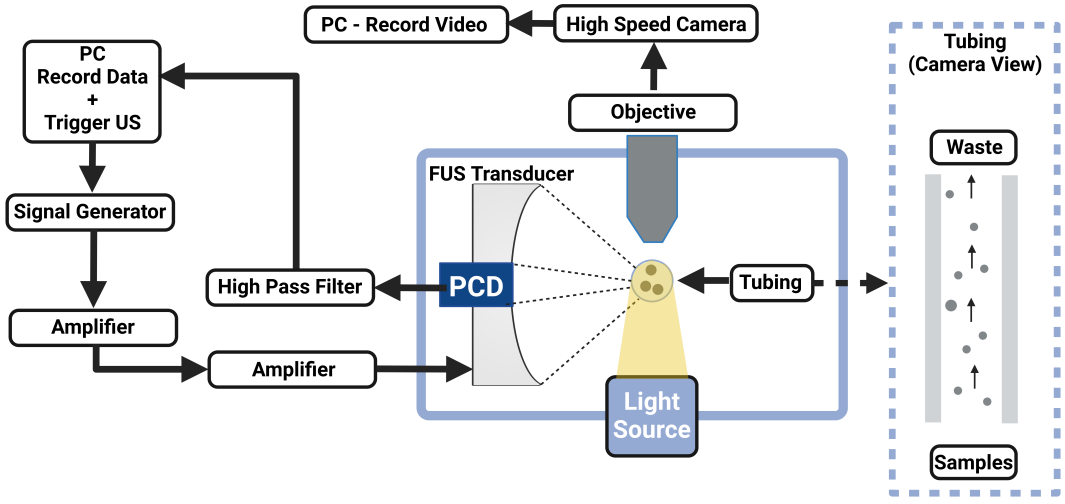

Figure 4.1: Setup for simultaneous optical and acoustic measurements. FUS = focused ultrasound; PCD = passive cavitation detector.
Adapted from Wu *et al.* [242]

A single-element spherically focused ultrasound (FUS) transducer (H107, Sonic Concepts, Bothell, WA, USA) with a center frequency of 0.5 MHz was used to stimulate the PDs. The transducer had an aperture of 64 mm and a geometric focus of 63.2 mm. It was driven by a programmable arbitrary waveform generator (33220 A, Agilent, Santa Clara, CA, USA). The signal was amplified using a 1000 W

radio-frequency power amplifier transducer via a 50 Ω matching network. PDs were contained in a polyethylene tube positioned at the focus of the FUS transducer. The transducer and tube were placed within a tank of degassed and de-ionised water. A low-pulsatility peristaltic pump (Minipulse Evolution, Gilson, Middleton, WI, USA) was used to convey the PD suspension through the polyethylene tube (180 µm diameter) at a rate of 0.3 mL/min (4.42 mm/s mean velocity). Flow was stopped for 2 min prior to US stimulation.

The PDs were excited by a single 10,000-cycle pulse with different peak negative pressures. The peak negative pressure of the FUS transducer was increased in increments of 260 kPa, from 0.4 to 2.48 MPa. An objective lens with a numerical aperture of 0.45 and a working distance of 8.2-6.9 mm (S Plan Fluor, Nikon Instruments Europe BV, Netherlands) was focused on the mid-plane of the tube and coupled to a high-speed camera (HPV-X2, Shimadzu, Tokyo, Japan). The camera was triggered using the output from the waveform generator. After a delay of 47 µs to allow for propagation of the ultrasound pulse to the focal region, the camera recorded 256 frames at 5 million frames per second (Mfps), with an exposure time of 200 ns per frame providing a temporal resolution of 0.2 µs. Digital images of 400 × 250 pixels were recorded; the image resolution was 0.34 µm/pixel, determined using a haemocytometer as a reference standard (Bright-Line, Hausser Scientific,

Horsham, PA, USA). Illumination in this setup was provided by a high-intensity light source (SOLIS-1 C, Solis High-Power LEDs, Thorlabs LTD. Ely, UK)

To capture acoustic emissions simultaneously with high-speed imaging, a single element ultrasound transducer of 7.5 MHz center frequency, an element diameter of 12.5 mm, and a focal length 75 mm (V320 Panametrics, Olympus, Waltham, MA, USA) was used as a PCD. This was inserted through the cutout in the FUS transducer to enable co-alignment of both transducers' foci. The lateral and axial full width half-amplitude dimensions of the focal volume for this transducer were 1.2 mm and 37.6 mm, respectively. The nominal bandwidth was 50%.

The acquired PCD signal was filtered using a 1.8 MHz high-pass filter (EF509, ThorLabs Inc., USA) to reject strong reflections from the tube at the fundamental FUS frequency and lower harmonics caused by non-linear propagation. After amplification (125 $\times$) with a low-noise amplifier (SR445 A, Stanford Research Systems, Sunnyvale, CA, USA), the PCD signal was recorded with a USB oscilloscope (Handyscope HS6, TiePie, Netherlands) at a sampling rate of 50 MHz (an integer multiple of the fundamental system drive frequency). Time-domain signals were converted to the frequency domain using Welch's method multiplied by a 10 kHz Hanning window, and digitally filtered above 1.8 MHz to remove fundamental frequency reflections. Power spectral density (PSD) was calculated using MATLAB

(R2024b, MathWorks, USA), and corrected for the system gain (125×), allowing comparison between sample types across the frequency range of 1.8-10 MHz. Total acoustic energy was computed by integrating the power spectral density (PSD) across this frequency range for each peak negative pressure tested. All experiments were performed at 39 °C unless stated otherwise. Data are presented as mean ± S.D. from three independent samples at each acoustic pressure level investigated.

The beam profile and focal pressure of the FUS transducer were measured using a needle hydrophone (0.2 mm, NH0200, Precision Acoustics , UK).

The lateral full-width at half maximum (FWHM) dimension was 3.9 mm when driven at 0.5 MHz. The focal pressure was calibrated for a peak negative pressure range of 0.4 to 3.09 MPa **(Fig. 4.2)**.

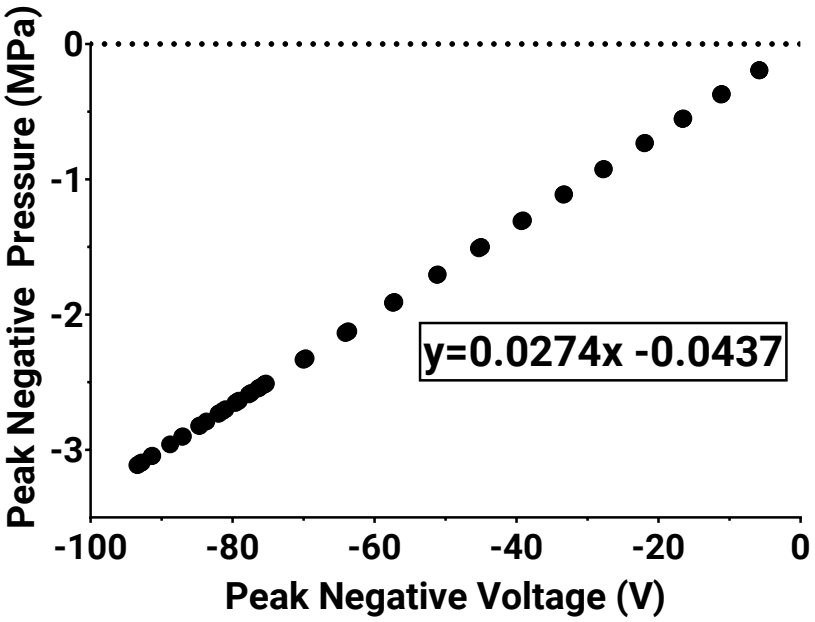

Figure 4.2: Pressure calibration curve for H107 FUS transducer driven at 0.5 MHz. The peak negative pressure was characterised from 0.4 to 3.09 MPa in water at the geometric focus (63.2 mm). Input voltage (peak negative) to the H107 is plotted against the measured peak negative pressure.

4.2.2 Biofilm Growth and Preparation

To model the complex environment of chronic wounds, a specialised wound constituent medium (WCM) was used, based on the Lubbock chronic wound pathogenic biofilm model [377] **(Fig. 4.3)**. WCM comprises Bolton broth (BB), laked horse blood (LHB), and plasma, and serves to emulate the physiological conditions of chronic wounds. BB is primarily composed of degraded animal tissues and resembles the nutrients present in a chronic wound bed [377]. LHB and plasma mimic the presence of lysed red blood cells and serum, which are often found in chronic wounds due to host tissue damage [378]. Fibronectin-coated culture dishes were used to facilitate initial bacterial attachment. Fibronectin is a key protein present in the wound bed that facilitates bacterial adhesion and biofilm formation [379, 102]. *P. aeruginosa* PAO1 is one of the most frequently studied strains of the bacterium and was isolated from a wound in 1954 (Melbourne, Australia) [380].

P. aeruginosa strain PAO1 was therefore used in the present study. WCM was prepared by combining 1X Bolton Broth (67454, Merck, Germany), 5% Laked Horse Blood (SR0048C, ThermoFisher, UK), and 20% plasma (P4639, Merck, Germany). An overnight culture of PAO1 was diluted in WCM to an OD_{700} of 0.1 (approximately 1×10^8 CFU/mL). 400 µL of this inoculum was added to the center of a fibronectin-coated (50 µg/mL, F1141) Ibidi® µ-Dish (35-mm high, ibiTreat) and

incubated at 37 °C for a total of 48 h. After 24 h, 1.6 mL of fresh WCM was gently added to each dish. DSPC:PEG40S 20% v/v PFP droplets were prepared as described in *Chapter 3*.

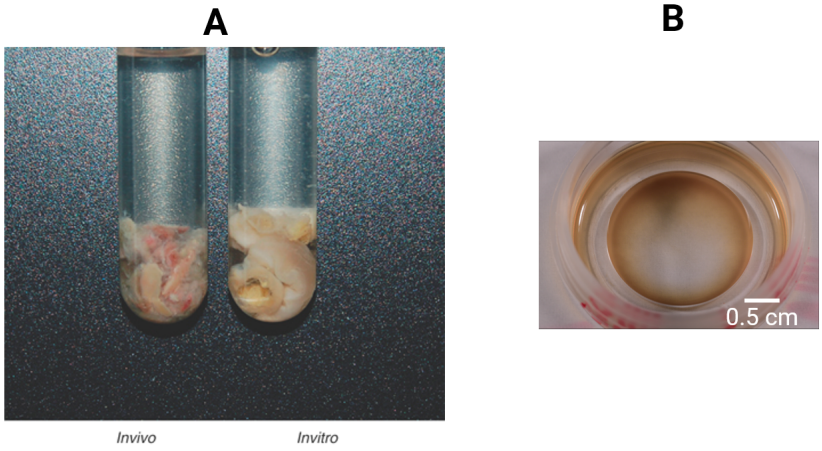

Figure 4.3: (A) Image showing an *in-vivo* example of a chronic wound biofilm on the left and the *in-vitro* Lubbock chronic wound biofilm on the right, highlighting the similarity in texture and consistency between the biofilms **(B)** Image of *P. aeruginosa* biofilms grown in an Ibidi® culture dish in WCM (BB, 5% LHB, 20% plasma) Adapted from Sun *et al.* [377].

4.2.3 Treatment Conditions and Application

Prior to treatment, biofilm samples were prepared by gently rinsing four times with 1 mL sterile DPBS and staining with fluorescent dyes. Pre-treatment microscopy images were acquired at 10 × magnification. The biofilms were then subjected to one of six treatment conditions: DPBS control (DPBS), DPBS with US control (US-Only), unloaded 20% PFP droplets (ULPD), NO-loaded 20% PFP droplets (NOPD), unloaded 20% PFP droplets with US stimulation (ULPD-US), or NO-loaded 20% PFP droplets with US stimulation (NOPD-US).

This study was conducted across three separate experimental days, with each day representing an independent biological replicate. For each experimental day, a fresh bacterial stock culture was prepared, from which six identical biofilm cultures were established as technical replicates. Each of these six biofilms was then assigned to one of the six treatment conditions, ensuring that all treatment conditions were tested once per experimental day.

All treatments were conducted at 39 °C for a total duration of 10 minutes. This was was the apparent temperature threshold of 39 °C required to achieve ADV, and this is discussed in *Section 4.3.1*.

Each treatment was administered in a 1 mL volume, with a PD concentration of 1×10^9 particles/mL. For treatments involving US, the following parameters were used: 0.5 MHz, 39 °C with a peak negative pressure of -2.48 MPa, 100 cycles, 1 Hz PRF, for a total of 60 pulses (60 s treatment time).

This conservative PRF and total duration were selected as a conservative baseline condition. Similar studies stimulating PDs with US on biofilm models typically use US durations of several minutes with unspecified pulse durations [381, 376, 300].

Ibidi® dishes containing the biofilms were placed on a coupling cone, positioning the biofilm within the geometric focus of the H107 transducer **(Fig. 4.4)**. The cone was filled with degassed ddH_2O at 39 °C prior to US stimulation.

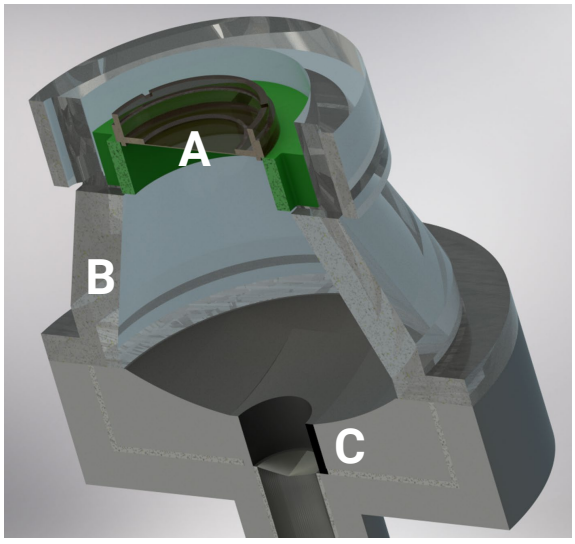

Figure 4.4: 3D-slice representation of the biofilm US stimulation apparatus. **(A)** Ibidi® culture dish containing the biofilm placed at the geometric focus of the H107 tranducer. **(B)** Custom coupling cone (filled with water).
(C) H107 single-element transducer.

For each experimental condition, the treatment protocol consisted of adding 1 mL of the designated treatment formulation to each biofilm culture. Non-US stimulated treatment conditions were incubated at 39 °C for a total duration of 10 minutes. For US-stimulated treatments conditions, the protocol involved an initial incubation at 39 °C for 9 minutes, followed by a 60-second US exposure at a temperature of 39 °C.

A hot plate stirrer (SHP-200, Cole-Parmer, USA) was used to maintain the temperature of the Ibidi® dishes at 39 °C. A separate hot plate was used to heat vacuum-degassed water to 39 °C, which was used to fill the coupling cone.

Following treatment, each sample underwent a series of standardised post-treatment procedures. First, each sample was gently rinsed with 4 × 1 mL sterile DPBS to remove non-adherent cells. The original treatment solution along with all rinse volumes (approximately 5 mL total) were collected for subsequent colony forming unit (CFU) analysis. For CFU quantification, five technical replicates (10 µL aliquots) of each dilution were performed across all three experimental days. Post-treatment microscopy imaging was then conducted at both 10 × and 4 × magnification to assess changes in biofilm structure and morphology. After imaging, samples were immediately stained with safranin to quantify the remaining biofilm biomass. The safranin quantification was performed on the same samples used for

imaging, resulting in three biological replicates per treatment condition (one from each experimental day).

4.2.4 Microscopy and Image Analysis

In addition to safranin staining and CFU counting, which provided quantitative data on biofilm biomass and cell viability, confocal laser scanning microscopy (CLSM) was employed to qualitatively assess the spatial effects of US-mediated NO-loaded PD treatment on biofilm morphology.

Fluorescent Staining

Three fluorescent dyes were used to visualise different biofilm components: SYTO9 is a green fluorescent nucleic acid stain that penetrates bacterial membranes, and is often used to count individual cells [382, 383]. Propidium iodide (PI) penetrates cells with compromised membrane integrity and is used as an indicator of dead or membrane-damaged cells [383]. When bound to DNA, both SYTO9 and PI fluorescence is greatly enhanced [384]. As the affinity of PI to DNA is higher than SYTO9, PI prefentially displaces SYTO9 [385]. These stains are often used in conjunction to evaluate the ratio of live to dead cells. Furthermore, SYTO9 can stain present within the biofilm matrix [386]. Concanavalin A (ConA) is a lectin that binds to -mannopyranosyl and -glucopyranosyl residues present in the EPS

matrix of biofilms. When conjugated with a fluorescent dye such as Alexa Fluor 647, ConA can be used to visualise the biofilm EPS matrix, allowing for analysis of changes in biofilm morphology [387, 388]. In combination, these fluorescent stains allow for visualisation of the spatial distribution between bacterial cells and the biofilm matrix.

Prior to staining, biofilms were gently rinsed four times with 1 mL sterile DPBS (14190144, Gibco, ThermoFisher, UK). The biofilms were then stained with a mixture containing 2.5 µM SYTO9 (S34854, Invitrogen, ThermoFisher, UK), 9 µM propidium iodide (P3566, Invitrogen, ThermoFisher, UK), and 96 nM Concanavalin A (Alexa Fluor 647 conjugate, C21421, Invitrogen, ThermoFisher, UK). A 1 mL volume of this stain mixture was added to each culture dish and incubated at room temperature for 30 minutes, protected from light. Following incubation, excess stain was removed by rinsing four times with 1 mL of sterile DPBS.

Confocal Laser Scanning Microscopy

CLSM offers significant advantages over widefield fluorescence microscopy, particularly in terms of axial resolution [389].

A distinct advantage of CLSM is the ability to block out-of-focus light, which reduces blur caused by light from planes above and below the focal plane. This is especially useful for thicker samples, where out-of-focus light can contribute a

'blurry haze' to each image plane and this reduces contrast [389]. CLSM provides a theoretical improvement in axial resolution of up to 1.31-fold over widefield [390].

Biofilm imaging was performed using a confocal laser scanning microscope (Nikon AX R + Ti2-E inverted microscope, Nikon Instruments Europe BV, Netherlands) with two separate imaging protocols **(Fig. 4.5)**. The first protocol involved higher-resolution imaging using a 10 × magnification objective (MRD70170, Nikon Instruments Europe BV, Netherlands), capturing a 4 × 4 tile scan with z-stack **(Fig. 4.5 A)**. This was performed before and after each treatment condition. The imaging area covered 4.192 mm × 4.192 mm (1048 µm × 1048 µm per tile), with a z-stack consisting of 25 slices over a 128.19 µm depth (5.148 µm per slice). Images were acquired at a resolution of 2048 × 2048 pixels, resulting in a pixel size of 0.522 µm. This protocol allowed for the visualisation of individual bacterial aggregates. The second protocol involved a lower-resolution overview using a 4 × magnification objective (MRD70040, Nikon Instruments Europe BV, Netherlands) to capture a 2 × 2 tile scan **(Fig. 4.5 B)**. The imaging area covered 8.192 mm × 8.192 mm (4096 µm × 4096 µm per tile). This was performed only after each treatment to minimise photobleaching. Images were acquired at a resolution of 1024 × 1024 pixels, resulting in a pixel size of 4 µm. This protocol allowed for the visualisation of larger scale changes to the biofilm morphology.

For all imaging, SYTO9 was excited using a 488 nm laser at 2.2% power with a gain of 25, PI with a 561 nm laser at 7.0% power and a gain of 20, and ConA with a 640 nm laser at 2.0% power and a gain of 25. The pinhole was set to 1.0 Airy Unit, and the Galvano mirror scanning method was employed.

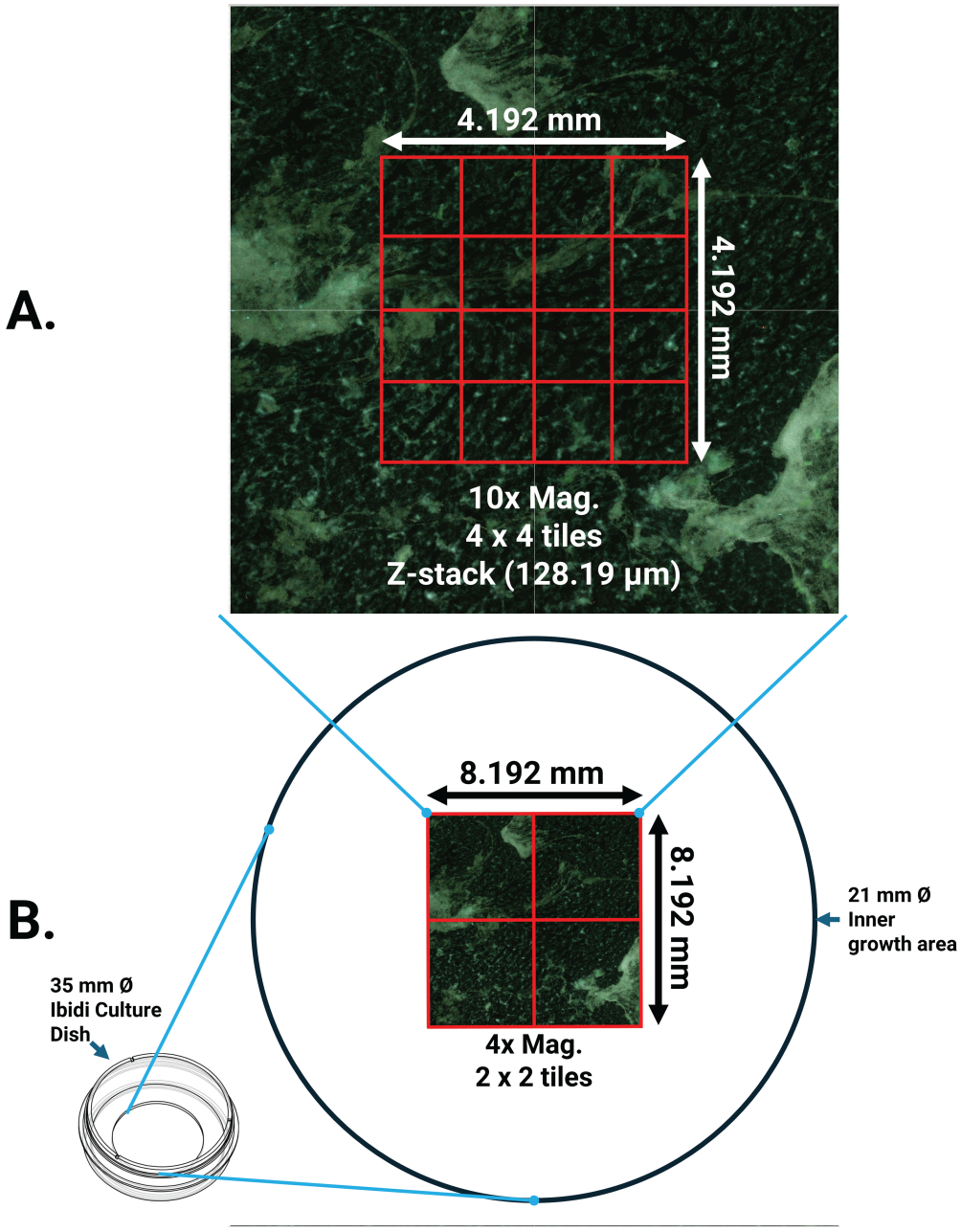

Figure 4.5: Multi-scale imaging of biofilm structure.

(A) Higher-resolution imaging: 10 × objective tile scan of a 4.192 mm × 4.192 mm region. Individual red squares represent 1048 µm × 1048 µm fields of view. This scan includes a z-stack acquisition, capturing 25 optical sections over a total depth of 128.19 µm.

(B) Lower-resolution overview: 4 × objective tile scan covering an 8.192 mm × 8.192 mm area. Each red square delineates a 4096 µm × 4096 µm field of view. Representative 4 × objective tile scan image to illustrate scale differences between 4 × objective and 10 × magnification

Image Processing and Analysis

10 × magnification z-stack images were processed using NIS-Elements Ar (Nikon Instruments Europe BV, Netherlands) using a manual thresholding method. Due to the low fluorescence intensity levels observed in post-treatment images, a manual threshold method was used to calculate biovolume. **(Fig. 4.6)** highlights the differences between Otsu automatic thresholding and manual thresholding on a representative post-treatment image.

The change in biovolume for the SYTO9 and PI channels was calculated by comparing pre- and post-treatment images. Each condition was normalised to the change in biovolume for the DPBS control for each experimental day. ImageJ (version 1.54j) was used to analyse the 4 × tilescans. Otsu thresholding was used to calculate the coverage area of each sample. The post-treatment percentage coverage area was calculated for the SYTO9, PI, and ConA channels for each sample.

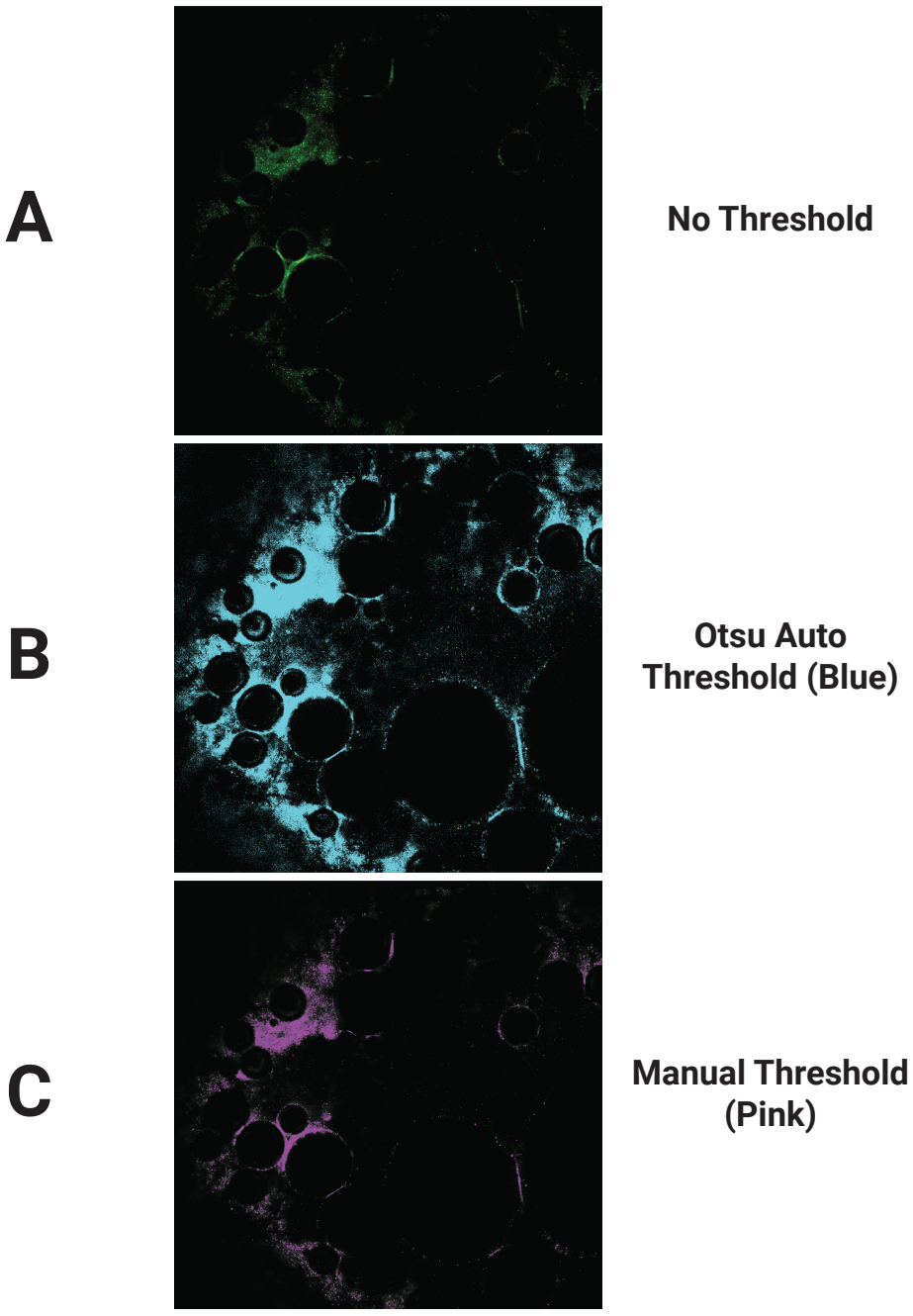

Figure 4.6: Differences in thresholding methods for 10 × z-stack.

(A) A representative slice of a post-treatment biofilm z-stack.

(B) Automatic Otsu thresholding, with included areas coloured in blue.

(C) Manual thresholding, with included areas coloured in pink, highlighting lower noise levels than the Otsu threshold.

4.2.5 Quantification Methods

CFU Counting

To quantify the viable bacteria detached from the biofilm during treatment, the treatment volume and subsequent rinse volumes were collected and processed. A total of 5 mL, comprising the treatment solution and rinse volumes, was collected in a 15 mL centrifuge tube (Centristar, Corning, UK). This suspension was then centrifuged at 3000 × g for 30 minutes to concentrate the bacterial cells. Following centrifugation, the supernatant was carefully removed, and the resultant bacterial pellet was resuspended in 1 mL of Luria-Bertani (LB) broth (12795027, ThermoFisher, UK). This suspension was then serially diluted 1:10 in LB broth to achieve dilutions ranging from 10^{-1} to 10^{-9}.

To count CFUs, five 10 µL aliquots of each dilution from 10^{-3} to 10^{-8} were placed onto LB agar plates. The plates were then incubated at 37 °C overnight. Colonies were counted on plates and the CFU/mL was calculated based on the dilution factor and the volume plated. This method is used to estimate the number of viable bacterial cells in a given volume of liquid. CFU counting is typically performed by aliquoting serial dilutions of liquid culture onto agar plates with a suitable growth medium [391, 392]. It is assumed that each individual colony arises from a single viable cell [393]. CFU counting does not account for viable but non-

culturable (VBNC) cells. When exposed to certain stresses, bacteria can enter the VBNC state, which hinders detection of these individuals by common plate counting techniques [394]. [395]

Biomass Quantification by Safranin Staining

Safranin is a positively charged dye that binds to negatively charged molecules and stains both bacteria and the biofilm EPS, and is used as a measure of biomass [396]. After the removal of the treatment formulation by rinsing, each Ibidi® culture dish was stained with 1 mL of 0.1% safranin solution (94635, Merck, Germany) and incubated for 30 minutes at room temperature ($\sim$ 24 °C). Following incubation, the staining solution was removed, and the biofilms were gently rinsed four times with 1 mL DPBS to remove excess stain. The bound safranin was then resolubilised by adding 1 mL of 33% glacial acetic acid to each dish and incubating for 30 minutes. The sample absorbance was measured at 520 nm using a FLUOstar Omega plate reader (BMG Labtech, UK) and normalised to the absorbance of the DPBS control.

4.2.6 Preliminary Observation of Droplet-Biofilm Interactions

To understand the interaction between PDs and bacterial biofilms, two different biofilm culture conditions and microscopy techniques were evaluated. These studies aimed to characterise biofilm morphology and observe passive (Non-US) droplet-biofilm interactions.

24 h Biofilm in Simple Media

Preliminary experiments used a simple media model to establish baseline biofilm characteristics. Each culture dish contained 400 µL of LB broth (Miller, Merck, Germany) inoculated with an overnight culture of *P. aeruginosa* that was diluted 1:100 with the LB. Biofilms were incubated at 37 °C for 24 h. Prior to staining, biofilms were washed three times with 1 mL DPBS (14190144, Gibco, ThermoFisher, UK). Biofilms were then stained with 2.5 µM SYTO9 9 (S34854, Invitrogen, ThermoFisher, UK).

Wide-field fluorescence microscopy was performed using an EVOS M5000 (ThermoFisher, UK) with a 100 × objective (AMPFOP100, Invitrogen, ThermoFisher, UK) and a GFP Light cube (AMEP4951, Invitrogen, ThermoFisher, UK). To evaluate droplet-biofilm interactions, 4.76% v/v PDs were diluted 1:500 in PBS and 400 µL was added to the biofilm, followed by incubation at 37 °C for 20 min. After

incubation, the free liquid was gently poured off the biofilm, which was then rinsed three times with 1 mL sterile DPBS and imaged.

Mature biofilms, typically grown for 48 h or longer, have been shown in previous work to better reflect the characteristics of chronic wound infections [397]. Therefore, biofilms were cultured in subsequent experiments for 48 h.

The selection of WCM provides additional physiological relevance to the biofilm model and is discussed in Section 4.2.2

48 h WCM Biofilm

WCM biofilm morphology was visualised at high magnification. To visualise PDs in proximity to PAO1 *P. aeruginosa* biofilm cultured in WCM, PDs were fluorescently labeled. DiI (1,1'-Dioctadecyl-3,3,3',3'-Tetramethylindocarbocyanine Perchlorate, ThermoFisher, UK) was added in a 0.025 molar ratio with DSPC and PEG40S, for a final ratio of 9:1:0.025 DSPC:PEG40S:DiI. Manufacture of 20% v/v PFP droplets was conducted as described in *Chapter 3*. DiI has been used previously to fluorescently label gas-filled MBs [212, 398].

Confocal microscopy was performed using the microscopy setup described in *Section 4.2.4* with a 100 × objective (MRD71970, Nikon Instruments Europe BV, Netherlands). SYTO9 was excited using a 488 nm laser at 2.2% power with a gain

of 25, ConA with a 640 nm laser at 2.0% power and a gain of 25, and DiI with a 561 nm laser at 6.0% power and a gain of 5. The pinhole was set to 1.0 Airy Unit, and the Galvano mirror scanning method was employed. PDs were diluted 1:500 in PBS and 400 µL was added to the biofilm. Images were acquired immediately after addition of PDs at a resolution of 2048 × 2048 pixels, resulting in a pixel size of 0.09 µm.

4.2.7 Statistical Analysis

Statistical analysis was performed with GraphPad Prism using a one-way analysis of variance (ANOVA) with a Dunnet multiple comparisons test. A P-value <0.05 was considered statistically significant.

4.3 Results and Discussion

4.3.1 Acoustic Droplet Vaporisation

Before evaluation of PD effects on CW biofilms, it was necessary to establish the US parameters required for ADV. Determining these parameters is essential to characterise the physical mechanisms underlying US-mediated PD therapies.

Dynamics of Droplet ADV

High-speed imaging enabled the dynamics of PD ADV to be visualised **(Fig. 4.7)**. Vaporisation was observed to occur during the first half of an acoustic cycle as the pressure dropped and the resulting bubble was then driven to expand and contract in response to the changing US pressure. Phenomena such as micro-jetting and bubble fragmentation were frequently observed, consistent with previous experiments reported by Wu *et al.* [242] with smaller perfluorobutane droplets. These phenomena are thought to mediate a variety of potentially biofilm-disrupting physical effects produced by cavitating bubbles [228].

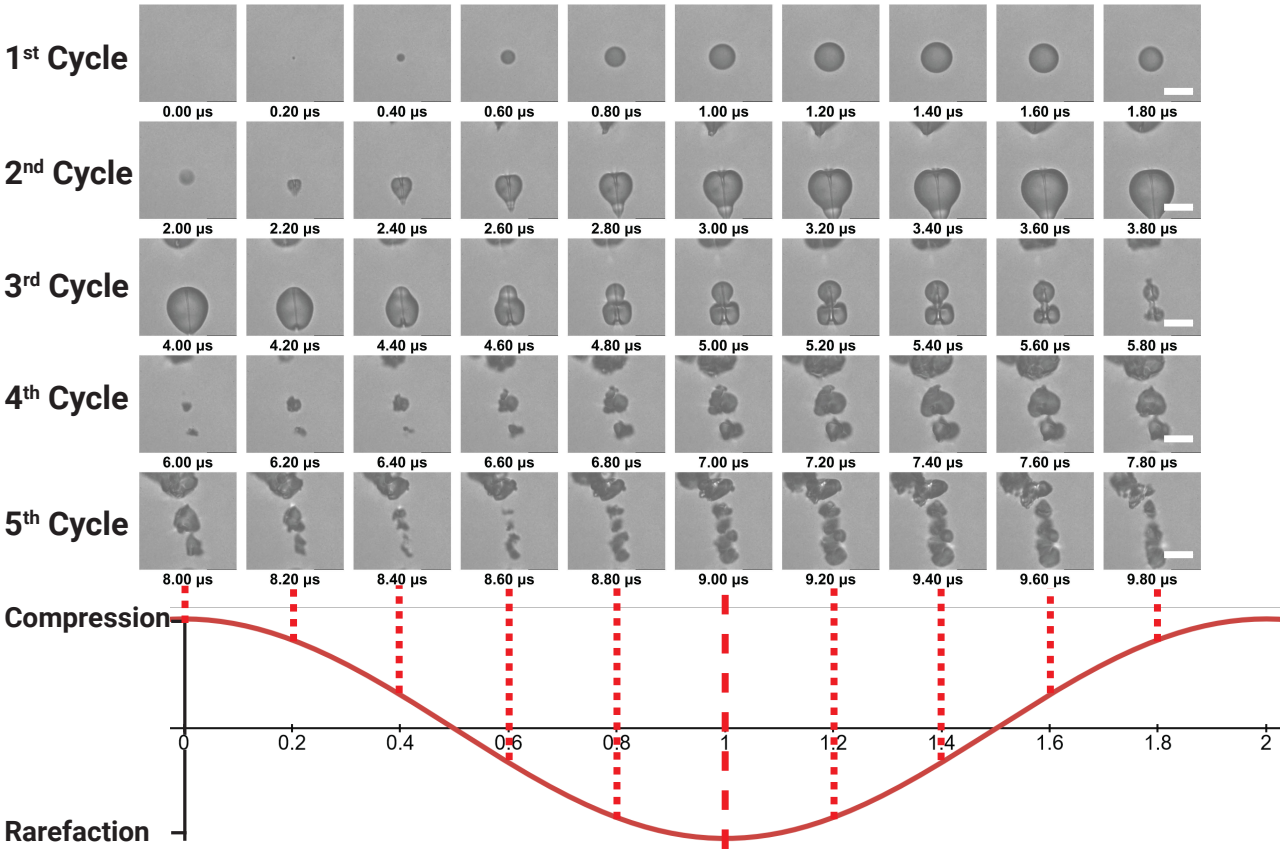

Figure 4.7: Representative example of a series of high-speed images of PFP droplet vaporisation captured over the first 5 cycles of a 10,000-cycle US pulse at 0.5 MHz, peak negative pressure of 1.48 MPa. Scale bar = 20 µm. Images were taken at 5 × 10^6 frames/s with an exposure time of 200 ns per frame. The dashed lines indicate the approximate phase relationship between each frame and the incident US pulse, assuming that the speed of sound in the liquid is 1481 m/s. In the second cycle the formation of a microjet is visible.

Simultaneous High-speed Imaging and PCD

High-speed imaging investigations revealed a distinct temperature threshold for consistent acoustic droplet vaporisation. Stimulation of PDs at 2.48 MPa peak negative pressure at 37 °C showed no vaporisation events occuring. At 38.3 °C, vaporisation was also not observed. However, increasing the temperature by just 0.7 °C to 39 °C resulted in reproducible ADV events, suggesting a narrow temperature window for reliable PD activation **(Fig. 4.8)**. PCD traces demonstrated an increase in total acoustic energy emitted by the vaporised PDs with increased driving pressure **(Fig. 4.9)**. However, in contrast to previous studies, no distinct ADV threshold was observed. This is likely due to several confounding factors. Notably, large gas bubbles frequently formed in the sample tube **(Fig. 4.10)**, presumably from spontaneous vaporisation of larger droplets which would have contributed to the overall acoustic emissions and/or potentially interfered with transmission of the acoustic radiation from the ADV process.

As there was no clear ADV threshold, the maximum pressure evaluated of 2.48 MPa (peak negative) was selected for subsequent biofilm testing along with a treatment time of 10 minutes and a temperature of 39 °C. As ADV was consistently observed at these parameters, there was a need to balance the potential thermal stress on the CW biofilm model with the efficacy of US-activated treatment.

Although *P. aeruginosa* is known to tolerate temperatures up to 45 °C [399], the treatment time was minimised to reduce exposure to elevated temperatures.

The temperature of the CW bed typically ranges from 31 to 35 °C [400]. Furthermore, there is ongoing research on the use of thermal wound dressings that raise the wound temperature to encourage blood flow perfusion for improved healing. Huang *et al.* [401] reviewed the work in this area, with several studies testing thermal dressings on patients at a temperature of 38 °C for several hours a day. The selection of treatment time was also informed by the expected rapid release of NO from the PD formulation.

Choi *et al.* showed that lipid-shelled perfluorodecane PDs released the majority of loaded NO within 10 min, with a total released amount of 2.0 µM/mL in 18 min.

The US parameters employed in this study were selected based on ADV observations and safety considerations towards a topical wound application. These parameters established a conservative baseline approach prioritizing both baseline therapeutic efficacy and safety. A driving frequency of 0.5 MHz was selected based on the specifications of a commercially available preclinical transducer (Sonic Concepts H107). This selection was made after preliminary experiment at higher driving frequencies (1.55 MHz, 3rd harmonic) failed to induce ADV, likely due to insufficient energy deposition. As noted in the literature, the ADV threshold typically decreases

with decreasing frequency [253]. As shown by Wu *et al.*, lowering the US frequency can substantially reduce the pressure needed to achieve ADV [242]. While the larger focal region enabled by lower frequencies could potentially allow treatment of larger wound areas, the corresponding increased penetration depth offers minimal benefits for topical applications targeting CW biofilms.

The pulse length was conservatively set to 100 cycles, as ADV was consistently observed within the first few acoustic cycles of ultrasound exposure. These conservative parameters were chosen considering that DFUs constitute highly sensitive regions with compromised tissue integrity, warranting minimisation of potential off-target effects [371]. The baseline parameters selected allow for future optimisation through increasing PRF and treatment duration if initial bioeffects prove insufficient.

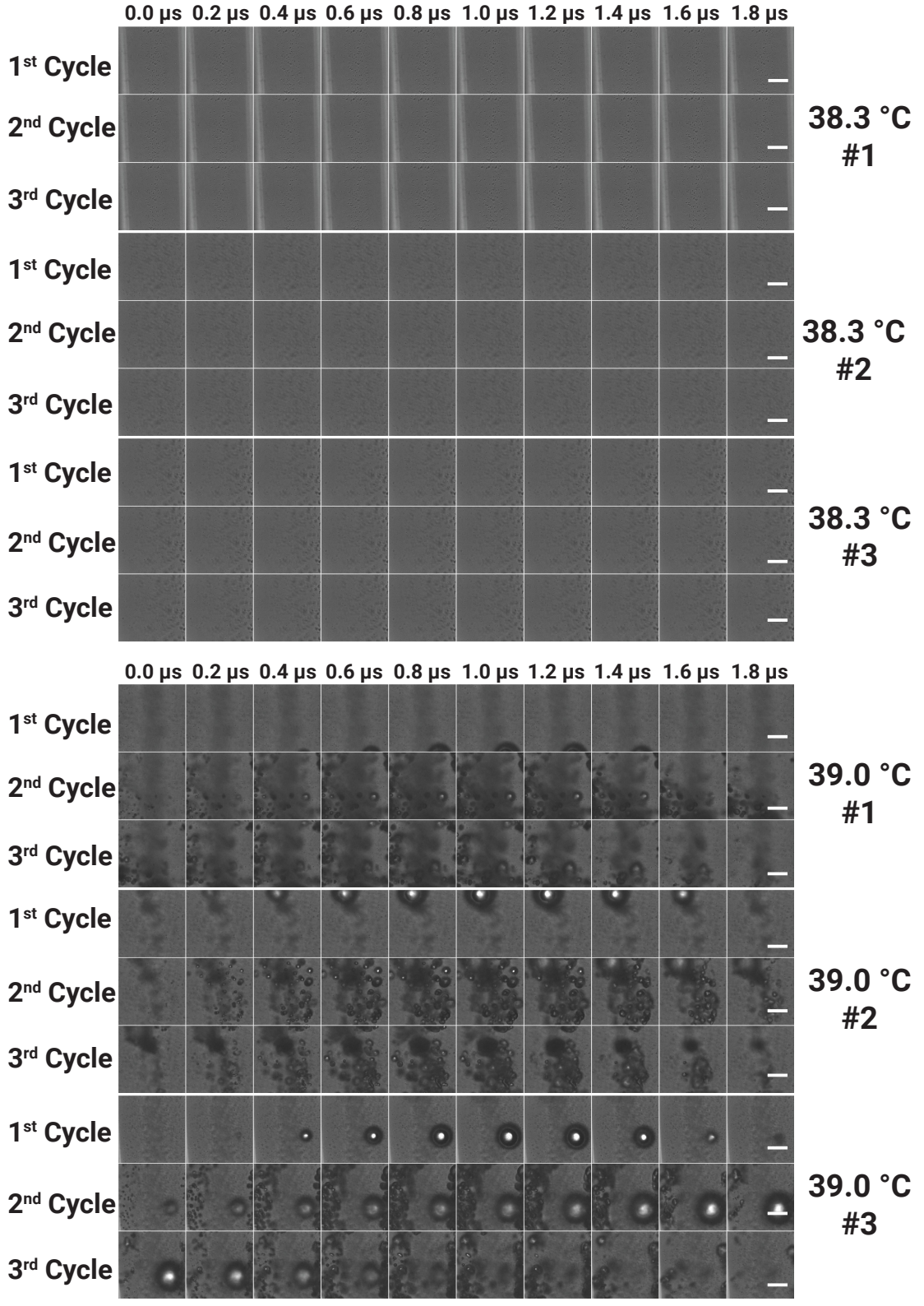

Figure 4.8: Temperature threshold of droplet vaporisation. A series of high-speed images of PFP droplet vaporisation captured over the first 3 cycles of a 10,000-cycle US pulse at 0.5 MHz, and peak negative pressure of 1.48 MPa. Figure caption cont. on next page.

Figure 4.8: Images were taken at 5×10^6 frames/s with an exposure time of 200 ns per frame. There was a clear temperature-dependent effect, with an increase in temperature from 38.3 °C to 39 °C resulting in consistent ADV being observed. n = 3 repeats were performed at each temperature. Scale bar = 20 µm.

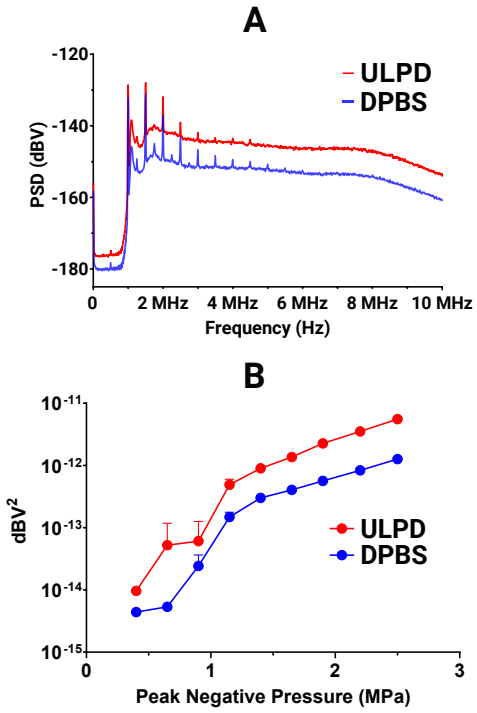

Figure 4.9: PCD measurements comparing acoustic emissions from ULPD and DPBS samples. **(A)** Representative PCD signals from DPBS and ULPD samples at 2.48 MPa peak negative pressure, showing increased acoustic emissions in ULPD samples. **(B)** Total acoustic energy at peak negative pressures ranging from 0.4 to 2.48 MPa for DPBS and ULPD samples. Data points represent mean ± S.D. (n = 3 independent samples).

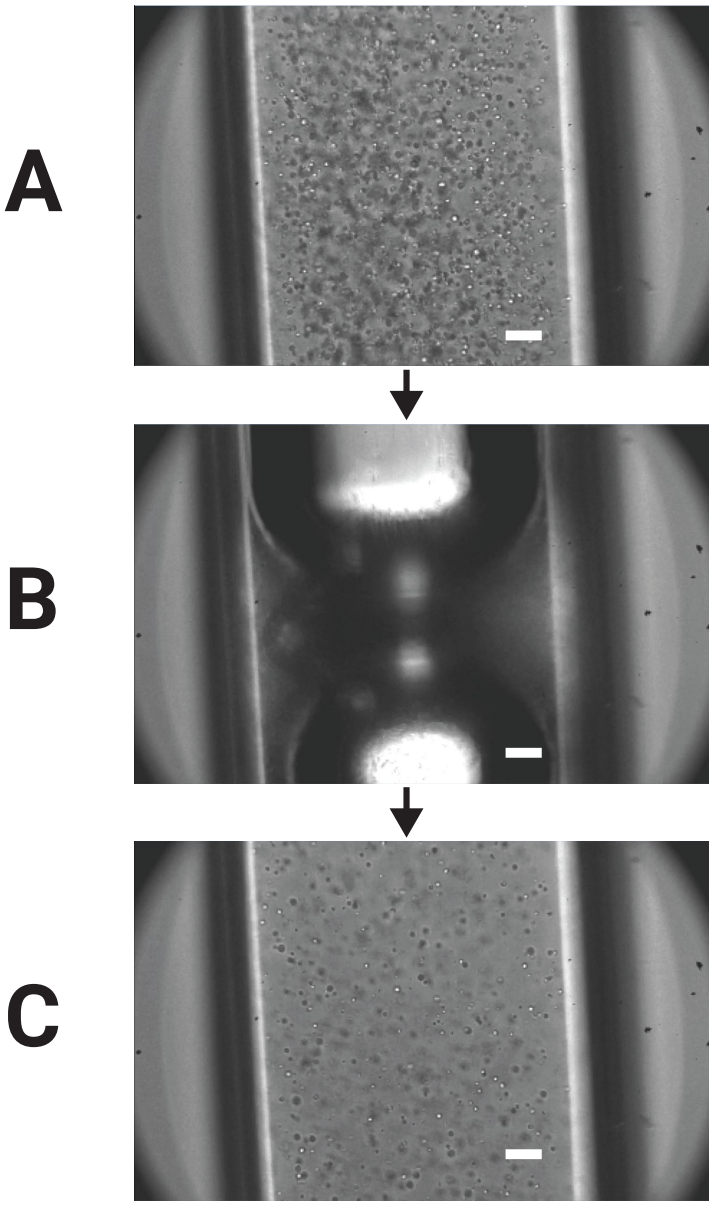

Figure 4.10: Observation of large bubble clusters and gas pockets during high-speed imaging experiments.

(A) Prior to a cluster of bubbles passing through the imaging field of view, a build-up in the number of droplets is visible.

(B) Large clusters of bubbles pass through the image.

(C) Once bubble clusters have passed through, the concentration of droplets returns to nominal levels. Scale bar = 50 µm.

4.3.2 Preliminary Evaluation of Droplet-Biofilm Interactions

To investigate interactions between PDs and bacterial biofilms, preliminary experiments were conducted using widefield microscopy of 24-hour biofilms grown in simple media. Subsequently, confocal microscopy of 48-hour biofilms cultured in WCM was carried out.

Widefield Microscopy of LB Biofilms

When examining biofilms cultured in LB and incubated with 4.76 v/v% PFP PDs, as shown in **(Fig. 4.11)**, circular structures presumed to be PDs could be observed. These were adjacent to the SYTO9-stained bacterial cells. The limited axial resolution of widefield microscopy made it challenging to precisely determine the spatial relationship between these structures and the bacterial cells.

Confocal Microscopy of WCM Biofilms

Higher-resolution imaging was achieved using CLSM to examine biofilms grown in WCM **(Fig. 4.12)**. This imaging technique allowed for improved visualisation of the biofilm structure. The WCM biofilm exhibited aggregate formations consistent with those observed in chronic wounds [397]. DiI-labeled particles (yellow) were observed to settle adjacent to the biofilm clusters, with no observable penetration into the aggregates.

Based on the particle size characterisation carried out in *Chapter 3*, these visible particles likely represent the larger subpopulation (2-4 µm diameter) of the 20% v/v PFP droplet formulation. A particle diameter of 100-130 nm has shown to be the cutoff for optimal penetration into *P. aeruginosa* biofilms [402]. Therefore, the lack of visible DiI particle penetration is unsurprising. Although DiI-labeled PDs used in this experiment provided valuable insight, they were not employed in subsequent studies. This decision was made to avoid potential alterations in droplet size and gas-loading characteristics that might result from the incorporation of the fluorescent dye.

Comparison of Biofilm Morphologies in LB and WCM

Striking differences in biofilm morphology were observed when comparing *P. aeruginosa* culture conditions **(Fig. 4.13)**. Biofilms grown in simple media often exhibit a uniform and dense covering on surfaces. However, biofilms found in CWs typically display a more complex morphology characterised by discrete, aggregate structures. The aggregate mode of growth significantly increases the tolerance of biofilms to various treatments, making it a desirable characteristic to reproduce in experimental models [403].

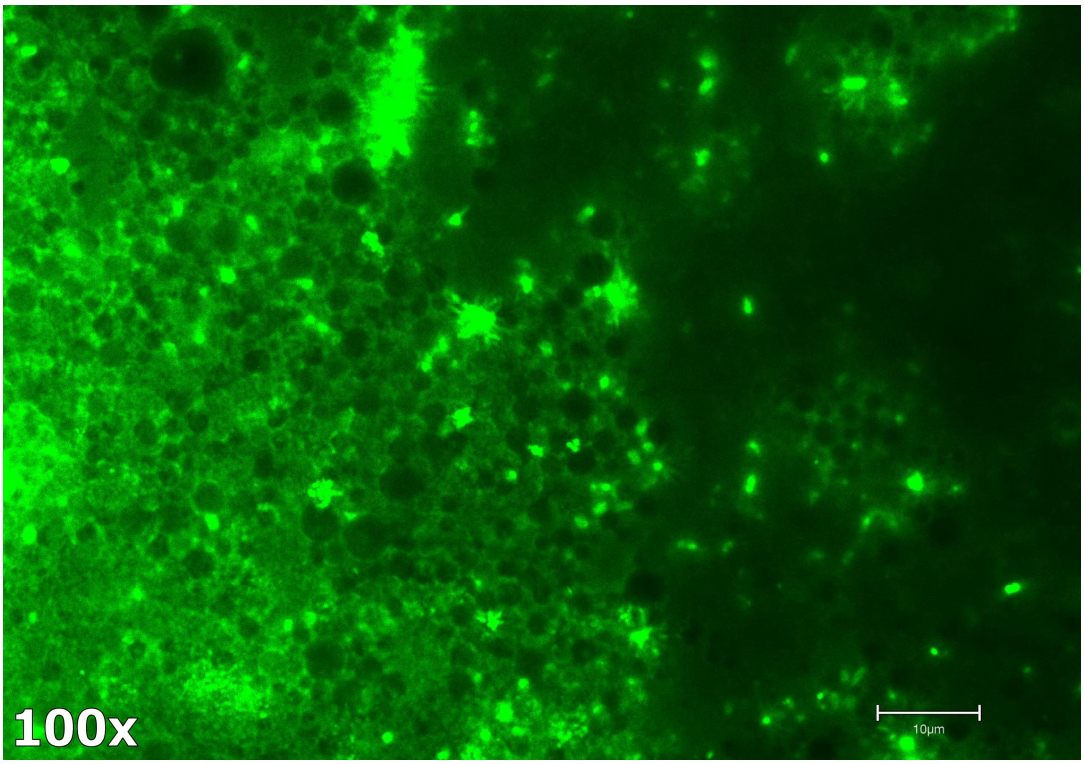

Figure 4.11: Wide-field microscopy image (100 × magnification) of simple media biofilm. *Pseudomonas aeruginosa* PAO1 biofilm cultured in LB media for 24 h at 37 °C and incubated with 4.76% v/v PFP PDs. The biofilm sample was stained with SYTO9 (green). Scale bar = 10 µm.

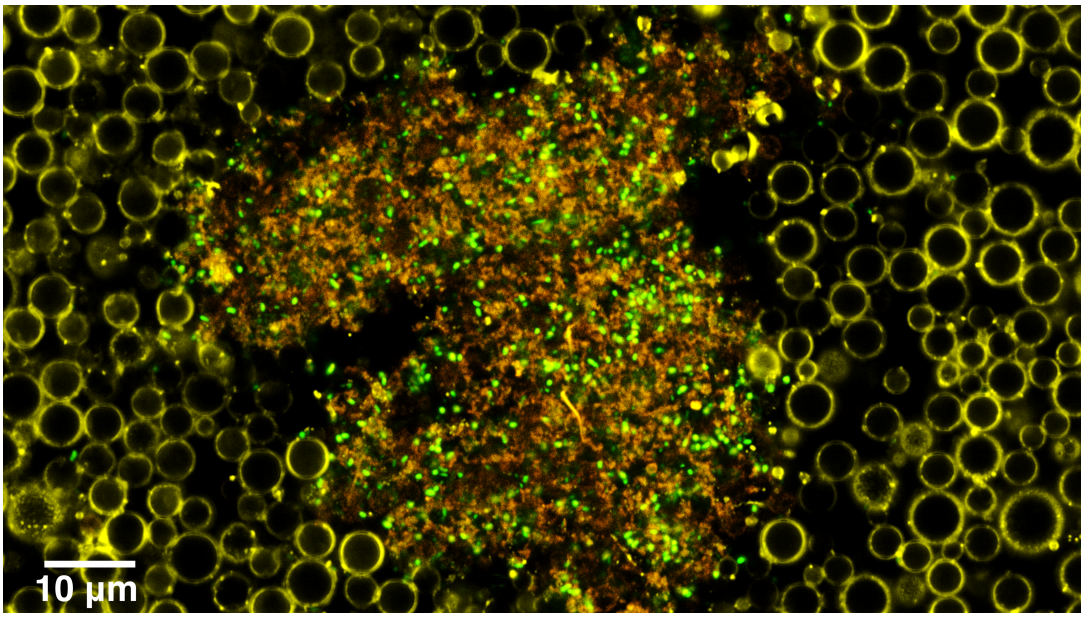

Figure 4.12: CLSM image (100 × magnification) of WCM biofilm. Pseudomonas aeruginosa PAO1 biofilm cultured in WCM for 48 h at 37 °C, incubated with 20% PFP PDs labeled with DiI (yellow). The biofilm sample was stained with SYTO9 (green) and ConA (Orange). Scale bar = 10 µm.

The biofilms grown in WCM exhibit a more heterogeneous, aggregate-like structure that better represents the morphology observed in clinical wound biofilms. The use of *P. aeruginosa* strain PAO1 in this study is particularly relevant due to its widespread use in biofilm research and its clinical significance. PAO1 is a well-characterised strain isolated from a wound infection, making it an ideal candidate for studying wound-associated biofilms [404].

Bacterial aggregates in biofilms often exhibit enhanced tolerance to antimicrobial treatments compared to planktonic cells or uniform biofilms, which is attributed to various factors including the protective EPS matrix, slow bacterial growth, and activation of stress responses such as multidrug efflux pumps [91, 405]. Based on these observations, the 48 h WCM biofilm model was selected for further experiments evaluating the effect of PD with and without NO-loading and with and without US stimulation. Furthermore, the addition of fresh media after 24 h incubation was incorporated to better mimic the physiological conditions of a CW, whereby the flow of wound exudate provides a source of nutrients to the bacteria that colonise the wound bed [73, 406].

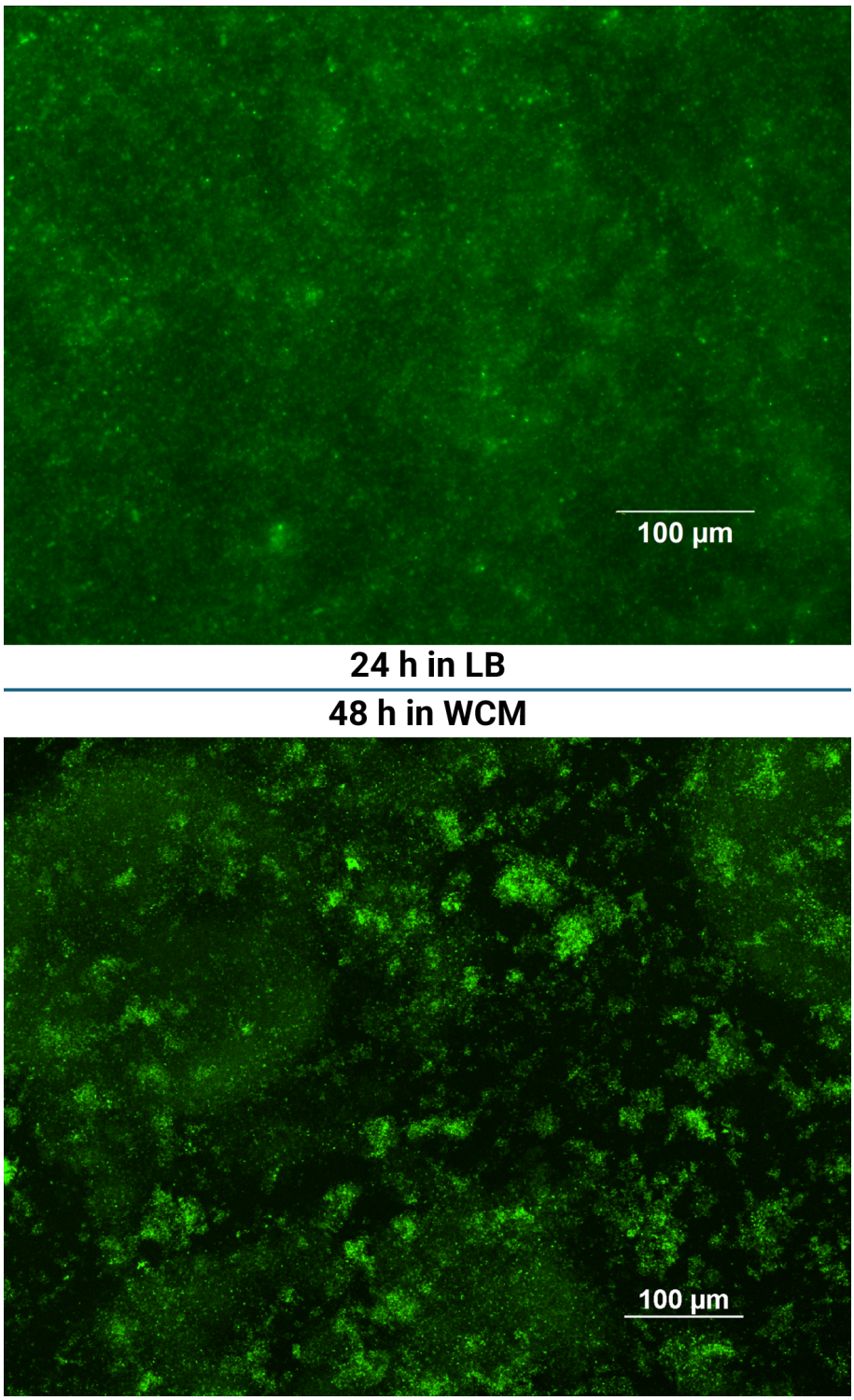

Figure 4.13: Representative images of *Pseudomonas aeruginosa* PAO1 cultured in LB for 24 h (top) compared to PAO1 cultured in WCM for 48 h (bottom). Bacteria cultured in WCM for 48 h appear to have a more discrete, aggregate morphology as opposed to the dense covering seen in the biofilm grown for 24 h in LB.
Scale bar = 100 µm.

4.3.3 Evaluation of the Antibiofilm Effect of NO-Loaded Perfluorocarbon Droplets

To investigate the antibiofilm efficacy of NO-loaded PDs activated by US on biofilms grown in WCM, six treatment conditions were assessed. These conditions were used to evaluate the individual and combined effects of US stimulation, PDs, and NO on biofilm disruption.

A DPBS control condition (DPBS) was used to simulate the mechanical effects of rinsing the biofilm, thereby accounting for the removal of biofilm and planktonic cells due to fluid shear stress alone. A US-stimulation control with DPBS (US-Only) was selected to assess the mechanical effects of US alone. The passive effect of unloaded PDs (ULPD) was compared with the passive effect of NO-loaded PDs (NOPD) on the biofilm to assess NO-specific effects independent of US stimulation. Finally, to explore the effects of US-activated PDs, both unloaded PDs and NO-loaded PDs were stimulated with US after an initial passive incubation period (ULPD-US and NOPD-US, respectively).

It was hypothesised that the combination of NO-PDs with US would have the greatest anti-biofilm effect, due to the potential additive effect of NO-mediated dispersal combined with the physical disruption provided by cavitation nuclei.

The concentration of NO in the PDs is theoretically suitable for inducing biofilm dispersal. The particle concentration of PDs was adjusted to 1×10^9 particles/mL immediately prior to biofilm treatment. Based on the average PD dilution factor across the three repeats the estimated NO_x mean concentration of the PD sample applied to the biofilm was 67.5 ± 2.5 nM. This was calculated using the 4.57 µM NO_x concentration of undiluted droplets determined in *Chapter 3*. This concentration is within the concentration range reported in the literature for NO-induced biofilm dispersal effects (25 pM to 2.5 µM) [279].

Multiple techniques were used to assess the response of WCM biofilms to treatment, with each method providing different insights. CFU counting was used to assess cellular viability, safranin staining quantified biofilm biomass, and coverage area measurements evaluated biofilm attachment. Confocal microscopy allowed for the qualitative observation of changes to the spatial distribution of the biofilm post-treatment.

Lower-Magnification Confocal Microscopy

Observations of 4 × tilescans across the six treatment conditions revealed distinct differences in biofilm morphology post-treatment **(Fig. 4.14)**. Overall, the biofilms treated with the US-Only condition showed no notable differences in appearance when compared to the DPBS control.

The addition of PDs to the biofilm led to distinct changes in the biofilm structure. Small gas pockets were visible in the ULPD treatment condition, and this effect was substantially enhanced in NOPD treatments, with an increase in both the number and size of gas pockets visible. The ULPD-US treatment condition displayed similar characteristics to the NOPD treatment, with clusters of large gas pockets remaining embedded within the biofilm post-treatment. The combination of NO-loading and US-stimulation appears to have had a markedly different effect, with the NOPD-US condition exhibiting few gas pockets and a noticable decrease in apparent biofilm attachment/coverage area. In general, the addition of PDs to biofilms generated gas pockets that coalesced and disrupted the biofilm structure to varying degrees.

While these 4 × tilescans provided insight into large-scale morphological changes of these treatment conditions, they lacked the axial resolution necessary to clearly visualise finer changes to the biofilm morphology, such as the distribution of the observed gas pockets.

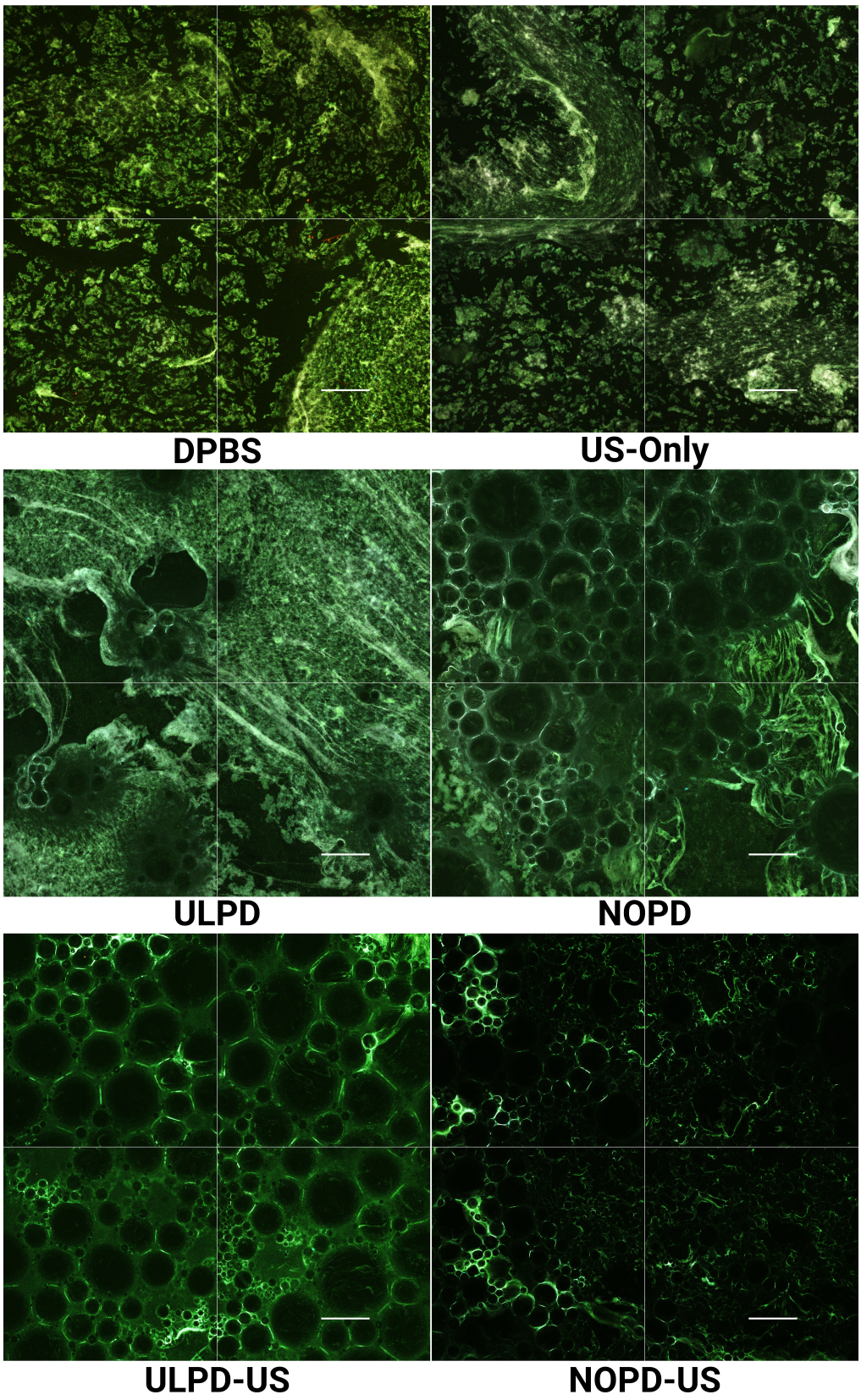

Figure 4.14: Representative 4 × tilescans of *P. aeruginosa* PAO1 biofilms cultured in WCM for 48 h, stained with SYTO9 (green), PI (red), and ConA (Blue) and treated with DPBS, US-Only, ULPD, NOPD, ULPD-US, or NOPD-US. Each panel is composed of 4 tiles covering a 8.192 mm × 8.192 mm area. Scale bars = 1 mm.

Higher-Magnification Confocal Microscopy

Higher-resolution, three-dimensional images taken over the full height of the biofilm enabled detailed insight into the effects of each treatment. Comparing DPBS and US-Only treatment conditions, there was no observable difference in biofilm morphology, consistent with the observations made in the 4 × tilescans **(Fig. 4.15)**. Evaluation of passive PD incubation conditions **(Fig. 4.16)** showed that the addition of PDs generated distinct gas pockets that disrupted the biofilm structure in a hemispherical pattern compared to the DPBS control. The gas pockets observed in the NOPD treatment condition appeared to be larger, more numerous and disrupted the biofilm across a larger height than those in the ULPD treatment condition.

The application of US enhanced these biofilm disrupting effects **(Fig. 4.17)**. The ULPD-US condition was characterised by a marked increase in the number of gas pockets present post-treatment compared to the ULPD treatment alone. The hemispherical regions of disruption that formed were between ∼15 to 100 µm in diameter. The NOPD-US condition demonstrated the most pronounced effect on biofilm structure, with evidence of gas pocket collapse, likely mediated by the US stimulation. The effect of the collapsing gas pockets presented as large circular regions of disruption, with the remaining biofilm structure exhibiting areas under shear and tension forces. The bacteria remaining at the edge of these disrupted

areas appeared as bright rings in the SYTO9 channel. A higher density of biofilm-associated bacterial clusters compressed by the expanding gas pockets contributed to this phenomena.

Additionally, the NOPD-US treated samples exhibited a lower amount of biofilm surface attachment when compared to the other treatment conditions. However, it's important to note that even under this maximal treatment condition, numerous bacterial clusters remained attached to the culture dish surface.

Images of the base of each biofilm acquired during the 10 × tilescans provided insight into how each treatment affected bacterial attachment to the culture surface. Examination of the ULPD treatment condition **(Appendix. Fig. A.1)**, demonstrated that despite lower-magnification observations showing the formation of gas pockets throughout the biofilm, these pockets did not necessarily affect attachment of the biofilm to the base of the culture dish. The NOPD condition exhibited some reduction in surface attachment compared to the control, though substantial portions of the biofilm remained adherent.

When observing the US-stimulated conditions **(Appendix. Fig. A.2)**, similar observations were made to those in **(Fig. 4.17)** where gas pockets formed in the ULPD-US treatment, but appear to have collapsed in the NOPD-US treatment. It is clear that the hemispherical disruption observed in **(Fig. 4.17, ULPD-US)**

manifests as clear circular regions of biofilm disruption in the base plane, indicating that the gas pockets caused effects through much of biofilm thickness, affecting attachment at the culture dish surface. Similarly, the collapse of these pockets seen in the NOPD-US conditions was accompanied by distinct regions undergoing shear and tension forces.

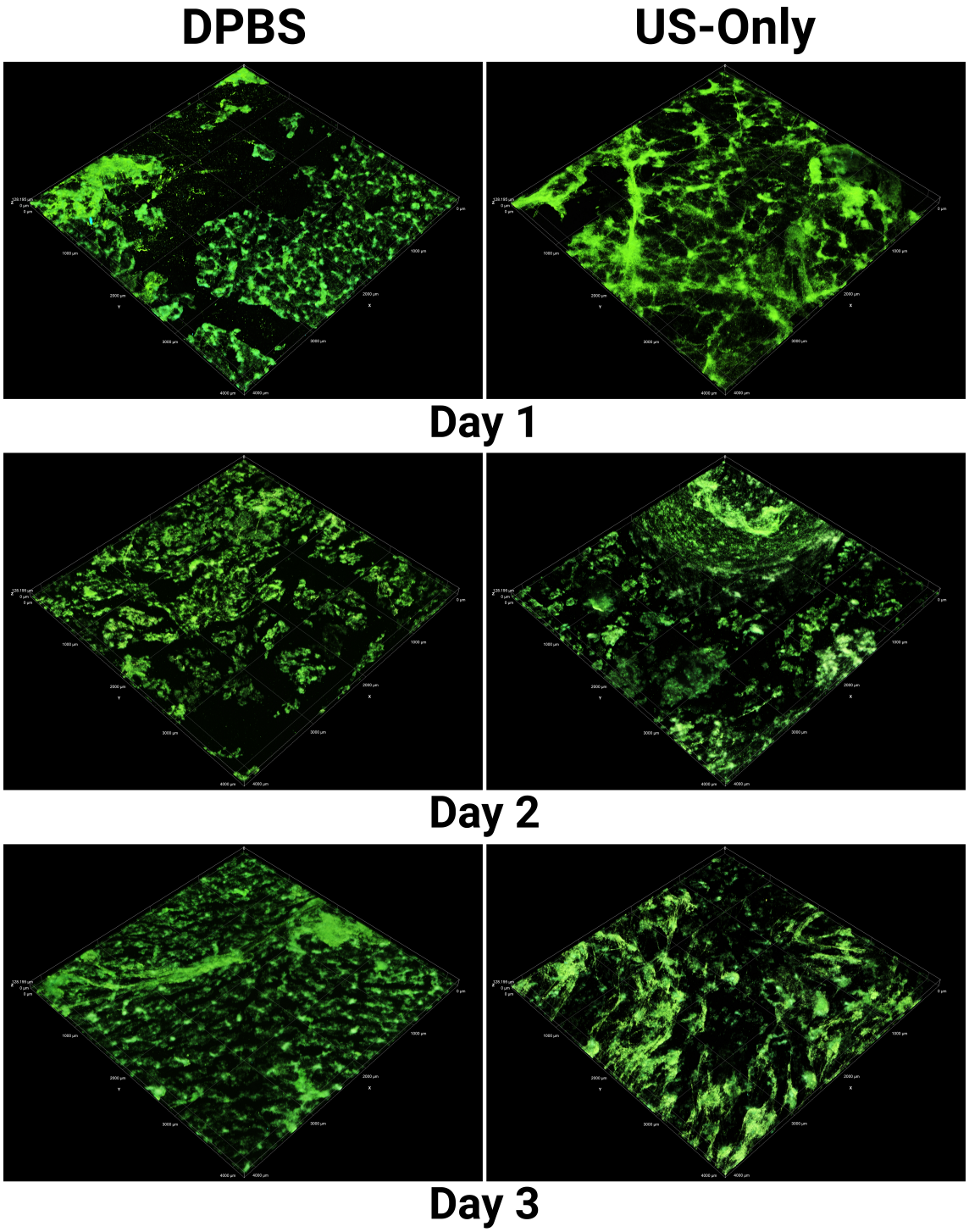

Figure 4.15: 3D CLSM images of *P. aeruginosa* PAO1 biofilms cultured in WCM for 48 h and subjected to either DPBS or US-Only treatment conditions. Biofilms were stained with SYTO9 (green), PI (red), and ConA (Blue). Each panel represents an independent biological repeat across one of three experimental days, and comprises 16 tiles imaged at 10 × magnification covering a 4.192 mm × 4.192 mm area. Images show z-stacks consisting of 25 slices over a 128.19 µm depth.

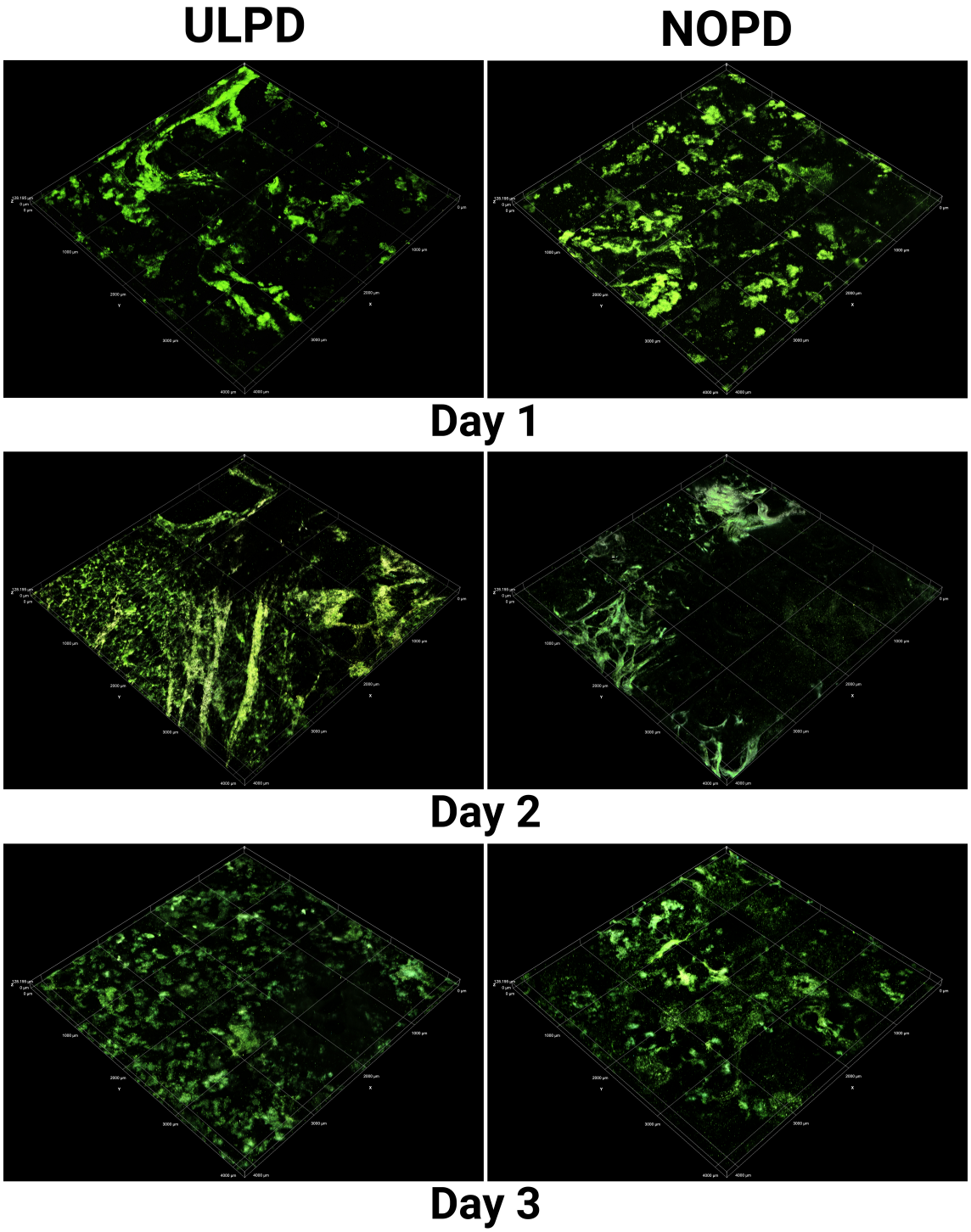

Figure 4.16: 3D CLSM images of *P. aeruginosa* PAO1 biofilms cultured in WCM for 48 h and subjected to either ULPD or NOPD treatment conditions. Biofilms were stained with SYTO9 (green), PI (red), and ConA (Blue). Each panel represents an independent biological repeat across one of three experimental days, and comprises 16 tiles imaged at 10 × magnification covering a 4.192 mm × 4.192 mm area. Images show z-stacks consisting of 25 slices over a 128.19 µm depth..

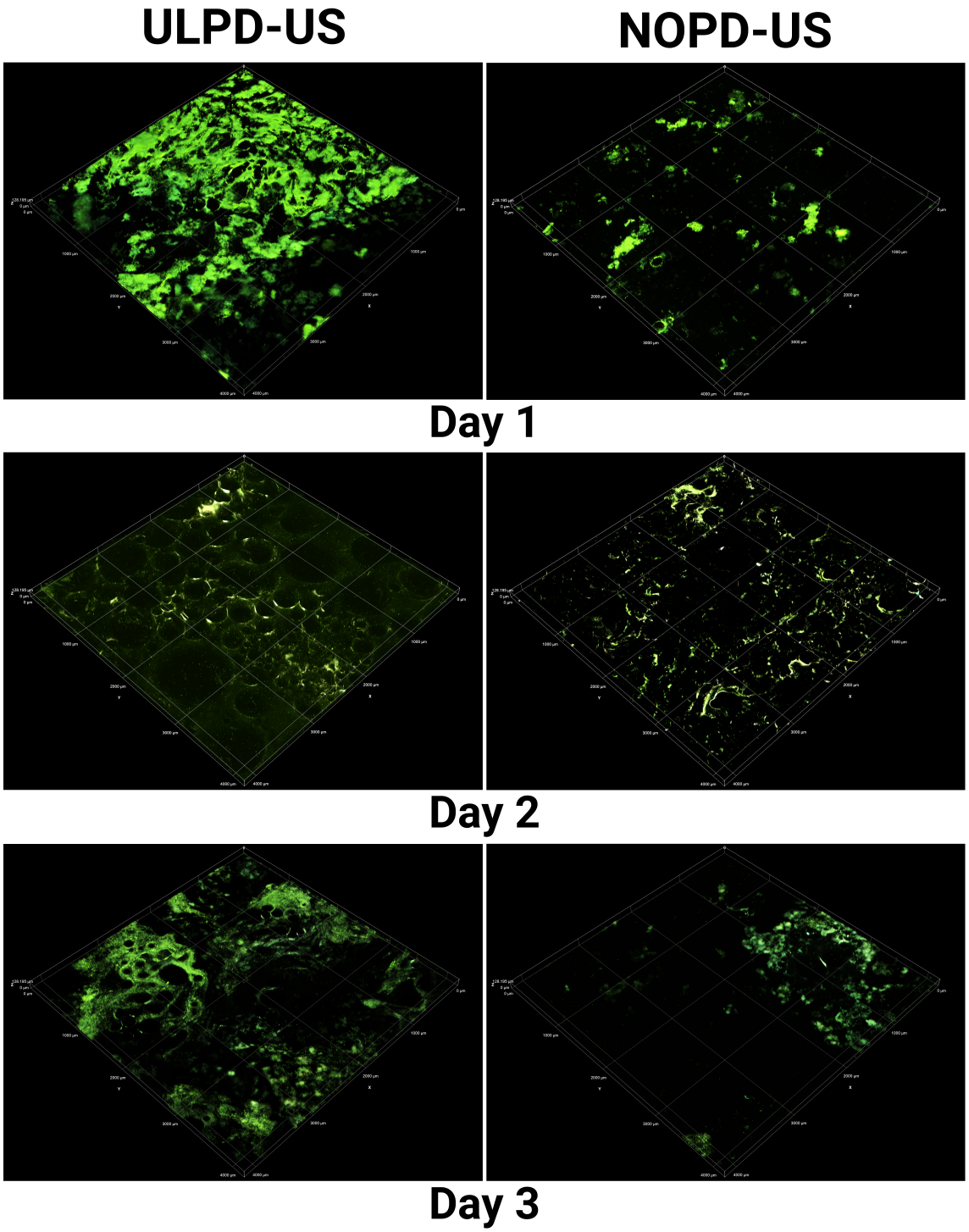

Figure 4.17: 3D CLSM images of *P. aeruginosa* PAO1 biofilms cultured in WCM for 48 h and subjected to ULPD-US or NOPD-US treatment conditions. Biofilms were stained with SYTO9 (green), PI (red), and ConA (Blue). Each panel represents an independent biological repeat across one of three experimental days, and comprises 16 tiles imaged at 10 × magnification covering a 4.192 mm × 4.192 mm area. Images show z-stacks consisting of 25 slices over a 128.19 µm depth.

These observations are consistent with previous studies investigating US-mediated biofilm disruption with various cavitation nuclei. The formation of spherical structures was observed by Ronan *et al.*, who described the formation of craters (5-20 µm diameter) in a *P. aeruginosa* biofilm upon exposure to US + MBs. US-parameters used were 0.5 MHz US frequency, 1.1 MPa peak negative pressure, 16-cycle tone burst, 1 kHz PRF, and exposure time of 5 minutes. In comparison, the morphological changes observed in this study appeared as hemispherical regions of disruption **(e.g. Fig. 4.17, ULPD-US)**.

Similar results have been reported in recent studies evaluating the effect of cavitation nuclei on the biofilm structure. Keller *et al.* [407] tested the effects of US-stimulated (1.5 MPa, 200 cycles, 5 Hz PRF, 30 s duration) protein cavitation nuclei (PCaN) on *S. aureus* and *P. aeruginosa* biofilms grown in channel slides. They reported significant biofilm disruption, with disruption patterns following the shape of the FUS transducer focal region. Notably, they found that US-alone did not significantly reduce biofilm biomass or visibly disrupt the biofilm structure, which is similar to observations in the present study. The US-alone condition was observed to have a limited effect when comparing the H107 US beam profile **(Fig. 4.18 A)** to biofilm disruption patterns. There was no discernible disruption of the biofilm in the focal region of the H107 transducer **(Fig. 4.18 B)**.

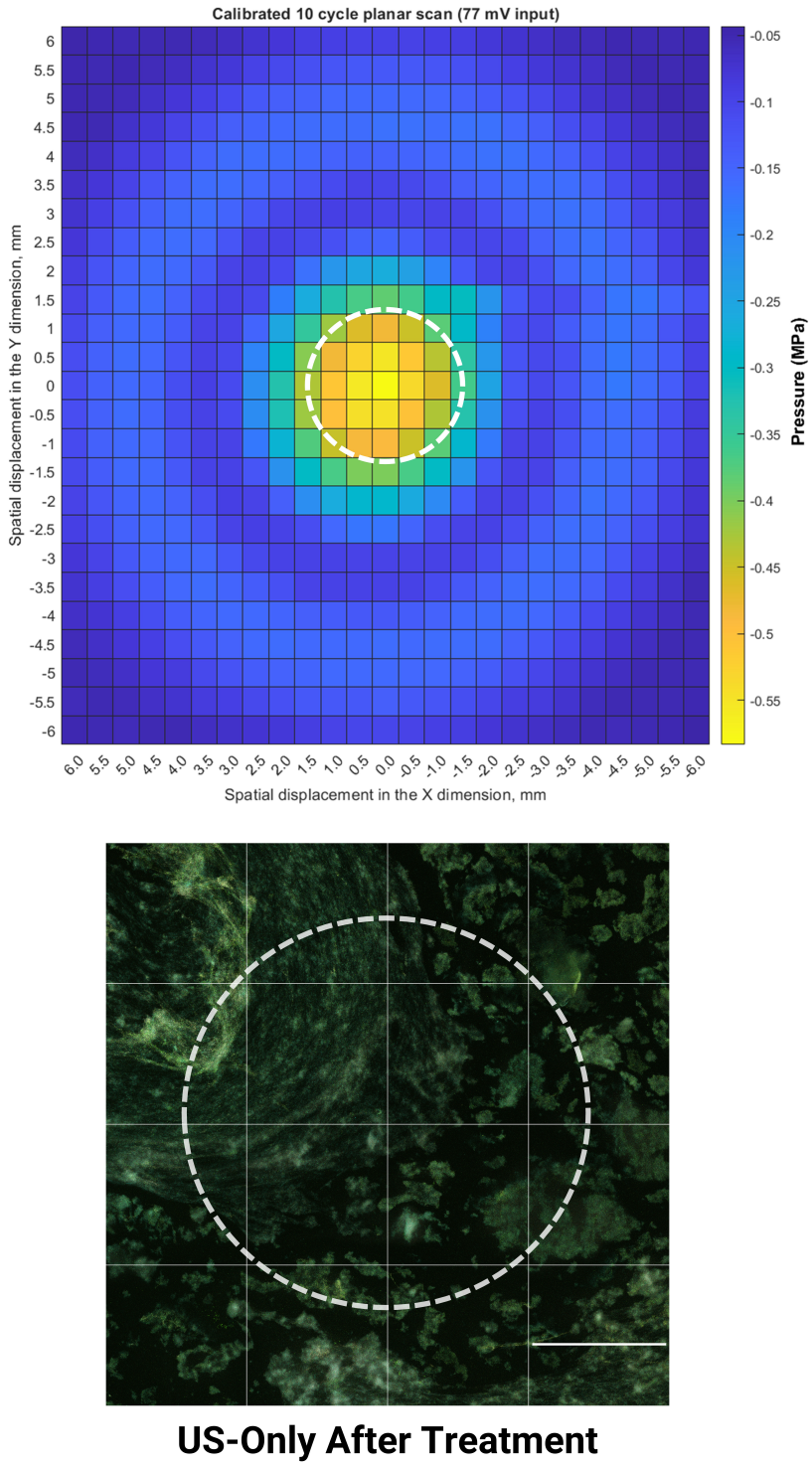

Figure 4.18: Comparison of US field characteristics and corresponding biofilm (48 h WCM PAO1) morphology. **(A)** Lateral beam profile of H107 FUS transducer measured in free field conditions using a needle hydrophone (0.5 MPa peak negative pressure, 10 cycles, 0.5 MHz). **(B)** Representative CLSM microscopy image showing biofilm morphology after US-Only treatment (2.48 MPa peak negative pressure, 100 cycles, 1 Hz PRF, 60 s duration). Dashed circles in both panels indicate the 3.9 mm FWHM focal region. Scale bar = 1 mm.

Qualitative visual observations of the biofilm culture dishes post-treatment showed the formation of a foam after incubation with droplets, both with and without US stimulation **(Fig. 4.19)**. These observations are in line with the observations made of the 4 × and 10 × tilescan images. As this phenomenon also occurred without US activation, it suggests that a passive mechanism such as droplet coalescence or spontaneous vaporisation could contribute to biofilm disruption. These observations are reflected in previous studies examining PD behaviour. For example, Ferri *et al.* demonstrated that PFP droplet samples incubated at 37 °C generated gas bubbles attributed to spontaneous vaporisation or coalescence effects [250]. In a biofilm context, Guo *et al.* observed the generation of large bubbles when incubating PFP PDs on a *S. aureus* biofilm, which continually coalesced over a 16 h incubation period, further disrupting the structure of the biofilm [300]. These effects suggest that longer exposure times to PDs exhibiting this behaviour could enhance biofilm disruption.

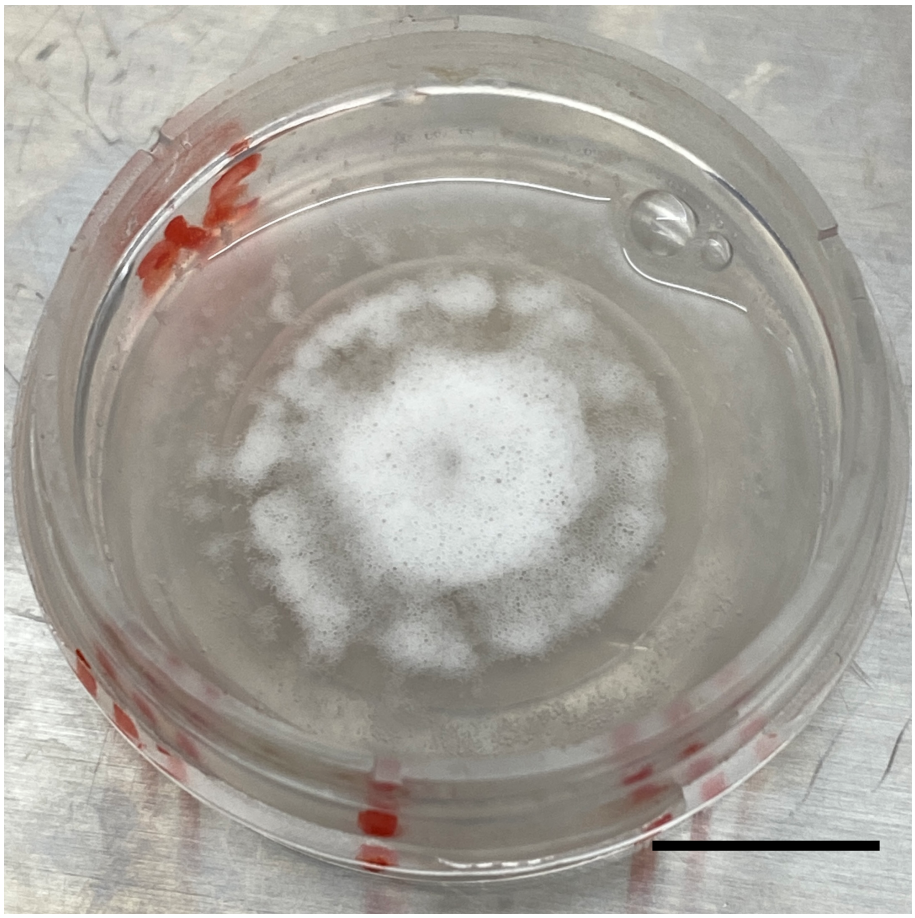

Figure 4.19: Image showing PDs + biofilm after stimulation on 48 h WCM PAO1 biofilm prior to rinsing and removal of treatment. A foam with gas pockets across the growth area of the Ibidi dish is visible. Scale bar = 10 mm

Assessment of Bacterial Viability

CFU counts were used to assess the number of viable bacteria present in the treatment supernatant, i.e. cells that had detached from the biofilm and retained their ability to form colonies on LB-agar plates. The CFU count of the bacteria present in the supernatant for various treatment conditions is shown in **Fig. 4.20**. Although there were no statistically significant differences ($P>0.05$) between any of the treatments tested, all conditions had a decrease in the mean CFU count compared to the DPBS control. The largest reduction in CFU was observed in the NOPD group, where counts decreased from $4.7 \times 10^7 \pm 6.3 \times 10^6$ CFU/mL for DPBS down to $1.7 \times 10^7 \pm 2.0 \times 10^6$ CFU/mL for NOPD. This equates to a ~0.44-log reduction in CFU.

Several factors likely contributed to the significant inter-day variability observed between CFU counts across treatment conditions. Bacterial aggregates, which are composed of numerous individual cells detached from the biofilm may form a single colony, potentially leading to an underestimation of the true bacterial count [408]. Groups of dispersed cells could potentially auto-aggregate in solution, further contributing to this effect [409]. Second, the presence of PDs adjacent to bacterial colonies on a culture plate could also affect the CFU count through coalescence and formation of bubble clusters. This was not observed macroscopically when culturing

CFU in these experiments, but it could be another source of CFU variability.

The observed reduction in CFU counts between treatment conditions compared to the DPBS control may be attributed to several mechanisms. The combined stress of elevated temperature, NO exposure, and/or US treatment could induce the formation of viable but non-culturable (VBNC) cells, resulting in a decrease in CFU counts [394]. Although *P. aeruginosa* PAO1 has been shown to grow at 45 °C, it is possible that the thermal stress to which it has been exposed in the present study (albeit short term) could affect CFU counts. The combined effects of thermal stress and other treatment conditions could synergistically impact bacterial viability and culturability [399].

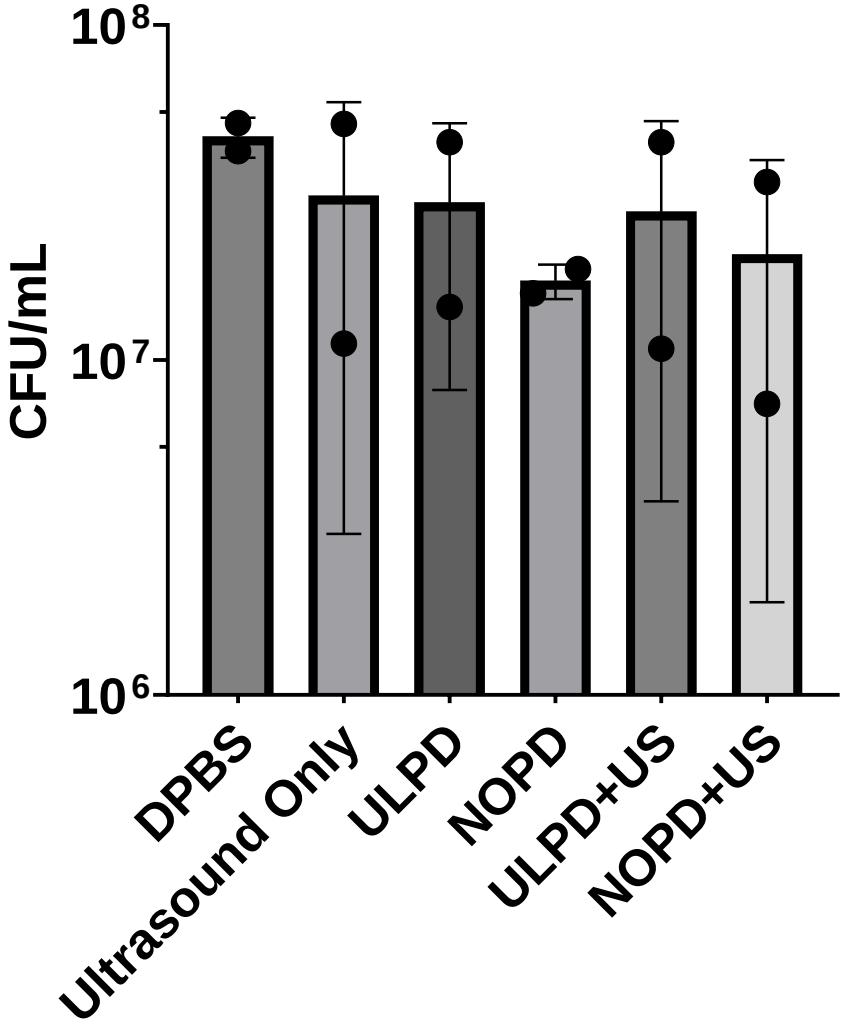

Figure 4.20: Quantification of viable bacteria following treatment of 48 h WCM PAO1 biofilms. CFU/mL recovered from the combined treatment and rinse volumes of biofilms subjected to various treatment conditions. Treatments: US-Only (Ultrasound only), ULPD (Unloaded PDs), NOPD (NO-loaded PDs), ULPD-US (Unloaded PDs with US-stimulation), NOPD (NO-PDs with US-stimulation). Each bar represents the mean CFU/mL, and error bars indicate ± 1 S.D.

Quantification of Biofilm Biomass

The changes in normalised biomass under different treatment conditions is shown in **Fig. 4.21**. Although no statistically significant differences (P>0.05) were observed between treatments, several trends were identified. The US-Only condition showed minimal change in biomass compared to the control, with a normalised biomass of 107.3 ± 16.1%. ULPD, NOPD, ULPD-US and NOPD-US treatments resulted in reduced normalised biomass values compared to control: 80.7 ± 7.98%, 86.3 ± 8.39%, 89.4 ± 23.8%, and 62.1 ± 8.20%, respectively. The NOPD-US treatment condition exhibited the largest decrease in biomass (37.9 % decrease). Both unloaded and NO-loaded PDs reduced biomass compared to the control.

Several factors could potentially explain the lack of statistical significance despite trends in biomass reduction. First, due to the temporal dynamics of biofilm dispersal, treatment durations longer than the brief 10-minute interval used in this study may be required. The time period necessary for dispersal can vary widely, with some studies observing dispersal over a 1 h period and others exposing biofilms to NO for up to 24 h [37, 410, 411].

Microscopy observations in *Section 4.3.3* revealed distinct bright rings surrounding gas pockets, suggesting that while the biofilm structure was physically disrupted, the biomass may have been compressed into denser clusters that remained biofilm-

associated and attached to the culture surface. This effect would result in biomass remaining available for safranin staining despite structural changes.

Additionally, spatial limitations of the FUS transducer output limits the treatment area. The small focal region of the FUS transducer limits US-stimulation effects to a 9.75 mm^2 region, which is substantially smaller than the 4.1 cm^2 culture area stained by safranin, covering only approximately 2.4% of the total staining area. This discrepancy could explain why there was no observable trend in biomass when comparing US and non-US stimulated conditions.

However, the non-US conditions also did not induce significant biomass decreases, suggesting that the small area of US-stimulation was not the only factor. While the NOPD-US treatment condition demonstrated the greatest decrease in biomass, this was a moderate reduction. With less than 50% biofilm removal, this level of efficacy would not represent a therapeutically viable outcome. Future work should explore alternative parameters such as longer incubation times or increasing the area exposed to US to improve antibiofilm effects.

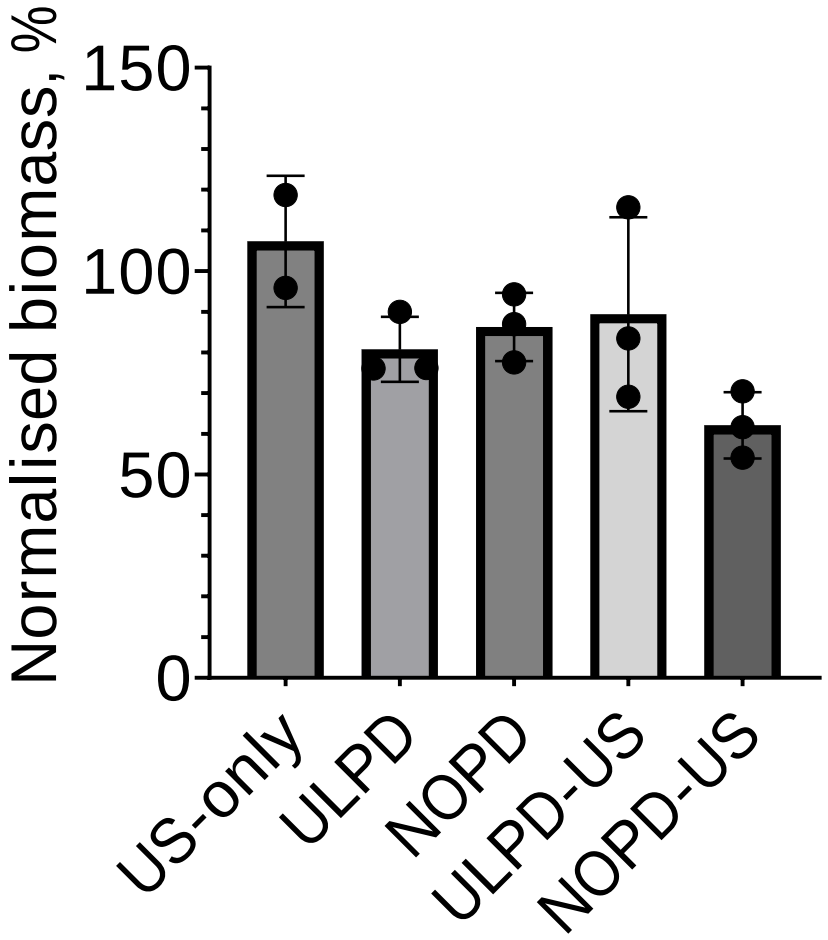

Figure 4.21: Effect of various treatments on WCM biofilm biomass. Quantification of remaining biofilm biomass following various treatments on 48 h WCM PAO1 biofilm. Biomass was quantified using a safranin stain and normalised to the DPBS control. Treatments: US-Only (Ultrasound only), ULPD (Unloaded PDs), NOPD (NO-loaded PDs), ULPD-US (Unloaded PDs with US-stimulation), NOPD (NO-PDs with US-stimulation). Each bar represents the mean normalised biomass, and error bars indicate ± 1 S.D. No significant difference between sample pairs ($P>0.05$).

Analysis of Biofilm Coverage Area

To assess changes in biofilm coverage area between control and treatment conditions, 4 × tile scans were captured after each treatment, encompassing an 8.192 mm × 8.192 mm area. Otsu thresholding was used to binarise the images and quantify biofilm coverage area. This method provides an estimate of the surface-attached portion of the biofilm remaining after the treatment and rinse steps. Images of SYTO9 **(Fig. 4.22)**, as well as PI and ConA **(Fig. 4.23)** channels were analysed and coverage areas compared. Significant differences were observed between DPBS and NOPD-US (*, P = 0.0133) and US-Only and NOPD-US (**, P = 0.0020). A slight increase in biofilm coverage was observed for the US-Only condition compared to the (DPBS control. The unloaded droplet conditions (ULPD and ULPD-US) showed similar decreases in mean coverage area, with post-treatment values of 12.2 ± 4.0 mm^2 and 10.9 ± 3.4 mm^2, respectively. The NOPD-US treatment condition had the largest decrease in SYTO9 coverage area compared to the control (63.1 ± 0.03%) **(Fig. 4.22)**.

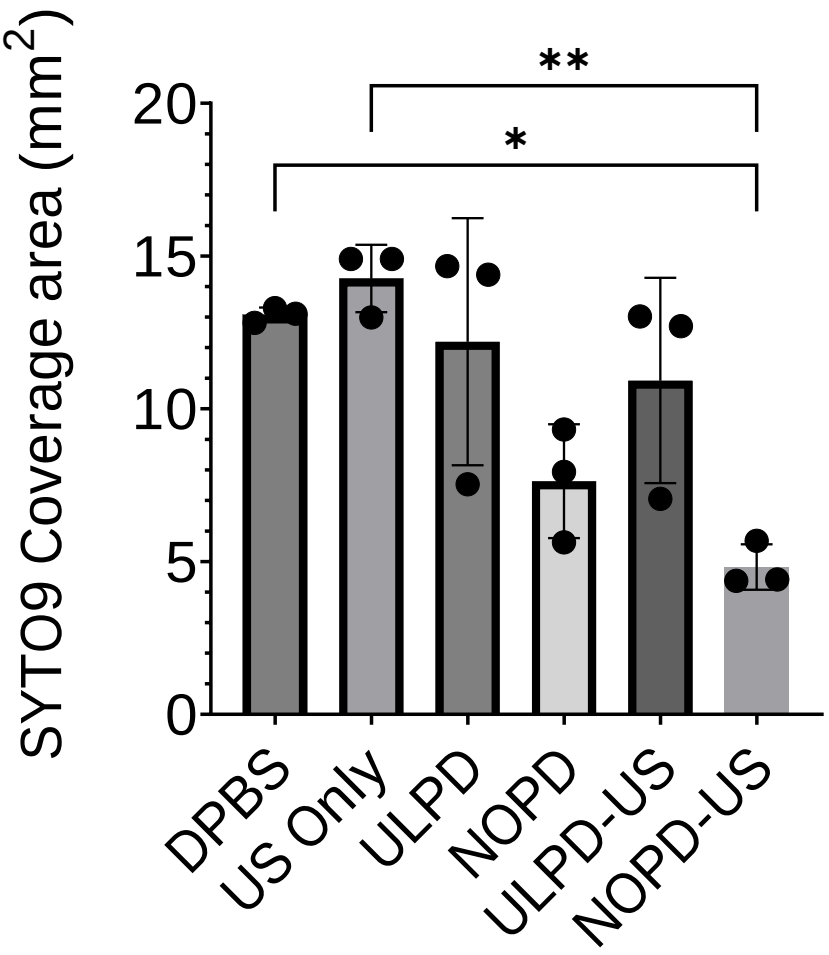

Figure 4.22: Coverage area of 48 h WCM PAO1 biofilms was compared post-treatment between different treatment conditions, measured from SYTO9 staining. Treatments: US-Only (Ultrasound only), ULPD (Unloaded PDs), NOPD (NO-loaded PDs), ULPD-US (Unloaded PDs with US-stimulation), NOPD (NO-PDs with US-stimulation). Each bar represents the mean biofilm coverage area in mm^2, and error bars indicate ± 1 S.D. (* = P<0.05), (** = P<0.01).

These trends were consistent across all three fluorescence channels (SYTO9, PI, and ConA). For the PI channel, there was a significant difference in coverage area between: DPBS and NOPD-US (**, P=0.0026), US-Only and NOPD (*, P=0.0341), and US-Only and NOPD-US (**, P=0.0095) **(Fig. 4.23)**. Similarly, for the ConA channel there was a significant difference in coverage area between: DPBS and NOPD-US (**, P=0.0016), US-Only and NOPD (*, P=0.0294), and US-Only and NOPD-US (**, P=0.0027) **(Fig. 4.23)**.

Although the qualitative observations in *Section 4.3.3* appear to show an NO-dependent effect on biofilm coverage area when comparing ULPD vs. NOPD and ULPD-US vs. NOPD-US conditions, there was no statistically significant difference when comparing the surface area of these treatments quantitatively. This trend suggests that either NO or the NO-loading process contributes to a decrease the biofilm coverage area, however the specific mechanism for this is unclear.

The rapid release of NO from NOPDs could induce dispersal and subsequently sensitise the biofilm to mechanical disruption by US stimulation. The release of NO from PDs could induce effects ranging from dispersal to a bactericidal effect, depending on the NO concentration, release kinetics and bacterial species [285, 412].

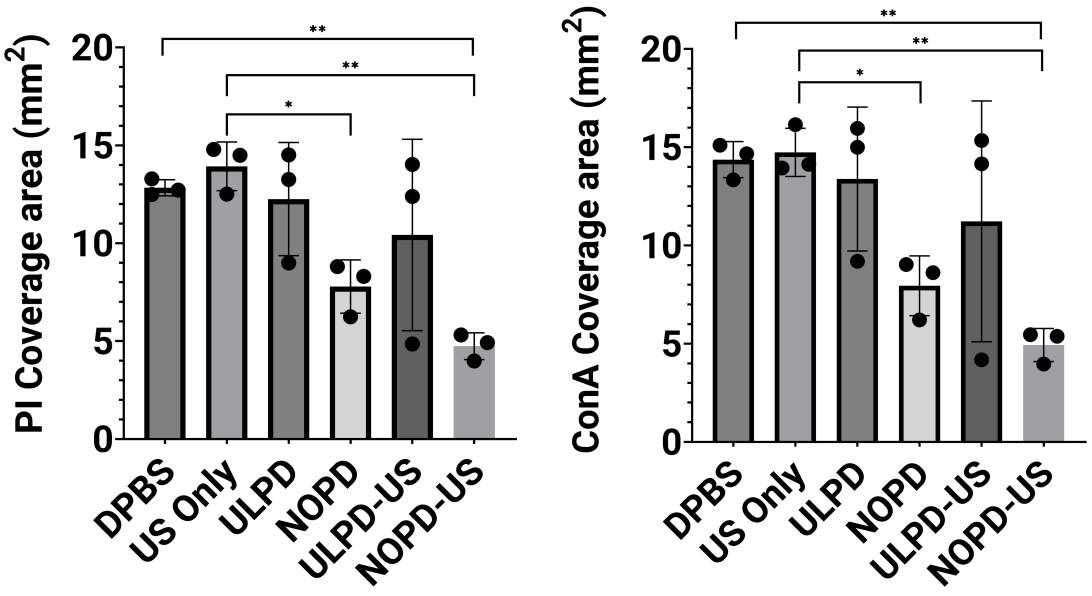

Figure 4.23: PI (left) and ConA (right) stain coverage area of 48 h WCM PAO1 biofilms after exposure to different treatment conditions. Treatments: US-Only (Ultrasound only), ULPD (Unloaded PDs), NOPD (NO-loaded PDs), ULPD-US (Unloaded PDs with US-stimulation), NOPD (NO-PDs with US-stimulation). Each bar represents the mean biofilm coverage area in μm^2, and error bars indicate $\pm$ 1 S.D. (* = P<0.05), (** = P<0.01)/

Quantification of Biovolume Changes

To further characterise the effects of the treatment conditions on biofilm structure, changes in biovolume were analysed across SYTO9, PI, and ConA fluorescence channels, using confocal z-stack images acquired before and after treatment. A significant challenge was noted during imaging of PD-treated samples, as the formation and coalescence of gas pockets caused continuous movement of the biofilm structure during z-stack acquisition.

This dynamic behavior severely affected the reliability of biovolume calculations. Statistical analysis revealed no significant differences ($P>0.05$) between treatment pairs across all three fluorescent channels. The SYTO9 biovolume represents bacterial cells (alive or dead) as well as eDNA present within the biofilm matrix **(Appendix Fig. A.3)** [386]. Analysis of SYTO9 staining revealed that the NOPD and NOPD-US treatment condition presented the largest decreases in biovolume of -14.2 ± 8.8 % and -18.9 ± 4.7 %, respectively. In contrast, the US-only condition resulted in an increase in biovolume of 27.1 ± 34.4 %, although there is a large amount of variability. PI is used to stain cells with compromised membrane integrity and is commonly used as an indicator of dead or membrane-damaged cells [383]. The PI biovolume decreased slightly for NOPD and NOPD-US conditions, while the remaining conditions showed slight increases in biovolume **(Appendix Fig. A.4)**.

ConA is a lectin that binds residues present in the EPS of biofilms, and was used to visualise the matrix structure. Across all fluorescence channels, the NOPD-US showed the greatest decrease in biovolume, which is consistent with the general trends seen in cell viability, biomass, and coverage area analyses discussed previously.

However, the high variability of the measurements and dynamic nature of the gas pockets during image acquisition make detailed analysis of the impact of these effects more difficult. To prevent movement of the biofilm, the use of a fixative agent such as paraformaldehyde to immobilise the structure of the EPS matrix would allow for unimpeded observation. Due to the bactericidal nature of this process, separate experiments would need to be incorporated to evaluate changes in cell viability for the treatment supernatant [413, 414].

Evaluation of Biofilm Thickness

Changes in biofilm thickness were quantified through the recording of the highest and lowest z-slice where bacterial cells were visible, both before and after treatment **(Appendix Fig. A.5)**. A limitation of the thickness measurement was its indirect nature, as the measurement solely used the z-value of the highest and lowest slice where bacteria were observed as an indicator of biofilm thickness. More sophisticated methods for calculating biofilm thickness are available, and are often implemented in conjunction with biovolume calculations using software packages such as BiofilmQ, which allows for the average biofilm thickness across a defined area to be calculated [415].

Similar to the biovolume calculations, the formation and coalescence of gas pockets caused continuous movement of the biofilm structure during z-stack acquisition, and strongly influenced the variability of these data. Fixation of the biofilm structure would likely improve the accuracy of thickness measurements by stabilizing the sample during imaging. This approach would also permit significantly longer acquisition times, which may be necessary to fully capture the axial effects of PD-mediated disruption, as certain sections of the biofilm appeared to be displaced substantially above the culture surface compared with the DPBS control **(Fig. 4.17, ULPD-US)**.

Although no statistically significant difference was observed between treatments, the following observations were made: All PD treatment conditions resulted in increased biofilm thickness, with the NOPD-US condition having the largest increase (49.8 ± 38.6 µm). In contrast, both DPBS and ULPD samples showed a decrease in biofilm thickness post-treatment, likely due to the effect of fluid shear removing some surface-detached biofilm when rinsing between stain and treatment steps. The observed increase in the thickness of the biofilm with PD treatments, combined with the formation of large gas pockets, suggests a potential mechanism for enhancing antimicrobial efficacy.

By increasing the exposed surface area of the biofilm, PD treatments could potentially reduce the proximity between antimicrobial agents and biofilm aggregates. In combination with the physical effects of US-mediated biofilm disruption, this could aid in increasing the efficacy and delivery of antimicrobials to the biofilm. This hypothesis is consistent with previous studies that demonstrate improved antibiotic efficacy when combined with physical disruption methods [229, 287]. Future studies could validate this effect through combination therapy with clinically relevant antibiotics such as gentamicin.

4.4 Conclusion

This *Chapter* evaluated the effect of US-activated NO-loaded PDs on a CW biofilm model. Initial work using a high-speed imaging setup revealed consistent ADV at 0.5 MHz and 2.48 MPa peak negative pressure at 39 °C within the first three US cycles. These parameters were selected for subsequent biofilm studies, employing a conservative PRF (1 Hz) and total exposure duration (60 s), compared to previous literature stimulating PDs on biofilm models. The combination of NO-loaded PDs with US-stimulation (NOPD-US) exhibited the most consistent biofilm disrupting effects across multiple analytical methods. This treatment condition achieved the greatest reduction in biofilm biomass, coverage area, and biovolume, potentially suggesting an additive effect between NO-mediated dispersal and the physical disruption effect of US-activated PDs. Significant reductions in biofilm coverage area were observed between NOPD-US and both DPBS and US-Only conditions. Interestingly, NO-loaded PDs were shown to induce biofilm disruption without US-stimulation. The formation of gas pockets was observed by microscopy for all PD treatment conditions, with NOPDs stimulated with US observed to have the strongest biofilm disrupting effect. This phenomena could be exploited in future studies as a means of increasing exposure of the biofilm structure to the action of antimicrobials.

The effect of passive incubation also merits further exploration, with the poten-

tial for significant disruption without US stimulation. No significant morphological changes were observed within the focal region of the US field, supporting the necessity of cavitation nuclei under these US parameters to mediate biofilm disrupting effects. Although these results demonstrate promise for this therapeutic approach, several limitations warrant consideration. These will discussed in *Chapter 5*. In conclusion, this work establishes the potential of NO-loaded PDs combined with US-activation as a novel strategy for CW biofilm disruption. The demonstrated effects on biofilm structure and viability warrant further development of this approach for CW treatment.

Chapter 5

Conclusions, Limitations and Future Directions

5.1 Conclusions

This *Thesis* explored the development of nitric oxide (NO)-loaded perfluorocarbon droplets (PDs), a novel approach towards the treatment of chronic wound (CW) biofilms. CWs such as diabetic foot ulcers (DFUs) present a significant health-care challenge that affects millions of patients worldwide and substantially burdens healthcare systems [1, 2]. The presence of bacterial biofilms within these wounds represent a key obstacle in their treatment and resolution, in part due to the biofilm's increased resistance to antimicrobial therapies [10]. The biofilm extracellular poly-

meric substances (EPS) matrix acts as a physical barrier to antimicrobial penetration. Additional bacterial resistance mechanisms, such as the persister cell phenotype, contribute to the tolerance of biofilms within the wound and allow for infections to repeatedly recolonise the wound after conventional treatment methods have been applied [19]. Recent approaches have explored the use of a range of stimuli-responsive drug delivery systems as an alternative to these conventional therapies. Ultrasound (US)-responsive particles such as gas microbubbles (MBs), have shown promise as a means to physically disrupt the biofilm and sensitise bacteria to antimicrobials [228].

PDs present several potential advantages over MBs, including improved stability and the ability to undergo a phase change into US-responsive MBs, a process termed acoustic droplet vaporisation (ADV). US-activated PDs have shown promise in combination with antimicrobials as a strategy to treat biofilms [300]. In addition, the high gas solubility of liquid perfluorocarbons has attracted attention for the use of PDs as bioactive gas carriers [31, 35].

NO in particular is of key interest due to its ability to induce the dispersal of bacterial biofilms [37]. These mechanisms could be exploited in the context of antibacterial therapies, due to the increased susceptibility of dispersed bacteria to

antibiotic compounds [105, 286]. However, the high reactivity and short half-life of NO introduces difficulties in its delivery, highlighting a need for alternative delivery vehicles such as PDs [34]. To the best of the author's knowledge, the use of US-responsive NO-loaded droplets as an anti-biofilm modality has not been investigated in previous research.

As discussed in *Chapter 1*, several key research gaps were identified. There was a need for the development of reproducible methods of PD manufacture that allowed the formulation to be adjusted to desired characteristics. Additionally, despite the established potential of PDs as gas carriers, there was very limited characterisation of the loading of NO into PDs in previous studies. Finally, the combination of NO-loaded PDs activated by US remained unexplored as a potential biofilm therapy. As such, the aim of this project was to develop a treatment solution for biofilms in chronic wounds. It was hypothesised that NO-loaded PDs could exert anti-biofilm effects due to the combined action of physical (US-induced) and biochemical (NO-induced) dispersal.

The challenge of developing a reproducible manufacturing method for PDs by sonication was addressed in *Chapter 2*. The development of a controlled positioning apparatus enabled precise and repeatable placement of the sonicator tip within the sample vessel. Given PFP's bulk boiling point of 29.2 °C, sample temperature

control was essential during PD manufacture. Various sonication pulse regimes were assessed alongside an ice-water and ice-saline cooling bath. A 2 s on, 15 s off pulse regime at 60% sonication amplitude successfully maintained sample temperatures below 15°C when combined with an ice-water bath. Higher sonication intensities (80-100% amplitude) led to increased sample heating, and so the 2 s on, 15 s off pulse regime with ice-water bath was selected for all further experiments.

The effects of varying sonicator tip height, PFP volumetric concentration, sonication intensity, and sonication duration on PD size characteristics were assessed by nanoparticle tracking analysis (NTA). Of these parameters, PFP volumetric concentration emerged as the dominant variable, with increasing PFP concentration corresponding to larger median droplet diameters. Additionally, the relationship between PFP concentration and particle diameter strengthened with increasing tip height, and was suggested to be due to more effective sample mixing [337]. The presence of >1 µm particles observed by light microscopy for PDs manufactured with >9.09 % PFP prompted the use of resistive pulse sensing (RPS) to quantitatively assess the presence of these larger droplets. Increasing PFP concentration (from 4.76% to 16.7% v/v) led to a consistent increase in median droplet diameter (0.54 ± 0.008 µm to 0.76 ± 0.03 µm, respectively).

Building on these insights, *Chapter 3* investigated methods for loading NO into PDs. The effect of a wider range of PFP volumetric concentrations on PD size characteristics was also assessed, as varying the amount of PFP may impact the NO loading capacity of PDs. Increasing the PFP concentration (from 10% to 50% v/v) significantly increased the median PD diameter and caused the formation of a secondary population of larger droplets. Inconsistent mixing during sonication was observed for 40% and 50% PFP PDs, and so development continued on the 10% and 20% PFP formulations. Due to the high reactivity of NO, an oxygen-free NO-loading method was developed for PDs. NO_x concentrations were characterised using an ozone-based chemiluminescence method in both 10% (4.31 ± 0.92 µM) and 20% (4.57 ± 0.34 µM) PFP PDs. The 20% v/v PFP formulation was selected for further development as it achieved a larger droplet size compared to the 10% PFP samples, which had the potential to reduce NO diffusion rates and would also be advantageous in reducing the US pressure magnitudes needed to achieve ADV .

Chapter 4 combined developments from the previous chapters to evaluate the potential of NO-loaded PDs as an anti-biofilm therapy. High-speed imaging of US-stimulated PDs established the parameters required for consistent ADV: 0.5 MHz, 2.48 MPa peak negative pressure, and a temperature of 39 °C. NO-loaded PDs combined with US (NOPD-US) demonstrated the most substantial anti-biofilm effects on a *P. aeruginosa* CW biofilm model across multiple assessment methods. The NOPD-US treatment achieved the greatest reduction in biomass (37.9% ± 8.20%) and reduction in coverage area (63.1 ± 0.03%) compared to all other conditions. NO-loaded PDs alone also resulted in a decrease in cell viability, biofilm coverage area and biovolume. Both NO-loaded treatment conditions (NOPD, NOPD-US) showed increased anti-biofilm effects over unloaded conditions (ULPD, ULPD-US). The estimated mean NO_x concentration of the NO-loaded PDs applied to biofilms was 67.5 ± 2.5 nM, within the concentration range known to induce biofilm dispersal. The effect of PD incubation on the morphology of the biofilm was distinct. All PD treatment conditions demonstrated the formation of gas pockets that appeared to disrupt the greater biofilm structure. These disruption effects increased with the addition of NO and US, suggesting a potential additive effect between NO- and US-induced disruption of the biofilm. The formation of gas pockets appears to disrupt the biofilm structure through the formation of hemispherical voids, and could potentially increase the surface area available for antimicrobials to act upon.

Overall, the findings in this *Thesis* establish for the first time the potential of US-activated NO-loaded PDs as a therapeutic strategy for the management of CW biofilms. The demonstrated effects on biofilm structure and biomass warrant further development of this approach towards CW biofilm treatment.

5.2 Limitations and Future Work

Throughout the development, characterisation, and evaluation of US-responsive NO-loaded PDs for CW biofilm treatment, several limitations were recognised that provide opportunities for further investigation.

The study in *Chapter 2* could be expanded through the assessment of PD stability in a range of physiologically relevant conditions. While the focus of this study was to understand the effect of manufacturing parameters on PD characteristics, the stability and behaviour of PDs in biological fluids such as blood, plasma, or urine would be crucial for potential broader clinical applications. Timelapse microscopy would be useful for observing the behaviour of PDs within these media, for example to observe spontaneous vaporisation. Investigation of alternative core and shell component presents another area for future exploration. Alternative PFC cores could enable the development of PDs for use in passive gas transport, which would not rely on US-activation to mediate a therapeutic event. For example, higher

boiling point PFCs such as perfluorodecalin (PFD, boiling point 142 °C) could offer additional stability [416]. Furthermore, modifying the composition of the lipid shell could be explored to enhance stability in specific physiological environments and interaction with intended therapeutic targets [417, 418].

Evaluation of NO release kinetics from PDs is a logical progression of the work presented in *Chapter 3*. Although the literature exploring NO release from PDs is limited, quantification of real-time release through chemiluminescence is reported in previous studies by Choi *et al.* [297, 342]. However, the large variation in reported release duration and total NO concentration values signifies that further explorations are warranted. The concentration and duration of NO exposure are crucial parameters that determine whether a dispersal or even bactericidal effect is mediated [419, 420]. Research into the kinetics of NO release from NO donors has shown that prolonged release can be beneficial in achieving biofilm dispersal [421]. The characterisation of NO-release profiles from PDs would allow comparison with other studies developing NO-releasing particles and enable further development towards improved therapeutic outcomes. This is especially important considering the role that NO can play in promoting wound healing [283].

While *P. aeruginosa* PAO1 is a clinically relevant pathogen in chronic wounds, the evaluation of NOPDs on a multi-species model would more closely replicate the often polymicrobial nature of CW infections. Indeed, mixed *P. aeruginosa* and *S. aureus* biofilms have been shown to have increased tolerance to antibiotics compared to mono-species communities [422, 423]. Future work could also use *in vivo* biofilm models, such as the multispecies mouse CW model developed by Dalton *et al.*, to provide improved therapeutic relevance [424]. The selection of US parameters presents another area to consider developing further. Although current parameters successfully induced ADV in PDs, the low PRF (1 Hz) and total duration (60 s) could be increased to potentially improve anti-biofilm outcomes through an increase in mediated physical effects.

Following this reasoning, the short treatment time (10 min) could be increased in line with other studies investigating both NO-mediated dispersal and wound therapies, to assess whether these prolonged exposure may increase anti-biofilm efficacy. Several studies investigating NO-mediated dispersal using NO-donors have used treatment times from 1 h to 24 h [279, 419, 425]. Future work could include the combination of NO-loaded PDs and US-activation with an antibiotic such as gentamicin. Previous work using a combination of NO delivery, US-nuclei and gentamycin or meropenem to treat CW biofilm models has shown promise [287, 299].

Furthermore, profiling changes in bacterial genetic expression in response to treatment can provide a useful mechanistic perspective and enable the development of more effective therapies [231, 426, 427]. Additional approaches could be taken to improve the analysis of biofilms post-treatment. Difficulties were encountered when imaging biofilms in *Chapter 4* due to the dynamic nature of the gas pockets formed over time. The use of a fixative agent, such as paraformaldehyde, could be used preserve the biofilm architecture at a specific time point and allow a more detailed analysis of the biofilm structure [428, 429].

Key Parameters for PD Development

Among all the different parameters tested in this *Thesis*, several were found to be particularly influential on PD characteristics. The diameter and size distribution of PDs emerged as crucial when determining suitable therapeutic targets. For example, if biofilm penetration is required, then PDs within the nanometre range, potentially as small as 100 nm will be required depending on species composition of the biofilm [402]. This is supported by the observations in *Chapter 4*, where larger PDs (>1 µm) were observed to remain adjacent to biofilm clusters rather than penetrating into them. However, given the effects observed in *Chapter 4*, penetration may not be a necessary characteristic to develop towards for physical disruption of the EPS matrix.

A critical bottleneck in the development of NO-loaded PDs is the limited understanding of NO-release profiles, and the limited literature on real-time or total NO release measurements, as discussed in *Chapter 3*. Future work should prioritise accurate characterisation of NO-release kinetics, as this is paramount to tailoring the effect of the NO payload within these PD formulations. Alternatively, the incorporation of NO-donors rather than molecular NO gas within PD formulations could be a beneficial step towards achieving a longer NO-release profile, which has shown success at promoting biofilm dispersal and could avoid the deleterious effect of excessive NO delivery potentially damaging off-target tissues [285, 410]. The acoustic responsiveness of PDs is another key parameter that directly impacts therapeutic efficacy.

The results in *Chapter 4* demonstrated that a temperature-dependent ADV threshold was present for the selected PD formulation. This presents translational challenges as the high temperature threshold could limit where PDs can be applied therapeutically. For thermally sensitive targets, it is pertinent that further characterisation and adjustment of PD characteristics that can lower the temperature required to achieve ADV are explored. To reduce this dependence on a 39 °C incubation temperature, exploring parameters such as increased peak rarefactional pressure, lower-boiling point PFCs, and PD shell composition could lower

the temperature dependence [242, 430]. Additionally, the modification of PD shell components and manufacture of larger diameter PDs to reduce their stability could increase the propensity for spontaneous vaporisation events to occur upon biofilm interaction and mediate anti-biofilm effects without the need for US-stimulation.

5.3 Future Directions

From a therapeutic translation perspective, US-responsive NO-loaded PDs could be developed in a number of ways. The development of a suitable delivery platform is a key step toward clinical translation. Recent advances in wearable, flexible transducers show encouraging progress towards accessible therapies that can be personalised to better fit individual patients [431]. For example, van Neer *et al.* developed a piezoelectric polymer into a flexible transducer-array that could potentially be incorporated into a skin patch [432]. Flexible ultrasonic patches offer a potential link between conventional wound therapies and advanced treatments. Additionally, PDs could be incorporated into conventional wound management devices, such as wound dressings or topical creams.

3D bioprinting is another area showing promise and could be combined with US-responsive therapies. The use of printable hydrogels could lead to the development of

personalised wound patches that match the specific geometry of a CW **(Fig. 5.1)** while maintaining US compatibility. Given that these wounds can be extremely varied in topology, advances in this area could significantly improve the feasibility of applying these therapies to CWs. In addition to the treatment of CWs, NO-loaded PDs could be applied to other types of bacterial infections. Device-associated and urinary tract infections both represent a significant clinical burden that could benefit from the combination of NO-delivery and US-mediated physical disruption. For example, PD formulations could be administered through a urinary catheter into the bladder and subsequently activated using an extracorporeal US probe.

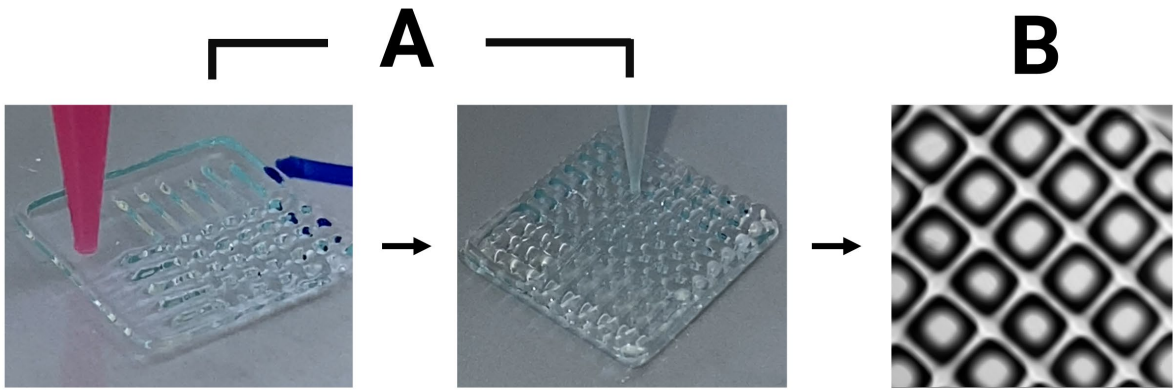

Figure 5.1: Test wound patch print using a 3D bioprinter (CELLINK BIO X6) performed in the present study. **(A)** Test prints of polypropylene glycol gel, forming a tight multilayered grid designed to emulate the morphology of a wound patch. **(B)** Optical microscopy to examine the geometry of apertures within the grid structure. These apertures could potentially be loaded with US-responsive therapies.

Bibliography

[1] X. Zhang, W. Shu, Q. Yu, W. Qu, Y. Wang, and R. Li, "Functional biomaterials for treatment of chronic wound," *Frontiers in Bioengineering and Biotechnology*, vol. 8, p. 516, 2020.

[2] C. K. Sen, "Human wounds and its burden: an updated compendium of estimates," 2019.

[3] J. Posnett and P. J. Franks, "The burden of chronic wounds in the uk," *Nursing times*, vol. 104, no. 3, pp. 44–45, 2008.

[4] J. F. Guest, G. W. Fuller, and P. Vowden, "Cohort study evaluating the burden of wounds to the uk's national health service in 2017/2018: update from 2012/2013," *BMJ open*, vol. 10, no. 12, p. e045253, 2020.

[5] G. Han and R. Ceilley, "Chronic wound healing: a review of current management and treatments," *Advances in therapy*, vol. 34, no. 3, pp. 599–610, 2017.

[6] M. Mahmoudi and L. J. Gould, "Opportunities and challenges of the management of chronic wounds: A multidisciplinary viewpoint," *Chronic Wound Care Management and Research*, vol. 7, p. 27, 2020.

[7] D. Pai and S. Madan, "Techniques in chronic wound management: review of the literature and recent concepts," *J Nov Physiother*, vol. 3, no. 2, p. 134, 2013.

[8] A. J. Boulton, L. Vileikyte, G. Ragnarson-Tennvall, and J. Apelqvist, "The global burden of diabetic foot disease," *The Lancet*, vol. 366, no. 9498, pp. 1719–1724, 2005.

[9] M. Fazli, T. Bjarnsholt, K. Kirketerp-Møller, B. Jørgensen, A. S. Andersen, K. A. Krogfelt, M. Givskov, and T. Tolker-Nielsen, "Nonrandom distribution of pseudomonas aeruginosa and staphylococcus aureus in chronic wounds," *Journal of clinical microbiology*, vol. 47, no. 12, pp. 4084–4089, 2009.

[10] D. Sharma, L. Misba, and A. U. Khan, "Antibiotics versus biofilm: an emerging battleground in microbial communities," *Antimicrobial Resistance & Infection Control*, vol. 8, pp. 1–10, 2019.

[11] H. Ceri, M. E. Olson, C. Stremick, R. Read, D. Morck, and A. Buret, "The calgary biofilm device: new technology for rapid determination of antibiotic susceptibilities of bacterial biofilms," *Journal of clinical microbiology*, vol. 37, no. 6, pp. 1771–1776, 1999.

[12] G. Seabrook, C. Edmiston, D. Schmitt, C. Krepel, D. Bandyk, and J. Towne, "Comparison of serum and tissue antibiotic levels in diabetes-related foot infections.," *Surgery*, vol. 110, no. 4, pp. 671–6, 1991.

[13] E. Olivares, S. Badel-Berchoux, C. Provot, G. Prévost, T. Bernardi, and F. Jehl, "Clinical impact of antibiotics for the treatment of pseudomonas aeruginosa biofilm infections," *Frontiers in microbiology*, vol. 10, p. 2894, 2020.

[14] R. K. Thapa, J. O. Kim, and J. Kim, "Antimicrobial strategies for topical biofilm-based wound infections: past, present, and future," *Journal of Pharmaceutical Investigation*, vol. 53, no. 5, pp. 627–641, 2023.

[15] L. Karygianni, Z. Ren, H. Koo, and T. Thurnheer, "Biofilm matrixome: extracellular components in structured microbial communities," *Trends in microbiology*, vol. 28, no. 8, pp. 668–681, 2020.

[16] H. Niu, J. Gu, and Y. Zhang, "Bacterial persisters: molecular mechanisms and therapeutic development," *Signal transduction and targeted therapy*, vol. 9, no. 1, p. 174, 2024.

[17] H. F. Stewart, J. L. Abzug, and G. R. Harris, "Considerations in ultrasound therapy and equipment performance," *Physical Therapy*, vol. 60, no. 4, pp. 424–428, 1980.

[18] K. Lewis, "Persister cells," *Annual review of microbiology*, vol. 64, no. 1, pp. 357–372, 2010.

[19] T. K. Wood, S. J. Knabel, and B. W. Kwan, "Bacterial persister cell formation and dormancy," *Applied and environmental microbiology*, vol. 79, no. 23, pp. 7116–7121, 2013.

[20] N. Vyas, K. Manmi, Q. Wang, A. J. Jadhav, M. Barigou, R. L. Sammons, S. A. Kuehne, and A. D. Walmsley, "Which parameters affect biofilm removal with acoustic cavitation? a review," *Ultrasound in medicine & biology*, vol. 45, no. 5, pp. 1044–1055, 2019.

[21] A. A. Ciarolla, N. Lapin, D. Williams, R. Chopra, and D. E. Greenberg, "Physical approaches to prevent and treat bacterial biofilm," *Antibiotics*, vol. 12, no. 1, p. 54, 2022.

[22] M. Erriu, C. Blus, S. Szmukler-Moncler, S. Buogo, R. Levi, G. Barbato, D. Madonnaripa, G. Denotti, V. Piras, and G. Orrù, "Microbial biofilm modulation by ultrasound: current concepts and controversies," *Ultrasonics sonochemistry*, vol. 21, no. 1, pp. 15–22, 2014.

[23] J. C. Carmen, C. M. Runyan, R. A. Robison, J. L. Nelson, B. L. Beckstead, W. G. Pitt, and G. B. Schaalje, "Ultrasonic-enhanced gentamicin transport through colony biofilms of pseudomonas aeruginosa and escherichia coli," *Journal of Infection and Chemotherapy*, vol. 10, no. 4, pp. 193–199, 2004.

[24] S. M. J. Mortazavi, L. Darvish, M. Abounajmi, S. Zarei, T. Zare, M. Taheri, and S. Nematollahi, "Alteration of bacterial antibiotic sensitivity after short-term exposure to diagnostic ultrasound," *Iranian Red Crescent medical journal*, vol. 17, no. 11, 2015.

[25] Y. Dong, S. Chen, Z. Wang, N. Peng, and J. Yu, "Synergy of ultrasound microbubbles and vancomycin against staphylococcus epidermidis biofilm," *Journal of Antimicrobial Chemotherapy*, vol. 68, no. 4, pp. 816–826, 2013.

[26] N. He, J. Hu, H. Liu, T. Zhu, B. Huang, X. Wang, Y. Wu, W. Wang, and D. Qu, "Enhancement of vancomycin activity against biofilms by us-

ing ultrasound-targeted microbubble destruction," *Antimicrobial Agents and Chemotherapy*, vol. 55, no. 11, pp. 5331–5337, 2011.

[27] Y. Dong, Y. Xu, P. Li, C. Wang, Y. Cao, and J. Yu, "Antibiofilm effect of ultrasound combined with microbubbles against staphylococcus epidermidis biofilm," *International Journal of Medical Microbiology*, vol. 307, no. 6, pp. 321–328, 2017.

[28] K. Kooiman, S. Roovers, S. A. Langeveld, R. T. Kleven, H. Dewitte, M. A. O'Reilly, J.-M. Escoffre, A. Bouakaz, M. D. Verweij, K. Hynynen, *et al.*, "Ultrasound-responsive cavitation nuclei for therapy and drug delivery," *Ultrasound in medicine & biology*, vol. 46, no. 6, pp. 1296–1325, 2020.

[29] A. Halford, C.-D. Ohl, A. Azarpazhooh, B. Basrani, S. Friedman, and A. Kishen, "Synergistic effect of microbubble emulsion and sonic or ultrasonic agitation on endodontic biofilm in vitro," *Journal of endodontics*, vol. 38, no. 11, pp. 1530–1534, 2012.

[30] P. G. Durham, A. E. Sidders, J. E. Beam, K. M. Kedziora, P. A. Dayton, B. P. Conlon, V. Papadopoulou, and S. E. Rowe, "Harnessing ultrasound-stimulated phase change contrast agents to improve antibiotic efficacy against methicillin-resistant staphylococcus aureus biofilms," *Biofilm*, vol. 3, p. 100049, 2021.

[31] N. Rapoport, "Phase-shift, stimuli-responsive perfluorocarbon nanodroplets for drug delivery to cancer," *Wiley Interdisciplinary Reviews: Nanomedicine and Nanobiotechnology*, vol. 4, no. 5, pp. 492–510, 2012.

[32] P. S. Sheeran and P. A. Dayton, "Phase-change contrast agents for imaging and therapy," *Current pharmaceutical design*, vol. 18, no. 15, pp. 2152–2165, 2012.

[33] J. G. Riess, "Oxygen carriers ("blood substitutes") raison d'être, chemistry, and some physiology blut ist ein ganz besondrer saft," *Chemical reviews*, vol. 101, no. 9, pp. 2797–2920, 2001.

[34] M. P. Krafft and J. G. Riess, "Therapeutic oxygen delivery by perfluorocarbon-based colloids," *Advances in Colloid and Interface Science*, vol. 294, p. 102407, 2021.

[35] P. Cabrales, B. Y. S. Vázquez, A. C. Negrete, and M. Intaglietta, "Perfluorocarbons as gas transporters for o2, no, co and volatile anesthetics," *Transfusion Alternatives in Transfusion Medicine*, vol. 9, no. 4, pp. 294–303, 2007.

[36] D. Ortiz, P. Cabrales, and J. C. Briceño, "Transport of nitric oxide by perfluorocarbon emulsion," *Biotechnology progress*, vol. 29, no. 6, pp. 1565–1572, 2013.

[37] N. Barraud, D. Schleheck, J. Klebensberger, J. S. Webb, D. J. Hassett, S. A. Rice, and S. Kjelleberg, "Nitric oxide signaling in pseudomonas aeruginosa biofilms mediates phosphodiesterase activity, decreased cyclic di-gmp levels, and enhanced dispersal," *Journal of bacteriology*, vol. 191, no. 23, pp. 7333–7342, 2009.

[38] M. Witte, T. Kiyama, and A. Barbul, "Nitric oxide enhances experimental wound healing in diabetes," *British journal of surgery*, vol. 89, no. 12, pp. 1594–1601, 2002.

[39] G. LuTheryn, C. Hind, P. Glynne-Jones, J. S. Webb, J. M. Sutton, and D. Carugo, "Ultrasound-responsive bioactive-microbubbles for the eradication of biofilms," in *24th Eur. Symp. Ultrasound Contrast Imaging*, 2019.

[40] K. A. Walters and M. S. Roberts, "The structure and function of skin," in *Dermatological and transdermal formulations*, pp. 19–58, CRC press, 2002.

[41] M. Boer, E. Duchnik, R. Maleszka, and M. Marchlewicz, "Structural and biophysical characteristics of human skin in maintaining proper epidermal barrier function," *Advances in Dermatology and Allergology/Postępy Dermatologii i Alergologii*, vol. 33, no. 1, pp. 1–5, 2016.

[42] C. Parrado, S. Mercado-Saenz, A. Perez-Davo, Y. Gilaberte, S. Gonzalez, and A. Juarranz, "Environmental stressors on skin aging. mechanistic insights," *Frontiers in pharmacology*, vol. 10, p. 759, 2019.

[43] S. Dhivya, V. V. Padma, and E. Santhini, "Wound dressings–a review," *BioMedicine*, vol. 5, no. 4, pp. 1–5, 2015.

[44] G. C. Gurtner, S. Werner, Y. Barrandon, and M. T. Longaker, "Wound repair and regeneration," *Nature*, vol. 453, no. 7193, pp. 314–321, 2008.

[45] S. A. Eming, T. Krieg, and J. M. Davidson, "Inflammation in wound repair: molecular and cellular mechanisms," *Journal of Investigative Dermatology*, vol. 127, no. 3, pp. 514–525, 2007.

[46] L. Cañedo-Dorantes and M. Cañedo-Ayala, "Skin acute wound healing: a comprehensive review," *International journal of inflammation*, vol. 2019, 2019.

[47] I. George Broughton, J. E. Janis, and C. E. Attinger, "Wound healing: an overview," *Plastic and reconstructive surgery*, vol. 117, no. 7S, pp. 1e–S, 2006.

[48] M. H. Periayah, A. S. Halim, and A. Z. M. Saad, "Mechanism action of platelets and crucial blood coagulation pathways in hemostasis," *International journal of hematology-oncology and stem cell research*, vol. 11, no. 4, p. 319, 2017.

[49] N. Laurens, P. d. Koolwijk, and M. De Maat, "Fibrin structure and wound healing," *Journal of Thrombosis and Haemostasis*, vol. 4, no. 5, pp. 932–939, 2006.

[50] E. Kolaczkowska and P. Kubes, "Neutrophil recruitment and function in health and inflammation," *Nature reviews immunology*, vol. 13, no. 3, pp. 159–175, 2013.

[51] T. A. Wilgus, S. Roy, and J. C. McDaniel, "Neutrophils and wound repair: positive actions and negative reactions," *Advances in wound care*, vol. 2, no. 7, pp. 379–388, 2013.

[52] A. Gonzalez, T. Costa, Z. Andrade, and A. Medrado, "Wound healing–a literature review. anais brasileiros de dermat 91: 614–620," 2016.

[53] N. X. Landén, D. Li, and M. Ståhle, "Transition from inflammation to proliferation: a critical step during wound healing," *Cellular and Molecular Life Sciences*, vol. 73, no. 20, pp. 3861–3885, 2016.

[54] J. Li, J. Chen, and R. Kirsner, "Pathophysiology of acute wound healing," *Clinics in dermatology*, vol. 25, no. 1, pp. 9–18, 2007.

[55] F. Cheng, Y. Shen, P. Mohanasundaram, M. Lindström, J. Ivaska, T. Ny, and J. E. Eriksson, "Vimentin coordinates fibroblast proliferation and keratinocyte differentiation in wound healing via tgf-β–slug signaling," *Proceedings of the National Academy of Sciences*, vol. 113, no. 30, pp. E4320–E4327, 2016.

[56] M. Alhajj and A. Goyal, "Physiology, granulation tissue," in *StatPearls [Internet]*, StatPearls Publishing, 2021.

[57] L. Häkkinen, H. Larjava, and L. Koivisto, "Granulation tissue formation and remodeling," *Endodontic Topics*, vol. 24, no. 1, pp. 94–129, 2011.

[58] S. A. Eming, P. Martin, and M. Tomic-Canic, "Wound repair and regeneration: mechanisms, signaling, and translation," *Science translational medicine*, vol. 6, no. 265, pp. 265sr6–265sr6, 2014.

[59] G. FrykbergRobert *et al.*, "Challenges in the treatment of chronic wounds," *Advances in wound care*, 2015.

[60] S. a. Guo and L. A. DiPietro, "Factors affecting wound healing," *Journal of dental research*, vol. 89, no. 3, pp. 219–229, 2010.

[61] K. Anderson and R. L. Hamm, "Factors that impair wound healing," *Journal of the American College of Clinical Wound Specialists*, vol. 4, no. 4, pp. 84–91, 2012.

[62] International Diabetes Federation, "IDF Diabetes Atlas, 10th edition." `https://diabetesatlas.org/`, 2021. Accessed: 2024-10-07.

[63] J. L. Burgess, W. A. Wyant, B. Abdo Abujamra, R. S. Kirsner, and I. Jozic, "Diabetic wound-healing science," *Medicina*, vol. 57, no. 10, p. 1072, 2021.

[64] G. K. Kolluru, S. C. Bir, and C. G. Kevil, "Endothelial dysfunction and diabetes: effects on angiogenesis, vascular remodeling, and wound healing," *International journal of vascular medicine*, vol. 2012, 2012.

[65] U. A. Okonkwo and L. A. DiPietro, "Diabetes and wound angiogenesis," *International journal of molecular sciences*, vol. 18, no. 7, p. 1419, 2017.

[66] C. Rask-Madsen and G. L. King, "Vascular complications of diabetes: mecha-

nisms of injury and protective factors," *Cell metabolism*, vol. 17, no. 1, pp. 20–33, 2013.

[67] A. Berbudi, N. Rahmadika, A. I. Tjahjadi, and R. Ruslami, "Type 2 diabetes and its impact on the immune system," *Current diabetes reviews*, vol. 16, no. 5, p. 442, 2020.

[68] C. K. Sen, "Wound healing essentials: let there be oxygen," *Wound repair and regeneration*, vol. 17, no. 1, pp. 1–18, 2009.

[69] C. Dunnill, T. Patton, J. Brennan, J. Barrett, M. Dryden, J. Cooke, D. Leaper, and N. T. Georgopoulos, "Reactive oxygen species (ros) and wound healing: the functional role of ros and emerging ros-modulating technologies for augmentation of the healing process," *International wound journal*, vol. 14, no. 1, pp. 89–96, 2017.

[70] D. M. Castilla, Z.-J. Liu, and O. C. Velazquez, "Oxygen: implications for wound healing," *Advances in wound care*, vol. 1, no. 6, pp. 225–230, 2012.

[71] S. Patel, S. Srivastava, M. R. Singh, and D. Singh, "Mechanistic insight into diabetic wounds: Pathogenesis, molecular targets and treatment strategies to pace wound healing," *Biomedicine & Pharmacotherapy*, vol. 112, p. 108615, 2019.

[72] S. M. Aitcheson, F. D. Frentiu, S. E. Hurn, K. Edwards, and R. Z. Murray, "Skin wound healing: normal macrophage function and macrophage dysfunction in diabetic wounds," *Molecules*, vol. 26, no. 16, p. 4917, 2021.

[73] R. D. Wolcott, "The effect of a hydroconductive dressing on the suppression of wound biofilm," *Wounds*, vol. 24, no. 5, pp. 132–137, 2012.

[74] E. P. Weledji and P. Fokam, "Treatment of the diabetic foot–to amputate or not?," *BMC surgery*, vol. 14, pp. 1–6, 2014.

[75] S. L. Percival, S. M. McCarty, and B. Lipsky, "Biofilms and wounds: an overview of the evidence," *Advances in wound care*, vol. 4, no. 7, pp. 373–381, 2015.

[76] J. Larouche, S. Sheoran, K. Maruyama, and M. M. Martino, "Immune reg-

ulation of skin wound healing: mechanisms and novel therapeutic targets," *Advances in wound care*, vol. 7, no. 7, pp. 209–231, 2018.

[77] P. Bowler, B. Duerden, and D. G. Armstrong, "Wound microbiology and associated approaches to wound management," *Clinical microbiology reviews*, vol. 14, no. 2, pp. 244–269, 2001.

[78] D. López, H. Vlamakis, and R. Kolter, "Biofilms," *Cold Spring Harbor perspectives in biology*, vol. 2, no. 7, p. a000398, 2010.

[79] W. Yin, Y. Wang, L. Liu, and J. He, "Biofilms: the microbial "protective clothing" in extreme environments," *International journal of molecular sciences*, vol. 20, no. 14, p. 3423, 2019.

[80] V. Tzaneva, I. Mladenova, G. Todorova, and D. Petkov, "Antibiotic treatment and resistance in chronic wounds of vascular origin," *Clujul medical*, vol. 89, no. 3, p. 365, 2016.

[81] F. Sadeghpour Heravi, M. Zakrzewski, K. Vickery, D. G Armstrong, and H. Hu, "Bacterial diversity of diabetic foot ulcers: current status and future prospectives," *Journal of clinical medicine*, vol. 8, no. 11, p. 1935, 2019.

[82] C. Pouget, C. Dunyach-Remy, A. Pantel, A. Boutet-Dubois, S. Schuldiner, A. Sotto, J.-P. Lavigne, and P. Loubet, "Alternative approaches for the management of diabetic foot ulcers," *Frontiers in microbiology*, p. 2877, 2021.

[83] G. A. James, E. Swogger, R. Wolcott, E. d. Pulcini, P. Secor, J. Sestrich, J. W. Costerton, and P. S. Stewart, "Biofilms in chronic wounds," *Wound Repair and regeneration*, vol. 16, no. 1, pp. 37–44, 2008.

[84] S. L. Percival, K. E. Hill, D. W. Williams, S. J. Hooper, D. W. Thomas, and J. W. Costerton, "A review of the scientific evidence for biofilms in wounds," *Wound repair and regeneration*, vol. 20, no. 5, pp. 647–657, 2012.

[85] V. Puca, R. Z. Marulli, R. Grande, I. Vitale, A. Niro, G. Molinaro, S. Prezioso, R. Muraro, and P. Di Giovanni, "Microbial species isolated from infected wounds and antimicrobial resistance analysis: Data emerging from a three-years retrospective study," *Antibiotics*, vol. 10, no. 10, p. 1162, 2021.

[86] M. Berlanga and R. Guerrero, "Living together in biofilms: the microbial cell factory and its biotechnological implications," *Microbial cell factories*, vol. 15, no. 1, pp. 1–11, 2016.

[87] N. Barraud, M. J Kelso, S. A Rice, and S. Kjelleberg, "Nitric oxide: a key mediator of biofilm dispersal with applications in infectious diseases," *Current pharmaceutical design*, vol. 21, no. 1, pp. 31–42, 2015.

[88] K. P. Rumbaugh and K. Sauer, "Biofilm dispersion," *Nature Reviews Microbiology*, vol. 18, no. 10, pp. 571–586, 2020.

[89] G. LuTheryn, P. Glynne-Jones, J. S. Webb, and D. Carugo, "Ultrasound-mediated therapies for the treatment of biofilms in chronic wounds: a review of present knowledge," *Microbial Biotechnology*, vol. 13, no. 3, pp. 613–628, 2020.

[90] J. W. Costerton, P. S. Stewart, and E. P. Greenberg, "Bacterial biofilms: a common cause of persistent infections," *science*, vol. 284, no. 5418, pp. 1318–1322, 1999.

[91] O. Ciofu, C. Moser, P. Ø. Jensen, and N. Høiby, "Tolerance and resistance of microbial biofilms," *Nature Reviews Microbiology*, vol. 20, no. 10, pp. 621–635, 2022.

[92] C. Uruén, G. Chopo-Escuin, J. Tommassen, R. C. Mainar-Jaime, and J. Arenas, "Biofilms as promoters of bacterial antibiotic resistance and tolerance," *Antibiotics*, vol. 10, no. 1, p. 3, 2020.

[93] C. W. Hall and T.-F. Mah, "Molecular mechanisms of biofilm-based antibiotic resistance and tolerance in pathogenic bacteria," *FEMS microbiology reviews*, vol. 41, no. 3, pp. 276–301, 2017.

[94] P. S. Stewart, "Antimicrobial tolerance in biofilms," *Microbiology spectrum*, vol. 3, no. 3, pp. 10–1128, 2015.

[95] P. Di Martino, "Extracellular polymeric substances, a key element in understanding biofilm phenotype," *AIMS microbiology*, vol. 4, no. 2, p. 274, 2018.

[96] H.-C. Flemming and J. Wingender, "The biofilm matrix," *Nature reviews microbiology*, vol. 8, no. 9, pp. 623–633, 2010.

[97] J. Donné and S. Dewilde, "The challenging world of biofilm physiology," in *Advances in microbial physiology*, vol. 67, pp. 235–292, Elsevier, 2015.

[98] E. K. Davenport, D. R. Call, and H. Beyenal, "Differential protection from tobramycin by extracellular polymeric substances from acinetobacter baumannii and staphylococcus aureus biofilms," *Antimicrobial agents and chemotherapy*, vol. 58, no. 8, pp. 4755–4761, 2014.

[99] D. H. Limoli, C. J. Jones, and D. J. Wozniak, "Bacterial extracellular polysaccharides in biofilm formation and function," *Microbiology spectrum*, vol. 3, no. 3, pp. 3–3, 2015.

[100] P. Gupta, P. A. Pruthi, and V. Pruthi, "Role of exopolysaccharides in biofilm formation," in *Introduction to biofilm engineering*, pp. 17–57, ACS Publications, 2019.

[101] T. Das, S. Sehar, and M. Manefield, "The roles of extracellular dna in the structural integrity of extracellular polymeric substance and bacterial biofilm development," *Environmental microbiology reports*, vol. 5, no. 6, pp. 778–786, 2013.

[102] A. S. Pugazhendhi, F. Wei, M. Hughes, and M. Coathup, "Bacterial adhesion, virulence, and biofilm formation," in *Musculoskeletal Infection*, pp. 19–64, Springer, 2022.

[103] S. L. Percival, K. E. Hill, S. Malic, D. W. Thomas, and D. W. Williams, "Antimicrobial tolerance and the significance of persister cells in recalcitrant chronic wound biofilms," *Wound repair and regeneration*, vol. 19, no. 1, pp. 1–9, 2011.

[104] M. Fauvart, V. N. De Groote, and J. Michiels, "Role of persister cells in chronic infections: clinical relevance and perspectives on anti-persister therapies," *Journal of medical microbiology*, vol. 60, no. 6, pp. 699–709, 2011.

[105] J. Wainwright, G. Hobbs, and I. Nakouti, "Persister cells: formation, resus-

citation and combative therapies," *Archives of Microbiology*, vol. 203, no. 10, pp. 5899–5906, 2021.

[106] H.-L. Mousa, "Aerobic, anaerobic and fungal burn wound infections," *Journal of hospital infection*, vol. 37, no. 4, pp. 317–323, 1997.

[107] I. Brook and E. H. Frazier, "Aerobic and anaerobic microbiology of chronic venous ulcers," *International journal of dermatology*, vol. 37, no. 6, pp. 426–428, 1998.

[108] R. D. Wolcott, J. D. Hanson, E. J. Rees, L. D. Koenig, C. D. Phillips, R. A. Wolcott, S. B. Cox, and J. S. White, "Analysis of the chronic wound microbiota of 2,963 patients by 16s rdna pyrosequencing," *Wound repair and regeneration*, vol. 24, no. 1, pp. 163–174, 2016.

[109] A. Uberoi, A. McCready-Vangi, and E. A. Grice, "The wound microbiota: microbial mechanisms of impaired wound healing and infection," *Nature Reviews Microbiology*, pp. 1–15, 2024.

[110] V. Anju, S. Busi, M. Imchen, R. Kumavath, M. S. Mohan, S. A. Salim, P. Subhaswaraj, and M. Dyavaiah, "Polymicrobial infections and biofilms: clinical significance and eradication strategies," *Antibiotics*, vol. 11, no. 12, p. 1731, 2022.

[111] M. Malone, T. Bjarnsholt, A. J. McBain, G. A. James, P. Stoodley, D. Leaper, M. Tachi, G. Schultz, T. Swanson, and R. D. Wolcott, "The prevalence of biofilms in chronic wounds: a systematic review and meta-analysis of published data," *Journal of wound care*, vol. 26, no. 1, pp. 20–25, 2017.

[112] I. Negut, V. Grumezescu, and A. M. Grumezescu, "Treatment strategies for infected wounds," *Molecules*, vol. 23, no. 9, p. 2392, 2018.

[113] R. Cooper and K. Kirketerp-Møller, "Non-antibiotic antimicrobial interventions and antimicrobial stewardship in wound care," *Journal of Wound Care*, vol. 27, no. 6, pp. 355–377, 2018.

[114] A. J. Boulton, D. G. Armstrong, M. J. Hardman, M. Malone, J. M. Embil, C. E. Attinger, B. A. Lipsky, J. Aragón-Sánchez, H. K. Li, G. Schultz, *et al.*,

"Diagnosis and management of diabetic foot infections," *Clinical Compendia*, 2020.

[115] G. Schultz, T. Bjarnsholt, G. A. James, D. J. Leaper, A. J. McBain, M. Malone, P. Stoodley, T. Swanson, M. Tachi, R. D. Wolcott, *et al.*, "Consensus guidelines for the identification and treatment of biofilms in chronic nonhealing wounds," *Wound Repair and Regeneration*, vol. 25, no. 5, pp. 744–757, 2017.

[116] L. Yazdanpanah, M. Nasiri, and S. Adarvishi, "Literature review on the management of diabetic foot ulcer," *World journal of diabetes*, vol. 6, no. 1, p. 37, 2015.

[117] M. Nowak, D. Mehrholz, W. Barańska-Rybak, and R. Nowicki, "Wound debridement products and techniques: clinical examples and literature review," *Advances in Dermatology and Allergology/Postępy Dermatologii i Alergologii*, vol. 39, no. 3, pp. 479–490, 2022.

[118] J. R. Wilcox, M. J. Carter, and S. Covington, "Frequency of debridements and time to heal: a retrospective cohort study of 312 744 wounds," *JAMA dermatology*, vol. 149, no. 9, pp. 1050–1058, 2013.

[119] D. A. Ramasubbu, V. Smith, F. Hayden, and P. Cronin, "Systemic antibiotics for treating malignant wounds," *Cochrane Database of Systematic Reviews*, no. 8, 2017.

[120] B. A. Lipsky, "Evidence-based antibiotic therapy of diabetic foot infections," *FEMS immunology & medical microbiology*, vol. 26, no. 3-4, pp. 267–276, 1999.

[121] N. M. Nasir, B. Lee, S. S. Yap, K. Thong, and S. L. Yap, "Cold plasma inactivation of chronic wound bacteria," *Archives of biochemistry and biophysics*, vol. 605, pp. 76–85, 2016.

[122] R. Hernandez, "The use of systemic antibiotics in the treatment of chronic wounds," *Dermatologic therapy*, vol. 19, no. 6, pp. 326–337, 2006.

[123] P. Kaiser, J. Wächter, and M. Windbergs, "Therapy of infected wounds: over-

coming clinical challenges by advanced drug delivery systems," *Drug Delivery and Translational Research*, vol. 11, no. 4, pp. 1545–1567, 2021.

[124] M. M. Alam, M. N. Islam, M. D. H. Hawlader, S. Ahmed, A. Wahab, M. Islam, K. R. Uddin, and A. Hossain, "Prevalence of multidrug resistance bacterial isolates from infected wound patients in dhaka, bangladesh: a cross-sectional study," *International Journal of Surgery Open*, vol. 28, pp. 56–62, 2021.

[125] R. Smith, J. Russo, J. Fiegel, and N. Brogden, "Antibiotic delivery strategies to treat skin infections when innate antimicrobial defense fails," *Antibiotics*, vol. 9, no. 2, p. 56, 2020.

[126] A. N. Neely, J. Gardner, P. Durkee, G. D. Warden, D. G. Greenhalgh, J. J. Gallagher, D. N. Herndon, R. G. Tompkins, and R. J. Kagan, "Are topical antimicrobials effective against bacteria that are highly resistant to systemic antibiotics?," *Journal of burn care & research*, vol. 30, no. 1, pp. 19–29, 2009.

[127] P. M. G. Filius and I. C. Gyssens, "Impact of increasing antimicrobial resistance on wound management," *American journal of clinical dermatology*, vol. 3, no. 1, pp. 1–7, 2002.

[128] C. Weller and V. Team, "Interactive dressings and their role in moist wound management," in *Advanced textiles for wound care*, pp. 105–134, Elsevier, 2019.

[129] T. C. Ezike, U. S. Okpala, U. L. Onoja, C. P. Nwike, E. C. Ezeako, O. J. Okpara, C. C. Okoroafor, S. C. Eze, O. L. Kalu, E. C. Odoh, *et al.*, "Advances in drug delivery systems, challenges and future directions," *Heliyon*, vol. 9, no. 6, 2023.

[130] M. A. D. S. Ramos, P. B. Da Silva, L. Spósito, L. G. De Toledo, B. V. Bonifácio, C. F. Rodero, K. C. Dos Santos, M. Chorilli, and T. M. Bauab, "Nanotechnology-based drug delivery systems for control of microbial biofilms: a review," *International journal of nanomedicine*, vol. 13, p. 1179, 2018.

[131] C. Martin, W. LiLow, A. Gupta, M. Cairul Iqbal Mohd Amin, I. Radecka, S. T Britland, P. Raj, *et al.*, "Strategies for antimicrobial drug delivery to biofilm," *Current pharmaceutical design*, vol. 21, no. 1, pp. 43–66, 2015.

[132] M. J. Mitchell, M. M. Billingsley, R. M. Haley, M. E. Wechsler, N. A. Peppas, and R. Langer, "Engineering precision nanoparticles for drug delivery," *Nature Reviews Drug Discovery*, vol. 20, no. 2, pp. 101–124, 2021.

[133] A. Akbarzadeh, R. Rezaei-Sadabady, S. Davaran, S. W. Joo, N. Zarghami, Y. Hanifehpour, M. Samiei, M. Kouhi, and K. Nejati-Koshki, "Liposome: classification, preparation, and applications," *Nanoscale research letters*, vol. 8, no. 1, pp. 1–9, 2013.

[134] D. Tretiakova and E. Vodovozova, "Liposomes as adjuvants and vaccine delivery systems," *Biochemistry (Moscow), Supplement Series A: Membrane and Cell Biology*, vol. 16, no. 1, pp. 1–20, 2022.

[135] T. O. Olusanya, R. R. Haj Ahmad, D. M. Ibegbu, J. R. Smith, and A. A. Elkordy, "Liposomal drug delivery systems and anticancer drugs," *Molecules*, vol. 23, no. 4, p. 907, 2018.

[136] Y. Wang, "Liposome as a delivery system for the treatment of biofilm-mediated infections," *Journal of Applied Microbiology*, vol. 131, no. 6, pp. 2626–2639, 2021.

[137] C. Mugabe, M. Halwani, A. O. Azghani, R. M. Lafrenie, and A. Omri, "Mechanism of enhanced activity of liposome-entrapped aminoglycosides against resistant strains of pseudomonas aeruginosa," *Antimicrobial agents and chemotherapy*, vol. 50, no. 6, pp. 2016–2022, 2006.

[138] P. Nakhaei, R. Margiana, D. O. Bokov, W. K. Abdelbasset, M. A. J. Kouhbanani, R. S. Varma, F. Marofi, M. Jarahian, and N. Beheshtkhoo, "Liposomes: Structure, biomedical applications, and stability parameters with emphasis on cholesterol," *Frontiers in Bioengineering and Biotechnology*, vol. 9, 2021.

[139] H.-J. Park, S. Park, J. Roh, S. Kim, K. Choi, J. Yi, Y. Kim, and J. Yoon, "Biofilm-inactivating activity of silver nanoparticles: a comparison with silver ions," *Journal of Industrial and Engineering Chemistry*, vol. 19, no. 2, pp. 614–619, 2013.

[140] K. Kalishwaralal, S. BarathManiKanth, S. R. K. Pandian, V. Deepak, and

S. Gurunathan, "Silver nanoparticles impede the biofilm formation by pseudomonas aeruginosa and staphylococcus epidermidis," *Colloids and Surfaces B: Biointerfaces*, vol. 79, no. 2, pp. 340–344, 2010.

[141] S. K. Boda, J. Broda, F. Schiefer, J. Weber-Heynemann, M. Hoss, U. Simon, B. Basu, and W. Jahnen-Dechent, "Cytotoxicity of ultrasmall gold nanoparticles on planktonic and biofilm encapsulated gram-positive staphylococci," *Small*, vol. 11, no. 26, pp. 3183–3193, 2015.

[142] R. Szmyd, A. G. Goralczyk, L. Skalniak, A. Cierniak, B. Lipert, F. L. Filon, M. Crosera, J. Borowczyk, E. Laczna, J. Drukala, *et al.*, "Effect of silver nanoparticles on human primary keratinocytes," *Biological Chemistry*, vol. 394, no. 1, pp. 113–123, 2013.

[143] A. Kushwaha, L. Goswami, and B. S. Kim, "Nanomaterial-based therapy for wound healing," *Nanomaterials*, vol. 12, no. 4, p. 618, 2022.

[144] A. Sani, C. Cao, and D. Cui, "Toxicity of gold nanoparticles (aunps): A review," *Biochemistry and biophysics reports*, vol. 26, p. 100991, 2021.

[145] F. Amaro, Á. Morón, S. Díaz, A. Martín-González, and J. C. Gutiérrez, "Metallic nanoparticles—friends or foes in the battle against antibiotic-resistant bacteria?," *Microorganisms*, vol. 9, no. 2, p. 364, 2021.

[146] A. Panáček, L. Kvítek, M. Smékalová, R. Večeřová, M. Kolář, M. Röderová, F. Dyčka, M. Šebela, R. Prucek, O. Tomanec, *et al.*, "Bacterial resistance to silver nanoparticles and how to overcome it," *Nature nanotechnology*, vol. 13, no. 1, pp. 65–71, 2018.

[147] M. A. Rahim, N. Jan, S. Khan, H. Shah, A. Madni, A. Khan, A. Jabar, S. Khan, A. Elhissi, Z. Hussain, *et al.*, "Recent advancements in stimuli responsive drug delivery platforms for active and passive cancer targeting," *Cancers*, vol. 13, no. 4, p. 670, 2021.

[148] X. Chen, R. Guo, C. Wang, K. Li, X. Jiang, H. He, and W. Hong, "On-demand ph-sensitive surface charge-switchable polymeric micelles for targeting pseudomonas aeruginosa biofilms development," *Journal of Nanobiotechnology*, vol. 19, pp. 1–12, 2021.

[149] A. Sousa, A. N. Phung, N. Škalko-Basnet, and S. Obuobi, "Smart delivery systems for microbial biofilm therapy: dissecting design, drug release and toxicological features," *Journal of Controlled Release*, vol. 354, pp. 394–416, 2023.

[150] C. Alvarez-Lorenzo, C. A. Garcia-Gonzalez, E. Bucio, and A. Concheiro, "Stimuli-responsive polymers for antimicrobial therapy: drug targeting, contact-killing surfaces and competitive release," *Expert opinion on drug delivery*, vol. 13, no. 8, pp. 1109–1119, 2016.

[151] B. Wang, H. Liu, L. Sun, Y. Jin, X. Ding, L. Li, J. Ji, and H. Chen, "Construction of high drug loading and enzymatic degradable multilayer films for self-defense drug release and long-term biofilm inhibition," *Biomacromolecules*, vol. 19, no. 1, pp. 85–93, 2018.

[152] T. Tagami, W. D. Foltz, M. J. Ernsting, C. M. Lee, I. F. Tannock, J. P. May, and S.-D. Li, "Mri monitoring of intratumoral drug delivery and prediction of the therapeutic effect with a multifunctional thermosensitive liposome," *Biomaterials*, vol. 32, no. 27, pp. 6570–6578, 2011.

[153] K. Ulbrich, K. Hola, V. Subr, A. Bakandritsos, J. Tucek, and R. Zboril, "Targeted drug delivery with polymers and magnetic nanoparticles: covalent and noncovalent approaches, release control, and clinical studies," *Chemical reviews*, vol. 116, no. 9, pp. 5338–5431, 2016.

[154] A. E. Deatsch and B. A. Evans, "Heating efficiency in magnetic nanoparticle hyperthermia," *Journal of Magnetism and magnetic Materials*, vol. 354, pp. 163–172, 2014.

[155] E. Cazares-Cortes, S. Cabana, C. Boitard, E. Nehlig, N. Griffete, J. Fresnais, C. Wilhelm, A. Abou-Hassan, and C. Ménager, "Recent insights in magnetic hyperthermia: From the "hot-spot" effect for local delivery to combined magneto-photo-thermia using magneto-plasmonic hybrids," *Advanced drug delivery reviews*, vol. 138, pp. 233–246, 2019.

[156] A. Pawar and P. Prabhu, "Nanosoldiers: A promising strategy to combat triple

negative breast cancer," *Biomedicine & Pharmacotherapy*, vol. 110, pp. 319–341, 2019.

[157] B. Nasseri, E. Alizadeh, F. Bani, S. Davaran, A. Akbarzadeh, N. Rabiee, A. Bahadori, M. Ziaei, M. Bagherzadeh, M. R. Saeb, *et al.*, "Nanomaterials for photothermal and photodynamic cancer therapy," *Applied Physics Reviews*, vol. 9, no. 1, 2022.

[158] M. Overchuk, R. A. Weersink, B. C. Wilson, and G. Zheng, "Photodynamic and photothermal therapies: synergy opportunities for nanomedicine," *ACS nano*, vol. 17, no. 9, pp. 7979–8003, 2023.

[159] J. Zhu, J. Tian, C. Yang, J. Chen, L. Wu, M. Fan, and X. Cai, "L-arg-rich amphiphilic dendritic peptide as a versatile no donor for no/photodynamic synergistic treatment of bacterial infections and promoting wound healing," *Small*, vol. 17, no. 32, p. 2101495, 2021.

[160] B. Zhao, H. Wang, W. Dong, S. Cheng, H. Li, J. Tan, J. Zhou, W. He, L. Li, J. Zhang, *et al.*, "A multifunctional platform with single-nir-laser-triggered photothermal and no release for synergistic therapy against multidrug-resistant gram-negative bacteria and their biofilms," *Journal of Nanobiotechnology*, vol. 18, pp. 1–25, 2020.

[161] S. Mallidi, S. Anbil, A.-L. Bulin, G. Obaid, M. Ichikawa, and T. Hasan, "Beyond the barriers of light penetration: strategies, perspectives and possibilities for photodynamic therapy," *Theranostics*, vol. 6, no. 13, p. 2458, 2016.

[162] American National Standards Institute, "Acoustical terminology," Standard ANSI/ASA S1.1-2013, American National Standards Institute, New York, NY, 2013. Accessed on 2024-10-10.

[163] A. Carovac, F. Smajlovic, and D. Junuzovic, "Application of ultrasound in medicine," *Acta Informatica Medica*, vol. 19, no. 3, p. 168, 2011.

[164] D. L. Miller, N. B. Smith, M. R. Bailey, G. J. Czarnota, K. Hynynen, I. R. S. Makin, and B. C. of the American Institute of Ultrasound in Medicine, "Overview of therapeutic ultrasound applications and safety considerations," *Journal of ultrasound in medicine*, vol. 31, no. 4, pp. 623–634, 2012.

[165] S. J. Patey and J. P. Corcoran, "Physics of ultrasound," *Anaesthesia & Intensive Care Medicine*, vol. 22, no. 1, pp. 58–63, 2021.

[166] N. M. Tole *et al.*, *Basic physics of ultrasonographic imaging*. World Health Organization, 2005.

[167] P. N. Wells and H.-D. Liang, "Medical ultrasound: imaging of soft tissue strain and elasticity," *Journal of the Royal Society Interface*, vol. 8, no. 64, pp. 1521–1549, 2011.

[168] C. M. Rumack and D. Levine, *Diagnostic ultrasound*. Elsevier Health Sciences, 2017.

[169] A. Ng and J. Swanevelder, "Resolution in ultrasound imaging," *Continuing Education in Anaesthesia, Critical Care & Pain*, vol. 11, no. 5, pp. 186–192, 2011.

[170] J. O. Szablowski, A. Bar-Zion, and M. G. Shapiro, "Achieving spatial and molecular specificity with ultrasound-targeted biomolecular nanotherapeutics," *Accounts of chemical research*, vol. 52, no. 9, pp. 2427–2434, 2019.

[171] H. Baek, K. J. Pahk, and H. Kim, "A review of low-intensity focused ultrasound for neuromodulation," *Biomedical engineering letters*, vol. 7, pp. 135–142, 2017.

[172] Y. Cao, Y. Chen, T. Yu, Y. Guo, F. Liu, Y. Yao, P. Li, D. Wang, Z. Wang, Y. Chen, *et al.*, "Drug release from phase-changeable nanodroplets triggered by low-intensity focused ultrasound," *Theranostics*, vol. 8, no. 5, p. 1327, 2018.

[173] X. Wang, F. Yan, X. Liu, P. Wang, S. Shao, Y. Sun, Z. Sheng, Q. Liu, J. F. Lovell, and H. Zheng, "Enhanced drug delivery using sonoactivatable liposomes with membrane-embedded porphyrins," *Journal of controlled release*, vol. 286, pp. 358–368, 2018.

[174] I. S. Elhelf, H. Albahar, U. Shah, A. Oto, E. Cressman, and M. Almekkawy, "High intensity focused ultrasound: The fundamentals, clinical applications and research trends," *Diagnostic and interventional imaging*, vol. 99, no. 6, pp. 349–359, 2018.

[175] G. Ter Haar, "Hifu tissue ablation: concept and devices," *Therapeutic ultrasound*, pp. 3–20, 2016.

[176] V. Choi, M. A. Rajora, and G. Zheng, "Activating drugs with sound: mechanisms behind sonodynamic therapy and the role of nanomedicine," *Bioconjugate Chemistry*, vol. 31, no. 4, pp. 967–989, 2020.

[177] W. W. Roberts, T. L. Hall, K. Ives, J. S. Wolf, J. B. Fowlkes, and C. A. Cain, "Pulsed cavitational ultrasound: a noninvasive technology for controlled tissue ablation (histotripsy) in the rabbit kidney," *The Journal of urology*, vol. 175, no. 2, pp. 734–738, 2006.

[178] H. Fang, K. Tsai, W. Cheng, M.-J. Shieh, P. Lou, W. Lin, and . W. Chen, "The effects of power on–off durations of pulsed ultrasound on the destruction of cancer cells," *International journal of hyperthermia*, vol. 23, no. 4, pp. 371–380, 2007.

[179] M. Cheng, F. Li, T. Han, C. Alfred, and P. Qin, "Effects of ultrasound pulse parameters on cavitation properties of flowing microbubbles under physiologically relevant conditions," *Ultrasonics sonochemistry*, vol. 52, pp. 512–521, 2019.

[180] J. M. Meunier, C. K. Holland, C. J. Lindsell, and G. J. Shaw, "Duty cycle dependence of ultrasound enhanced thrombolysis in a human clot model," *Ultrasound in medicine & biology*, vol. 33, no. 4, pp. 576–583, 2007.

[181] G. Ter Haar, "Safety and bio-effects of ultrasound contrast agents," *Medical & biological engineering & computing*, vol. 47, no. 8, pp. 893–900, 2009.

[182] F. Ahmadi and I. V. McLoughlin, "A new mechanical index for gauging the human bioeffects of low frequency ultrasound," in *2013 35th Annual International Conference of the IEEE Engineering in Medicine and Biology Society (EMBC)*, pp. 1964–1967, IEEE, 2013.

[183] C. M. I. Quarato, D. Lacedonia, M. Salvemini, G. Tuccari, G. Mastrodonato, R. Villani, L. A. Fiore, G. Scioscia, A. Mirijello, A. Saponara, *et al.*, "A review on biological effects of ultrasounds: key messages for clinicians," *Diagnostics*, vol. 13, no. 5, p. 855, 2023.

[184] K. R. Nightingale, C. C. Church, G. Harris, K. A. Wear, M. R. Bailey, P. L. Carson, H. Jiang, K. L. Sandstrom, T. L. Szabo, and M. C. Ziskin, "Conditionally increased acoustic pressures in nonfetal diagnostic ultrasound examinations without contrast agents: A preliminary assessment," *Journal of Ultrasound in Medicine*, vol. 34, no. 7, pp. 1–41, 2015.

[185] X. Jiang, O. Savchenko, Y. Li, S. Qi, T. Yang, W. Zhang, and J. Chen, "A review of low-intensity pulsed ultrasound for therapeutic applications," *IEEE Transactions on Biomedical Engineering*, vol. 66, no. 10, pp. 2704–2718, 2018.

[186] M. Lafond, A. Payne, and C. Lafon, "Therapeutic ultrasound transducer technology and monitoring techniques: a review with clinical examples," *International Journal of Hyperthermia*, vol. 41, no. 1, p. 2389288, 2024.

[187] T. J. Manuel, J. Kusunose, X. Zhan, X. Lv, E. Kang, A. Yang, Z. Xiang, and C. F. Caskey, "Ultrasound neuromodulation depends on pulse repetition frequency and can modulate inhibitory effects of ttx," *Scientific Reports*, vol. 10, no. 1, p. 15347, 2020.

[188] P. Reuter, J. Masomi, H. Kuntze, I. Fischer, K. Helling, C. Sommer, B. Alessandri, A. Heimann, T. Gerriets, J. Marx, *et al.*, "Low-frequency therapeutic ultrasound with varied duty cycle: effects on the ischemic brain and the inner ear," *Ultrasound in medicine & biology*, vol. 36, no. 7, pp. 1188–1195, 2010.

[189] P. Koukouvinis, G. Bergeles, and M. Gavaises, "A cavitation aggressiveness index within the reynolds averaged navier stokes methodology for cavitating flows," *Journal of Hydrodynamics*, vol. 27, no. 4, pp. 579–586, 2015.

[190] T. A. Bigelow, C. C. Church, K. Sandstrom, J. G. Abbott, M. C. Ziskin, P. D. Edmonds, B. Herman, K. E. Thomenius, and T. J. Teo, "The thermal index: its strengths, weaknesses, and proposed improvements," *Journal of Ultrasound in Medicine*, vol. 30, no. 5, pp. 714–734, 2011.

[191] S.-L. Huang and R. C. MacDonald, "Acoustically active liposomes for drug encapsulation and ultrasound-triggered release," *Biochimica et Biophysica Acta (BBA)-Biomembranes*, vol. 1665, no. 1-2, pp. 134–141, 2004.

[192] P. S. Sheeran, S. Luois, P. A. Dayton, and T. O. Matsunaga, "Formulation and acoustic studies of a new phase-shift agent for diagnostic and therapeutic ultrasound," *Langmuir*, vol. 27, no. 17, pp. 10412–10420, 2011.

[193] P. Wei, E. J. Cornel, and J. Du, "Ultrasound-responsive polymer-based drug delivery systems," *Drug delivery and translational research*, vol. 11, pp. 1323–1339, 2021.

[194] H. Lee, H. Kim, H. Han, M. Lee, S. Lee, H. Yoo, J. H. Chang, and H. Kim, "Microbubbles used for contrast enhanced ultrasound and theragnosis: a review of principles to applications," *Biomedical Engineering Letters*, vol. 7, pp. 59–69, 2017.

[195] V. Paefgen, D. Doleschel, and F. Kiessling, "Evolution of contrast agents for ultrasound imaging and ultrasound-mediated drug delivery," *Frontiers in pharmacology*, vol. 6, p. 197, 2015.

[196] V. Rafailidis, D. Y. Huang, G. T. Yusuf, and P. S. Sidhu, "General principles and overview of vascular contrast-enhanced ultrasonography," *Ultrasonography*, vol. 39, no. 1, p. 22, 2020.

[197] S. Sirsi and M. Borden, "Microbubble compositions, properties and biomedical applications," *Bubble Science, Engineering & Technology*, vol. 1, no. 1-2, pp. 3–17, 2009.

[198] L. J. Jablonowski, M. C. Cochran, J. R. Eisenbrey, N. T. Teraphongphom, and M. A. Wheatley, "Shell effects on acoustic performance of a drug-delivery system activated by ultrasound," *Journal of Biomedical Materials Research Part A*, vol. 105, no. 11, pp. 3189–3196, 2017.

[199] L. M. Thomson, B. D. Polizzotti, F. X. McGowan, and J. N. Kheir, "Manufacture of concentrated, lipid-based oxygen microbubble emulsions by high shear homogenization and serial concentration," *JoVE (Journal of Visualized Experiments)*, no. 87, p. e51467, 2014.

[200] E. Stride and M. Edirisinghe, "Novel preparation techniques for controlling microbubble uniformity: a comparison," *Medical & biological engineering & computing*, vol. 47, pp. 883–892, 2009.

[201] Q. Xu, M. Nakajima, S. Ichikawa, N. Nakamura, and T. Shiina, "A comparative study of microbubble generation by mechanical agitation and sonication," *Innovative food science & emerging technologies*, vol. 9, no. 4, pp. 489–494, 2008.

[202] K. W. Pulsipher, D. A. Hammer, D. Lee, and C. M. Sehgal, "Engineering theranostic microbubbles using microfluidics for ultrasound imaging and therapy: a review," *Ultrasound in medicine & biology*, vol. 44, no. 12, pp. 2441–2460, 2018.

[203] P. S. Epstein and M. S. Plesset, "On the stability of gas bubbles in liquid-gas solutions," *The Journal of Chemical Physics*, vol. 18, no. 11, pp. 1505–1509, 1950.

[204] A. Katiyar and K. Sarkar, "Stability analysis of an encapsulated microbubble against gas diffusion," *Journal of colloid and interface science*, vol. 343, no. 1, pp. 42–47, 2010.

[205] K. Sarkar, A. Katiyar, and P. Jain, "Growth and dissolution of an encapsulated contrast microbubble: effects of encapsulation permeability," *Ultrasound in medicine & biology*, vol. 35, no. 8, pp. 1385–1396, 2009.

[206] Y. Zhou, "Application of acoustic droplet vaporization in ultrasound therapy," *Journal of therapeutic ultrasound*, vol. 3, no. 1, pp. 1–18, 2015.

[207] K. W. Ferrara, M. A. Borden, and H. Zhang, "Lipid-shelled vehicles: engineering for ultrasound molecular imaging and drug delivery," *Accounts of chemical research*, vol. 42, no. 7, pp. 881–892, 2009.

[208] M. A. Borden, D. E. Kruse, C. F. Caskey, S. Zhao, P. A. Dayton, and K. W. Ferrara, "Influence of lipid shell physicochemical properties on ultrasound-induced microbubble destruction," *IEEE transactions on ultrasonics, ferroelectrics, and frequency control*, vol. 52, no. 11, pp. 1992–2002, 2005.

[209] K. Ferrara, R. Pollard, and M. Borden, "Ultrasound microbubble contrast agents: fundamentals and application to gene and drug delivery," *Annu. Rev. Biomed. Eng.*, vol. 9, no. 1, pp. 415–447, 2007.

[210] J. J. Kwan and M. A. Borden, "Lipid monolayer collapse and microbubble stability," *Advances in colloid and interface science*, vol. 183, pp. 82–99, 2012.

[211] C. C. Chen and M. A. Borden, "The role of poly (ethylene glycol) brush architecture in complement activation on targeted microbubble surfaces," *Biomaterials*, vol. 32, no. 27, pp. 6579–6587, 2011.

[212] J. Owen, S. Kamila, S. Shrivastava, D. Carugo, J. Bernardino de la Serna, C. Mannaris, V. Pereno, R. Browning, E. Beguin, A. P. McHale, *et al.*, "The role of peg-40-stearate in the production, morphology, and stability of microbubbles," *Langmuir*, vol. 35, no. 31, pp. 10014–10024, 2018.

[213] M. M. Lozano and M. L. Longo, "Microbubbles coated with disaturated lipids and dspe-peg2000: phase behavior, collapse transitions, and permeability," *Langmuir*, vol. 25, no. 6, pp. 3705–3712, 2009.

[214] S. Zullino, M. Argenziano, I. Stura, C. Guiot, and R. Cavalli, "From micro- to nano-multifunctional theranostic platform: effective ultrasound imaging is not just a matter of scale," *Molecular imaging*, vol. 17, p. 1536012118778216, 2018.

[215] S. F. Flaim, "Pharmacokinetics and side effects of perfluorocarbon-based blood substitutes," *Artificial Cells, Blood Substitutes, and Biotechnology*, vol. 22, no. 4, pp. 1043–1054, 1994.

[216] S. Garg, A. A. Thomas, and M. A. Borden, "The effect of lipid monolayer in-plane rigidity on in vivo microbubble circulation persistence," *Biomaterials*, vol. 34, no. 28, pp. 6862–6870, 2013.

[217] K. H. Martin and P. A. Dayton, "Current status and prospects for microbubbles in ultrasound theranostics," *Wiley Interdisciplinary Reviews: Nanomedicine and Nanobiotechnology*, vol. 5, no. 4, pp. 329–345, 2013.

[218] E. J. Lee, A. Fomenko, and A. M. Lozano, "Magnetic resonance-guided focused ultrasound: current status and future perspectives in thermal ablation and blood-brain barrier opening," *Journal of Korean Neurosurgical Society*, vol. 62, no. 1, p. 10, 2019.

[219] Z. Fan, R. E. Kumon, and C. X. Deng, "Mechanisms of microbubble-facilitated sonoporation for drug and gene delivery," *Therapeutic delivery*, vol. 5, no. 4, pp. 467–486, 2014.

[220] W. T. Shi, F. Forsberg, A. Tornes, J. Østensen, and B. B. Goldberg, "Destruction of contrast microbubbles and the association with inertial cavitation," *Ultrasound in medicine & biology*, vol. 26, no. 6, pp. 1009–1019, 2000.

[221] J. Wu and W. L. Nyborg, "Ultrasound, cavitation bubbles and their interaction with cells," *Advanced drug delivery reviews*, vol. 60, no. 10, pp. 1103–1116, 2008.

[222] M. S. Karthikesh and X. Yang, "The effect of ultrasound cavitation on endothelial cells," *Experimental Biology and Medicine*, vol. 246, no. 7, pp. 758–770, 2021.

[223] Y.-J. R. Chang, J. Perry, and K. Cross, "Low-frequency ultrasound debridement in chronic wound healing: a systematic review of current evidence," *Plastic Surgery*, vol. 25, no. 1, pp. 21–26, 2017.

[224] Z. Izadifar, P. Babyn, and D. Chapman, "Ultrasound cavitation/microbubble detection and medical applications," *Journal of Medical and Biological Engineering*, vol. 39, no. 3, pp. 259–276, 2019.

[225] K. Kooiman, H. J. Vos, M. Versluis, and N. de Jong, "Acoustic behavior of microbubbles and implications for drug delivery," *Advanced drug delivery reviews*, vol. 72, pp. 28–48, 2014.

[226] Y. Gu, C. Chen, J. Tu, X. Guo, H. Wu, and D. Zhang, "Harmonic responses and cavitation activity of encapsulated microbubbles coupled with magnetic nanoparticles," *Ultrasonics Sonochemistry*, vol. 29, pp. 309–316, 2016.

[227] M. Giordano, A. Calabro, C. Esposito, A. D'Amore, and L. Nicolais, "An acoustic-emission characterization of the failure modes in polymer-composite materials," *Composites science and technology*, vol. 58, no. 12, pp. 1923–1928, 1998.

[228] K. R. Lattwein, H. Shekhar, J. J. Kouijzer, W. J. van Wamel, C. K. Holland,

and K. Kooiman, "Sonobactericide: an emerging treatment strategy for bacterial infections," *Ultrasound in medicine & biology*, vol. 46, no. 2, pp. 193–215, 2020.

[229] Y. Dong, J. Li, P. Li, and J. Yu, "Ultrasound microbubbles enhance the activity of vancomycin against staphylococcus epidermidis biofilms in vivo," *Journal of Ultrasound in Medicine*, vol. 37, no. 6, pp. 1379–1387, 2018.

[230] E. Ronan, N. Edjiu, O. Kroukamp, G. Wolfaardt, and R. Karshafian, "Usmb-induced synergistic enhancement of aminoglycoside antibiotics in biofilms," *Ultrasonics*, vol. 69, pp. 182–190, 2016.

[231] L. D. Bharatula, E. Marsili, S. A. Rice, and J. J. Kwan, "Influence of high intensity focused ultrasound on the microstructure and c-di-gmp signaling of pseudomonas aeruginosa biofilms," *Frontiers in microbiology*, vol. 11, p. 599407, 2020.

[232] E. S. Gloag, S. Fabbri, D. J. Wozniak, and P. Stoodley, "Biofilm mechanics: Implications in infection and survival," *Biofilm*, vol. 2, p. 100017, 2020.

[233] M. Klausen, A. Heydorn, P. Ragas, L. Lambertsen, A. Aaes-Jørgensen, S. Molin, and T. Tolker-Nielsen, "Biofilm formation by pseudomonas aeruginosa wild type, flagella and type iv pili mutants," *Molecular microbiology*, vol. 48, no. 6, pp. 1511–1524, 2003.

[234] L. D. Bharatula, E. Marsili, and J. J. Kwan, "Impedimetric detection of pseudomonas aeruginosa attachment on flexible ito-coated polyethylene terephthalate substrates," *Electrochimica Acta*, vol. 332, p. 135390, 2020.

[235] R. Melich, P. Bussat, L. Morici, A. Vivien, E. Gaud, T. Bettinger, and S. Cherkaoui, "Microfluidic preparation of various perfluorocarbon nanodroplets: characterization and determination of acoustic droplet vaporization (adv) threshold," *International Journal of Pharmaceutics*, vol. 587, p. 119651, 2020.

[236] P. S. Sheeran, J. E. Streeter, L. B. Mullin, T. O. Matsunaga, and P. A. Dayton, "Toward ultrasound molecular imaging with phase-change contrast agents: an

in vitro proof of principle," *Ultrasound in medicine & biology*, vol. 39, no. 5, pp. 893–902, 2013.

[237] L. Martinengo, M. Olsson, R. Bajpai, M. Soljak, Z. Upton, A. Schmidtchen, J. Car, and K. Järbrink, "Prevalence of chronic wounds in the general population: systematic review and meta-analysis of observational studies," *Annals of Epidemiology*, vol. 29, pp. 8–15, 2019.

[238] J. G. Riess, "Understanding the fundamentals of perfluorocarbons and perfluorocarbon emulsions relevant to in vivo oxygen delivery," *Artificial cells, blood substitutes, and biotechnology*, vol. 33, no. 1, pp. 47–63, 2005.

[239] J. Jägers, A. Wrobeln, and K. B. Ferenz, "Perfluorocarbon-based oxygen carriers: from physics to physiology," *Pflügers Archiv-European Journal of Physiology*, vol. 473, pp. 139–150, 2021.

[240] T. O. Matsunaga, P. S. Sheeran, S. Luois, J. E. Streeter, L. B. Mullin, B. Banerjee, and P. A. Dayton, "Phase-change nanoparticles using highly volatile perfluorocarbons: toward a platform for extravascular ultrasound imaging," *Theranostics*, vol. 2, no. 12, p. 1185, 2012.

[241] D. Qin, Q. Zou, S. Lei, W. Wang, and Z. Li, "Predicting initial nucleation events occurred in a metastable nanodroplet during acoustic droplet vaporization," *Ultrasonics Sonochemistry*, vol. 75, p. 105608, 2021.

[242] Q. Wu, C. Mannaris, J. P. May, L. Bau, A. Polydorou, S. Ferri, D. Carugo, N. D. Evans, and E. Stride, "Investigation of the acoustic vaporization threshold of lipid-coated perfluorobutane nanodroplets using both high-speed optical imaging and acoustic methods," *Ultrasound in Medicine & Biology*, vol. 47, no. 7, pp. 1826–1843, 2021.

[243] M. L. Fabiilli, K. J. Haworth, N. H. Fakhri, O. D. Kripfgans, P. L. Carson, and J. B. Fowlkes, "The role of inertial cavitation in acoustic droplet vaporization," *IEEE transactions on ultrasonics, ferroelectrics, and frequency control*, vol. 56, no. 5, pp. 1006–1017, 2009.

[244] K. C. Schad and K. Hynynen, "In vitro characterization of perfluorocarbon

droplets for focused ultrasound therapy," *Physics in Medicine & Biology*, vol. 55, no. 17, p. 4933, 2010.

[245] P. S. Sheeran and P. A. Dayton, "Improving the performance of phase-change perfluorocarbon droplets for medical ultrasonography: current progress, challenges, and prospects," *Scientifica*, vol. 2014, 2014.

[246] P. S. Sheeran, N. Matsuura, M. A. Borden, R. Williams, T. O. Matsunaga, P. N. Burns, and P. A. Dayton, "Methods of generating submicrometer phase-shift perfluorocarbon droplets for applications in medical ultrasonography," *IEEE transactions on ultrasonics, ferroelectrics, and frequency control*, vol. 64, no. 1, pp. 252–263, 2016.

[247] A. Woodward, F. Mattrey, R, and C. de Gracia Lux, "Direct emulsification of stable superheated perfluorobutane nanodroplets by sonication: Addressing the limitations of the microbubble condensation technique," *Ultrasound in Medicine and Biology*, vol. 50, pp. 445–452, 2024.

[248] T. D. Martz, D. Bardin, P. S. Sheeran, A. P. Lee, and P. A. Dayton, "Microfluidic Generation of Acoustically Active Nanodroplets," *Small*, vol. 8, pp. 1876–1879, 6 2012.

[249] H. Lea-Banks, M. O'reilly, and K. Hynynen, "Ultrasound-responsive droplets for therapy: A review," *Journal of Controlled Release*, vol. 293, pp. 144–154, 2019.

[250] S. Ferri, Q. Wu, A. De Grazia, A. Polydorou, J. P. May, E. Stride, N. D. Evans, and D. Carugo, "Tailoring the size of ultrasound responsive lipid-shelled nanodroplets by varying production parameters and environmental conditions," *Ultrasonics sonochemistry*, vol. 73, p. 105482, 2021.

[251] K. Loskutova, D. Grishenkov, and M. Ghorbani, "Review on acoustic droplet vaporization in ultrasound diagnostics and therapeutics," *BioMed Research International*, vol. 2019, 2019.

[252] P. S. Sheeran, V. P. Wong, S. Luois, R. J. McFarland, W. D. Ross, S. Feingold, T. O. Matsunaga, and P. A. Dayton, "Decafluorobutane as a phase-change

contrast agent for low-energy extravascular ultrasonic imaging," *Ultrasound in medicine & biology*, vol. 37, no. 9, pp. 1518–1530, 2011.

[253] M. Aliabouzar, K. N. Kumar, and K. Sarkar, "Effects of droplet size and perfluorocarbon boiling point on the frequency dependence of acoustic vaporization threshold," *The Journal of the Acoustical Society of America*, vol. 145, no. 2, pp. 1105–1116, 2019.

[254] C.-Y. Lin and W. G. Pitt, "Acoustic droplet vaporization in biology and medicine," *BioMed research international*, vol. 2013, 2013.

[255] C. Contado, "Particle characterization: parameters and selected methods," in *Particle Separation Techniques*, pp. 63–114, Elsevier, 2022.

[256] A. Kim, W. B. Ng, W. Bernt, and N.-J. Cho, "Validation of size estimation of nanoparticle tracking analysis on polydisperse macromolecule assembly," *Scientific reports*, vol. 9, no. 1, p. 2639, 2019.

[257] N. Comfort, K. Cai, T. R. Bloomquist, M. D. Strait, A. W. Ferrante Jr, and A. A. Baccarelli, "Nanoparticle tracking analysis for the quantification and size determination of extracellular vesicles," *Journal of visualized experiments: JoVE*, no. 169, 2021.

[258] R. A. Dragovic, C. Gardiner, A. S. Brooks, D. S. Tannetta, D. J. Ferguson, P. Hole, B. Carr, C. W. Redman, A. L. Harris, P. J. Dobson, *et al.*, "Sizing and phenotyping of cellular vesicles using nanoparticle tracking analysis," *Nanomedicine: Nanotechnology, Biology and Medicine*, vol. 7, no. 6, pp. 780–788, 2011.

[259] W. Jiskoot and D. Crommelin, *Methods for structural analysis of protein pharmaceuticals*. Springer Science & Business Media, 2005.

[260] V. Filipe, A. Hawe, and W. Jiskoot, "Critical evaluation of nanoparticle tracking analysis (nta) by nanosight for the measurement of nanoparticles and protein aggregates," *Pharmaceutical research*, vol. 27, no. 5, pp. 796–810, 2010.

[261] J. Stetefeld, S. A. McKenna, and T. R. Patel, "Dynamic light scattering: a

practical guide and applications in biomedical sciences," *Biophysical reviews*, vol. 8, no. 4, pp. 409–427, 2016.

[262] S. K. Singh and M. R. Toler, "Monitoring of subvisible particles in therapeutic proteins," *Therapeutic Proteins: Methods and Protocols*, pp. 379–401, 2012.

[263] F. Caputo, R. Vogel, J. Savage, G. Vella, A. Law, G. Della Camera, G. Hannon, B. Peacock, D. Mehn, J. Ponti, *et al.*, "Measuring particle size distribution and mass concentration of nanoplastics and microplastics: addressing some analytical challenges in the sub-micron size range," *Journal of colloid and interface science*, vol. 588, pp. 401–417, 2021.

[264] W. Anderson, D. Kozak, V. A. Coleman, Å. K. Jämting, and M. Trau, "A comparative study of submicron particle sizing platforms: accuracy, precision and resolution analysis of polydisperse particle size distributions," *Journal of colloid and interface science*, vol. 405, pp. 322–330, 2013.

[265] B. Giebel and C. Helmbrecht, "Methods to analyze evs," *Exosomes and Microvesicles: Methods and Protocols*, pp. 1–20, 2017.

[266] H. Bayley and C. R. Martin, "Resistive-pulse sensing from microbes to molecules," *Chemical reviews*, vol. 100, no. 7, pp. 2575–2594, 2000.

[267] J. Sun, C. C. Stowers, E. M. Boczko, and D. Li, "Measurement of the volume growth rate of single budding yeast with the mosfet-based microfluidic coulter counter," *Lab on a Chip*, vol. 10, no. 21, pp. 2986–2993, 2010.

[268] H. Kobayashi, K. Arao, T. Murayama, K. Iokibe, R. Koga, and M. Shiobara, "High-resolution measurement of size distributions of asian dust using a coulter multisizer," *Journal of Atmospheric and Oceanic Technology*, vol. 24, no. 2, pp. 194–205, 2007.

[269] J. Lancaster Jr, "A tutorial on the diffusibility and reactivity of free nitric oxide," *Nitric oxide*, vol. 1, no. 1, pp. 18–30, 1997.

[270] M. N. Hughes, "Chemistry of nitric oxide and related species," *Methods in enzymology*, vol. 436, pp. 3–19, 2008.

[271] L. J. Ignarro, G. M. Buga, K. S. Wood, R. E. Byrns, and G. Chaudhuri,

"Endothelium-derived relaxing factor produced and released from artery and vein is nitric oxide.," *Proceedings of the National Academy of Sciences*, vol. 84, no. 24, pp. 9265–9269, 1987.

[272] A. Sandoo, J. J. V. van Zanten, G. S. Metsios, D. Carroll, and G. D. Kitas, "The endothelium and its role in regulating vascular tone," *The open cardiovascular medicine journal*, vol. 4, p. 302, 2010.

[273] L. J. Ignarro, J. M. Fukuto, J. M. Griscavage, N. E. Rogers, and R. E. Byrns, "Oxidation of nitric oxide in aqueous solution to nitrite but not nitrate: comparison with enzymatically formed nitric oxide from l-arginine," *Proceedings of the National Academy of Sciences*, vol. 90, no. 17, pp. 8103–8107, 1993.

[274] N. Naghavi, A. de Mel, O. S. Alavijeh, B. G. Cousins, and A. M. Seifalian, "Nitric oxide donors for cardiovascular implant applications," *Small*, vol. 9, no. 1, pp. 22–35, 2013.

[275] P. Sonveaux, B. F. Jordan, B. Gallez, and O. Feron, "Nitric oxide delivery to cancer: why and how?," *European journal of cancer*, vol. 45, no. 8, pp. 1352–1369, 2009.

[276] J.-d. Luo and A. F. Chen, "Nitric oxide: a newly discovered function on wound healing," *Acta Pharmacologica Sinica*, vol. 26, no. 3, pp. 259–264, 2005.

[277] D. P. Arora, S. Hossain, Y. Xu, and E. M. Boon, "Nitric oxide regulation of bacterial biofilms," *Biochemistry*, vol. 54, no. 24, pp. 3717–3728, 2015.

[278] S. Dhall, D. Do, M. Garcia, D. S. Wijesinghe, A. Brandon, J. Kim, A. Sanchez, J. Lyubovitsky, S. Gallagher, E. A. Nothnagel, *et al.*, "A novel model of chronic wounds: importance of redox imbalance and biofilm-forming bacteria for establishment of chronicity," *PLoS One*, vol. 9, no. 10, p. e109848, 2014.

[279] N. Barraud, M. V. Storey, Z. P. Moore, J. S. Webb, S. A. Rice, and S. Kjelleberg, "Nitric oxide-mediated dispersal in single-and multi-species biofilms of clinically and industrially relevant microorganisms," *Microbial biotechnology*, vol. 2, no. 3, pp. 370–378, 2009.

[280] D. E. Williams and E. M. Boon, "Towards understanding the molecular basis

of nitric oxide-regulated group behaviors in pathogenic bacteria," *Journal of innate immunity*, vol. 11, no. 3, pp. 205–215, 2019.

[281] N. Barraud, S. Kjelleberg, and S. A. Rice, "Dispersal from microbial biofilms," *Microbial Biofilms*, pp. 343–362, 2015.

[282] U. Jenal, A. Reinders, and C. Lori, "Cyclic di-gmp: second messenger extraordinaire," *Nature Reviews Microbiology*, vol. 15, no. 5, pp. 271–284, 2017.

[283] M. J. Malone-Povolny, S. E. Maloney, and M. H. Schoenfisch, "Nitric oxide therapy for diabetic wound healing," *Advanced healthcare materials*, vol. 8, no. 12, p. 1801210, 2019.

[284] X. Zhu, H.-S. Oh, Y. C. B. Ng, P. Y. P. Tang, N. Barraud, and S. A. Rice, "Nitric oxide-mediated induction of dispersal in pseudomonas aeruginosa biofilms is inhibited by flavohemoglobin production and is enhanced by imidazole," *Antimicrobial agents and chemotherapy*, vol. 62, no. 3, pp. 10–1128, 2018.

[285] W. H. Poh and S. A. Rice, "Recent developments in nitric oxide donors and delivery for antimicrobial and anti-biofilm applications," *Molecules*, vol. 27, no. 3, p. 674, 2022.

[286] A. D. Verderosa, M. Totsika, and K. E. Fairfull-Smith, "Bacterial biofilm eradication agents: a current review," *Frontiers in chemistry*, p. 824, 2019.

[287] G. LuTheryn, C. Hind, C. Campbell, A. Crowther, Q. Wu, S. B. Keller, P. Glynne-Jones, J. M. Sutton, J. S. Webb, M. Gray, *et al.*, "Bactericidal and anti-biofilm effects of uncharged and cationic ultrasound-responsive nitric oxide microbubbles on pseudomonas aeruginosa biofilms," *Frontiers in cellular and infection microbiology*, vol. 12, p. 956808, 2022.

[288] D. D. Thomas, X. Liu, S. P. Kantrow, and J. R. Lancaster Jr, "The biological lifetime of nitric oxide: implications for the perivascular dynamics of no and o2," *Proceedings of the National Academy of Sciences*, vol. 98, no. 1, pp. 355–360, 2001.

[289] V. G. Kharitonov, A. R. Sundquist, and V. S. Sharma, "Kinetics of nitric oxide

autoxidation in aqueous solution.," *Journal of Biological Chemistry*, vol. 269, no. 8, pp. 5881–5883, 1994.

[290] D. Power and J. Webb, "Nitric oxide-mediated dispersal as an adjunctive strategy for the control of biofilm-associated infection," in *Antibiofilm Strategies: Current and Future Applications to Prevent, Control and Eradicate Biofilms*, pp. 501–519, Springer, 2022.

[291] Y.-M. Cai, Y.-D. Zhang, and L. Yang, "No donors and no delivery methods for controlling biofilms in chronic lung infections," *Applied Microbiology and Biotechnology*, vol. 105, pp. 3931–3954, 2021.

[292] M. P. Krafft, "Fluorocarbons and fluorinated amphiphiles in drug delivery and biomedical research," *Advanced drug delivery reviews*, vol. 47, no. 2-3, pp. 209–228, 2001.

[293] R. Sander, "Compilation of henry's law constants for inorganic and organic species of potential importance in environmental chemistry," 1999.

[294] J. N. Kheir, L. A. Scharp, M. A. Borden, E. J. Swanson, A. Loxley, J. H. Reese, K. J. Black, L. A. Velazquez, L. M. Thomson, B. K. Walsh, *et al.*, "Oxygen gas–filled microparticles provide intravenous oxygen delivery," *Science translational medicine*, vol. 4, no. 140, pp. 140ra88–140ra88, 2012.

[295] J. Tong, J. Ding, X. Shen, L. Chen, Y. Bian, G. Ma, Y. Yao, and F. Yang, "Mesenchymal stem cell transplantation enhancement in myocardial infarction rat model under ultrasound combined with nitric oxide microbubbles," *PloS one*, vol. 8, no. 11, p. e80186, 2013.

[296] Z. Liang, H. Chen, X. Gong, B. Shi, L. Lin, F. Tao, Q. Wu, M. Fang, H. Li, C. Lu, *et al.*, "Ultrasound-induced destruction of nitric oxide–loaded microbubbles in the treatment of thrombus and ischemia–reperfusion injury," *Frontiers in pharmacology*, vol. 12, 2021.

[297] M. Choi, A. M. Jazani, J. K. Oh, and S. M. Noh, "Perfluorocarbon nanodroplets for dual delivery with ultrasound/gsh-responsive release of model drug and passive release of nitric oxide," *Polymers*, vol. 14, no. 11, p. 2240, 2022.

[298] M. Lafond, H. Shekhar, W. Panmanee, S. D. Collins, A. Palaniappan, C. T. McDaniel, D. J. Hassett, and C. K. Holland, "Bactericidal activity of lipid-shelled nitric oxide-loaded microbubbles," *Frontiers in Pharmacology*, p. 1540, 2020.

[299] L. Xin, C. Zhang, J. Chen, Y. Jiang, Y. Liu, P. Jin, X. Wang, G. Wang, and P. Huang, "Ultrasound-activatable phase-shift nanoparticle as a targeting antibacterial agent for efficient eradication of pseudomonas aeruginosa biofilms," *ACS Applied Materials & Interfaces*, vol. 14, no. 42, pp. 47420–47431, 2022.

[300] H. Guo, Z. Wang, Q. Du, P. Li, Z. Wang, and A. Wang, "Stimulated phase-shift acoustic nanodroplets enhance vancomycin efficacy against methicillin-resistant staphylococcus aureus biofilms," *International Journal of Nanomedicine*, vol. 12, p. 4679, 2017.

[301] T. C. Fabian, "Perfluorocarbons," *Journal of Trauma - Injury, Infection and Critical Care*, vol. 70, 5 2011.

[302] T. D. Martz, P. S. Sheeran, D. Bardin, A. P. Lee, and P. A. Dayton, "Precision manufacture of phase-change perfluorocarbon droplets using microfluidics," *Ultrasound in medicine & biology*, vol. 37, no. 11, pp. 1952–1957, 2011.

[303] R. Paliwal, R. J. Babu, and S. Palakurthi, "Nanomedicine scale-up technologies: feasibilities and challenges," *Aaps Pharmscitech*, vol. 15, no. 6, pp. 1527–1534, 2014.

[304] C. K. Campbell, K. O'Brien, D. Kosk, R. M. Rumney, P. Glynne-Jones, P. R. Birkin, G. LuTheryn, J. S. Webb, E. Stride, D. Carugo, *et al.*, "Optimising the manufacture of perfluorocarbon nanodroplets through varying sonication parameters," *Ultrasonics Sonochemistry*, vol. 118, p. 107332, 2025.

[305] S. Mahdi Jafari, Y. He, and B. Bhandari, "Nano-emulsion production by sonication and microfluidization—a comparison," *International journal of food properties*, vol. 9, no. 3, pp. 475–485, 2006.

[306] P. S. Sheeran, S. H. Luois, L. B. Mullin, T. O. Matsunaga, and P. A. Dayton, "Design of ultrasonically-activatable nanoparticles using low boiling point perfluorocarbons," *Biomaterials*, vol. 33, no. 11, pp. 3262–3269, 2012.

[307] E. Blanco, H. Shen, and M. Ferrari, "Principles of nanoparticle design for overcoming biological barriers to drug delivery," *Nature biotechnology*, vol. 33, no. 9, pp. 941–951, 2015.

[308] J. Collis, R. Manasseh, P. Liovic, P. Tho, A. Ooi, K. Petkovic-Duran, and Y. Zhu, "Cavitation microstreaming and stress fields created by microbubbles," *Ultrasonics*, vol. 50, no. 2, pp. 273–279, 2010.

[309] E. Stride and C. Coussios, "Cavitation and contrast: the use of bubbles in ultrasound imaging and therapy," *Proceedings of the Institution of Mechanical Engineers, Part H: Journal of Engineering in Medicine*, vol. 224, no. 2, pp. 171–191, 2010.

[310] O. D. Kripfgans, M. L. Fabiilli, P. L. Carson, and J. B. Fowlkes, "On the acoustic vaporization of micrometer-sized droplets," *The Journal of the Acoustical Society of America*, vol. 116, no. 1, pp. 272–281, 2004.

[311] T. J. Mason and P. Cintas, "Sonochemistry," *Handbook of Green Chemistry and Technology*, pp. 372–396, 2002.

[312] M. Zembyla, B. S. Murray, and A. Sarkar, "Water-in-oil emulsions stabilized by surfactants, biopolymers and/or particles: A review," *Trends in Food Science & Technology*, vol. 104, pp. 49–59, 2020.

[313] Y. Ji, J. Zheng, Z. Geng, T. Tan, J. Hu, L. Zhang, and Y. Zhang, "Controllable formation of bulk perfluorohexane nanodroplets by solvent exchange," *Soft Matter*, vol. 18, no. 2, pp. 425–433, 2022.

[314] M. Aliabouzar, K. N. Kumar, and K. Sarkar, "Acoustic vaporization threshold of lipid-coated perfluoropentane droplets," *The Journal of the Acoustical Society of America*, vol. 143, no. 4, pp. 2001–2012, 2018.

[315] H. Lea-banks, Y. Meng, S.-k. Wu, and R. Belhadjhamida, "Ultrasound-sensitive nanodroplets achieve targeted neuromodulation," *Journal of Controlled Release*, vol. 332, no. January, pp. 30–39, 2021.

[316] R. W. DeBlois and C. Bean, "Counting and sizing of submicron particles by

the resistive pulse technique," *Review of Scientific Instruments*, vol. 41, no. 7, pp. 909–916, 1970.

[317] S. Ferri, Q. Wu, A. De Grazia, A. Polydorou, J. P. May, E. Stride, N. D. Evans, and D. Carugo, "Tailoring the size of ultrasound responsive lipid-shelled nanodroplets by varying production parameters and environmental conditions," *Ultrasonics Sonochemistry*, vol. 73, p. 105482, 5 2021.

[318] P. Zhang and T. Porter, "An in vitro study of phase shift nano-emulsion in focused ultrasound surgery: Its potential for enhancing ultrasound-mediated hyperthermia," in *2009 IEEE 35th Annual Northeast Bioengineering Conference*, pp. 1–2, IEEE, 2009.

[319] N. Matsuura, R. Williams, I. Gorelikov, J. Chaudhuri, J. Rowlands, K. Hynynen, S. Foster, P. Burns, and N. Resnik, "Nanoparticle-loaded perfluorocarbon droplets for imaging and therapy," in *2009 IEEE International Ultrasonics Symposium*, pp. 5–8, IEEE, 2009.

[320] R. Williams, C. Wright, E. Cherin, N. Reznik, M. Lee, I. Gorelikov, F. S. Foster, N. Matsuura, and P. N. Burns, "Characterization of submicron phase-change perfluorocarbon droplets for extravascular ultrasound imaging of cancer," *Ultrasound in medicine & biology*, vol. 39, no. 3, pp. 475–489, 2013.

[321] N. Reznik, G. Lajoinie, O. Shpak, E. C. Gelderblom, R. Williams, N. de Jong, M. Versluis, and P. N. Burns, "On the acoustic properties of vaporized submicron perfluorocarbon droplets," *Ultrasound in medicine & biology*, vol. 40, no. 6, pp. 1379–1384, 2014.

[322] Y.-J. Ho and C.-K. Yeh, "Combination of anti-angiogenesis treatment and chemotherapy in solid tumors by using drug-loaded nanodroplets vaporization," in *2016 IEEE International Ultrasonics Symposium (IUS)*, pp. 1–4, IEEE, 2016.

[323] W. Zhang, H. Metzger, S. Vlatakis, A. Claxton, M. A. Carbajal, L. F. Fung, J. Mason, K. A. Chan, A. N. Pouliopoulos, R. A. Fleck, *et al.*, "Characterising the chemical and physical properties of phase-change nanodroplets," *Ultrasonics Sonochemistry*, vol. 97, p. 106445, 2023.

[324] D. Griffiths, P. Carnell-Morris, and M. Wright, "Nanoparticle tracking analysis for multiparameter characterization and counting of nanoparticle suspensions," in *Nanoparticles in biology and medicine: Methods and protocols*, pp. 289–303, Springer, 2020.

[325] M. Y. Chan, Q. M. Dowling, S. J. Sivananthan, and R. M. Kramer, "Particle sizing of nanoparticle adjuvant formulations by dynamic light scattering (dls) and nanoparticle tracking analysis (nta)," *Vaccine Adjuvants: Methods and Protocols*, pp. 239–252, 2017.

[326] N. D. Legband, J. A. Feshitan, M. A. Borden, and B. S. Terry, "Evaluation of peritoneal microbubble oxygenation therapy in a rabbit model of hypoxemia," *IEEE Transactions on Biomedical Engineering*, vol. 62, no. 5, pp. 1376–1382, 2015.

[327] R. Melich, J.-P. Valour, S. Urbaniak, F. Padilla, and C. Charcosset, "Preparation and characterization of perfluorocarbon microbubbles using shirasu porous glass (spg) membranes," *Colloids and Surfaces A: Physicochemical and Engineering Aspects*, vol. 560, pp. 233–243, 2019.

[328] M. Baker, "1,500 scientists lift the lid on reproducibility," *Nature*, vol. 533, no. 7604, 2016.

[329] P. R. Gogate and A. M. Kabadi, "A review of applications of cavitation in biochemical engineering/biotechnology," *Biochemical Engineering Journal*, vol. 44, no. 1, pp. 60–72, 2009.

[330] N. A. Pchelintsev, P. D. Adams, and D. M. Nelson, "Critical parameters for efficient sonication and improved chromatin immunoprecipitation of high molecular weight proteins," *PloS one*, vol. 11, no. 1, p. e0148023, 2016.

[331] M. Ashokkumar, "The characterization of acoustic cavitation bubbles–an overview," *Ultrasonics sonochemistry*, vol. 18, no. 4, pp. 864–872, 2011.

[332] S. G. Gaikwad and A. B. Pandit, "Ultrasound emulsification: effect of ultrasonic and physicochemical properties on dispersed phase volume and droplet size," *Ultrasonics sonochemistry*, vol. 15, no. 4, pp. 554–563, 2008.

[333] S. M. M. Modarres-Gheisari, R. Gavagsaz-Ghoachani, M. Malaki, P. Safarpour, and M. Zandi, "Ultrasonic nano-emulsification–a review," *Ultrasonics Sonochemistry*, vol. 52, pp. 88–105, 2019.

[334] Y.-F. Maa and C. C. Hsu, "Performance of sonication and microfluidization for liquid–liquid emulsification," *Pharmaceutical development and technology*, vol. 4, no. 2, pp. 233–240, 1999.

[335] Z. Gao, A. M. Kennedy, D. A. Christensen, and N. Y. Rapoport, "Drug-loaded nano/microbubbles for combining ultrasonography and targeted chemotherapy," *Ultrasonics*, vol. 48, pp. 260–270, 8 2008.

[336] S. M. Jafari, Y. He, and B. Bhandari, "Production of sub-micron emulsions by ultrasound and microfluidization techniques," *Journal of food engineering*, vol. 82, no. 4, pp. 478–488, 2007.

[337] S. Ferdous, J. L. Dopp, and N. F. Reuel, "Optimization of E. coli tip-sonication for high-yield cell-free extract using finite element modeling," *AIChE Annual Meeting, Conference Proceedings*, vol. 2021-November, 2021.

[338] V. Filipe, A. Hawe, and W. Jiskoot, "Critical Evaluation of Nanoparticle Tracking Analysis (NTA) by NanoSight for the Measurement of Nanoparticles and Protein Aggregates," *Pharmaceutical Research*, vol. 27, p. 796, 5 2010.

[339] K. P. Mercado, K. Radhakrishnan, K. Stewart, L. Snider, D. Ryan, and K. J. Haworth, "Size-isolation of ultrasound-mediated phase change perfluorocarbon droplets using differential centrifugation," *The Journal of the Acoustical Society of America*, vol. 139, no. 5, pp. EL142–EL148, 2016.

[340] A. Kabalnov, D. Klein, T. Pelura, E. Schutt, and J. Weers, "Dissolution of multicomponent microbubbles in the bloodstream: 1. theory," *Ultrasound in medicine & biology*, vol. 24, no. 5, pp. 739–749, 1998.

[341] B. D. Spiess, "Perfluorocarbon gas transport: an overview of medical history with yet unrealized potentials," *Shock*, vol. 52, no. 1S, pp. 7–12, 2019.

[342] M. Choi, S. Park, K. Park, H. Jeong, and J. Hong, "Nitric oxide delivery

using biocompatible perfluorocarbon microemulsion for antibacterial effect," *ACS Biomaterials Science & Engineering*, vol. 5, no. 3, pp. 1378–1383, 2019.

[343] M. B. Grisham, G. G. Johnson, and J. R. Lancaster Jr, "Quantitation of nitrate and nitrite in extracellular fluids," in *Methods in enzymology*, vol. 268, pp. 237–246, Elsevier, 1996.

[344] D. Tsikas, "Analysis of nitrite and nitrate in biological fluids by assays based on the griess reaction: appraisal of the griess reaction in the l-arginine/nitric oxide area of research," *Journal of Chromatography B*, vol. 851, no. 1-2, pp. 51–70, 2007.

[345] N. S. Bryan and M. B. Grisham, "Methods to detect nitric oxide and its metabolites in biological samples," *Free radical biology and medicine*, vol. 43, no. 5, pp. 645–657, 2007.

[346] Y. C. Boo, S. L. Tressel, and H. Jo, "An improved method to measure nitrate/nitrite with an no-selective electrochemical sensor," *Nitric Oxide*, vol. 16, no. 2, pp. 306–312, 2007.

[347] R. V. Pinto, F. Antunes, J. Pires, A. Silva-Herdade, and M. L. Pinto, "A comparison of different approaches to quantify nitric oxide release from no-releasing materials in relevant biological media," *Molecules*, vol. 25, no. 11, p. 2580, 2020.

[348] L. Bellavia, D. B. Kim-Shapiro, and S. B. King, "Detecting and monitoring no, sno and nitrite in vivo," *Future science OA*, vol. 1, no. 1, p. FSO36, 2015.

[349] R. A. Hunter, W. L. Storm, P. N. Coneski, and M. H. Schoenfisch, "Inaccuracies of nitric oxide measurement methods in biological media," *Analytical chemistry*, vol. 85, no. 3, pp. 1957–1963, 2013.

[350] A. Fontijn, A. J. Sabadell, and R. J. Ronco, "Homogeneous chemiluminescent measurement of nitric oxide with ozone. implications for continuous selective monitoring of gaseous air pollutants," *Analytical chemistry*, vol. 42, no. 6, pp. 575–579, 1970.

[351] C. E. Sparacino-Watkins and J. R. Lancaster Jr, "Direct measurement of

nitric oxide (no) production rates from enzymes using ozone-based gas-phase chemiluminescence (cl)," *Nitric Oxide*, vol. 117, pp. 60–71, 2021.

[352] J. Li, A. LoBue, S. K. Heuser, and M. M. Cortese-Krott, "Determination of nitric oxide and its metabolites in biological tissues using ozone-based chemiluminescence detection: A state-of-the-art review," *Antioxidants*, vol. 13, no. 2, p. 179, 2024.

[353] E. Goshi, G. Zhou, and Q. He, "Nitric oxide detection methods in vitro and in vivo," *Medical gas research*, vol. 9, no. 4, pp. 192–207, 2019.

[354] I. B. Butler, M. A. Schoonen, and D. T. Rickard, "Removal of dissolved oxygen from water: a comparison of four common techniques," *Talanta*, vol. 41, no. 2, pp. 211–215, 1994.

[355] E. Wilhelm, R. Battino, and R. J. Wilcock, "Low-pressure solubility of gases in liquid water," *Chemical reviews*, vol. 77, no. 2, pp. 219–262, 1977.

[356] T. A. Tabish, M. Z. Hussain, S. Zervou, W. K. Myers, W. Tu, J. Xu, I. Beer, W. E. Huang, R. Chandrawati, M. J. Crabtree, *et al.*, "S-nitrosocysteamine-functionalised porous graphene oxide nanosheets as nitric oxide delivery vehicles for cardiovascular applications," *Redox Biology*, vol. 72, p. 103144, 2024.

[357] R. del Barrio-Galán, I. Nevares, S. Pérez-Magariño, and M. del Alamo-Sanza, "Dissolved oxygen removal in wines by gas sparging, its optimization and chemical impact," *Beverages*, vol. 10, no. 1, p. 3, 2023.

[358] A. E. Keithley, P. Woodruff, D. J. Williams, N. R. Dugan, and D. A. Lytle, "Nitrogen-sparging assisted anoxic biological drinking water treatment system," *AWWA Water Science*, vol. 5, no. 5, p. e1359, 2023.

[359] M. U. Vera, A. Saint-Jalmes, and D. J. Durian, "Scattering optics of foam," *Applied optics*, vol. 40, no. 24, pp. 4210–4214, 2001.

[360] R. Battino and H. L. Clever, "The solubility of gases in liquids," *Chemical Reviews*, vol. 66, no. 4, pp. 395–463, 1966.

[361] W. Krämer, R. Schubert, and U. Massing, "Small-scale preparation of

perfluorocarbon-nanoemulsions utilizing dual centrifugation," *International Journal of Pharmaceutics*, vol. 572, p. 118753, 2019.

[362] M. Moller, H. Botti, C. Batthyany, H. Rubbo, R. Radi, and A. Denicola, "Direct measurement of nitric oxide and oxygen partitioning into liposomes and low density lipoprotein," *Journal of Biological Chemistry*, vol. 280, no. 10, pp. 8850–8854, 2005.

[363] T. Yingchoncharoen, T. Rakyhao, S. Chuncharunee, P. Sritara, P. Pienvichit, K. Paiboonsukwong, P. Sathavorasmith, K. Sirirat, T. Sriwantana, S. Srihirun, *et al.*, "Inhaled nebulized sodium nitrite decreases pulmonary artery pressure in β-thalassemia patients with pulmonary hypertension," *Nitric oxide*, vol. 76, pp. 174–178, 2018.

[364] S. Velmurugan, J. M. Gan, K. S. Rathod, R. S. Khambata, S. M. Ghosh, A. Hartley, S. Van Eijl, V. Sagi-Kiss, T. A. Chowdhury, M. Curtis, *et al.*, "Dietary nitrate improves vascular function in patients with hypercholesterolemia: a randomized, double-blind, placebo-controlled study," *The American journal of clinical nutrition*, vol. 103, no. 1, pp. 25–38, 2016.

[365] L. A. Tortajada-Genaro and P. Campins-Falco, "Multivariate standardisation for non-linear calibration range in the chemiluminescence determination of chromium," *Talanta*, vol. 72, no. 3, pp. 1004–1012, 2007.

[366] M. Feelisch, T. Rassaf, S. Mnaimneh, N. Singh, N. S. Bryan, D. Jourd'Heuil, and M. Kelm, "Concomitant s-, n-, and heme-nitros (yl) ation in biological tissues and fluids: implications for the fate of no in vivo," *The FASEB journal*, vol. 16, no. 13, pp. 1775–1785, 2002.

[367] A. K. Pal, I. Aalaei, S. Gadde, P. Gaines, D. Schmidt, P. Demokritou, and D. Bello, "High resolution characterization of engineered nanomaterial dispersions in complex media using tunable resistive pulse sensing technology," *ACS nano*, vol. 8, no. 9, pp. 9003–9015, 2014.

[368] S. Ten Klooster, V. J. Boerkamp, M. Hennebelle, J. P. van Duynhoven, K. Schroën, and C. C. Berton-Carabin, "Unravelling the effect of droplet size

on lipid oxidation in o/w emulsions by using microfluidics," *Scientific Reports*, vol. 14, no. 1, p. 8895, 2024.

[369] R. P. Howlin, K. Cathie, L. Hall-Stoodley, V. Cornelius, C. Duignan, R. N. Allan, B. O. Fernandez, N. Barraud, K. D. Bruce, J. Jefferies, *et al.*, "Low-dose nitric oxide as targeted anti-biofilm adjunctive therapy to treat chronic pseudomonas aeruginosa infection in cystic fibrosis," *Molecular Therapy*, vol. 25, no. 9, pp. 2104–2116, 2017.

[370] S. Li, S. Lin, Y. Cheng, T. O. Matsunaga, R. J. Eckersley, and M.-X. Tang, "Quantifying activation of perfluorocarbon-based phase-change contrast agents using simultaneous acoustic and optical observation," *Ultrasound in medicine & biology*, vol. 41, no. 5, pp. 1422–1431, 2015.

[371] G. Zhao, M. L. Usui, S. I. Lippman, G. A. James, P. S. Stewart, P. Fleckman, and J. E. Olerud, "Biofilms and inflammation in chronic wounds," *Advances in wound care*, vol. 2, no. 7, pp. 389–399, 2013.

[372] R. Wolcott, D. Rhoads, M. Bennett, B. Wolcott, L. Gogokhia, J. Costerton, and S. Dowd, "Chronic wounds and the medical biofilm paradigm," *Journal of wound care*, vol. 19, no. 2, pp. 45–53, 2010.

[373] K. Kirketerp-Møller, P. S. Stewart, and T. Bjarnsholt, "The zone model: A conceptual model for understanding the microenvironment of chronic wound infection," *Wound Repair and Regeneration*, vol. 28, no. 5, pp. 593–599, 2020.

[374] K. Gjødsbøl, J. J. Christensen, T. Karlsmark, B. Jørgensen, B. M. Klein, and K. A. Krogfelt, "Multiple bacterial species reside in chronic wounds: a longitudinal study," *International wound journal*, vol. 3, no. 3, pp. 225–231, 2006.

[375] M. Wu, H. Pan, W. Leng, X. Lei, L. Chen, and Z. Liang, "Distribution of microbes and drug susceptibility in patients with diabetic foot infections in southwest china," *Journal of diabetes research*, vol. 2018, no. 1, p. 9817308, 2018.

[376] J. Dang, M. Zhu, F. Dong, R. Zhong, Z. Liu, J. Fang, J. Zhang, and

J. Pan, "Ultrasound-activated nanodroplet disruption of the enterococcus faecalis biofilm in dental root canal," *ACS Applied Bio Materials*, 2022.

[377] Y. Sun, S. E. Dowd, E. Smith, D. D. Rhoads, and R. D. Wolcott, "In vitro multispecies lubbock chronic wound biofilm model," *Wound repair and regeneration*, vol. 16, no. 6, pp. 805–813, 2008.

[378] I. C. Thaarup and T. Bjarnsholt, "Current in vitro biofilm-infected chronic wound models for developing new treatment possibilities," *Advances in wound care*, vol. 10, no. 2, pp. 91–102, 2021.

[379] A. Arhin and C. Boucher, "The outer membrane protein oprq and adherence of pseudomonas aeruginosa to human fibronectin," *Microbiology*, vol. 156, no. 5, pp. 1415–1423, 2010.

[380] A. Grace, R. Sahu, D. R. Owen, and V. A. Dennis, "Pseudomonas aeruginosa reference strains pao1 and pa14: A genomic, phenotypic, and therapeutic review," *Frontiers in Microbiology*, vol. 13, p. 1023523, 2022.

[381] R. Yang, H. Zhang, Z. Marfavi, Q. Lv, Y. Han, K. Sun, C. Yuan, and K. Tao, "Infiltrating perfluorocarbon nanoemulsion and sensitizing ultrasound cavitation to eradicate biofilms," *ACS Applied Materials & Interfaces*, vol. 16, no. 3, pp. 3126–3138, 2024.

[382] M. M. T. Khan, B. H. Pyle, and A. K. Camper, "Specific and rapid enumeration of viable but nonculturable and viable-culturable gram-negative bacteria by using flow cytometry," *Applied and environmental microbiology*, vol. 76, no. 15, pp. 5088–5096, 2010.

[383] M. Rosenberg, N. F. Azevedo, and A. Ivask, "Propidium iodide staining underestimates viability of adherent bacterial cells," *Scientific reports*, vol. 9, no. 1, p. 6483, 2019.

[384] P. Stiefel, S. Schmidt-Emrich, K. Maniura-Weber, and Q. Ren, "Critical aspects of using bacterial cell viability assays with the fluorophores syto9 and propidium iodide," *BMC microbiology*, vol. 15, no. 1, pp. 1–9, 2015.

[385] S. Stocks, "Mechanism and use of the commercially available viability stain,

baclight," *Cytometry Part A: The Journal of the International Society for Analytical Cytology*, vol. 61, no. 2, pp. 189–195, 2004.

[386] S. Wang, X. Liu, H. Liu, L. Zhang, Y. Guo, S. Yu, D. J. Wozniak, and L. Z. Ma, "The exopolysaccharide psl–edna interaction enables the formation of a biofilm skeleton in p seudomonas aeruginosa," *Environmental microbiology reports*, vol. 7, no. 2, pp. 330–340, 2015.

[387] I. Goldstein, C. Hollerman, and J. M. Merrick, "Protein-carbohydrate interaction i. the interaction of polysaccharides with concanavalin a," *Biochimica et Biophysica Acta (BBA)-General Subjects*, vol. 97, no. 1, pp. 68–76, 1965.

[388] M. Strathmann, J. Wingender, and H.-C. Flemming, "Application of fluorescently labelled lectins for the visualization and biochemical characterization of polysaccharides in biofilms of pseudomonas aeruginosa," *Journal of Microbiological Methods*, vol. 50, no. 3, pp. 237–248, 2002.

[389] J. Jonkman and C. M. Brown, "Any way you slice it—a comparison of confocal microscopy techniques," *Journal of biomolecular techniques: JBT*, vol. 26, no. 2, p. 54, 2015.

[390] G. Cox and C. J. Sheppard, "Practical limits of resolution in confocal and non-linear microscopy," *Microscopy research and technique*, vol. 63, no. 1, pp. 18–22, 2004.

[391] B. D. Jett, K. L. Hatter, M. M. Huycke, and M. S. Gilmore, "Simplified agar plate method for quantifying viable bacteria," *Biotechniques*, vol. 23, no. 4, pp. 648–650, 1997.

[392] B. Herigstad, M. Hamilton, and J. Heersink, "How to optimize the drop plate method for enumerating bacteria," *Journal of microbiological methods*, vol. 44, no. 2, pp. 121–129, 2001.

[393] A. L. Koch, "Growth measurement," *Methods for general and molecular microbiology*, pp. 172–199, 2007.

[394] L. Li, N. Mendis, H. Trigui, J. D. Oliver, and S. P. Faucher, "The importance

of the viable but non-culturable state in human bacterial pathogens," *Frontiers in microbiology*, vol. 5, p. 258, 2014.

[395] M. Ayrapetyan, T. Williams, and J. D. Oliver, "Relationship between the viable but nonculturable state and antibiotic persister cells," *Journal of bacteriology*, vol. 200, no. 20, pp. 10–1128, 2018.

[396] P. Ommen, N. Zobek, and R. L. Meyer, "Quantification of biofilm biomass by staining: Non-toxic safranin can replace the popular crystal violet," *Journal of microbiological methods*, vol. 141, pp. 87–89, 2017.

[397] M. Sønderholm, K. N. Kragh, K. Koren, T. H. Jakobsen, S. E. Darch, M. Alhede, P. Ø. Jensen, M. Whiteley, M. Kühl, and T. Bjarnsholt, "Pseudomonas aeruginosa aggregate formation in an alginate bead model system exhibits in vivo-like characteristics," *Applied and environmental microbiology*, vol. 83, no. 9, pp. e00113–17, 2017.

[398] J. S.-M. Yeh, C. A. Sennoga, E. McConnell, R. Eckersley, M.-X. Tang, S. Nourshargh, J. M. Seddon, D. O. Haskard, and P. Nihoyannopoulos, "A targeting microbubble for ultrasound molecular imaging," *PloS one*, vol. 10, no. 7, p. e0129681, 2015.

[399] A. Kropinski, V. Lewis, and D. Berry, "Effect of growth temperature on the lipids, outer membrane proteins, and lipopolysaccharides of pseudomonas aeruginosa pao," *Journal of bacteriology*, vol. 169, no. 5, pp. 1960–1966, 1987.

[400] G. Power, Z. Moore, and T. O'connor, "Measurement of ph, exudate composition and temperature in wound healing: a systematic review," *Journal of wound care*, vol. 26, no. 7, pp. 381–397, 2017.

[401] J. Huang, C. Fan, Y. Ma, and G. Huang, "Exploring thermal dynamics in wound healing: The impact of temperature and microenvironment," *Clinical, Cosmetic and Investigational Dermatology*, pp. 1251–1258, 2024.

[402] K. Forier, A.-S. Messiaen, K. Raemdonck, H. Nelis, S. De Smedt, J. Demeester, T. Coenye, and K. Braeckmans, "Probing the size limit for nanomedicine penetration into burkholderia multivorans and pseudomonas aeruginosa biofilms," *Journal of Controlled Release*, vol. 195, pp. 21–28, 2014.

[403] T. Bjarnsholt, M. Alhede, M. Alhede, S. R. Eickhardt-Sørensen, C. Moser, M. Kühl, P. Ø. Jensen, and N. Høiby, "The in vivo biofilm," *Trends in microbiology*, vol. 21, no. 9, pp. 466–474, 2013.

[404] C. Stover, X. Pham, A. Erwin, S. Mizoguchi, P. Warrener, M. Hickey, F. Brinkman, W. Hufnagle, D. Kowalik, M. Lagrou, *et al.*, "Complete genome sequence of pseudomonas aeruginosa pao1, an opportunistic pathogen," *Nature*, vol. 406, no. 6799, pp. 959–964, 2000.

[405] J. Liao, M. J. Schurr, and K. Sauer, "The merr-like regulator brlr confers biofilm tolerance by activating multidrug efflux pumps in pseudomonas aeruginosa biofilms," *Journal of bacteriology*, vol. 195, no. 15, pp. 3352–3363, 2013.

[406] Y. Cheng, P. A. De Bank, and A. Bolhuis, "An in vitro and ex vivo wound infection model to test topical and systemic treatment with antibiotics," *Journal of Applied Microbiology*, vol. 133, no. 5, pp. 2993–3006, 2022.

[407] S. Keller, G. LuTheryn, M. Gray, B. Lyons, R. O. Cleveland, E. Stride, and C. C. Coussios, "Quantitative evaluation of anti-biofilm cavitation activity seeded from microbubbles or protein cavitation nuclei by passive acoustic mapping," *Physics in Medicine and Biology*, 2024.

[408] D. Fleming, W. Redman, G. S. Welch, N. V. Mdluli, C. N. Rouchon, K. L. Frank, and K. P. Rumbaugh, "Utilizing glycoside hydrolases to improve the quantitation and visualization of biofilm bacteria," *Biofilm*, vol. 2, p. 100037, 2020.

[409] T. Trunk, H. S. Khalil, and J. C. Leo, "Bacterial autoaggregation," *AIMS microbiology*, vol. 4, no. 1, p. 140, 2018.

[410] A. Crowther, G. LuTheryn, R. Garcia-Maset, M. Parhizkar, J. M. Sutton, C. Hind, and D. Carugo, "Efficacy of nitric oxide donors and edta against pseudomonas aeruginosa biofilms: Implications for antimicrobial therapy in chronic wounds," *Biofilm*, vol. 9, p. 100280, 2025.

[411] E. J. Brisbois, J. Bayliss, J. Wu, T. C. Major, C. Xi, S. C. Wang, R. H. Bartlett, H. Handa, and M. E. Meyerhoff, "Optimized polymeric film-based

nitric oxide delivery inhibits bacterial growth in a mouse burn wound model," *Acta biomaterialia*, vol. 10, no. 10, pp. 4136–4142, 2014.

[412] D. O. Schairer, J. S. Chouake, J. D. Nosanchuk, and A. J. Friedman, "The potential of nitric oxide releasing therapies as antimicrobial agents," *Virulence*, vol. 3, no. 3, pp. 271–279, 2012.

[413] B. Q. Huang and E. C. Yeung, "Chemical and physical fixation of cells and tissues: an overview," *Plant microtechniques and protocols*, pp. 23–43, 2015.

[414] J. Y. Chung, Y. Ahn, J. H. Lee, S. Yang, S. C. Lee, H. Kong, and H. J. Chung, "Microbubble-controlled delivery of biofilm-targeting nanoparticles to treat mrsa infection," *Advanced Functional Materials*, May 2025.

[415] R. Hartmann, H. Jeckel, E. Jelli, P. K. Singh, S. Vaidya, M. Bayer, D. K. Rode, L. Vidakovic, F. Díaz-Pascual, J. C. Fong, *et al.*, "Quantitative image analysis of microbial communities with biofilmq," *Nature microbiology*, vol. 6, no. 2, pp. 151–156, 2021.

[416] S. Li, K. Pang, S. Zhu, K. Pate, and J. Yin, "Perfluorodecalin-based oxygenated emulsion as a topical treatment for chemical burn to the eye," *Nature Communications*, vol. 13, no. 1, p. 7371, 2022.

[417] D. Chen, S. Ganesh, W. Wang, and M. Amiji, "The role of surface chemistry in serum protein corona-mediated cellular delivery and gene silencing with lipid nanoparticles," *Nanoscale*, vol. 11, no. 18, pp. 8760–8775, 2019.

[418] S. K. Yarmoska, H. Yoon, and S. Y. Emelianov, "Lipid shell composition plays a critical role in the stable size reduction of perfluorocarbon nanodroplets," *Ultrasound in medicine & biology*, vol. 45, no. 6, pp. 1489–1499, 2019.

[419] Y.-m. Cai and J. S. Webb, "Optimization of nitric oxide donors for investigating biofilm dispersal response in pseudomonas aeruginosa clinical isolates," *Applied microbiology and biotechnology*, vol. 104, pp. 8859–8869, 2020.

[420] J. R. Hall, K. R. Rouillard, D. J. Suchyta, M. D. Brown, M. J. R. Ahonen, and M. H. Schoenfisch, "Mode of nitric oxide delivery affects antibacterial action," *ACS biomaterials science & engineering*, vol. 6, no. 1, pp. 433–441, 2019.

[421] T.-K. Nguyen, R. Selvanayagam, K. K. Ho, R. Chen, S. K. Kutty, S. A. Rice, N. Kumar, N. Barraud, H. T. Duong, and C. Boyer, "Co-delivery of nitric oxide and antibiotic using polymeric nanoparticles," *Chemical science*, vol. 7, no. 2, pp. 1016–1027, 2016.

[422] P. K. Vestweber, J. Wächter, V. Planz, N. Jung, and M. Windbergs, "The interplay of pseudomonas aeruginosa and staphylococcus aureus in dual-species biofilms impacts development, antibiotic resistance and virulence of biofilms in in vitro wound infection models," *Plos one*, vol. 19, no. 5, p. e0304491, 2024.

[423] L. Camus, P. Briaud, F. Vandenesch, A. Doléans-Jordheim, and K. Moreau, "Mixed populations and co-infection: Pseudomonas aeruginosa and staphylococcus aureus," in *Pseudomonas aeruginosa: Biology, Pathogenesis and Control Strategies*, pp. 397–424, Springer, 2022.

[424] T. Dalton, S. E. Dowd, R. D. Wolcott, Y. Sun, C. Watters, J. A. Griswold, and K. P. Rumbaugh, "An in vivo polymicrobial biofilm wound infection model to study interspecies interactions," *PloS one*, vol. 6, no. 11, p. e27317, 2011.

[425] R. J. Barnes, R. R. Bandi, W. S. Wong, N. Barraud, D. McDougald, A. Fane, S. Kjelleberg, and S. A. Rice, "Optimal dosing regimen of nitric oxide donor compounds for the reduction of pseudomonas aeruginosa biofilm and isolates from wastewater membranes," *Biofouling*, vol. 29, no. 2, pp. 203–212, 2013.

[426] S. M. Daboor, R. Raudonis, and Z. Cheng, "Characterizations of the viability and gene expression of dispersal cells from pseudomonas aeruginosa biofilms released by alginate lyase and tobramycin," *PLoS One*, vol. 16, no. 10, p. e0258950, 2021.

[427] N. K. D. Ragupathi, D. P. M. Sethuvel, H. T. Dwarakanathan, D. Murugan, Y. Umashankar, P. N. Monk, E. Karunakaran, and B. Veeraraghavan, "The influence of biofilm formation on carbapenem resistance in clinical klebsiella pneumoniae infections: phenotype vs genome-wide analysis," *BioRxiv*, pp. 2020–07, 2020.

[428] P. Flores, J. Luo, D. W. Mueller, F. Muecklich, and L. Zea, "Space biofilms–

an overview of the morphology of pseudomonas aeruginosa biofilms grown on silicone and cellulose membranes on board the international space station," *Biofilm*, p. 100182, 2024.

[429] R. P. Dassanayake, S. M. Falkenberg, J. A. Stasko, A. L. Shircliff, J. D. Lippolis, and R. E. Briggs, "Identification of a reliable fixative solution to preserve the complex architecture of bacterial biofilms for scanning electron microscopy evaluation," *PLoS One*, vol. 15, no. 5, p. e0233973, 2020.

[430] M. Aliabouzar, O. D. Kripfgans, J. B. Fowlkes, and M. L. Fabiilli, "Bubble nucleation and dynamics in acoustic droplet vaporization: a review of concepts, applications, and new directions," *Zeitschrift für Medizinische Physik*, vol. 33, no. 3, pp. 387–406, 2023.

[431] H. Hu, C. Hu, W. Guo, B. Zhu, and S. Wang, "Wearable ultrasound devices: An emerging era for biomedicine and clinical translation," *Ultrasonics*, p. 107401, 2024.

[432] P. L. van Neer, L. C. Peters, R. G. Verbeek, B. Peeters, G. de Haas, L. Hörchens, L. Fillinger, T. Schrama, E. J. Merks-Swolfs, K. Gijsbertse, *et al.*, "Flexible large-area ultrasound arrays for medical applications made using embossed polymer structures," *Nature communications*, vol. 15, no. 1, p. 2802, 2024.

Appendix A

Additional Figures

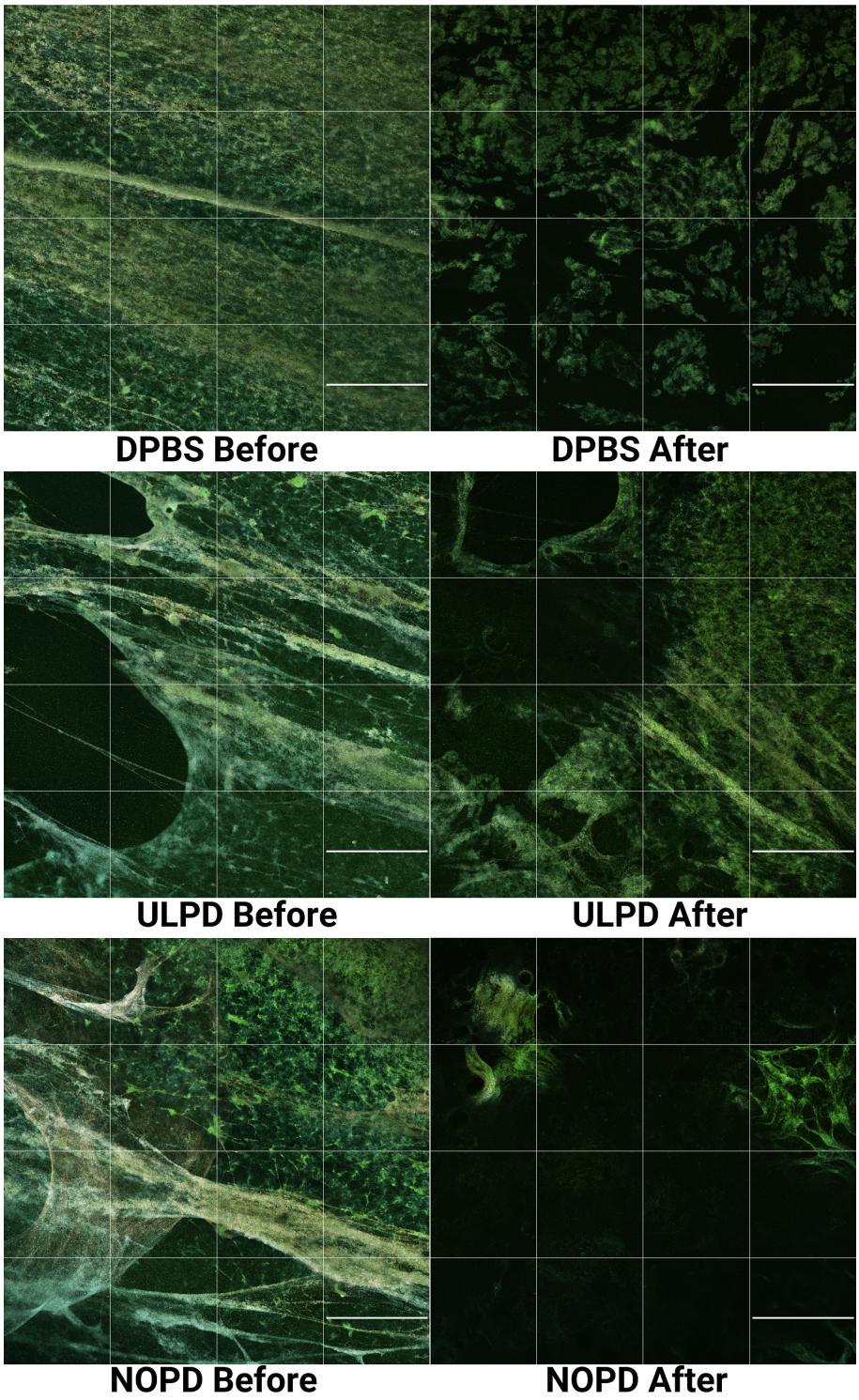

Figure A.1: Representative surface slice 10 × tilescan images of 48 h WCM biofilms, before and after exposure to DPBS, ULPD, and NOPD treatment conditions. Biofilms were stained with SYTO9 (green), PI (red), and ConA (Blue) with each panel composed of 16 tiles imaged at 10 × magnification covering a 4.192 mm × 4.192 mm area. Scale bar = 1 mm.

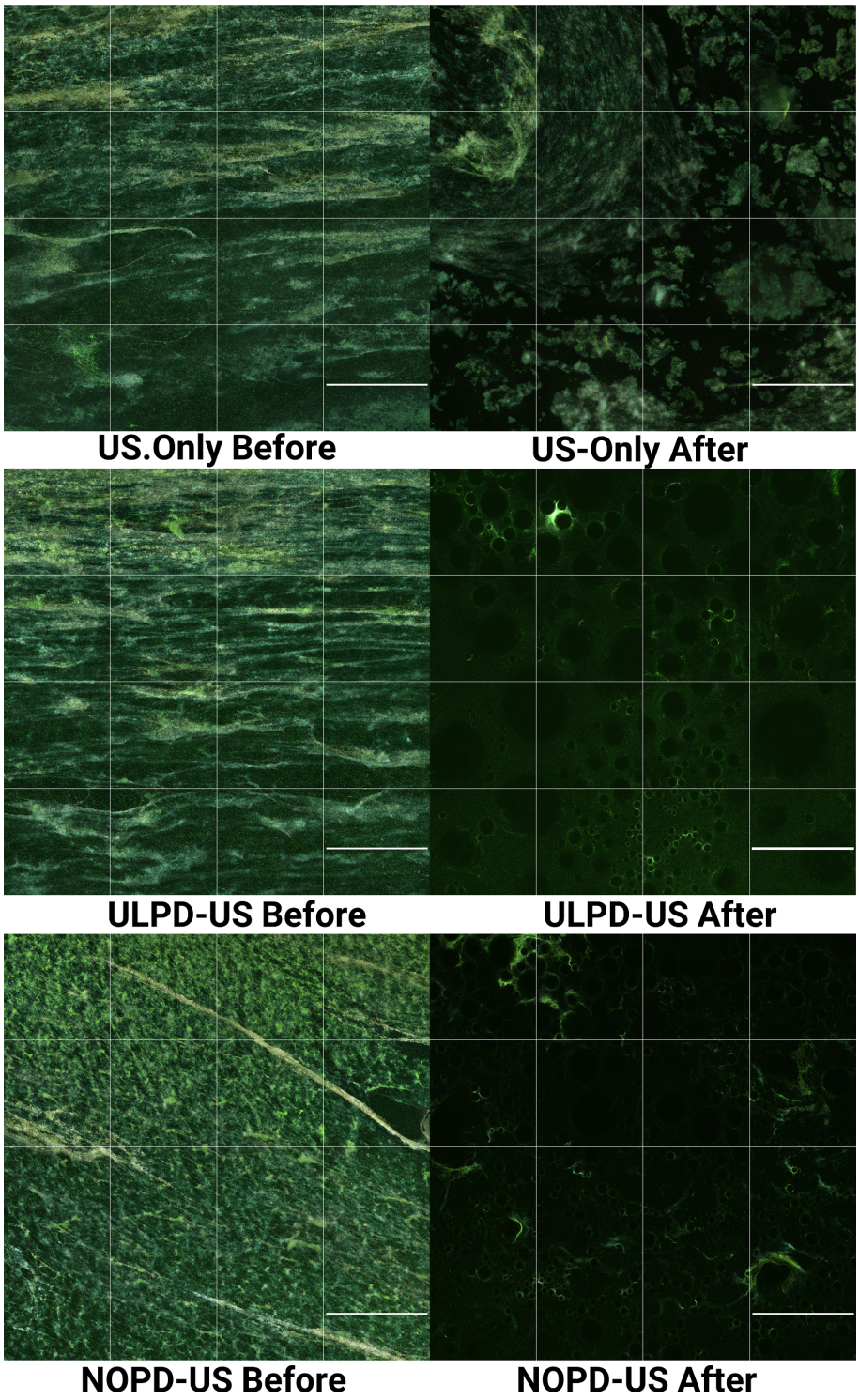

Figure A.2: Representative surface slice 10 × tilescan images of WCM biofilms before and after exposure to NOPD, ULPD-US, and NOPD-US treatment conditions. Biofilms were stained with SYTO9 (green), PI (red), and ConA (Blue) with each panel composed of 16 tiles imaged at 10 × magnification covering a 4.192 mm × 4.192 mm area. Scale bar = 1 mm.

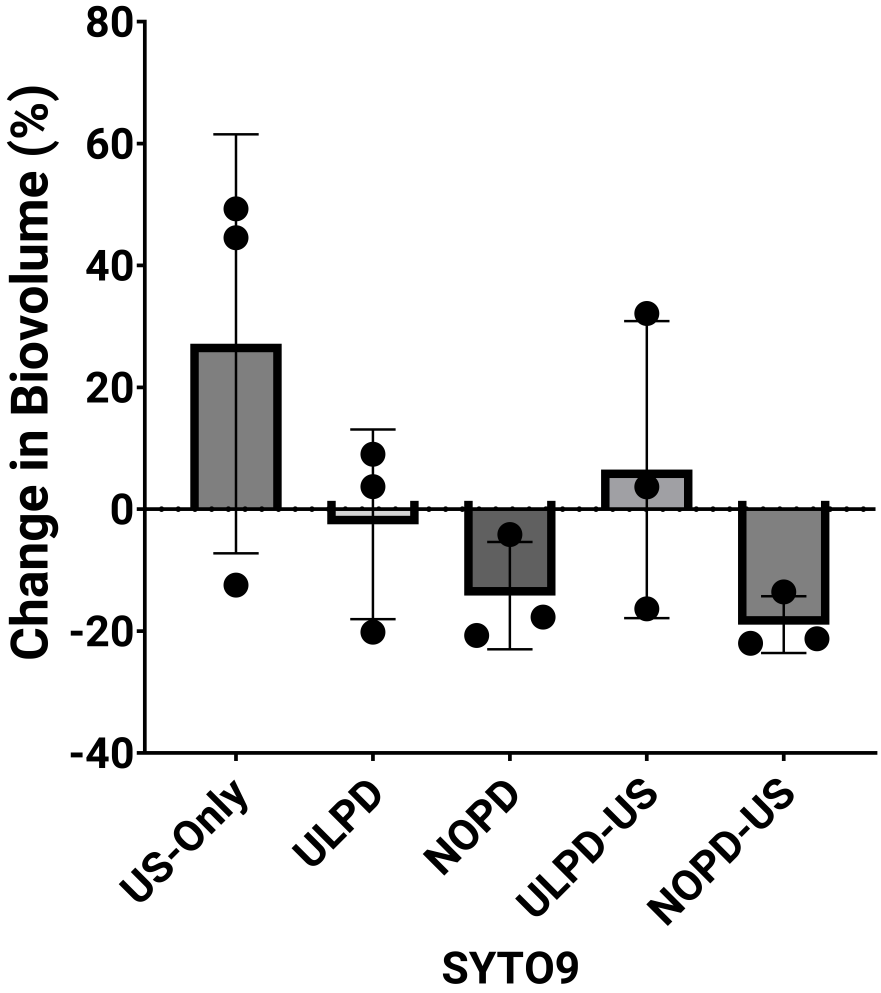

Figure A.3: Quantification of changes in SYTO9 biovolume before and after treatment. NO-loaded PDs combined with US show the greatest reduction in biofilm biovolume. Treatments: US-Only (Ultrasound only), ULPD (Unloaded PDs), NOPD (NO-loaded PDs), ULPD-US (Unloaded PDs with US-stimulation), NOPD (NO-PDs with US-stimulation) Bars represent mean ± S.D. from three independent experiments (n = 3). No significant difference between sample pairs (P>0.05)

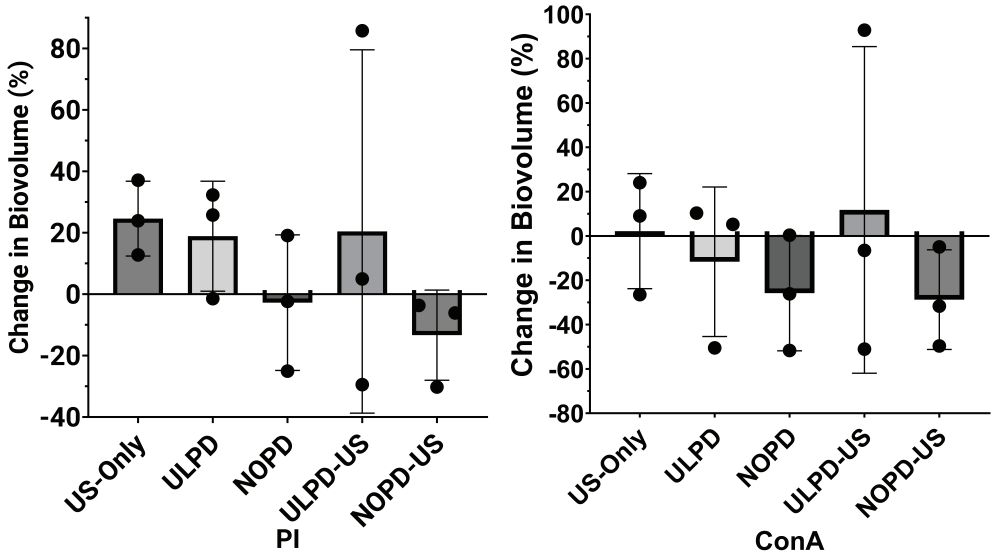

Figure A.4: Quantification of changes in PI (left) and ConA (right) biovolume before and after treatment. Treatments: US-Only (Ultrasound only), ULPD (Unloaded PDs), NOPD (NO-loaded PDs), ULPD-US (Unloaded PDs with US-stimulation), NOPD (NO-PDs with US-stimulation) Bars represent mean ± S.D. from three independent experiments (n = 3). No significant difference between sample pairs (P>0.05)

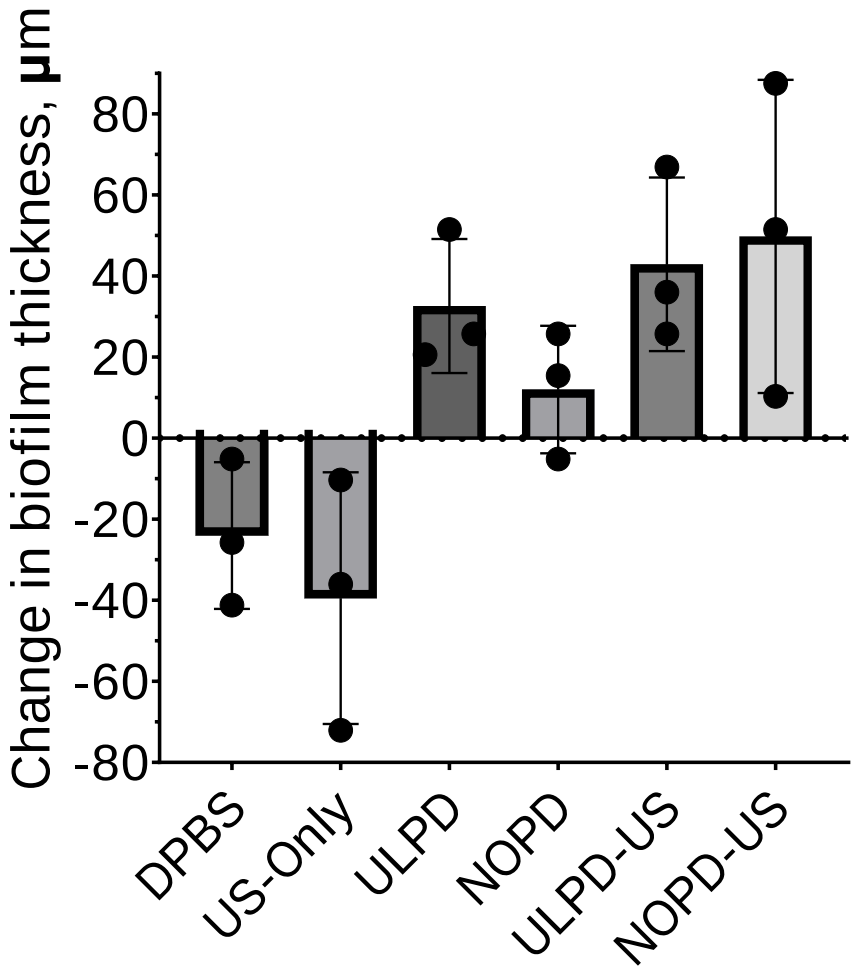

Figure A.5: Quantification in changes to biofilm thickness post-treatment. Treatments: US-Only (Ultrasound only), ULPD (Unloaded PDs), NOPD (NO-loaded PDs), ULPD-US (Unloaded PDs with US-stimulation), NOPD (NO-PDs with US-stimulation) Each bar represents the mean thickness change from three independent biological replicates, with each replicate conducted on a separate experimental day using a freshly prepared bacterial stock culture. Error bars indicate standard deviation (S.D.) (n = 3).